DETONATION DIFFRACTION THROUGH AN ABRUPT AREA EXPANSION

Thesis by

Eric Schultz

In Partial Fulfillment of the Requirements

for the Degree of

Doctor of Philosophy

California Institute of Technology

Pasadena, California

2000

(Submitted April 20, 2000)

Acknowledgments

The efforts of many people have facilitated the research presented in this thesis. Professor Joe Shepherd has served as my advisor, providing me with all of the responsibilities and challenges that one could hope for and making this a true learning experience. Pavel Svitek has been an indispensable technician whose contributions can not be overstated, and many of the experimental facilities were designed and constructed with the help of Joe Haggerty, Larry Frazier, and Ali Kiani in the machine shop. Larry Shaw and Jack Stiles of the Lawrence Livermore National Laboratory helped significantly by providing the framing camera and information necessary to get it running. The assistance and discussions provided by past graduate students, Raza Akbar, Mike Kaneshige, and Chris Krok, past post-doctoral researcher, Julian Lee, and current graduate students, Joanna Austin and Chris Eckett are greatly appreciated. Assistant Professor Andrew Higgins at McGill University has been a reliable source of engagement, ideas, and encouragement throughout my graduate education. My doctoral committee, consisting of Professors Hans Hornung, Brad Sturtevant, Andy Ingersoll, and Jim Beck, deserve my thanks for their input and patience as I have progressed during the past several years. Finally, Suzy Dake has proven to be an invaluable administrative assistant.

This research has been funded by the National Defense Science and Engineering Graduate (NDSEG) Fellowship Program, a NASA Small Business Technology Transfer (STTR) collaborative contract between Caltech and Tom Sobota and Jim Sterling of Advanced Projects Research Inc., and a Multidisciplinary Research Program of the University Research Initiative (MURI) award from the Office of Naval Research.

Abstract

The problem of a self-sustaining detonation wave diffracting from confinement into an unconfined space through an abrupt area change is characterized by the geometric scale of the confinement and the reaction scale of the detonation. Previous investigations have shown that this expansion associated with a detonation transitioning from planar to spherical geometry can result in two possible outcomes depending upon the combustible mixture composition, initial thermodynamic state, and confining geometry. Competition between the energy release rate and expansion rate behind the diffracting wave is crucial. The sub-critical case is characterized by the rate of expansion exceeding the energy release rate. As the chemical reactions are quenched, the shock wave decouples from the reaction zone and rapidly decays. The energy release rate dominates the expansion rate in the super-critical case, maintaining the coupling between the shock and reaction zone which permits successful transition across the area change. A critical diffraction model has been developed in the present research effort from which the initial conditions separating the sub-critical and super-critical cases can be analytically determined. Chemical equilibrium calculations and detonation simulations with validated detailed reaction mechanisms provide the model input parameters. Experiments over a wide range of initial conditions with single- and multi-sequence shadowgraphy and digital chemiluminescence imaging support the model derivation and numerical calculations. Good agreement has been obtained between the critical diffraction model and experimental results.

Contents

List of Figures

List of Tables

Nomenclature

α	angle between disturbance trajectory and the undiffracted shock normal
Δ	reaction length
γ	ratio of specific heats
Δh^0	reaction energy release
λ	detonation cell width
ρ	density
τ	reaction time
Ω	kinetic production rate
σ_i	thermicity coefficients
θ	non-dimensional effective activation energy
A	proportionality constant
c	frozen acoustic speed
CJ	Chapman-Jouguet state
C_{p}	constant pressure specific heat
C_{v}	constant volume specific heat
d	tube diameter
d_c	critical tube diameter
e	specific internal energy
E_a	activation energy
h	specific enthalpy
i	species index

k	pre-exponential kinetic rate constant
M	Mach number
P	pressure
R	radial distance
R_g	gas constant
s	post-shock state
t	time
t_c	critical time for disturbance to reach tube axis
T	temperature
u	fluid velocity (lab frame)
U_s	shock velocity
v	transverse disturbance velocity
V_{CJ}	Chapman-Jouguet detonation velocity
vN	von-Neumann post-shock state
w	fluid velocity (shock frame)
W	molecular mass
x	distance
x_c	critical distance for disturbance to reach tube axis
y	mass fraction
Z	reaction progress variable

1 Introduction

A simple, one-dimensional model of a gaseous detonation, the so-called Zeldovich-von Neumann-Doring (ZND) model, consists of a strong shock wave tightly coupled to a reaction zone, propagating through a combustible gas mixture at the Chapman-Jouguet (CJ) detonation velocity as shown in Fig.1.1 (Fickett and Davis 1979, Strehlow 1984). Chemical reactions are initiated at the elevated post-shock von Neumann (vN) pressure and temperature. The induction zone behind the shock is usually thermally neutral or slightly endothermic as radical species are generated in chain-branching reactions. The temperature increases through the energy release zone as the radical and other intermediate species form the primary products in exothermic three-body recombination reac-

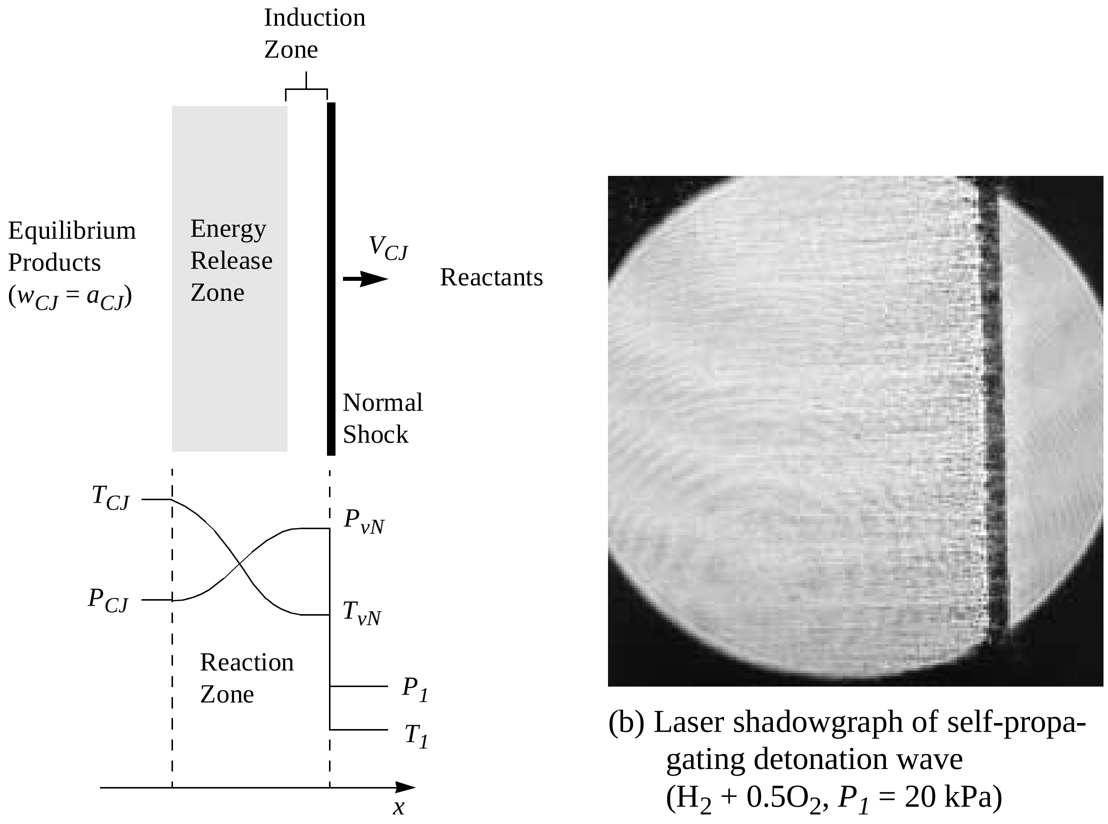

(a) Steady, one-dimensional ZND model.

(b) Laser shadowgraph of self-propagating detonation wave ($H_2 + 0.5O_2$, $P_1 = 20$ kPa)

Figure 1.1 Idealized and real detonation waves.

tions. The reaction zone, encompassing the induction and energy release zones, terminates when chemical equilibrium is reached at the Chapman-Jouguet condition for which the fluid velocity is sonic with respect to the shock wave. Decreasing pressure within the reaction zone arises from expansion of the hot products, emanating compression waves into the adjacent fluid parcels. These compressions reinforce the shock wave and counteract momentum and energy loss mechanisms which tend to cause the shock wave to decay. Self-propagating detonation waves exist due to this feedback mechanism wherein the shock wave generates the thermodynamic conditions under which the gas combusts and the energy release from the reaction zone maintains the strength of the shock.

Spatial and temporal instabilities arising from the non-linear dependence of chemical reaction rates on the temperature complicate this idealistic model. A detonation is actually a three-dimensional shock-reaction zone complex with a dynamic wavefront composed of curved incident, Mach stem, and reflected shock waves as depicted in Fig. 1.2 (Strehlow 1970, Lee 1984). Shock strength and curvature varies along the front, resulting in non-uniform reaction zones and fluctuating shock waves. The reflected shocks sweep transversely across the front and the triple-point paths roughly form a diamond-shaped cellular pattern. The shear and/or pressure distribution in the vicinity of the triple points rearranges soot deposited on metal sheets, leaving a record of the triple-point paths. The cell width measured from so-called soot foil experiments is a characteristic length scale of detonations which is indicative of the coupling between the gasdynamic and chemical processes. Manual sampling of cell widths on soot foils reveals a range of values in which the minimum and maximum typically deviate from the average by ±50%

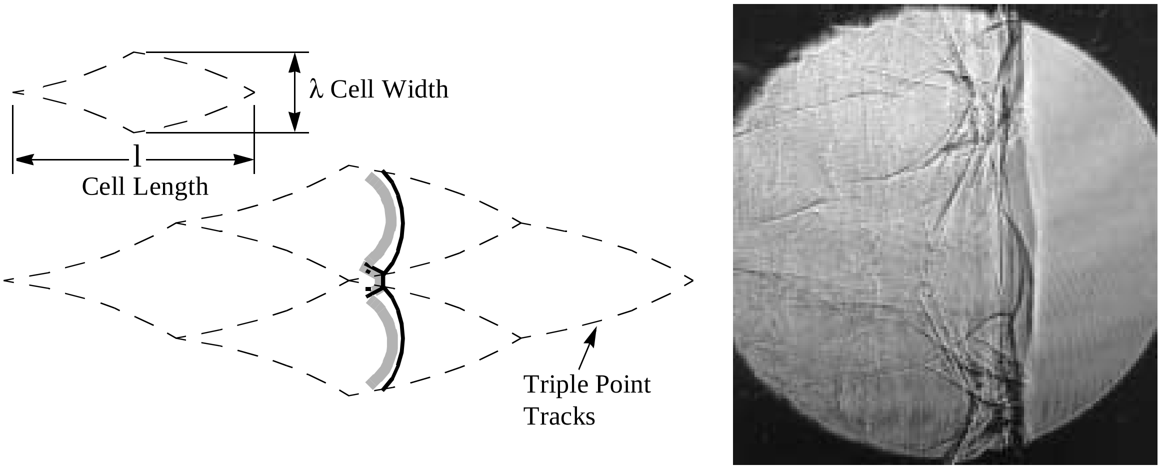

(a) Schematic of cellular structure.

(b) Laser shadowgraph ($H_2 + 0.5O_2 + 10Ar$, P_1 = 20 kPa, Akbar 1997)

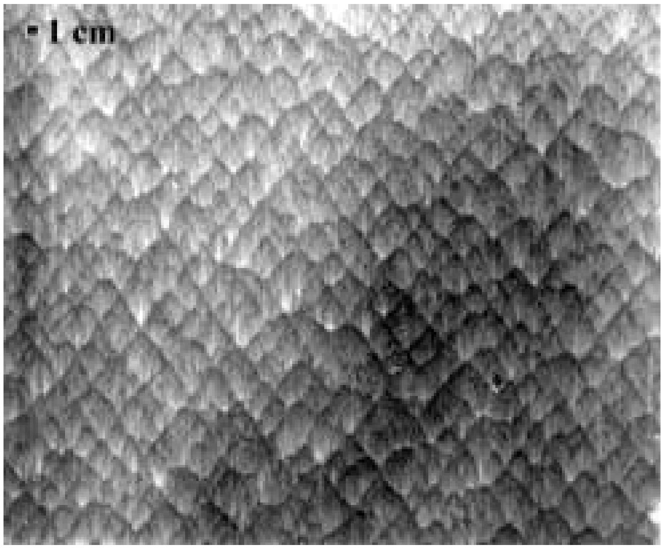

(c) Soot foil recording of cellular structure ($C_3H_8 + 5O_2 + 10N_2$, P_1 = 40 kPa)

Figure 1.2 Detonation cellular structure.

because of the various instability modes which exist (Fickett and Davis 1979), the three-dimensional wave structure is recorded on a two-dimensional sheet, and soot foil interpretation is quite subjective. Strehlow (1968) classified the observed cellular structure into various qualitative categories such as poor, irregular, good, and excellent. Shepherd et al. (1986a) collected statistical measurements of soot foil cell widths using a digital analysis technique, quantifying the wavelength spectrum for different mixtures. Those with narrow spectral content are referred to as having regular cellular structure, while irregular structure is characterized by a broad range of cell widths. Note that cellular structure is present in Fig. 1.1b but the instability wavelengths are small and the wave appears planar.

A detonation propagating from the confinement of a tube into an unconfined space diffracts upon reaching the area change. Expansion waves propagate at a finite rate along the detonation wave and into the fluid behind the wavefront as the presence of the corner is communicated through the flowfield. The diverging streamtubes induced by this disturbance generate unsteadiness and curvature which reduce the pressure and temperature of the fluid. The chemical reaction rates responsible for the energy release which sustains the detonation are dependent upon these thermodynamic conditions. The time required for a fluid particle to react following the shock can be approximately modeled over a range of temperatures relevant to gaseous detonations by the Arrhenius expression

$$\tau = \frac{k}{\rho_s}\exp\left(\frac{E_a}{R_g T_s}\right) = \frac{k R_g T_s}{P_s}\exp\left(\frac{E_a}{R_g T_s}\right) \tag{1.1}$$

from which it can be seen that the reaction time is most sensitive to the temperature. Reaction times calculated by constant-volume explosion simulations with varying shock velocity are presented in Fig. 1.3, illustrating the exponential increase in reaction time with decreasing post-shock temperature. Shock velocities ten percent less than V_{CJ} result in a factor of four increase in reaction time and an order of magnitude or greater reaction time increase with a 15% shock velocity deficit.

The outcome of a detonation wave diffracting from confinement will fall into one of two regimes depending upon the mixture composition, initial thermodynamic state, and

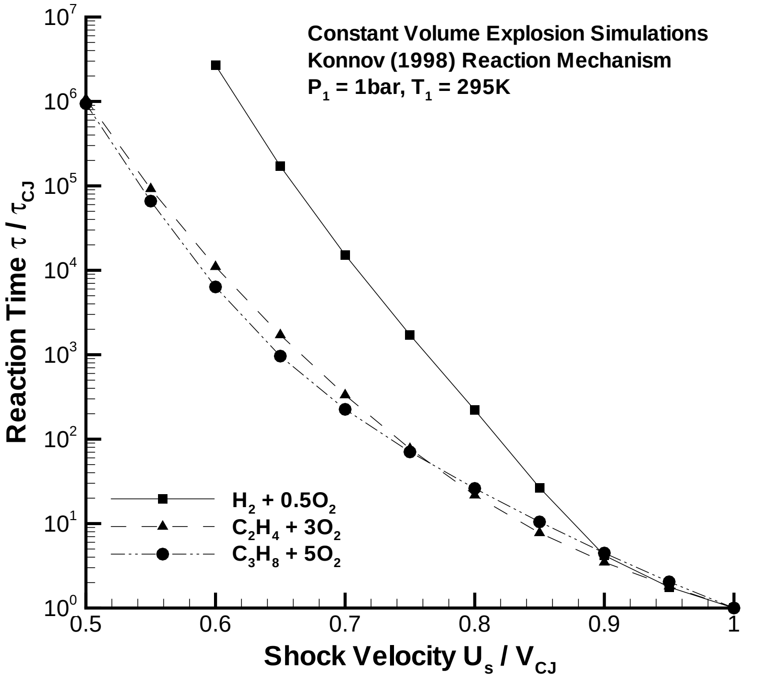

Figure 1.3 Reaction time sensitivity to shock velocity.

geometry of the confinement (Fig. 1.4). The energy release rate overcomes the expansion rate introduced by the disturbance allowing the detonation to successfully transit the area change in the super-critical regime. Sudden expansion from confinement results in decay of the reaction zone and decoupling from the shock wave in the sub-critical regime. For sufficiently rapid quenching of the reactions, detonation diffraction closely corresponds to self-similar non-reacting shock diffraction. Critical diffraction conditions represent those initial conditions which separate the two regimes. Self-similarity is not present in super-critical cases and near-critical conditions due to the influence of the reaction zone.

The fundamental problem of a detonation transitioning from planar to spherical geometry has received considerable attention and has eluded complete understanding in the combustion community for many years. The fluid dynamic complexities associated

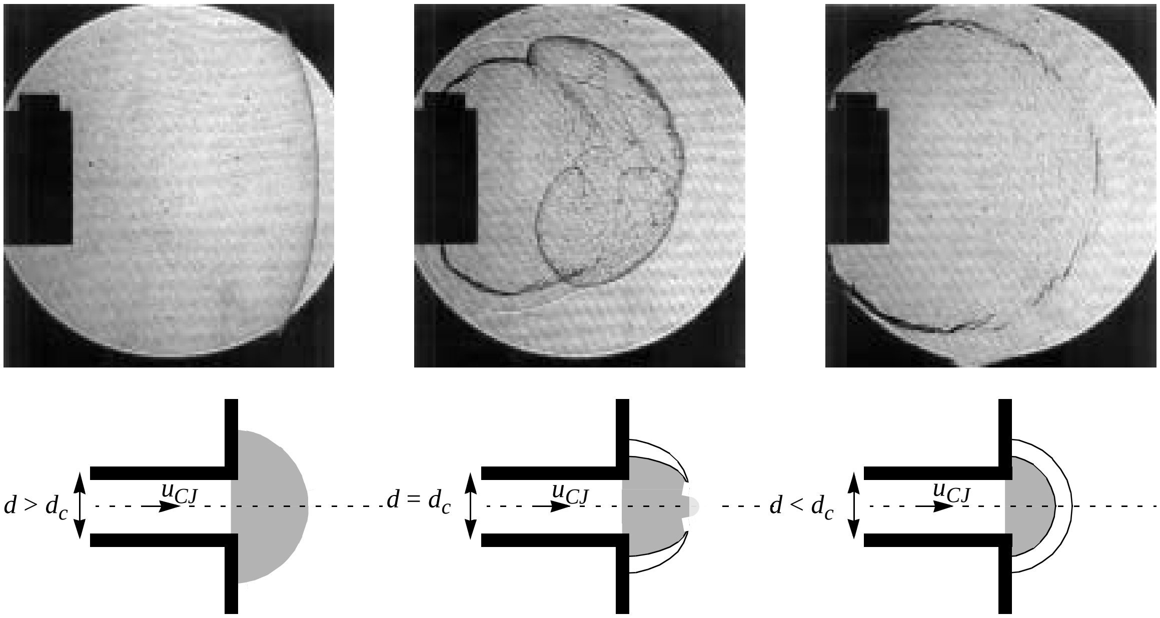

(a) Supercritical: successful transmission.

(b) Critical: re-initiation as shock decouples from reaction zone.

(c) Subcritical: complete failure as shock decouples from reaction zone.

Figure 1.4 Regimes of detonation diffraction.

with detonation waves, along with the high pressures, high temperatures, and short length/time scales involved, pose formidable difficulties throughout detonation research. The present investigation is comprised of a combined experimental and analytical approach to characterize the diffraction of gaseous detonations and develop a model which allows for the prediction of critical diffraction conditions. Failure and re-initiation phenomena involved in detonation diffraction are also present in direct initiation, deflagration-to-detonation transition (DDT), near-limit propagation, and the self-propagation of cellular detonations, and thus, this study sheds light on those problems as well. Beyond the scientific value of this effort, detonation diffraction through area expansions is important in the fields of propulsion, weapons research, and safety/hazard analysis.

2 Literature Review

Experimental, analytical, and computational research regarding the problem of detonation diffraction will be reviewed following a summary of some literature on non-reacting shock diffraction. Diffraction in this context is taken to correspond to wave propagation in a gaseous mixture through an area expansion, or equivalently, around a convex corner. The efforts of Gvozdeva (1961), Thomas (1979), and Thibault (1985) are acknowledged, but their publications were not available.

2.1 Shock diffraction

2.1.1 Mathematical treatment

Lighthill (1949) and Chester (1953) treat the problem of a plane shock wave of arbitrary strength moving through gradual area changes by linearizing the governing equations. Resulting shock shapes and pressure distributions were calculated by Lighthill (1949) for shock Mach numbers from one to infinity. Chester (1953) obtained a differential expression for the change in shock strength with area, and provides an analytical expression of the pressure in the disturbance pulse for the cases of subsonic and supersonic post-shock fluid velocity.

Jones et al. (1951) considered the unsteady, compressible flowfield behind a shock diffracting through any area expansion as a steady flow problem with external forces and sinks applied through the use of self-similarity concepts. They found that a region of the post-shock flowfield becomes steady and uniform, while another region is adequately described by a steady Prandtl-Meyer expansion fan. Dumitrescu and Predas (1975) also reduced the governing unsteady equations to an equivalent steady flow case and showed how this is related to a Prandtl-Meyer expansion. The interaction of shocks in ducts with diverging and converging area changes is discussed by Kahane et al. (1954). Idealization of the area change as a step discontinuity along with pressure and velocity matching through shock jump conditions and expansion relations leads to solution of the resulting unsteady wave systems and establishment of steady flow regions.

Chisnell (1957) reproduces the differential equation relating shock strength and small area changes of Chester (1953) and then integrates the differential equation to obtain a closed-form equation in which the product of the channel area with a function of the shock pressure ratio and specific heat ratio is constant. Given the gas composition, initial shock strength, initial area, and final area, the final shock strength can be calculated. The calculated shock strength is somewhat of an averaged quantity and does not account for local perturbations along the wave front. Whitham (1957, 1959) extends the work of Chisnell to problems of shock dynamics with application to diffraction and stability problems in two and three dimensions. An orthogonal coordinate system is defined based on rays normal to the shock front and the shock position at any given instant. Neighboring rays form ray tubes which are essentially treated as streamtubes, a significant approximation which is rigorously true only immediately post-shock. Chisnell's (1957) equation relating area and shock strength is applied in each ray tube, which can be taken as small as desired to conform to the gradual area change criterion. From this, a set of characteristic equations is obtained which describes local changes in shock Mach number and angle. Analytical solutions are obtained for the weak and strong shock limit cases; intermediate shock strengths require numerical integration. Skews (1966) summarizes Whitham's theory and presents the results of many calculations which determine the shape of diffracting shock waves for a range of incident shock strengths and corner angles.

2.1.2 Qualitative observations

The sketch presented in Fig.2.1 contains many of the flowfield features observed through various experimental efforts. The investigation of Skews (1967a, 1967b) provides an extensive description of the flowfield generated by Mach 1 to 5 shock waves in air diffracting from a rectangular tube through divergence angles of 15° to 165°. Multiple Schlieren images clearly show the propagation of the leading unsteady expansion characteristic into the undisturbed incident shock which causes it to diffract. The shape of the unsteady expansion head is indicative of the post-incident shock flow, entirely convected downstream of the area change in the case of post-shock supersonic flow. At relatively high Mach number, a point of inflection was observed between the diffracted shock and

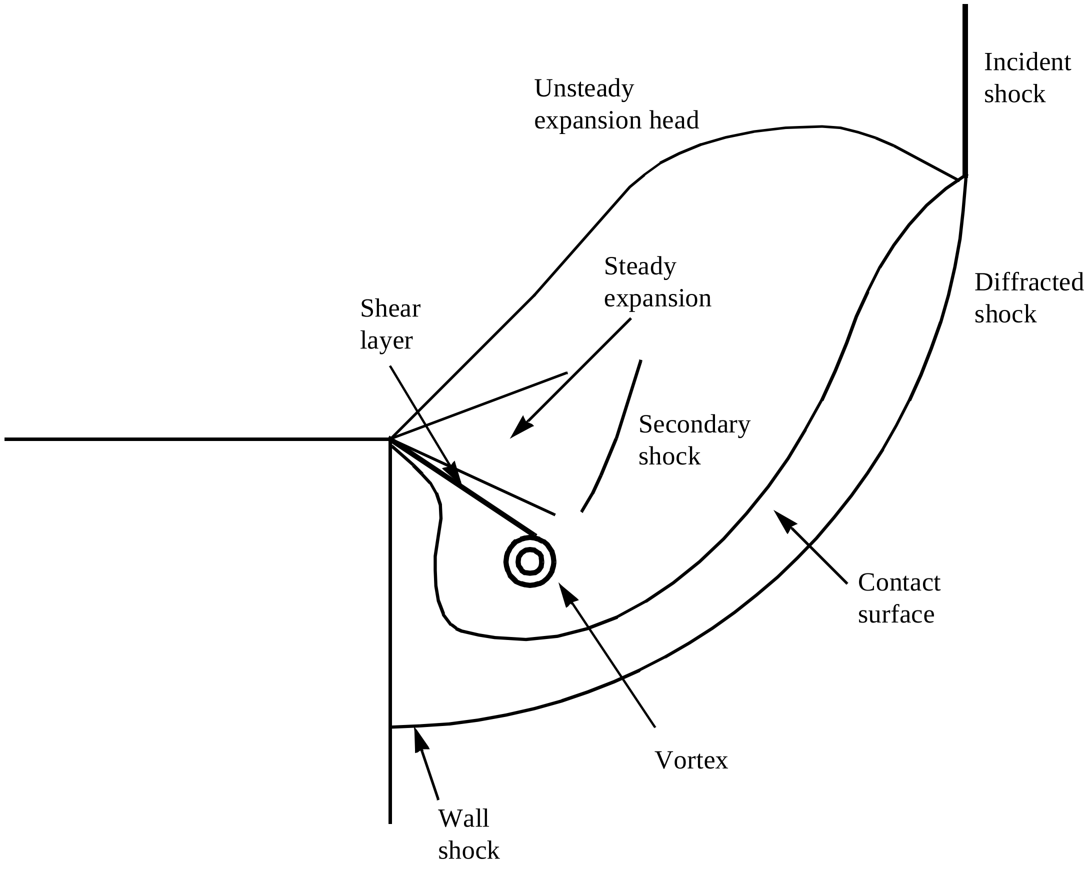

Figure 2.1 Qualitative flowfield features of a non-reacting shock diffracting around a corner.

wall shock. A so-called terminator line represents the tail of a steady Prandtl-Meyer expansion, and a shear layer from the separated boundary layer rolls up into a vortex ring. A secondary shock exists near the vortex, and a contact surface is evident which separates the gas processed by the incident shock from that passing through the diffracted shock. All of these features are described in detail by Skews (1967b) along with the variation observed with divergence angle and incident shock Mach number. In particular, a qualitative flowfield difference was observed for divergence angles greater and less than 45°. At approximately 45°, the slipstream appears downstream of the corner, with the boundary layer separation point moving closer to the corner with increasing divergence angle. This is accompanied by the contact surface folding under near the wall.

Bazhenova et al. (1971, 1972, 1979) conducted shock diffraction experiments in air, nitrogen, and carbon dioxide from a square shock tube with incident shock Mach numbers from 1.8 to 10 and divergence angles from 15° to 170°. They provide a good qualitative description of the flowfield similar to that of Skews (1967b), as does Quirk (1994) who presents a computational fluid dynamic simulation with pseudo-schlieren images of a shock diffracting around a 90° corner. Bazhenova et al. (1979) and Quirk (1994) note the Mach reflection configuration which the wall shock can assume, giving rise to an associated Mach stem, triple point, reflected shock, and slipstream.

Visual documentation of shock diffraction phenomena has been conducted by many other researchers. Kahane et al. (1954) present interferograms of shocks interacting with area changes in ducts. Schlieren images of the vortex ring formed following shock diffraction from a rectangular shock tube were obtained by James (1965), and Guy (1969) acquired Schlieren imagery of shock diffraction, reflection from confining walls and within branched ducts, toroidal vortex formation, and the interaction of successive shock waves with the vortex. Oshima et al. (1965) acquired single-sequence Schlieren and interferogram images of shocks diffracting around a 90° corner, and Deckker and Gururaja (1970) present multi-sequence schlieren images of shocks diffracting through a two-dimensional area expansion. Dumitrescu and Predas (1975) acquired Schlieren images of Mach 2 to 2.5 shocks in air diffracting through divergence angles of 45° and 60° with particular attention paid to boundary layer separation and shock-boundary layer interaction.

2.1.3 Experimental measurements

Oshima et al. (1965) studied the relation between distances propagated by the undisturbed incident shock and the wall shock with Schlieren and interferogram images of Mach 1.5 to 2.8 shock waves diffracting from a rectangular shock tube around a 90° corner. At long times the ratio of these distances was constant, but at early times the constant relation, and therefore self-similarity, was not observed. Schlieren images from Skews (1967a) and Bazhenova et al. (1971, 1979) over a wide range of incident shock Mach numbers and divergence angles indicate that the shock shapes are self-similar to within the experimental accuracy because of the linear relation observed between the incident and wall shock Mach numbers.

Skews (1967a) derives an expression for the unsteady expansion interaction location with the undisturbed shock based on the incident shock velocity, post-shock velocity, and acoustic speed (Section 3.2). The resulting disturbance trajectory from this expression is significantly greater than that predicted by Whitham’s theory at incident shock Mach numbers less than five. Excellent agreement is obtained between the calculated lead disturbance trajectory from Skews with measurements of the trajectory from schlieren images for incident shock Mach numbers from 1 to 3.5 and divergence angles of 15° to 165°. Deckker and Gururaja (1970) present data on axial versus wall shock location for divergence angles from 10° to 45° and incident shock Mach numbers less than two. Shock velocity along the axis is also plotted versus axial shock distance for 10° and 20° divergence angles. Comparison with calculations based on Chisnell's (1957) area-shock strength relation indicates that the calculations overpredict the shock attenuation, with better agreement for weaker incident shocks.

Sloan and Nettleton (1975) investigated the decay of the shock wave along the tube axis for three- and two-dimensional shock diffractions (Mach 1.5 to 2.5 incident shocks) through abrupt area changes from cylindrical and rectangular shock tubes, respectively. The location where the axial shock began to decay was accurately predicted with the expression presented by Skews (1967a) and overpredicted by Whitham's (1957) theory by a factor of 1.7 to 2. The axial shock decay rate was faster and spherical symmetry was achieved sooner for the three-dimensional experiments than the two-dimensional experiments with cylindrical symmetry. Chisnell's (1957) theory was used in conjunction with measurements of axial shock decay to determine the location at which the shock radius of curvature began to increase linearly with distance. This is the location where the decaying shock achieves spherical or cylindrical symmetry, and extrapolation gave the apparent center of curvature about which the symmetrical expansion proceeds. Observations show that symmetry is achieved faster, and the apparent center of curvature moves closer to the area change plane, as the incident shock Mach number increases.

Wall shock Mach numbers were accurately predicted by Whitham's theory for divergence angles less than 45°, beyond which Whitham's theory underpredicts the wall shock Mach number at incident shock Mach numbers less than 3 and vice versa for larger incident shock Mach numbers (Skews 1967a). The data of Bazhenova et al. (1971, 1979) are used to produce an empirical expression for the wall shock Mach number given the incident shock Mach number and divergence angle. The decay of the wall shock was studied by Sloan and Nettleton (1978) for incident shock Mach numbers of 1.5 to 3.5. They develop a model for the wall shock in which the initial wall shock Mach number is given by Whitham (1957), Chisnell's (1957) theory is used to account for decay due to cylindrical expansion of the wall shock, and Whitham's (1957) theory corrects for the slight concavity of the experiment side walls. The model accurately reproduced the attenuation of the wall shock between two locations but overestimates the absolute wall shock Mach number due to discrepancies between the measured and calculated initial Mach number. Bazhenova et al. (1979) focused on the occurrence of wall shock Mach reflections and presented wall shock Mach number and pressure ratio data versus incident shock Mach number over a wide range of divergence angles and Mach numbers.

Skews (1967b) presents measurements of the slipstream angle, terminator angle, secondary shock velocity, contact surface velocity, and vortex propagation angle and velocity variations with incident shock Mach number. Complementary measurements of the slipstream angles and head and tail angles of the steady Prandtl-Meyer expansion fan are presented by Bazhenova et al. (1971). This is accompanied by analysis of the pressure drop across the steady expansion and experimental observations to determine at what pressure ratio the boundary layer separates for a given divergence angle. James (1965) diffracted Mach 1.2 to 1.8 shock waves in air from the end of a rectangular shock tube and presents static and dynamic pressure measurements, positive phase duration, and positive phase impulse for various distances and angles from the area change.

Kahane et al. (1954) performed shock tube experiments with area changes, acquiring pressure measurements and interferograms which were in good agreement with the results of their discontinuous area change analytical treatment at relatively long times after the shock-area change interaction. Guy (1969), Guy and Davies (1970), and Davies and Guy (1971) performed shock diffraction experiments around 90° corners and through various branched ducts. Finite element calculations based on Whitham's theory were able to simulate the shock shape with reasonable accuracy except in the vicinity of the toroidal vortex originating from boundary layer separation at the corner. Comparison between experimental and calculated shock strength was not good, especially for larger expansion ratios. Tyler (1968) presents numerical results of pressure loading for blast waves propagating and diffracting through various duct configurations. Hot-wire measurements of the vortex velocity field were also obtained by Guy (1969). Shock strength measurements during diffractions through expansion ratios from two to five with divergence angles of 1.5° to 90° in air and argon by Nettleton (1973) were compared to Chisnell's (1957) relation between shock strength and area change. As expected for Chisnell's linearized theory, Nettleton found that theory gave better agreement with experiments for smaller divergence angles, smaller expansion ratios, and for measurements obtained farther from the area change after significant wave interactions had decayed.

2.2 Detonation diffraction

2.2.1 Qualitative observations

Streak camera experiments of Zeldovich et al. (1956) demonstrated diffracting detonations decaying to a flame under some conditions and continuing as a detonation for other conditions; this was the first documentation of the sub- and super-critical diffraction regimes. With all other conditions held constant, the tube diameter from which the detonation diffracted governed which regime occurred. The detonation wave failed for tube diameters smaller than the critical tube diameter and vice versa for diameters larger than the critical tube diameter (Fig. 1.4). It was noted that in almost all super-critical diffractions, the shock decoupled from the reaction zone near the tube exit plane edge. Mitrofanov and Soloukhin (1965) used open-shutter photography of the detonation cellular structure and multi-sequence Schlieren imaging to identify the sub-critical and super-critical regimes, finding that the cellular structure disappears completely in the sub-critical case. Figure 2.2 illustrates the observed cellular structure behavior during detonation diffraction through an abrupt area expansion. The Schlieren framing camera and streak camera images of Soloukhin and Ragland (1969) show complete shock wave decoupling from the reaction zone in the sub-critical regime, and re-initiation of the partially decoupled wave by localized explosions in the super-critical regime. Re-initiation never appeared to occur after the unsteady expansion originating at the edges of the exit plane reached the tube axis. They also observed the boundary layer separation from the tube walls and roll-up into a toroidal vortex.

Strehlow and Salm (1976) recorded the disappearance of cellular structure on soot foils for sub-critical diffractions. Edwards et al. (1979, 1981) also used soot foils and

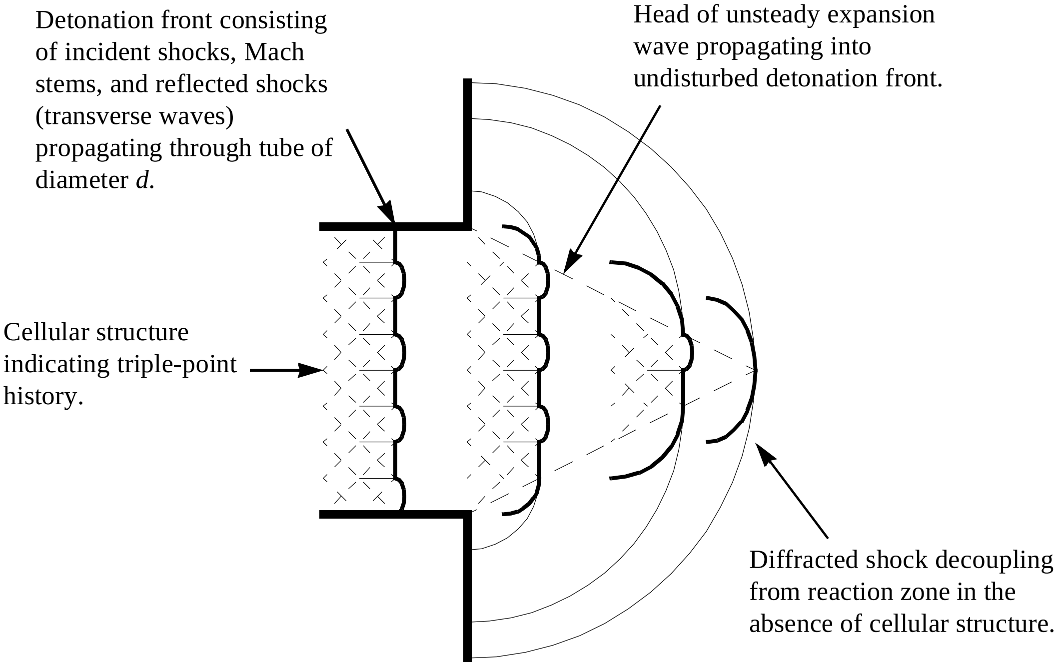

Figure 2.2 Diagram of sub-critical diffracting detonation with cellular structure.

described re-initiation at criticality occurring in the immediate vicinity of the unsteady expansion head intersection with the tube axis. Very fine cellular structure observed after re-initiation is suggestive of an overdriven detonation. Gubin et al. (1982) saw the same indication of an overdriven detonation following re-initiation and reported that the cell width returned to what would be expected for a detonation propagating at V_{CJ} after some distance. Detonation diffraction experiments with soot foils by Murray and Lee (1983) revealed two re-initiation mechanisms. The first is the aforementioned re-initiation via localized explosions near the undisturbed core of the diffracting detonation, and the second occurs when the decoupled shock wave reflects from a confining surface of the volume into which the detonation has diffracted.

Moen et al. (1982) acquired chemiluminescence images from a high speed movie camera and described the localized explosions during re-initiation as being located near the interaction point between the unsteady expansion head and the planar detonation front. Edwards et al. (1979, 1981) presents streak camera records of the shock velocity along the tube axis versus distance for a sub-critical and a near-critical super-critical experiment. The shock velocity decayed steadily after the unsteady expansion head propagated to the tube axis in the sub-critical case, while the shock velocity dropped to $0.6V_{CJ}$ before accelerating back to V_{CJ} in the super-critical case. The authors describe these streak records as reminiscent of the shock front behavior in ignition of spherical detonations by a blast wave generated with a concentrated source of energy.

A significant amount of flow visualization data supports the observations summarized above. Additional single- and multi-sequence Schlieren and shadowgraph images are presented by Bazhenova et al. (1969), Edwards et al. (1979, 1981), Thomas et al. (1986), Bartlma and Schroder (1986), Sugimara (1995), and Pantow et al. (1996). Streak camera measurements were obtained by Vasileev and Grigoreev (1980), Gubin et al. (1982), and Ungut et al. (1984). Ungut et al. (1984), Thomas et al. (1986), Desbordes and Vachon (1986), Vasileev (1988), Desbordes (1988), and Borisov and Mikhalkin (1989) obtained soot foil records. High speed movie camera images of detonation chemiluminescence were acquired by Rinnan (1982), Ungut et al. (1984), Benedick et al. (1984), and Moen et al. (1984a, 1984b). Murray and Lee (1983) and Vasileev (1988) recorded additional open-shutter chemiluminosity images.

2.2.2 Experimental measurements

Original sources of critical diffraction conditions are summarized in Table 2.1 and the notations made are discussed below. Some other sources are not listed because they contain critical diffraction data reproduced from the original sources. The geometry col-

Table 2.1: Sources of critical diffraction conditions.

Source	Geometry	Mixtures	Notes
Zeldovich et al. (1956)	Circular	C_2H_2-O_2-N_2, C_2H_4-O_2, C_3H_6-O_2-N_2, iC_4H_8-O_2, C_5H_{12}-O_2, $C_4H_{10}O$,H_2-O_2, C_3H_6O-O_2, C_6H_6-O_2, CH_4-O_2	no wave velocity measurements
Friewald and Koch (1963)	Circular	C_2H_2-O_2-N_2	
Mitrofanov and Soloukhin (1965)	Circular, Rectangular	C_2H_2-O_2	
Strehlow and Salm (1976)	Rectangular	H_2-O_2-Ar	thin channel, 10° to 45°
Edwards et al. (1979)	Rectangular	C_2H_2-O_2	
Matsui and Lee (1979)	Circular	C_2H_2-O_2-N_2, C_2H_4-O_2-N_2, C_2H_4O-O_2-N_2, C_3H_6-O_2-N_2, C_2H_6-O_2-N_2, C_3H_8-O_2-N_2, CH_4-O_2-N_2, H_2-O_2-N_2	
Vasileev and Grigoreev (1980)	Circular	C_2H_2-O_2-N_2	
Edwards et al. (1981)	Rectangular	C_2H_2-O_2, H_2-O_2-Ar, C_2H_6-O_2, CH_4-O_2, C_3H_8-O_2, C_3H_6O-O_2	
Moen et al. (1981)	Circular	C_2H_4-O_2-N_2	
Knystautas et al. (1982)	Circular	CH_4-O_2-N_2, C_2H_2-O_2-N_2, C_2H_4-O_2-N_2, C_2H_6-O_2-N_2, C_3H_6-O_2-N_2, C_3H_8-O_2-N_2, C_4H_{10}-O_2-N_2, MAPP-O_2-N_2	
Gubin et al. (1982)	Circular	H_2-O_2, CH_4-O_2	45° and 60°
Lee et al. (1982)	Circular	H_2-O_2-N_2, C_2H_2-O_2-N_2, CH_4-O_2-N_2, C_3H_8-O_2-N_2, C_3H_6-O_2-N_2, C_4H_{10}-O_2-N_2, C_2H_4-O_2-N_2, C_2H_6-O_2-N_2	same as Knystautas et al. (1982)

Table 2.1: Sources of critical diffraction conditions.

Source	Geometry	Mixtures	Notes
Moen et al. (1982)	Circular	C_2H_4-O_2-N_2, C_2H_2-O_2-N_2	some orifice data
Guirao et al. (1982)	Circular	H_2-O_2-N_2	
Rinnan (1982)	Circular, Rectangular	C_2H_2-O_2-N_2, C_2H_4-O_2-N_2	some orifice and multiple orifice data
Murray and Lee (1983)	Circular	C_2H_2-O_2	diffraction into cylindrical geometry
Ungut et al. (1984)	Circular	C_2H_6-O_2-N_2, C_3H_8-O_2-N_2	
Liu et al. (1984)	Circular, Square, Triangular, Elliptical	H_2-O_2-N_2, C_2H_4-O_2-N_2	orifice data
Benedick et al. (1984)	Rectangular	H_2-O_2-N_2, C_2H_4-O_2-N_2	yielding side wall
Knystautas et al. (1984)	Circular	H_2-O_2-N_2, C_2H_2-O_2-N_2, C_2H_4-O_2-N_2, C_2H_6-O_2-N_2, C_3H_8-O_2-N_2, C_4H_{10}-O_2-N_2	
Moen et al. (1984a)	Circular	C_2H_2-O_2-N_2, C_2H_4-O_2-N_2, C_2H_6-O_2-N_2, C_3H_8-O_2-N_2, CH_4-O_2-N_2, H_2-O_2-N_2	
Moen et al. (1984b)	Circular	C_2H_4-O_2-N_2, H_2-O_2 with additives CF_3Br, CF_4, CO_2	
Thomas et al. (1986)	Rectangular	H_2-O_2, C_2H_2-O_2-Ar	0° to 90°
Bartlma and Schroder (1986)	Rectangular	C_3H_8-O_2-N_2, C_3H_8-O_2-Ar	15° to 135°
Desbordes and Vachon (1986)	Circular	C_2H_2-O_2-Ar	some overdriven and orifice data
Shepherd et al. (1986a)	Circular	C_2H_2-O_2-Ar, H_2-O_2-Ar, C_2H_6-O_2-Ar	

Table 2.1: Sources of critical diffraction conditions.

Source	Geometry	Mixtures	Notes
Moen et al. (1986)	Circular, Annular	C_2H_2-O_2-Ar, C_2H_2-O_2-N_2, C_3H_8-O_2, C_2H_4-O_2-N_2	some orifice data
Vasileev (1988)	Rectangular	C_2H_2-O_2	0° to 90°, some overdriven and orifice data, thin channel
Desbordes (1988)	Circular	C_2H_2-O_2-Ar	overdriven
Desbordes et al. (1993)	Circular	C_2H_2-O_2-Ar, C_2H_2-O_2-He, C_2H_2-O_2-Kr	
Makris et al. (1994)	Circular	H_2-O_2, C_2H_4-O_2, C_3H_8-O_2, CH_4-O_2, C_2H_2-O_2-Ar	orifice data and diffracting into porous media
Sugimara (1995)	Rectangular	C_2H_2-O_2	thin channel, 18° to 54°
Pantow et al. (1996)	Rectangular	H_2-O_2-Ar, H_2-O_2-N_2	
Higgins and Lee (1998)	Circular	C_3H_8-O_2, H_2-O_2-Ar, C_2H_2-O_2-Ar	orifice data
Schultz and Shepherd (2000)	Circular	H_2-O_2-N_2, C_2H_4-O_2-N_2, C_3H_8-O_2-N_2	some two mixture data

umn indicates the type of cross section of varying size from which the detonation diffracts. Other than the fuel and diluent type, variations of the mixtures typically include stoichiometry, dilution level, and initial pressure. Experiments of some researchers fix the tube diameter and identify the critical limits of these mixture properties, while others fix the mixture properties and vary the tube diameter.

Mitrofanov and Soloukhin (1965) found that the critical diameter was equal to thirteen times the cell width for stoichiometric acetylene-oxygen mixtures of varying initial pressure. Edwards et al. (1979, 1981) verified this correlation with cell width for acetylene mixtures and extended it to hydrogen mixtures. The $d_c = 13\lambda$ correlation was discussed as universal after Moen et al. (1981) and Knystautas et al. (1982) demonstrated its validity for a variety of fuel-oxygen-nitrogen mixtures at varying levels of dilution and initial pressure. Since then, $d_c = 13\lambda$ has approximately held for all other critical diameter tests in which a detonation propagating at V_{CJ} in fuel-oxygen-nitrogen mixtures of varying stoichiometry, dilution, and initial pressure diffracts from a circular tube through an abrupt area expansion into a relatively unconfined space. The correlation is referred to as approximate because of the cellular structure irregularity discussed in Chapter 1. Unfortunately, the cellular structure wavelength spectrum for a given mixture is often not reported along with d_c / λ correlations.

The uncertainty associated with cell width measurements is clear from the correlations of many investigations. For example, Vasileev and Grigoreev (1980) observe that the critical diameter to cell width ratio is dependent upon initial pressure and that the ratio for acetylene-air mixtures is significantly greater than for acetylene-oxygen mixtures. Edwards et al. (1981) found $d_c = 14\lambda$ for ethane and propane mixtures, and $d_c = 18\lambda$ for methane and acetone mixtures. The comparison between critical diameters measured and predicted with a 13λ correlation by Knystautas et al. (1982) tends to be worse when the cell width data of other researchers is used, highlighting the influence of subjective interpretation in cell width measurements. Critical diameter to cell width ratios of 14 to 16 were identified by Ungut et al. (1984) in propane and ethane mixture diffractions. Moen et al. (1984a) finds that d_c / λ ranges from 13 to 24 for a variety of fuel-air mixtures.

Critical diameter experiments in acetylene, hydrogen, and ethane mixtures with monatomic diluents (argon, helium, and krypton) by Moen et al. (1986), Shepherd et al.

(1986a), and Desbordes et al. (1988, 1993) demonstrated that d_c varied between 4λ and 30λ depending on the type and concentration of diluent. The d_c / λ ratio generally increased with increasing diluent concentration, and this was associated with increasing cellular regularity evaluated subjectively and by Shepherd et al. (1986a) utilizing a digital analysis technique to characterize the cellular structure imprints on soot foils. Moen et al. (1986) claims that relatively low activation energies correspond with increasing monatomic dilution of acetylene-oxygen-argon mixtures and cellular regularity. Desbordes (1988) also claims that the activation energy is reduced for heavy argon dilution of acetylene-oxygen mixtures, and states that this also leads to more stable waves in the context of one-dimensional detonation stability theory (Fickett and Davis 1979). Shepherd et al. (1986a) calculated reaction zone lengths, activation energies, and the overdrive Mach number in which part of the reaction zone becomes endothermic for acetylene, hydrogen, and ethane mixtures diluted with argon, but no clear correlations with cellular regularity were identified. Activation energies were shown not to be significantly smaller for highly argon-diluted mixtures; this is supported by the activation energy data presented in Section 4.3.1.

In summary, various researchers have found that the critical diameter ranges from 4 to 30 times the cell width, and determination of the cell width is a highly subjective exercise. Currently there is no clear understanding of detonation cellular structure and the role it plays in transient events such as diffraction. It is obvious that in quantitatively defining the cellular structure it is necessary to at least report statistical average and standard deviation data of the wavelength spectrum because of the subjectivity of individual measurements and the lack of understanding of the importance of some or all of the wavelength spectrum. Therefore, the correlation “constant” of 13 is taken as a ballpark rule-of-thumb value for back of the envelope calculations only, representative when in the context of plus or minus a factor of two for cell width measurements.

Moen et al. (1982) conducted some experiments in which the detonation diffracted through a circular orifice in a plate at the end of a larger diameter tube (Fi g.2.3). They found that the critical orifice diameter was the same as the critical tube diameter for a tube of diameter equal to that of the orifice. The conclusion drawn was that the phenomena governing whether or not a detonation diffraction is sub-critical or super-critical must be local to the wave front because the following flow conditions in critical tube and critical orifice experiments are very different. Experiments by Rinnan (1982), Liu et al. (1984), Desbordes and Vachon (1986), and Vasileev (1988) concur with the equivalence of critical tube and critical orifice diameter. Sugimura (1995) discovered a dependence between the critical initial pressure and orifice plate thickness for detonations expanding into a channel with divergence angles of 18° and 30°. These results indicate that orifice plate experiments may be sensitive to the plate thickness and/or that critical orifice experiments are not equivalent to critical diameter experiments in which the area change is not abrupt.

The critical channel width for detonations diffracting from rectangular tubes was identified as approximately ten cell widths by Mitrofanov and Soloukhin (1965) and

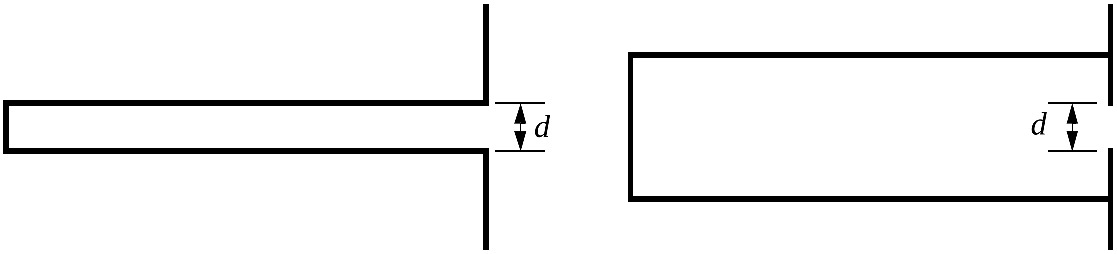

(a) Tube diameter *d*.

(b) Orifice plate diameter *d*.

Figure 2.3 Schematic of equivalent critical tube and critical orifice experiments.

Edwards et al. (1979, 1981) for acetylene and hydrogen mixtures. Edwards et al. (1981) obtained a critical channel to cell width ratio of 14 for ethane and propane mixtures, and a ratio of 18 for methane and acetone mixtures. They note that a high degree of cellular irregularity and boundary layer influence in their narrow channel experiments could be responsible for the inequality of these ratios. Orifice plate experiments of Liu et al. (1984) included rectangular, square, triangular, and elliptical orifices. The latter three geometries produced results which are in agreement with the approximate $d_c = 13\lambda$ correlation when the diameter is defined as the average of the diameters inscribing and circumscribing the orifice. Rectangular orifice experiments revealed a critical channel width to cell width ratio dependence upon the orifice aspect ratio, decreasing from a ratio of ten for an aspect ratio of one to a ratio of three for aspect ratios greater than seven. Detonation diffraction tests run by Benedick et al. (1984) from rectangular cross section tubes of variable aspect ratio arrived at the same dependence between critical width and aspect ratio. Moen et al. (1986) conducted diffraction experiments through an orifice with annular geometry. For open area ratios between 0.2 and 0.9, super-critical diffractions were obtained under conditions when the annulus outer diameter was up to two times less than the critical tube diameter.

The experiments of Strehlow and Salm (1976) in a rectangular channel with expansion divergence angles of 10° to 45° obtained super-critical diffractions at lower initial pressure and corresponding greater cell widths for smaller divergence angles (Fig. 2.4). This same observation was made by Sugimara (1995) for divergence angles of 18°, 30°, and 54°. Thomas et al. (1986) found that the critical channel width to cell width ratio increased for divergence angles up to 55° and then remained constant from 55° to

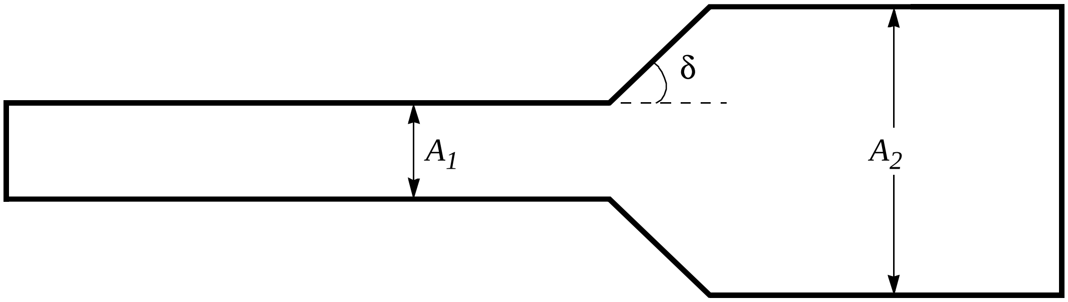

Figure 2.4 Schematic of diffraction experiment with varying divergence angle and expansion ratio.

90°. Vasileev (1988) observed a divergence angle dependence of up to 45° and no variance in the critical conditions thereafter. Vasileev noted that the expansion surface provides a boundary from which the transverse waves can reflect, and that the independence of criticality of the divergence angle may be related to the fact that the transverse wave angle is approximately 30°.

Schultz and Shepherd (2000) identified critical conditions for diffractions through abrupt area changes in which the diffraction tube was filled with a fuel-oxygen mixture and the unconfined volume a fuel-oxygen-nitrogen mixture. This configuration permitted super-critical diffractions to be obtained under conditions in which sub-critical diffractions were observed for the fuel-oxygen-nitrogen mixture filling the entire apparatus. Sochet et al. (1999) also conducted diffraction experiments through mixture gradients with a receptor mixture of air. Detailed measurements were made of the transmitted shock decay and non-dimensional analyses led to collapse of the shock trajectory and pressure data. Makris et al. (1994) considered detonation diffraction through orifice plates into a space filled with the combustible mixture and tightly packed ceramic spheres. Fuel-oxygen mixtures with a high degree of cellular irregularity were not influenced by the orifice diameter. Rather, the wave propagation in the porous media was the same as that observed through porous media without initial diffraction through an orifice plate. The results in acetylene-oxygen-argon mixtures with enhanced cellular regularity did exhibit a dependence upon the orifice diameter.

Results from the diffraction experiments ofVasileev (1988) indicated that repeat experiments conducted near the critical conditions can have sub-critical and super-critical outcomes. Higgins and Lee (1998) and Higgins (1999) performed many critical orifice tests under the same conditions and observed this phenomenon. They quantified the so-called fuzziness of the critical diameter statistically in terms of the observed percentage of repeat experiments resulting in sub-critical and super-critical diffractions. For example, sub-critical and super-critical cases were found for a ±7% variation off the average critical initial pressure value. Systematic influence of cellular regularity on the fuzziness was not identified.

Desbordes and Vachon (1986) and Desbordes (1988) investigated diffraction of overdriven detonations propagating up to 1.3 V_{CJ}. For relatively low degree of overdrive they found that the $d_c = 13\lambda$ correlation holds when the cell width is measured at the overdriven conditions. Their measurements indicate that the cell width is very sensitive to the degree of overdrive, with 10% overdrive reducing the cell width by approximately one-half. The work of Desbordes (1988) at overdrive approaching 1.3 V_{CJ} revealed that the critical diameter to cell width correlation becomes $d_c = 26\lambda$, similar to that found for detonations propagating at V_{CJ} in mixtures with high concentrations of monatomic diluent. The author related this to one-dimensional detonation stability theory in which increasing overdrive and decreasing activation energy increase the wave stability (Fickett and Davis 1979). Detonations propagating at up to 1. 3V_{CJ} were used in diffraction experiments by

Soloukhin and Ragland (1969), and Bazhenova et al. (1969) concluded that their diffraction experiments involved overdriven detonation waves from measurements of the corner disturbance propagating into the undisturbed detonation (see Section 3.2).

Experiments in tubes with short length to diameter ratios can inadvertently result in overdriven detonation diffraction, especially when a deflagration to detonation initiation technique is used. Overdriven waves which take some time to decay to V_{CJ} are a product of DDT initiation just as is observed during re-initiation processes in diffraction experiments. The efforts of Knystautas et al. (1982), Moen et al. (1982), Guirao et al. (1982), Rinnan (1982), Ungut et al. (1984), Moen et al. (1984a), and Moen et al. (1984b) involved diffraction tubes with length to diameter ratios less than 20, and sometimes less than 10. Techniques used to alleviate the uncertainty of detonation overdrive include direct detonation initiation by a powerful ignition source, careful monitoring of the detonation wave velocity before it diffracts, and varying the initiator configuration or tube length to check indirectly for an effect of overdrive on the critical conditions. Note that detonation wave velocities were not even measured by Zeldovich et al. (1956).

On the other hand, the use of very small diameter tubes or narrow channels can influence the critical conditions because the boundary layer imposes another important length scale. Very narrow channels also result in the damping out of transverse waves in the narrow dimension. Strehlow and Salm (1976) referred to detonations in a 6. 4mm wide channel as marginal, observing that the detonation velocity was below V_{CJ}, the cell widths were larger than normal, and the strength of the transverse waves was greater than normal. The results of Edwards et al. (1979, 1981) from a 6 mm channel, Vasileev (1988) from a 1.5 mm channel, and Sugimara (1995) from a 4mm channel are likely influenced by boundary layer effects and transverse wave damping in the narrow dimension. The effect of boundary layers also can not be discounted in the experiments ofVasileev and Grigoreev (1980) with tube diameters down to 2 mm.

Murray and Lee (1983) and Thomas et al. (1986) noticed that one detonation re-initiation mechanism during diffraction involves reflection of the decoupled shock wave from a rigid wall of the expansion chamber. This phenomenon changes the critical conditions, in fact facilitates super-critical diffractions, from what would be obtained in diffraction into a truly unconfined space. It is easily discriminated against when some sort of visualization technique is used, but critical conditions have been reported from experiments with relatively small expansion ratios (Fig. 2.4) and using only pressure transducer diagnostics. Vasileev (1988) did not observe wall re-initiation in narrow channel diffraction experiments for channel width ratios greater than three. Rectangular channel diffraction experiments by Pantow et al. (1996) achieved wall re-initiation up to channel width ratios of five. The circular tube experimental results presented in Chapter 5 are all obtained with a combination of flow visualization and pressure transducer diagnostics in a facility with an expansion area ratio of 16. There were cases when the pressure transducer indicated a detonation but the imagery indicated that re-initiation occurred due to decoupled shock interaction with the expansion chamber wall. Some of the critical conditions reported by Zeldovich et al. (1956), Matsui and Lee (1979), Knystautas et al. (1982), and Guirao et al. (1982) were conducted without visualization diagnostics in facilities with expansion area ratios less than 16.

Quantitative measurements of various aspects of diffracting detonations have been obtained by many researchers. Mitrofanov and Soloukhin (1965) and Soloukhin and Ragland (1969) present shock velocities at many radial and azimuthal locations from their Schlieren movies, from which are calculated the post-shock conditions and induction times to support a discussion of detonation failure. Bazhenova et al. (1969) measured wall shock velocities and unsteady expansion disturbance propagation angles with a framing camera shadowgraph system. They note that the sub-critical diffraction process is self-similar due to rapid quenching of chemical reactions and decoupling of the shock wave, supported by shock position data collapsing onto a straight line in radius versus time coordinates. Streak camera records of the shock velocity along the wall and symmetry axis are presented by Edwards et al. (1979, 1981) for sub-critical and super-critical diffraction experiments. Ungut et al. (1984) collected similar records with a multi-beam laser Schlieren time-of-flight anemometer. The shock velocity along the tube axis decayed significantly before accelerating back to the CJ velocity near the critical conditions. Edwards et al. (1981) overlays Schlieren images with shock shape profiles from Whitham’s (1957) theory and finds reasonable agreement which gets worse with increasing time. Pressure measurements are also provided behind the undisturbed and diffracted regions of the detonation. Comparison of wave front shapes from Whitham’s (1957) theory and Schlieren images of Ungut et al. (1984) in self-similarity coordinates reveals good agreement, but in contrast to Edwards et al. (1981), shows better correspondence with increasing time.

The soot foil diffraction experiments of Gubin et al. (1982) are used to plot increasing cell width versus distance as the wave propagates through the area expansion. Murray and Lee (1983) present measurements of the time it takes for a re-initiated detonation at the symmetry axis under near-critical conditions to propagate back to the side wall through the shocked but unreacted gas layer behind the decoupled shock. Desbordes and

Vachon (1986) plot the distance from the tube exit to the point where the unsteady expansion intersects the tube axis, the axial distance to the re-initiation location, and the radial distance along the side wall to the re-initiation location versus width and shows that these distances seem to be constant until near the critical cell width. Borisov and Mikhalkin (1989) tabulate unsteady expansion disturbance propagation velocities from soot foil diffraction experiments and found them to be 3% to 30% greater than that calculated from the Skews expression evaluated at the post-shock condition (Section 3.2). They also provide data on how much the cell width increases before disappearing and the distance that this occurs away from the unsteady expansion head.

2.2.3 Modeling

There has been a significant amount of qualitative and empirical discussion on the relation between length scales present in detonation diffraction experiments. Work on the relations between cell width and the critical diameter have already been summarized. Zeldovich et al. (1956) and Edwards et al. (1979, 1981) include some discussion relating the success or failure of a planar detonation wave transitioning from a given tube diameter to a spherical wave through reaction lengths and equivalent times. The hydrodynamic thickness, equivalent to an effective reaction zone length or distance to the sonic plane for a cellular detonation, is proposed by Lee et al. (1982) as the fundamental characteristic length although not readily measurable. Measurements of the cell width and length were related to the hydrodynamic thickness through the critical diameter. The papers of Liu et al. (1984) and Benedick et al. (1984) discuss detonation diffraction in terms of a critical radius of curvature as related to expansion waves penetrating into the hydrodynamic thickness.

Soloukhin and Ragland (1969) offer an ad hoc expression giving the maximum post-shock reaction time for coupling of the shock and reaction zone in terms of the shock radius and velocity. Development of the expression involves the assumption that the post-shock gas all lies within a certain distance from the shock, and the reaction time must be less than the transit time of a fluid particle through this distance. Evaluation of this expression and validation against experimental data is not available in the literature. Edwards et al. (1979, 1981) present a model for the critical diameter problem based on notions regarding critical shock strength gradients for the shock and reaction zone to remain coupled. Whitham's (1957) theory is used to evaluate the shock decay and the critical criterion comes from the Shchelkin (1959) failure criterion, consideration of measured shock decay in detonation cells, and reaction scale properties from kinetics calculations. An expression is obtained which allows calculation of the critical diameter once the cell width has been determined.

Two types of ad hoc models have been developed for the purpose of relating the critical diameter to the critical energy required for detonation initiation. The first type, known as the work-done model of Lee and Matsui (1977), equates the work done by the combustion products expanding from the critical tube on the gas in the unconfined space to the energy required for critical initiation. The work done is considered to come from the pressure and velocity of the detonation core beginning when it exits the tube and ending when the corner signal, assumed to propagate at the sound speed of the detonation products, reaches the tube axis. A similar work-done model is developed by Urtiew and Tarver (1981) with emphasis between the detonation cellular structure and the critical diameter. The $d_c = 13\lambda$ lambda correlation relates the cell width to the critical diameter, from which the work-done model gives the critical energy. The second type of model, the so-called surface energy model, is presented by Guirao et al. (1982) and Knystautas et al. (1984). The critical tube diameter area is equated to the area of a blast sphere created by the point source release of critical energy when the blast has decayed to V_{CJ}. From this concept and strong blast theory, an expression is derived for the critical energy as a function of the critical diameter. Both types of models give E_c - d_c relations which represent the experimental data to within an order of magnitude agreement.

Westbrook (1982) and Westbrook and Urtiew (1982) calculated reaction length scales through constant volume explosion simulations with detailed reaction mechanisms for hydrogen and a number of small-hydrocarbon mixtures. They correlated the reaction lengths with critical diameter data and found that a linear proportionality in the form of $d_c = A\Delta$ fit the experimental data fairly well. The ease with which these types of simulations can be conducted makes them useful for considering how a variation of initial conditions will affect the critical diameter. Westbrook (1982) found that $A = 380$ was the most suitable proportionality constant, but the correlations between reaction length and critical diameter of Moen et al. (1982, 1984a) indicate that a single constant is not always applicable. For example, a satisfactory correlation was not obtained for fuel-air mixtures with varying equivalence ratio, especially for lean mixtures. Reaction length correlations with cell width by Akbar et al. (1997) resulted in proportionality constants between 10 and 100 depending on the particular mixture and thermodynamic condition variations, and a power law correlation was found to be more appropriate instead of a linear correlation. Combining these observations with varying correlations between cell width and critical diameter supports the notion that a single proportionality constant is inadequate for describing the relation between the critical diameter and reaction zone thickness.

Computational fluid dynamics simulations of diffracting detonations with cellular structure have been performed by Pantow et al. (1996) and Jones et al. (1996). Both efforts were two-dimensional reacting Euler simulations with a two-step chemistry model and resulted in cases of sub-critical and super-critical diffraction. Two detonation re-initiation mechanisms were identified, the first of which is the aforementioned reflection of the decoupled shock wave from a rigid confining wall. The second occurs in the vicinity of a transverse wave propagating into the unsteady expansion fan from the undisturbed detonation core. Sometimes the transverse wave does not cause re-initiation, but in other cases the transverse wave strength is rapidly amplified and the reaction zone re-couples with the decaying shock wave. The presented experimental and simulated Schlieren images of self-reinitiation by a diffracting detonation appear similar. Detailed consideration is not given to the details of the transverse wave strengthening and shock-reaction zone re-coupling.

The extension of Whitham's (1957) theory for non-reacting shock diffraction to gaseous detonation diffraction has been pursued by Akbar (1991) and Li and Ben-Dor (1998), although these extensions are only applicable when the shock velocity is greater than the CJ detonation velocity. Energy release is accounted for in the area-Mach number relation of the theory, with Akbar (1991) holding the specific heat ratio constant and Li and Ben-Dor (1998) allowing for a change in the ratio. Akbar (1991) does not apply the modified theory to detonation diffraction through an area expansion, but notes that the modified theory is very sensitive to the degree of overdrive and singularity problems occur for propagation velocities near V_{CJ}. Li and Ben-Dor (1998) were only able to apply their modified theory for overdriven detonations diffracting through an area expansion until the shock decayed to the CJ velocity. Therefore, these extensions of Whitham's (1957) theory to diffracting detonation waves are not useful for consideration of reaction zone decoupling from the shock wave while expanding through an area change.

2.2.4 Overviews

A short overview of the detonation diffraction problem is provided by Oppenheim and Soloukhin (1973). Desbordes (1995) discusses the experimental diffraction results of various researchers and focuses on the relation of scales such as critical curvature radii, critical diameter, cell width, induction length, etc. Extensive reviews of critical tube diameter efforts are given by Lee (1984, 1996). Lee (1996) concisely points out the fundamental problem of detonation diffraction research: "Currently there is no general theory for the prediction of the critical diameter." He also focuses on perceived fundamental differences in behavior depending upon the relation between critical diameter and cell width. Lee (1996) believes that the mixtures for which the 13λ correlation seems to hold tend to have irregular cellular structure, high chemical activation energies, and detonation initiation is marked by localized explosions. Extreme temperature sensitivity is characteristic of high activation energy mixtures, and so it might be expected that the expansion of a diffracting detonation near criticality results in immediate decoupling of the shock from the reaction zone. Lee (1996) postulates that the problem of re-initiation then becomes chemistry independent, so that similar gasdynamic and thermodynamic conditions present in these mixtures which lead to the formation of localized explosions for re-initiation result in the nearly universal correlation. On the other hand, Lee states that mixtures with high concentrations of monatomic diluents generally exhibit very regular cellular structure, have low activation energies, and observations provide a picture of uniform detonation initiation rather than explosion of discrete sites. Due to the decreased temperature sensitivity of these mixtures, a chemistry-dependent failure occurs gradually which is linked to a critical curvature of the diffracting detonation front.

However, in light of the complex detonation cellular structure and continuous variation in the d_c - λ relation with proportionality constants found to lie between 4 and 30, it is not likely that two such distinct failure mechanisms exist in detonation diffraction. In addition, activation energies alone have not been rigorously shown to correlate with the cellular structure regularity. Furthermore, high monatomic dilution only slightly decreases the activation energy for some mixtures (Shepherd 1986a and Section 4.3.1).

Research on detonation propagation through structures with yielding confinement, such as presented by Murray and Lee (1986), have a great deal of similarity with the detonation diffraction problem. The expansion associated with yielding walls competes with the detonation energy release and the authors were able to identify critical conditions with varying mixture composition, number of yielding walls, and wall material and thickness. Benedick et al. (1984) conducted detonation diffraction experiments in which one channel wall was plastic sheet, but does not discuss the effect of yielding confinement.

While the present investigation of detonation diffraction has been restricted to gas phase mixtures, the same physical processes are important in the case of liquid and solid phase detonations turning convex corners and when the containment vessel is yielding. The corner turning problem for high explosives is analogous to the critical tube diameter of gaseous detonation diffraction, and the high explosive critical charge diameter is analgous to the work of Murray and Lee (1986) mentioned above. Efforts in these areas of high explosives are discussed by Dremin (1962), Dremin and Trofimov (1965), Price (1967), Urtiew (1975), Campbell and Engelke (1976), and Bdzil and Stewart (1986, 1989).

3 Analytical

The primary objective of the present research is to develop a model from which an analytical expression can be derived for the calculation of critical diffraction conditions and then validate the calculations against experimental data. A qualitative description of the model is provided in this section, followed by the analytical derivation in the remaining sections of this chapter. Chemical equilibrium, ZND detonation, and constant volume explosion calculations necessary for evaluation of the critical diffraction model are presented in Chapter 4. Experimental results from this investigation and the literature which support the model derivation assumptions and provide validation data are presented in Chapter 5. The calculations and experimental results are given for hydrogen, ethylene, and propane fuel-oxygen and fuel-air mixtures of varying stoichiometry, initial pressure, and dilution (argon, helium, carbon dioxide, and nitrogen). However, this critical diffraction model can be applied to any other mixture of interest given an appropriate reaction mechanism. Validation of the model results against experimental data and discussion of the agreement and discrepancies found are provided at the end of Chapter 5.

3.1 Model description

The current understanding of the role of detonation cellular structure in propagation and behavior under transient conditions is largely empirical and is not amenable to this analytical effort. Therefore, the detonation diffracting from confinement through an abrupt area expansion will be described by a single shock front followed by a reaction zone. In light of this simplification, consider the schematic diagram of a diffracting detonation presented in Fig.3.1. A detonation described by the ZND model is propagating at

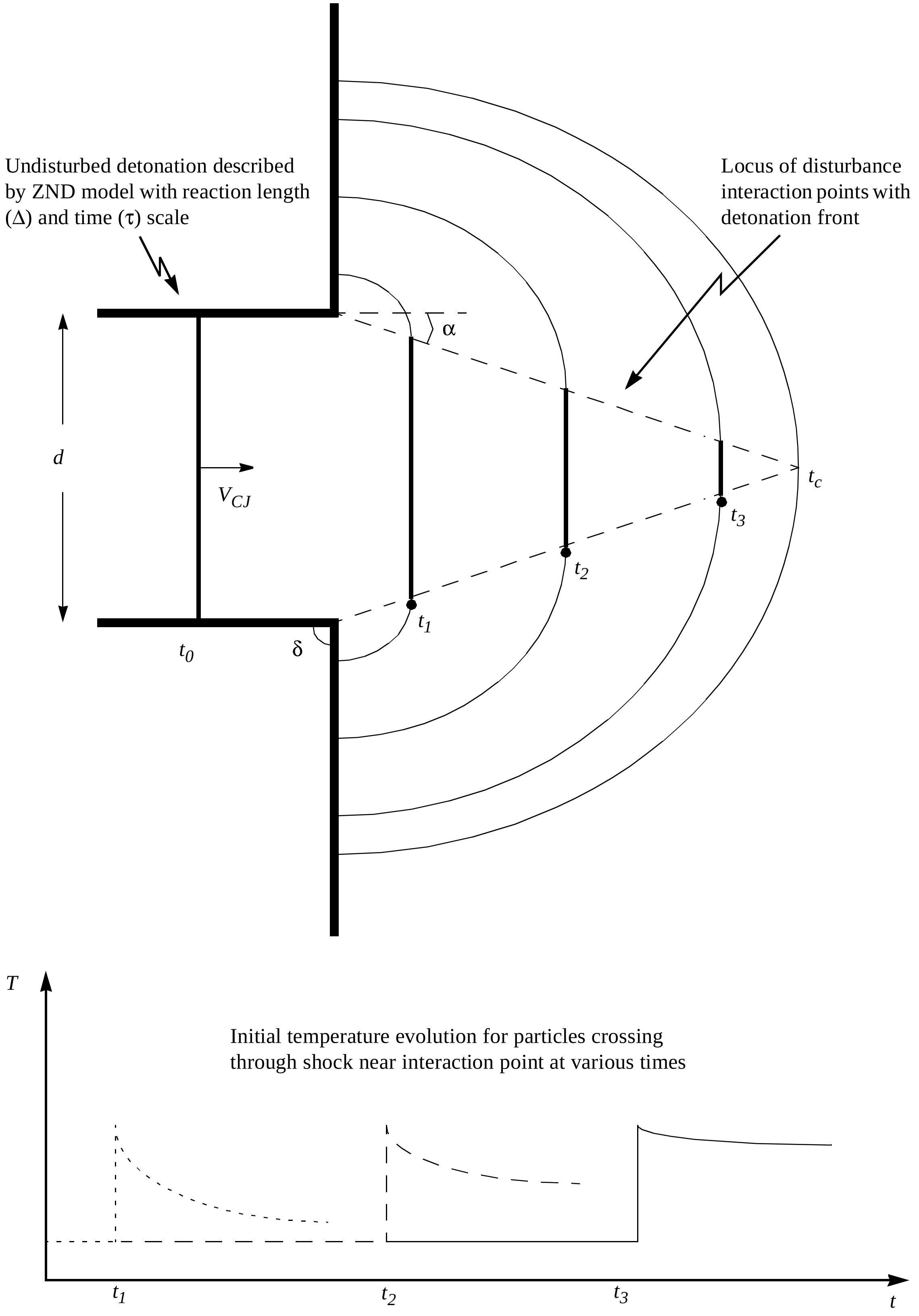

Figure 3.1 Schematic model of a diffracting detonation.

the CJ velocity into a quiescent combustible gas mixture occupying a confining tube of diameter *d* and the unconfined space. When the detonation reaches the area change, it begins to diffract around the corner which is characterized by an angle of divergence relative to the tube wall. The magnitude of this angle is assumed to be greater than approximately 50°, the angle at which Thomas et al. (1986) and Vasileev (1988) found that the critical conditions became independent of the divergence angle (Section 2.2.2). The expansive disturbance introduced by the corner propagates into the detonation at a finite velocity. The locus of points at which the head of the expansion interacts with the planar detonation front form an angle α relative to the tube wall. These points coincide with the tube axis at a distance x_c from the area change given by the tube diameter and disturbance propagation angle, or equivalently at some time t_c given by the tube diameter and disturbance transverse velocity. An undisturbed detonation front exists inside of the cone formed by the locus of interaction points, and the detonation diffracts on the outside.

Expansion from planar to spherical geometry causes unsteadiness and curvature in the post-shock flowfield of the disturbed detonation. These two effects compete against the energy release which acts to sustain the detonation. The divergence of the streamlines is greatest at the corner, resulting in a maximum in unsteadiness and curvature which decreases as the detonation propagates further from the area change. The energy release rate behind the undisturbed detonation front is constant, and therefore, the expansion rate is decreasing relative to the energy release rate in the vicinity of the disturbance interaction point. The hypothetical temperature profiles of fluid particles crossing through the shock wave just after the disturbance has reached a portion of the detonation front illustrate the competition result on the thermodynamic variable most responsible for continued support of the detonation (Fig. 3.1). Close to the corner at time t_1, a fluid particle passes through the diffracted shock and experiences relatively large unsteadiness and curvature effects. Further from the area change at time t_2, the post-shock influence of unsteadiness and curvature is not as severe and the temperature decays less rapidly. At time t_3, the post-shock temperature history is approaching the point at which rapid energy release might be achieved in close proximity to the shock front and maintain coupling between the shock wave and reaction zone.

In the vicinity of the disturbance interaction point with the planar detonation front, the energy release must overcome the competition from unsteadiness and curvature if the diffraction is to be super-critical. Conversely, a sub-critical diffraction will result if the unsteadiness and curvature effects are of such a magnitude that they quench the chemical reactions responsible for the energy release. These postulates are consistent with the experimental results reviewed in Chapter 2 and that which will be presented in Chapter 5. The re-initiation evidence indicates that the primary competition occurs in the vicinity of the disturbance interaction point with the detonation front (Chapter 2). The chemical reaction rates are so temperature sensitive (Chapter 1) that some distance away from the interaction point the energy release is negligible in the sub-critical case. The qualitative experimental evidence also suggests that the critical time at which the competition dictates the diffraction regime is approximately t_c. However, streak camera measurements of the shock decay along the tube axis after the critical time indicates that the shock velocity decreases significantly before accelerating back to the CJ velocity under critical conditions (Section 2.2.2). Therefore, determination of which diffraction regime will occur, and hence a critical diffraction model, requires a quantitative evaluation of the competing effects for the fluid particle passing through the shock wave along the tube axis soon after the critical time.

3.2 Disturbance propagation

Skews' (1967) geometric construction for the head of a disturbance propagating into the fluid behind a non-reacting diffracting shock is illustrated in Fig.3.2. The corner signal is convected downstream with the post-shock fluid velocity and travels radially outward at the post-shock acoustic speed, during which time the undiffracted portion of the

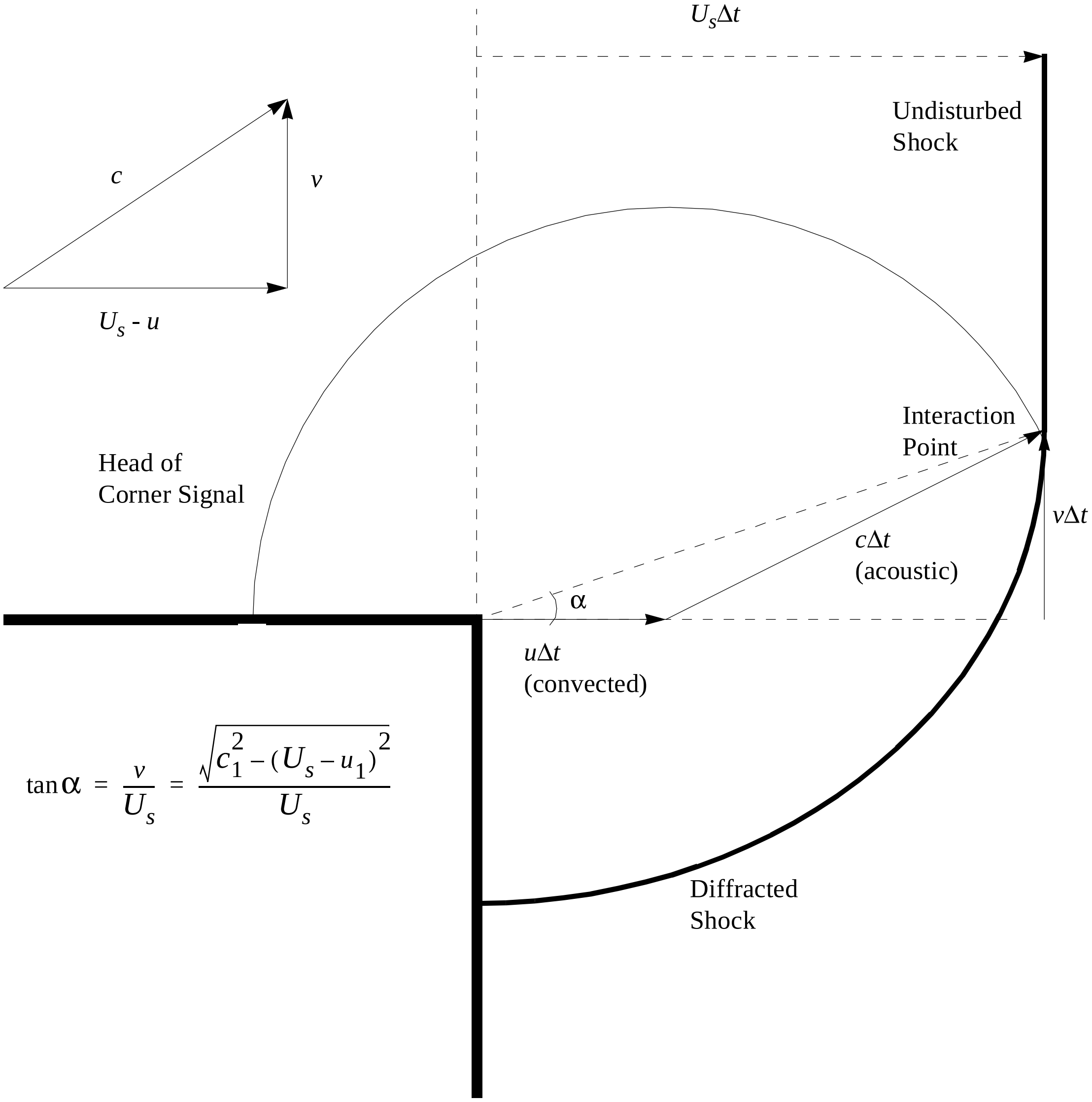

Figure 3.2 Schematic of a diffracting non-reacting shock.

shock continues to propagate at its original velocity. Note that the shape of the corner signal head is shown circular for convenience and will actually depend upon the flow following the undisturbed shock. The transverse velocity of the disturbance along the shock, or the equivalent angle between the disturbance trajectory and the normal to the undiffracted shock, is given by the geometry shown as

$$\tan\alpha = \frac{v}{U_s} = \frac{\sqrt{c_1^2 - (U_s - u_1)^2}}{U_s} \tag{3.1}$$

where state 1 refers to the post-shock condition. Skews (1967) conducted shock diffraction experiments for a variety of corner turning angles (15° - 165°) and shock Mach numbers (1.0 - 3.5), and demonstrated excellent agreement between the measurements and this analytical expression (Section 2.1.3).

In the CJ model of a detonation, there exists no characteristic scale because the entire wave is treated as a discontinuity travelling at V_{CJ} with chemical equilibrium and sonic outflow conditions. Application of the Skews' construction to a diffracting detonation described by the CJ model results in a degenerate case of zero transverse disturbance velocity and angle (Fig. 3.3a). This is a direct result of the sonic outflow condition in the discontinuity treatment and is obvious from the physical standpoint that information can not be communicated through a sonic plane.

The ZND model of a detonation provides a region for the disturbance to propagate into the wavefront, namely through the finite reaction zone (Fig. 3.3b). In this case, the

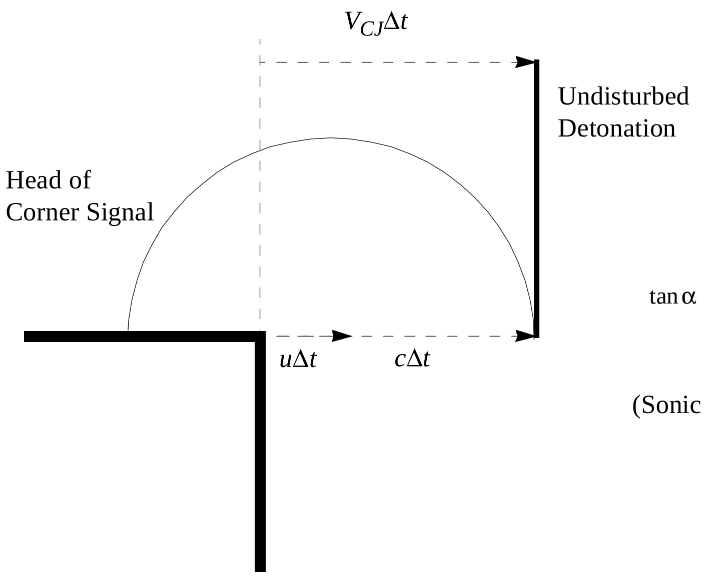

$$\tan\alpha = \frac{v}{V_{CJ}} = \frac{\sqrt{c^2 - (V_{CJ} - u)^2}}{V_{CJ}} = 0$$

(Sonic outflow requires that $u = V_{CJ} - c$)

(a) Application to the CJ (discontinuity) detonation model.

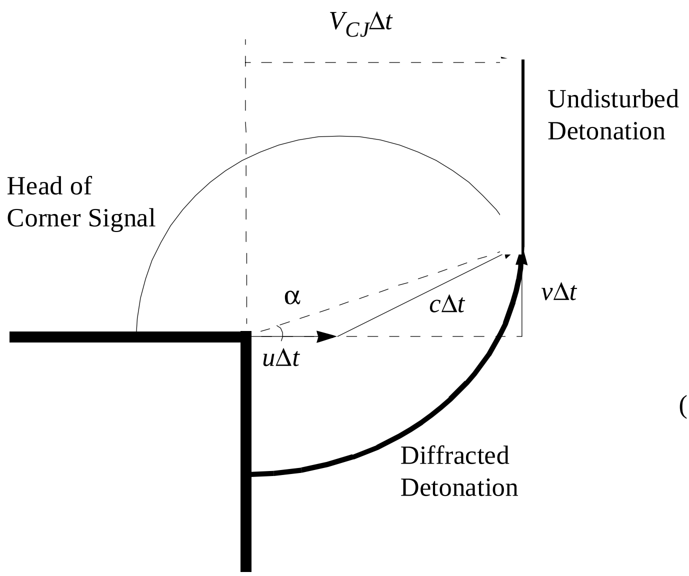

$$\tan\alpha = \frac{v}{V_{CJ}} = \frac{\sqrt{c_{rz}^2 - (V_{CJ} - u_{rz})^2}}{V_{CJ}}$$

($u < V_{CJ} - c$ within the reaction zone)

(b) Application to the ZND detonation model.

Figure 3.3 Extension of Skews' construction to disturbance propagating into a detonation front.

preceeding analytical expression of Skews (Eqn.3.1) becomes

$$\tan\alpha = \frac{v}{V_{CJ}} = \frac{\sqrt{c_{rz}^2 - (V_{CJ} - u_{rz})^2}}{V_{CJ}} \qquad (3.2)$$

where state *rz* represents some location within the reaction zone. Calculation of the values necessary to evaluate this expression is presented in Section 4.2.2. The von Neumann state may seem to be the obvious reaction zone location, but usually does not correspond to the maximum transverse disturbance velocity. Experimental results presented in Section 5.3 are used to identify the appropriate choice of disturbance propagation angle and from this, the critical time and equivalent distance for the disturbance to reach the tube axis are given by

$$x_c = \frac{d}{2\tan\alpha} \qquad t_c = \frac{d}{2V_{CJ}\tan\alpha} = \frac{x_c}{V_{CJ}} \qquad (3.3)$$

3.3 Critical diffraction model

A fluid particle passing through the shock along the tube axis at the critical time t_c (Fig. 3.1) and equivalent distance x_c from the area change will be subject to an approximately spherical expansion. This assumption of spherical symmetry is supported by the shock diffraction observations of Davies and Guy (1971) that the axial shock decays strongly when the lead unsteady expansion characteristics meet and reflect at the symmetry axis (Chapter 2), the work of Sloan and Nettleton (1975) in their study of the decay of the shock along the tube axis (Section 2.1.3), axisymmetric non-reacting shock diffraction simulations (Section 4.4), and also follows from experimental measurements of shock decay along the tube axis for sub-critical detonation diffractions (Section 5.4). The results of Edwards et al. (1979) for shock decay along the tube axis following sub-critical detonation diffraction (Section 2.2.2) are difficult to apply due to the two-dimensional geometry of their experiments and probable boundary layer influence in their thin channel.

The laboratory reference frame reactive Euler equations of mass, momentum, energy, and species for spherically symmetric geometry are

$$\frac{D\rho}{Dt} + \rho\frac{\partial u}{\partial r} + \frac{2}{r}\rho u = 0 \tag{3.4}$$

$$\frac{Du}{Dt} + \frac{1}{\rho}\frac{\partial P}{\partial r} = 0 \tag{3.5}$$

$$\frac{De}{Dt} - \frac{P}{\rho^2}\frac{D\rho}{Dt} = 0 \tag{3.6}$$

$$\frac{Dy_i}{Dt} = \Omega_i \tag{3.7}$$

These equations will be manipulated following the procedure of Eckett et al. (1997, 2000) to obtain differential equations for the velocity, pressure, and density of a fluid particle in the following manner. The energy equation and thermodynamic relations can be used to obtain the adiabatic change equation (Fickett and Davis 1979):

$$\frac{DP}{Dt} = c^2\frac{D\rho}{Dt} + \rho c^2\sum\sigma_i\Omega_i = c^2\frac{D\rho}{Dt} + \rho c^2\dot{\sigma} \tag{3.8}$$

where the thermicity coefficients are given by

$$\sigma_i = \left.\frac{1}{\rho c^2}\frac{\partial P}{\partial y_i}\right|_{e,\,\rho,\,y_{j\neq i}} \tag{3.9}$$

Combining the mass (Eqn. 3.4), momentum (Eqn. 3.5), and adiabatic change (Eqn. 3.8) equations and converting to a shock-fixed reference frame defined by

$$x = R(t) - r \tag{3.10}$$

$$w(x, t) = U_s(t) - u(r, t) \tag{3.11}$$

one obtains the following differential equations:

$$(1-M^2)\frac{Dw}{Dt} = w\dot{\sigma} - \frac{2w(U_s - w)}{R-x} - M^2\frac{dU_s}{dt} + \frac{\partial w}{\partial t} - \frac{w}{\rho c^2}\frac{\partial P}{\partial t} \tag{3.12}$$

$$(1-M^2)\frac{D\rho}{Dt} = -\rho\dot{\sigma} + \frac{2\rho M^2(U_s - w)}{R-x} + \frac{\rho w}{c^2}\frac{dU_s}{dt} - \frac{\rho w}{c^2}\frac{\partial w}{\partial t} + \frac{1}{c^2}\frac{\partial P}{\partial t} \tag{3.13}$$

$$(1-M^2)\frac{DP}{Dt} = -\rho w^2\dot{\sigma} + \frac{2\rho w^2(U_s - w)}{R-x} + \rho w\frac{dU_s}{dt} - \rho w\frac{\partial w}{\partial t} + \frac{\partial P}{\partial t} \tag{3.14}$$

where the flow Mach number $M = w/c$. The competing effects of energy release, curvature, and unsteadiness are clearly distinguishable in the right-hand sides of these equations.

As discussed in Chapter 1, the chemical reactions responsible for sustaining the detonation wave are most sensitive to the temperature. A differential equation for the temperature of a fluid particle can be obtained by considering a system of ideal gases for which the thermal equation of state is

$$P = \rho R_g T \tag{3.15}$$

where the mixture gas constant R_g is the ratio of the universal gas constant $\mathcal{R}$ and the average mixture molar mass W. The acoustic speed (frozen sound speed) is given by

$$c^2 = \gamma R_g T \tag{3.16}$$

and the thermicity coefficients are

$$\sigma_i = \frac{1}{\gamma}\left(\frac{W}{W_i} - \frac{e_i}{C_v T}\right) \tag{3.17}$$

Combining these expressions (Eqns. 3.15 - 3.17) with the equations for the gradients of velocity (Eqn. 3.12), density (Eqn. 3.13), and pressure (Eqn.3.14) gives the temperature gradient equation for a system of ideal gases in a shock-fixed, spherically symmetric reference frame:

$$\begin{aligned} C_p(1-M^2)\frac{DT}{Dt} &= -(1-\gamma M^2)\sum e_i\Omega_i - \frac{c^2}{\gamma}\sum\frac{W}{W_i}\Omega_i + \\ &\quad \frac{2w^2(U_s-w)}{R-x} + w\frac{dU_s}{dt} - w\frac{\partial w}{\partial t} + \frac{1}{\rho}\frac{\partial P}{\partial t} \end{aligned} \tag{3.18}$$

In order to reduce this temperature equation to one that can be evaluated analytically, consider a one-step irreversible reaction A→B with the internal energy of species A and B given by

$$e_A = C_{v,A}T \qquad e_B = C_{v,B}T - \Delta h^0 \tag{3.19}$$

Equation 3.18 becomes

$$\begin{aligned} C_p(1-M^2)\frac{DT}{Dt} &= -(1-\gamma M^2)[C_{v,A}T\Omega_A + C_{v,B}T\Omega_B - \Delta h^0\Omega_B] + \\ &\quad \left(-\frac{c^2W}{\gamma}\left[\frac{\Omega_A}{W_A}+\frac{\Omega_B}{W_B}\right]\right) + \frac{2w^2(U_s-w)}{R-x} + w\frac{dU_s}{dt} - w\frac{\partial w}{\partial t} + \frac{1}{\rho}\frac{\partial P}{\partial t} \end{aligned} \tag{3.20}$$

Defining the reaction progress variable as the mass fraction of product species B

$$Z = y_B = 1 - y_A \tag{3.21}$$

and assuming the specific heats and molecular masses of species A and B are equal, Eqn. 3.20 results in

$$\begin{aligned} C_p(1-M^2)\frac{DT}{Dt} &= \Delta h^0(1-\gamma M^2)\frac{DZ}{Dt} + \\ &\quad \frac{2w^2(U_s-w)}{R-x} + w\frac{dU_s}{dt} - w\frac{\partial w}{\partial t} + \frac{1}{\rho}\frac{\partial P}{\partial t} \end{aligned} \tag{3.22}$$

Replacing the reaction progress variable rate of change term with a first order Arrhenius kinetic rate law with linear depletion

$$\frac{DZ}{Dt} = k(1-Z)\exp\left[-\frac{E_a}{\mathcal{R}T}\right] \tag{3.23}$$

transforms Eqn. 3.22 to

$$\begin{aligned} C_p(1-M^2)\frac{DT}{Dt} = {} & \Delta h^0 k(1-Z)(1-\gamma M^2)\exp\left[-\frac{E_a}{\mathcal{R}T}\right] + \\ & \frac{2w^2(U_s-w)}{R-x} + w\frac{dU_s}{dt} - w\frac{\partial w}{\partial t} + \frac{1}{\rho}\frac{\partial P}{\partial t} \end{aligned} \tag{3.24}$$

This equation can be approximated as an ordinary differential equation by assuming negligible reactant consumption ($Z = 0$), and evaluating the flow Mach number, and curvature and unsteady terms on the right-hand side at the post-shock condition ($x = 0$).

$$\begin{aligned} C_p(1-M_s^2)\frac{DT}{Dt} = {} & \Delta h^0 k(1-\gamma M_s^2)\exp\left[-\frac{E_a}{\mathcal{R}T}\right] + \\ & \frac{2w_s^2(U_s-w_s)}{R} + w_s\frac{dU_s}{dt} - w_s\frac{dw_s}{dt} + \frac{1}{\rho_s}\frac{dP_s}{dt} \end{aligned} \tag{3.25}$$

These approximations are considered in details in Eckett et al. (2000) and justified by comparing the results of these approximations with detailed numerical simulations.

A non-dimensional effective activation energy parameter is defined by

$$\theta_s = \frac{E_a}{\mathcal{R}T_s} \tag{3.26}$$

The ZND reaction time obtained from high activation energy asymptotics ($\theta_s >> 1$, $T = T_s + T'$, and $\theta_s T' << T_s$) is given by (Eckett et al. 2000)

$$\tau = \frac{1}{k}\left(\frac{1-M_s{}^2}{1-\gamma M_s{}^2}\right)\frac{e^{\theta_s}}{\theta_s}\frac{C_p T_s}{\Delta h^0} \tag{3.27}$$

Combining Eqns. 3.25 - 3.27 results in the following ordinary differential equation for the post-shock temperature:

$$\frac{DT}{Dt} = \frac{T_s}{\tau\theta_s}\exp\left(\frac{\theta T'}{T_s}\right) + \frac{1}{C_p(1-M_s^2)}\left[\frac{2}{R}w_s^2(U_s-w_s) + w_s\frac{dU_s}{dt} - w_s\frac{dw_s}{dt} + \frac{1}{\rho_s}\frac{dP_s}{dt}\right] \tag{3.28}$$

The post-shock state has been chosen for evaluation because it is the thermodynamic state which sets the initial conditions for the chemical reactions which follow. Analogous to the critical initiation criteria of Eckett et al. (1997, 2000), a critical diffraction criterion of $DT / Dt = 0$ and $T' = 0$ will be imposed, i.e., the critical conditions occur when the unsteadiness and curvature terms are exactly balanced by the energy release term. Therefore, the detonation diffraction is super-critical if the right-hand side is positive (i.e., energy release overcomes quenching effects) and sub-critical if negative (i.e., quenching effects dominate so that the temperature of the fluid particle decreases behind the shock). This choice of criterion is supported by detonation initiation simulations in which the critical state for initiation was found to occur when the post-shock temperature gradient was approximately zero (Eckett et al. 2000). The contribution due to curvature in the final expression for the critical diameter will be shown to be small.

The constant pressure specific heat is related to the ratio of specific heats and the mixture gas constant through

$$C_p = \frac{\gamma R_g}{\gamma - 1} \tag{3.29}$$

The post-shock variables can be put in terms of the shock velocity through the perfect gas strong shock jump conditions

$$w_s = \left(\frac{\gamma - 1}{\gamma + 1}\right) U_s \tag{3.30}$$

$$T_s = \frac{2(\gamma - 1) U_s^{\ 2}}{R_g (\gamma + 1)^2} \tag{3.31}$$

$$\rho_s = \left(\frac{\gamma + 1}{\gamma - 1}\right) \rho_0 \tag{3.32}$$

$$M_s^{\ 2} = \frac{\gamma - 1}{2\gamma} \tag{3.33}$$

and the required derivatives:

$$\frac{dw_s}{dt} = \left(\frac{\gamma - 1}{\gamma + 1}\right) \frac{dU_s}{dt} \tag{3.34}$$

$$\frac{dP_s}{dt} = \left(\frac{4\rho_0 U_s}{\gamma + 1}\right) \frac{dU_s}{dt} \tag{3.35}$$

Use of the strong shock jump conditions is an excellent approximation for detonation shock Mach numbers which typically range from five to eight. Some error is introduced through the strong shock approximation of the fluid velocity time derivative. This derivative is increased by approximately 20% for a Mach five detonation and 8% for a Mach eight detonation when using the strong shock approximation. Hydrocarbon detonations tend to have greater Mach numbers than hydrogen detonations and therefore, will be less influenced by this error.

Substituting for the constant pressure specific heat and the post-shock conditions into Eqn. 3.28 and setting *DT* / *Dt* = 0 and *T' = 0* gives

$$\frac{U_s}{\tau \theta_s} + \frac{4 U_s^2 (\gamma - 1)^2}{R (\gamma + 1)^2} + 6\left(\frac{\gamma - 1}{\gamma + 1}\right) \frac{dU_s}{dt} = 0 \tag{3.36}$$

As previously mentioned, the non-reacting shock diffraction experiments of Sloan and

Nettleton (Section 2.1.3), axisymmetric simulations of non-reacting shock diffraction (Section 4.4), and detonation diffraction experiments (Section 5.4) support a spherically symmetric decay of the shock along the tube axis after the critical time. Therefore, the Taylor-Sedov strong blast similarity solution will be used for the shock decay along the axis just after the critical time when the detonation shock Mach number is large. The similarity solution for a non-reacting, spherically decaying shock neglecting the initial pressure is given by (Taylor 1950, Sedov 1959)

$$R = \left(\frac{E_{source}}{A_2\rho_0}\right)^{\frac{1}{5}} t^{\frac{2}{5}} \tag{3.37}$$

$$U_s = \frac{2}{5}\left(\frac{E_{source}}{A_2\rho_0}\right)^{\frac{1}{2}} R^{-\frac{3}{2}} \tag{3.38}$$

$$\frac{dU_s}{dt} = -\frac{6}{25}\left(\frac{E_{source}}{A_2\rho_0}\right) R^{-4} \tag{3.39}$$

The shock velocity U_s along the axis at the instant of the critical time is the detonation velocity V_{CJ}. The non-reacting shock diffraction experiments of Sloan and Nettleton (Section 2.1.3), axisymmetric simulations of non-reacting shock diffraction (Section 4.4), and detonation diffraction experiments (Section 5.4) indicate that the spherically symmetric shock decay along the axis has an apparent radius of curvature given by the distance from the area change to the shock at the critical time. Therefore, the Taylor-Sedov energy parameter can be determined by setting $U_s = V_{CJ}$ and $R = x_c$ in Eqn. 3.38

$$\frac{E_{source}}{A_2\rho_0} = \frac{25}{4} V_{CJ}{}^2 x_c{}^3 \tag{3.40}$$

from which follows expressions for the shock radius and acceleration along the tube axis when Eqn. 3.40 is combined with Eqns. 3.38 and 3.39:

$$R = x_c\left(\frac{V_{CJ}}{U_s}\right)^{\frac{2}{3}} \tag{3.41}$$

$$\frac{dU_s}{dt} = -\frac{3}{2}x_c U_s^2\left(\frac{U_s}{V_{CJ}}\right)^{\frac{2}{3}} \tag{3.42}$$

Note that Eqn.3.40 can be used to pursue a model for the critical conditions in direct detonation initiation from a point source of energy release.

Consideration can now be given to the contribution of the curvature term in Eqn. 3.36. The ratio of the unsteadiness and curvature terms evaluated with the Taylor-Sedov solution (Eqns. 3.41 and 3.42) at the critical time ($U_s = V_{CJ}$ and $R = x_c$) is

$$\frac{6\left(\frac{\gamma-1}{\gamma+1}\right)\frac{dU_s}{dt}}{\frac{4U_s^2(\gamma-1)^2}{R(\gamma+1)^2}} = -\frac{9}{4}\left(\frac{\gamma+1}{\gamma-1}\right)$$

which varies in magnitude from 10 to 25 for specific heat ratios from 1.6 to 1.2. Therefore, the curvature term is at least one order of magnitude less than the unsteadiness term and can be neglected. Also note that the curvature term is positive in its effect on the temperature of a fluid particle and as such, does not provide a quenching mechanism through the temperature equation.

Evaluating Eqn. 3.36 (neglecting the curvature term) with the Taylor-Sedov similarity solution (Eqns. 3.41 and 3.42) at some critical shock velocity ($U_s = U_c$) gives the axial distance from the area change plane for critical diffraction conditions

The critical shock velocity is some minimum shock velocity at which the post-shock ther-

$$x_c = 9\left(\frac{\gamma - 1}{\gamma + 1}\right)\left(\frac{U_c}{V_{CJ}}\right)^{\frac{2}{3}} U_c \tau \theta \tag{3.43}$$

modynamic state permits a sufficient energy release rate for recoupling of the reaction zone with the shock. As discussed in Section 2.2.2, streak camera and laser Schlieren time-of-flight anemometer measurements of the shock velocity along the tube axis under critical conditions indicate that the shock decays significantly from the CJ velocity before re-initiation occurs. He and Clavin (1994) derived an expression from high activation energy asymptotics for a minimum critical shock velocity at which a quasi-steady curved detonation can exist:

$$U_c = V_{CJ}\left[1 - \left(\frac{1}{2\theta_{CJ}}\right)\right] \tag{3.44}$$

Yao and Stewart (1995) developed a similar critical shock velocity expression with the same assumptions of curvature and steady flow while neglecting unsteadiness. Analytical and experimentally observed critical shock velocities will be considered further in Chapters 4 and 5.

The critical axial distance (Eqn.3.43) is related to the critical diameter through the propagation angle of the disturbance as it moves into the undisturbed detonation

$$x_c = \frac{d_c}{2\tan\alpha} \tag{3.45}$$

and therefore, the critical tube diameter is given by

$$d_c = 18\left(\frac{\gamma - 1}{\gamma + 1}\right)\left(\frac{U_c}{V_{CJ}}\right)^{\frac{2}{3}} U_c \tau \theta \tan\alpha \tag{3.46}$$

Evaluation of this expression requires knowledge of six parameters. The specific heat ratio comes from the reactant mixture properties and the CJ detonation velocity is found through a chemical equilibrium calculation. A critical shock velocity can be analytically determined from Eqn. 3.44 or based on experimental observations, and is used as an initial condition for calculating the reaction time and activation energy. The post-shock reaction time is provided by constant-volume simulations and the effective activation energy parameter is computed through temperature perturbations of constant volume explosion simulations. The disturbance propagation angle is calculated from Eqn. 3.2, with the reaction zone particle velocity and acoustic speed given by either the post-shock state or corresponding to the maximum reaction zone transverse disturbance velocity from steady, one-dimensional ZND detonation simulations. Calculation results for all of these parameters are presented in Chapter 4.

4 Computational

The critical diffraction model input parameters are the specific heat ratio of the reactants, CJ detonation velocity, critical shock velocity, characteristic reaction time, effective activation energy, and the disturbance propagation angle. Plots of these parameters and a description of the calculations made to determine them are presented in the following sections. The combustible mixtures considered included variations of fuel type (hydrogen, ethylene, propane), equivalence ratio (0.2 - 3.0), diluent (argon, carbon dioxide, helium, nitrogen), diluent concentration (0% - 90%), and initial pressure (20 - 200 kPa). All relevant data from the calculations are tabulated in Appendix A.

The simulations used to obtain characteristic reaction times and effective activation energies require a detailed reaction mechanism. Detailed reaction mechanisms consist of a comprehensive set of species and reaction rates, attempting to represent all chemical processes within a given system. Many detailed reaction mechanisms describing the oxidation of a variety of fuels exist in the literature, but little emphasis has been placed on validating these mechanisms under detonation thermodynamic conditions. As part of this research an extensive effort was made to determine which mechanism is most accurate in representing detonation chemistry. The results of the validation study are provided in a comprehensive report by Schultz and Shepherd (1999) and a summary of the pertinent results follows.

Induction time data from over 2000 shock tube experiments on hydrogen, ethylene, and propane oxidation were compiled from the literature, along with 19 detailed reaction mechanisms which included the chemistry for some or all of these fuels. Note that post-shock thermodynamic conditions in detonations propagating at the CJ velocity under initial conditions of 1 bar and 295 K are approximately bounded by pressures from 10bar to 100bar and temperatures from 1000K to 2200K. Most of the shock tube data were acquired at relatively low pressures and temperatures, and so further reaction mechanism validation studies will be required as more appropriate shock tube data become available.

A constant volume explosion simulation (described in Section 4.3) corresponding to each shock tube experiment was run with every applicable mechanism. A quantitative measure of accuracy was obtained by statistically comparing the simulation data to the experimental data for a given mechanism, fuel type, and temperature range. The average deviation between the simulated ($\tau_{s,i}$) and experimental ($\tau_{e,i}$) induction times is defined by

$$Deviation = \frac{1}{N}\sum_{j=1}^{N}\log\left(\frac{\tau_{s,j}}{\tau_{e,j}}\right) \tag{4.1}$$

The average deviation was calculated for a group of data corresponding to a particular subset of temperature range (increments of 100 K except at the highest and lowest temperatures) and fuel type (hydrogen, ethylene, propane), where N is the total number of simulations/experiments in the group. Zero represents perfect correspondence between simulation and experiment whereas average deviations of 1.0 and -1.0 indicate that the simulated induction times in that group were an order of magnitude greater than and less than the experimental induction times, respectively.

The Konnov (1998) reaction mechanism was identified as the most accurate among those which include the chemistry for all three fuels, simulating the experimental induction time data to within an average factor of 2.5 for temperatures above 1200 K. The average deviation versus temperature and fuel type for this mechanism is presented in

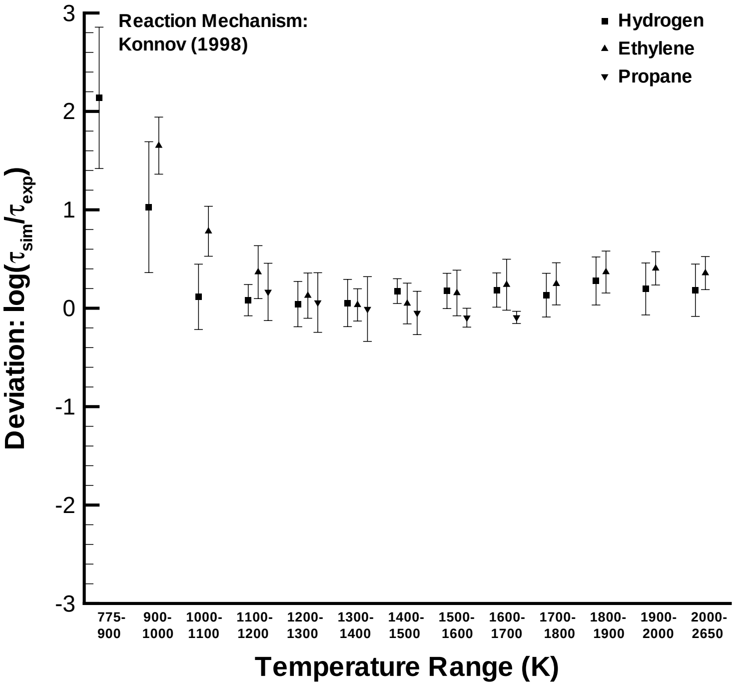

Figure 4.1 Simulation-to-experiment induction time deviation for the Konnov (1998) reaction mechanism.

Fig. 4.1. The vertical bars attached to each average deviation data point indicate one statistical standard deviation and therefore, indicate the range in which approximately 70% of the deviation lies on a point-by-point basis. Reaction mechanisms are not solely responsible for the deviation between simulated and experimental induction times. Uncertainties associated with the experimental data, numerical integration, and the constant-volume approximation are also present and were analyzed by Schultz and Shepherd (1999).

Note that soot formation in hydrocarbon mixtures is known to occur at relatively high equivalence ratios and the effect on the present calculations, which do not account for soot, is unknown. Strehlow (1984) provides a carbon-to-oxygen atom ratio of 0.5 as a rule-of-thumb for the onset of soot formation in pre-mixed flames. This atomic ratio corresponds to equivalence ratios of 1.5 and 1.7 for ethylene and propane mixtures, respectively. Glassman (1996) gives corresponding equivalence ratios ranging from 1.6 to 2.0, discusses the strong temperature dependence in the soot formation process, and notes that soot production in shock tube experiments is low relative to flame-based studies due to the instantaneous jump in reactant temperature. The effect of equivalence ratio on discrepancies between simulated and experimental induction time data was investigated by Schultz and Shepherd (1999) but no systematic correlations were identified.

4.1 Thermochemical equilibrium calculations

Specific heat ratios and CJ detonation velocities were calculated (Schultz and Shepherd 1999) with the STANJAN thermochemical equilibrium program (Reynolds 1986). The thermochemical database does not include the entire species set used in the detailed reaction mechanisms, but rather a subset including all reactants, primary products, and several intermediate species which may have non-negligible equilibrium concentrations.

4.1.1 Specific heat ratio

The pre-shock specific heat ratios are plotted versus equivalence ratio for fuel-oxygen and fuel-air mixtures in Fig. 4.2. The hydrogen-oxygen and hydrogen-air data overlap and do not vary with equivalence ratio because the mixtures are composed entirely of diatomic molecules. Increasing the equivalence ratio decreases the specific heat ratio for the hydrocarbon mixtures due to greater vibrational degrees of freedom. The specific heat ratios do not vary with initial pressure. Specific heat ratios are plotted versus percent volumetric dilution for stoichiometric fuel-oxygen-diluent mixtures with hydrogen, ethylene, and propane fuel in Figs .4.3, 4.4, and 4.5, respectively. Monatomic dilu-

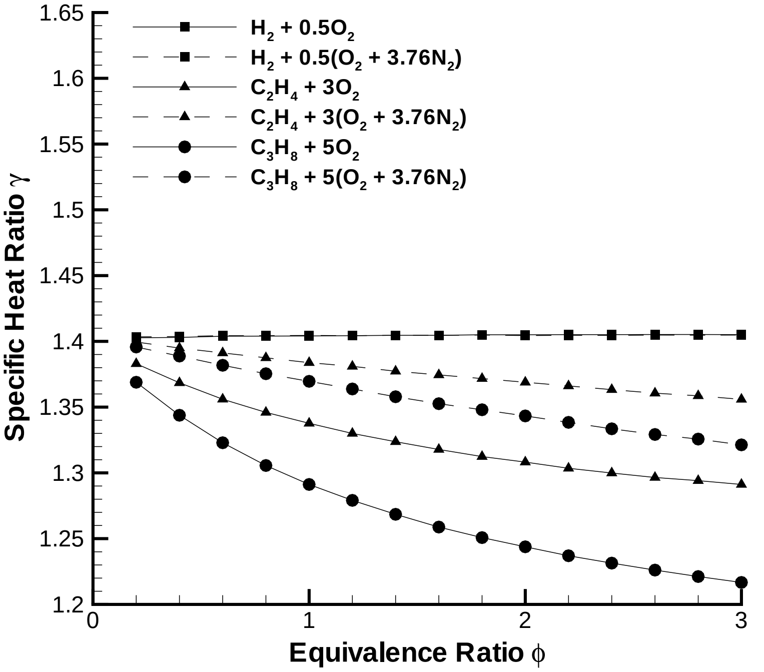

Figure 4.2 Specific heat ratio versus equivalence ratio for fuel-oxygen and fuel-air mixtures (P_1 = 100 kPa, T_1 = 295 K).

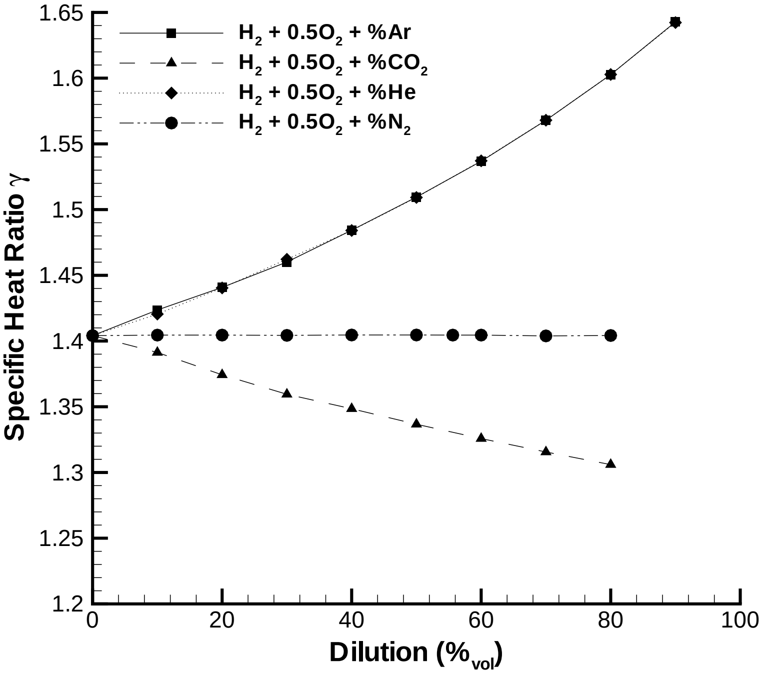

Figure 4.3 Specific heat ratio versus dilution for stoichiometric hydrogen-oxygen mixtures (P_1 = 100 kPa, T_1 = 295 K).

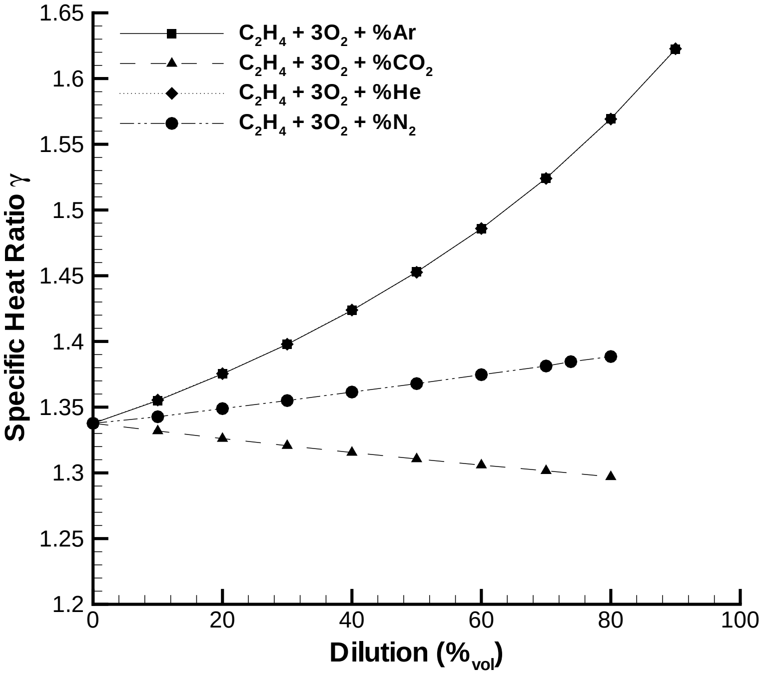

Figure 4.4 Specific heat ratio versus dilution for stoichiometric ethylene-oxygen mixtures (P_1 = 100 kPa, T_1 = 295 K).

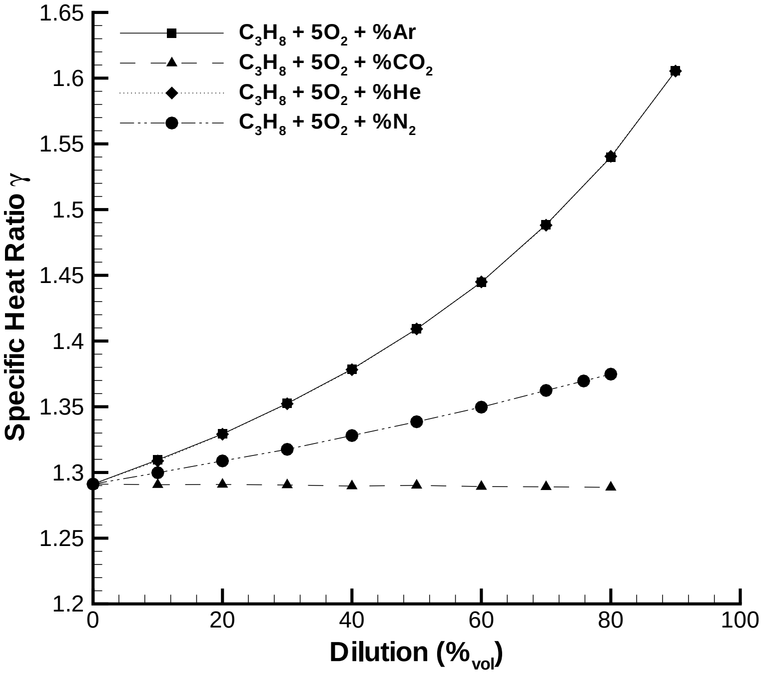

Figure 4.5 Specific heat ratio versus dilution for stoichiometric propane-oxygen mixtures (P_1 = 100 kPa, T_1 = 295 K).

tion with argon and helium increases the specific heat ratio; these diluents have quantitatively identical effects, causing the data to overlap. Nitrogen dilution maintains a constant specific heat ratio for hydrogen mixtures and slightly increases the ratio for hydrocarbon mixtures. Dilution with carbon dioxide decreases the specific heat ratio for all mixtures.

The function of the specific heat ratio contained in the critical diameter expression (Eqn. 3.46) is plotted in Fig. 4.6. The pre-shock specific heat ratios shown in Figs .4.2 - 4.5 vary from 1.2 to 1.65 and calculated post-shock specific heat ratios in these mixtures range from 1.1 to 1.6 because of increased heat capacity in the post-shock state. Pre-shock specific heat ratios are used to evaluate the critical diameter expression because this is consistent with the perfect gas shock jump conditions used in deriving the critical diffraction model. However, the perfect gas assumption made for analytical simplicity does

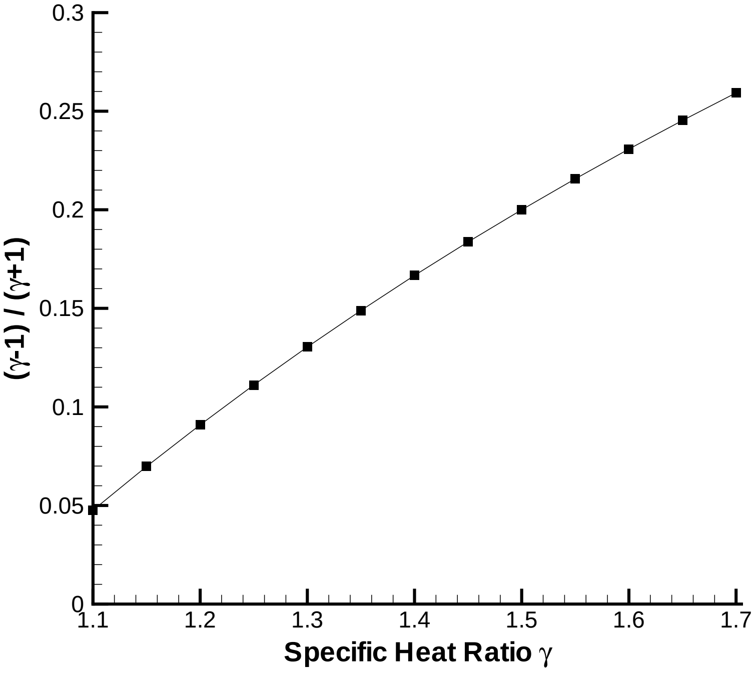

Figure 4.6 Variation of the specific heat ratio function in the critical diameter expression (Eqn 3.46).

introduce some error by not accounting for the specific heat ratio decrease across the shock. For any given mixture, the specific heat ratio varies by 2.5% to 14% (0.04 to 0.2 absolute decrease) between the pre- and post-shock states. This corresponds to changes in the specific heat ratio function (Fig. 4.6) of 5% to 60%, respectively, with an average error incurred among all the mixtures of approximately 20%.

4.1.2 Detonation velocity

Detonation velocities are plotted versus equivalence ratio for fuel-oxygen and fuel-air mixtures in Fig. 4.7. Fuel-oxygen detonation velocities are always greater than those for fuel-air mixtures. Nitrogen dilution reduces the energy per unit mass and the detonation velocity is dependent upon the square root of this energy (Thompson 1988, Schultz and Shepherd 1999). The monotone increase of detonation velocity from lean to rich equivalence ratios for hydrogen mixtures is related to the decreasing molecular mass

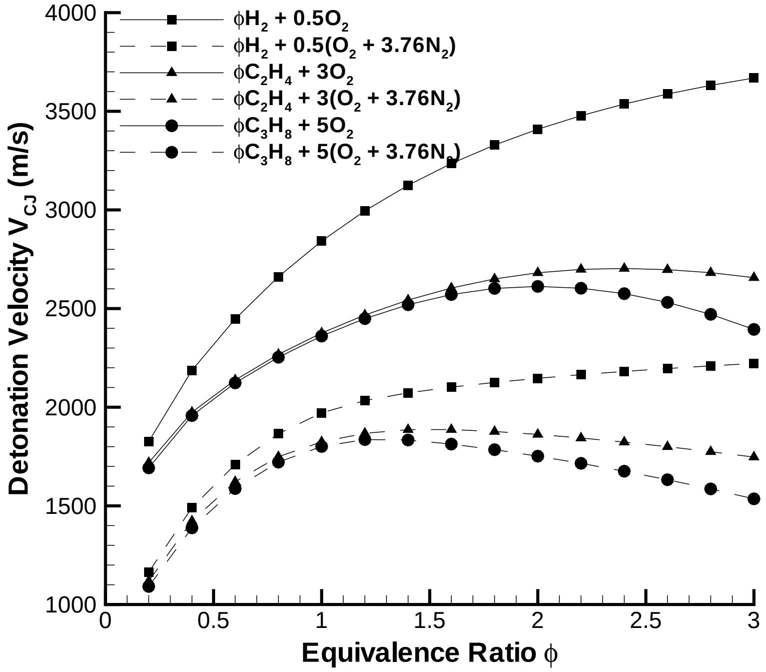

Figure 4.7 Detonation velocity versus equivalence ratio for fuel-oxygen and fuel-air mixtures (P_1 = 100 kPa, T_1 = 295 K).

of the mixture. Hydrocarbon detonation velocities exhibit maximum detonation velocities at rich equivalence ratios, especially for the hydrocarbon-oxygen mixtures because of dissociative competition between intermediate and major product species (Schultz and Shepherd 1999).

Detonation velocities are plotted versus initial pressure for stoichiometric fuel-oxygen and fuel-air mixtures in Fig. 4.8. The calculations indicate that detonation velocity is insensitive to pressure. The slight rise in velocity with increasing initial pressure arises because there is less dissociation of the final products, resulting in more energy release per unit mass.

Detonation velocities are plotted versus percent volumetric dilution for stoichiometric fuel-oxygen-diluent mixtures with hydrogen, ethylene, and propane fuel in

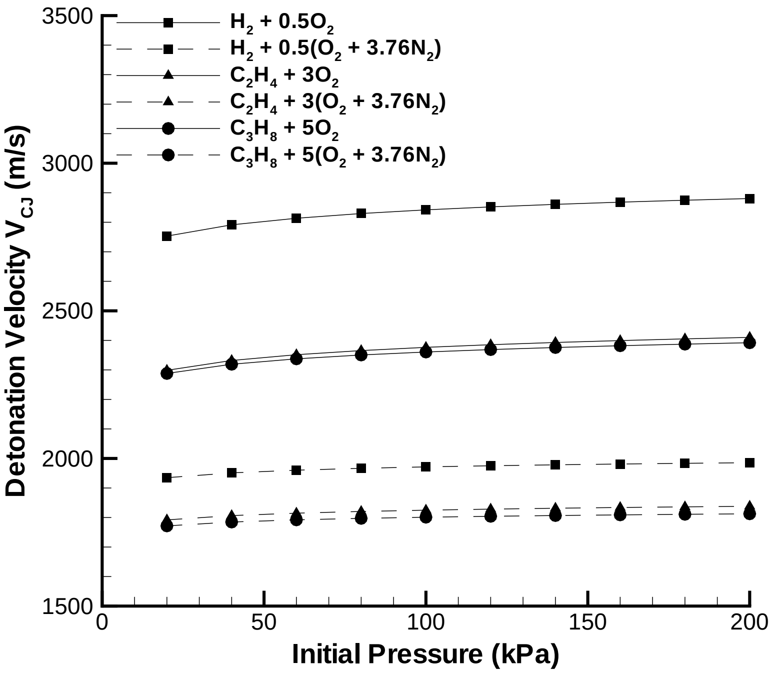

Figure 4.8 Detonation velocity versus initial pressure for stoichiometric fuel-oxygen and fuel-air mixtures (T_1 = 295 K).

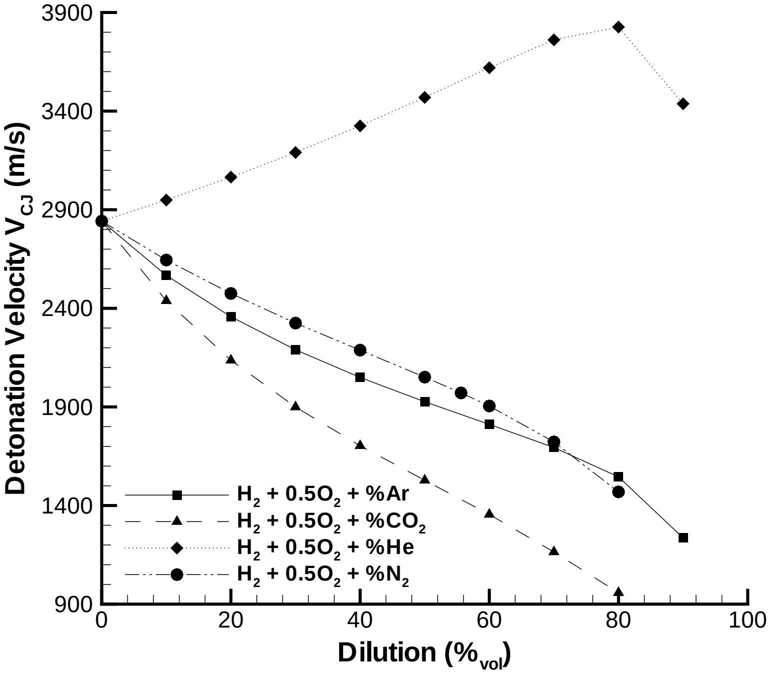

Figure 4.9 Detonation velocity versus dilution for stoichiometric hydrogen-oxygen mixtures (P_1 = 100 kPa, T_1 = 295 K).

Figs. 4.9, 4.10, and 4.11, respectively. Helium dilution increases the detonation velocity for all fuels due to the decreasing molecular mass of the mixtures. All other diluents reduce the detonation velocity because the energy per unit mass is decreased and there is an attendant increase in mixture molecular mass. Carbon dioxide dilution has the most pronounced effect.

4.2 ZND detonation simulations

Simulations of steady, one-dimensional detonations were performed with a program developed by Shepherd (1986b) which incorporates the thermochemical data and detailed reaction mechanism through the Chemkin II chemical kinetics package (Kee et al. 1989), and the *ddebdf* integrator (Shampine and Watts 1979) for systems of stiff, ordinary differential equations. The code is based on the one-dimensional, steady reactive Euler

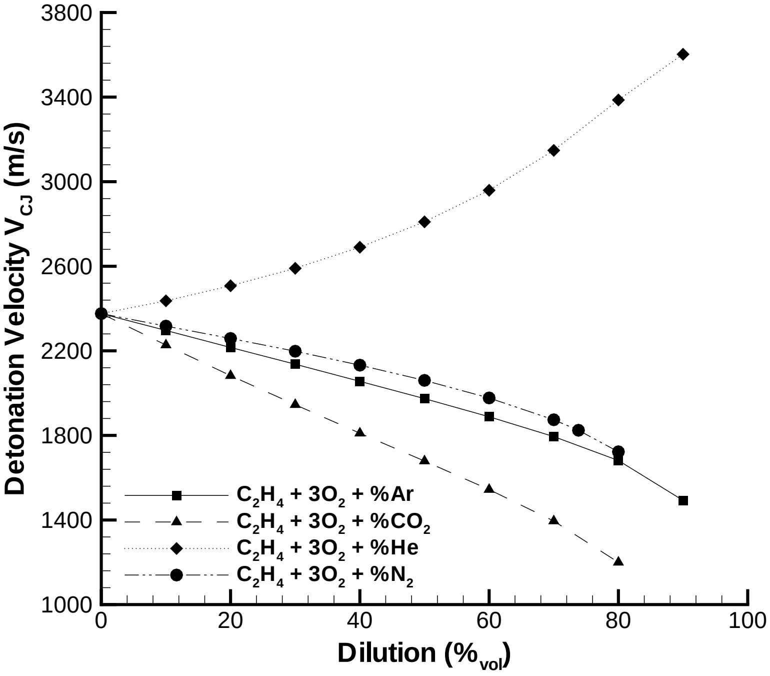

Figure 4.10 Detonation velocity versus dilution for stoichiometric ethylene-oxygen mixtures (P_1 = 100 kPa, T_1 = 295 K).

equations known as the Zeldovich-von Neumann-Doring (ZND) detonation model (Fickett and Davis 1979):

$$\frac{Dw}{Dt} = \frac{w\dot{\sigma}}{1 - M^2} \tag{4.2}$$

$$\frac{D\rho}{Dt} = \frac{-\rho\dot{\sigma}}{1 - M^2} \tag{4.3}$$

$$\frac{DP}{Dt} = \frac{-\rho w^2\dot{\sigma}}{1 - M^2} \tag{4.4}$$

$$\frac{Dy_i}{Dt} = \Omega_i \tag{4.5}$$

$$\dot{\sigma} = \sum_{i=1}^{K} \sigma_i \Omega_i \qquad \sigma_i = \frac{1}{\rho c^2}\frac{\partial P}{\partial y_i}\bigg|_{P,\,\rho,\,y_{j \neq i}} \tag{4.6}$$

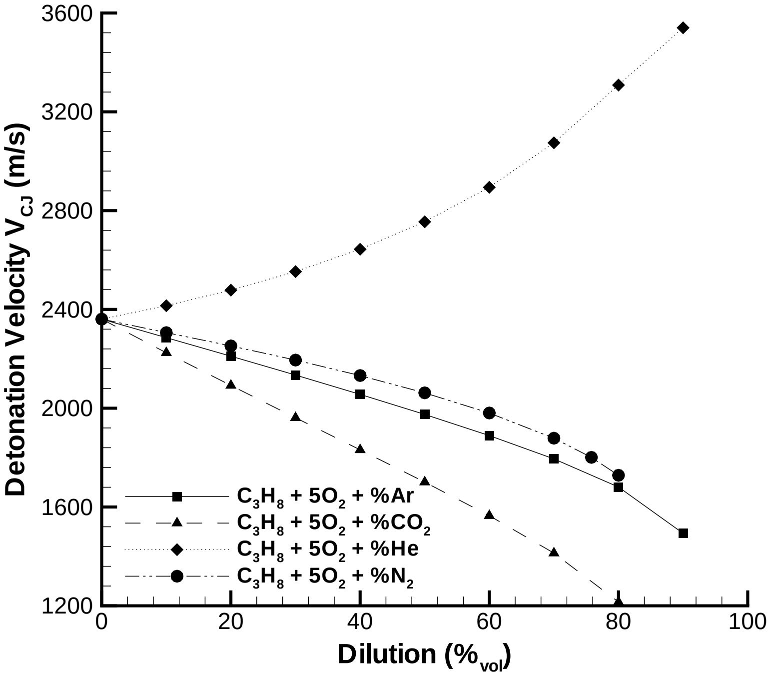

Figure 4.11 Detonation velocity versus dilution for stoichiometric propane-oxygen mixtures (P_1 = 100 kPa, T_1 = 295 K).

where the species production rates are calculated with the Konnov (1998) detailed reaction mechanism. The initial conditions consist of the mixture composition, initial pressure, initial temperature, and V_{CJ} shock velocity. Detonation velocities are presented in the previous section and the post-shock conditions were determined with the shock jump conditions using frozen chemistry. Output from the program includes the spatial evolution of chemical species, velocity, and thermodynamic variables behind the shock wave. Absolute and relative numerical tolerance constraints of $1\text{x}10^{-9}$ and $1\text{x}10^{-10}$, respectively, were imposed on the integrator for all simulations.

The reaction zone structure from a representative ZND simulation in stoichiometric propane-oxygen at initial conditions of 295K and 1atm is presented in Fig.4.12. The

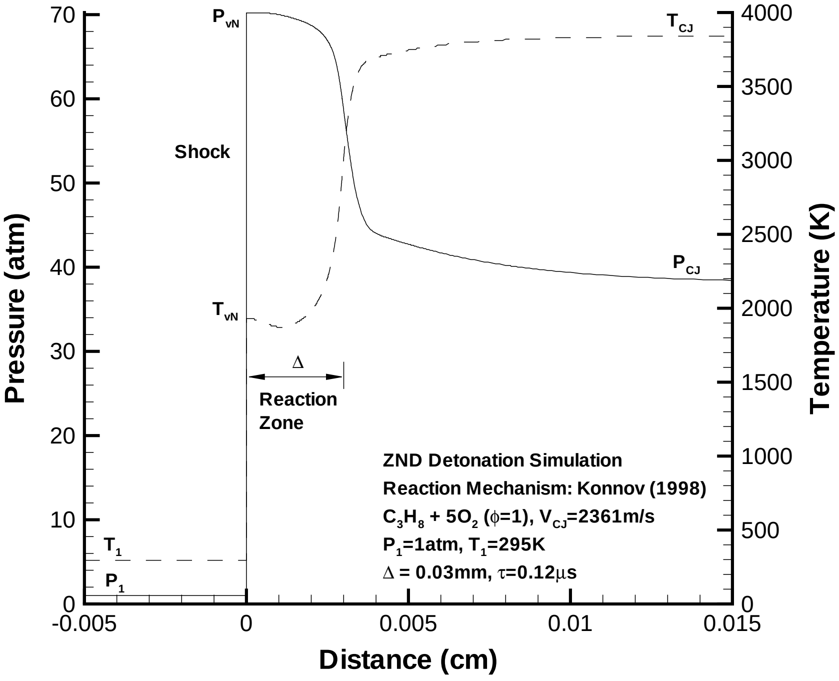

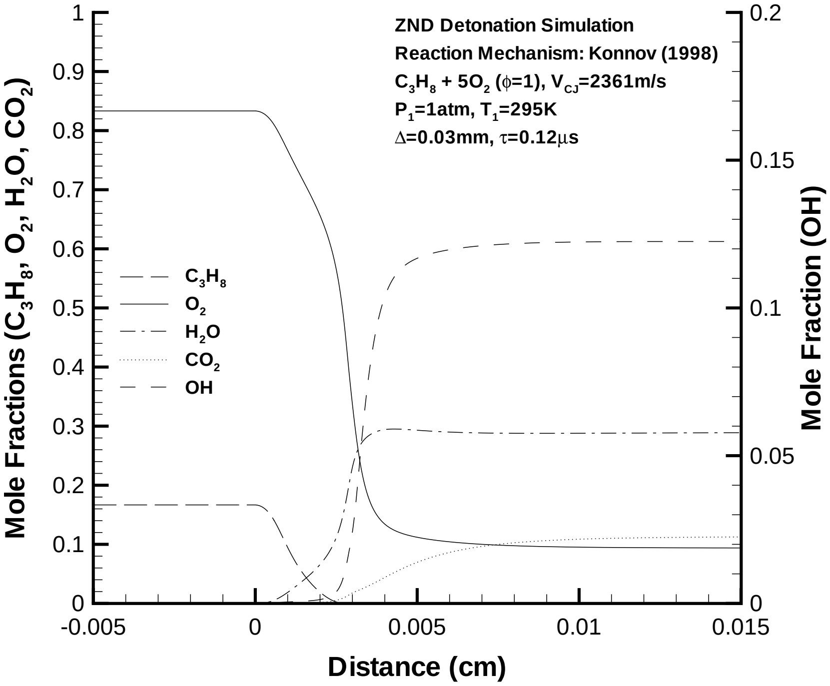

Figure 4.12 Representative steady, one-dimensional detonation simulation.

pressure and temperature rise discontinuously from the initial values to the post-shock (vN) state. The shock is followed by an induction zone through which the thermodynamic state remains relatively constant while free radical (such as OH) concentrations increase. Significant energy release is indicated by the rapid rise in temperature, decrease in pressure, and formation of the major products in the recombination zone. The reaction zone length and the associated reaction time is defined as the distance from the shock to the maximum temperature gradient location. The reaction length is dominated by the post-shock temperature and radical chemistry reaction rates within the endothermic or thermally neutral induction zone. Significant energy release occurs late in the reaction zone and so does not directly affect the reaction length with the maximum temperature gradient definition. Exothermicity indirectly affects the reaction length by influencing the detonation shock velocity and, therefore, the post-shock temperature.

4.2.1 Reaction length

Characteristic detonation reaction lengths are plotted versus equivalence ratio for fuel-oxygen and fuel-air mixtures in Fig. 4.13. The reaction lengths are always greater for the fuel-air mixtures relative to the corresponding fuel-oxygen mixtures. Reaction lengths for the fuel-air mixtures exhibit a minimum near stoichiometric, sharply increase towards the lean side, and gradually rise for rich conditions. Fuel-oxygen mixture curves are relatively flat with all reaction lengths less than 1 mm. All of these trends are due to the post-shock temperature variation with equivalence ratio among fuel-oxygen and fuel-air mixtures discussed by Schultz and Shepherd (1999). There is a clear hierarchy of reaction lengths in the fuel-air mixtures, increasing from hydrogen to ethylene and finally, propane.

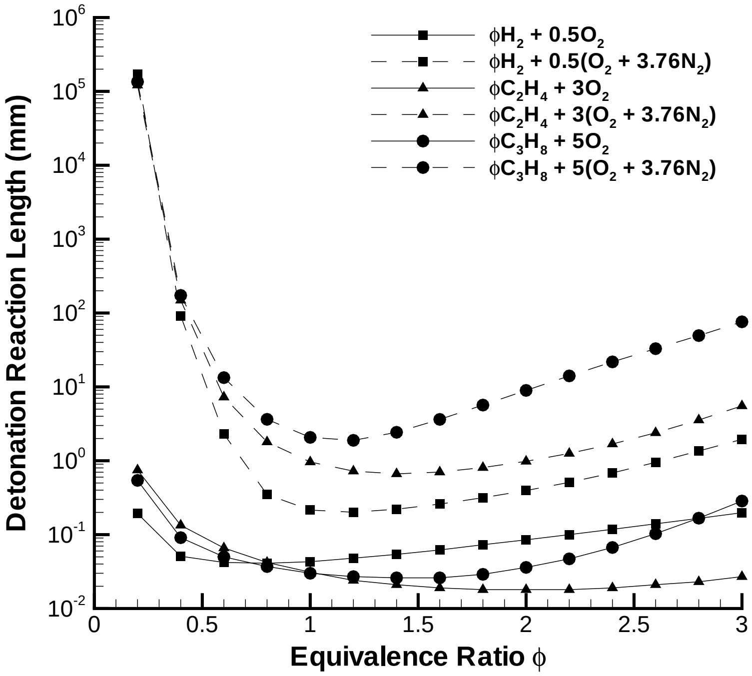

Figure 4.13 Detonation reaction length versus equivalence ratio for fuel-oxygen and fuel-air mixtures (P_1 = 100 kPa, T_1 = 295 K).

The post-shock temperatures for these fuel-air mixtures are comparable and, therefore, the radical chemistry reaction rates determine this hierarchy.

Reaction lengths for stoichiometric fuel-oxygen and fuel-air mixtures with varying initial pressure are presented in Fig. 4.14. Increasing initial pressure results in decreasing reaction lengths varying approximately as $\Delta \sim P^{-1.0}$ for the fuel-oxygen mixtures. This variation is expected from the pressure dependence of rate-limiting bimolecular reactions. The fuel-air mixture pressure dependence is somewhat less relative to the fuel-oxygen dependence due to the prevalence of three-body effects in the nitrogen-diluted mixtures. Fuel-air mixture reaction lengths are always greater than the corresponding fuel-oxygen mixture lengths as expected from post-shock temperature considerations (Schultz and Shepherd 1999).

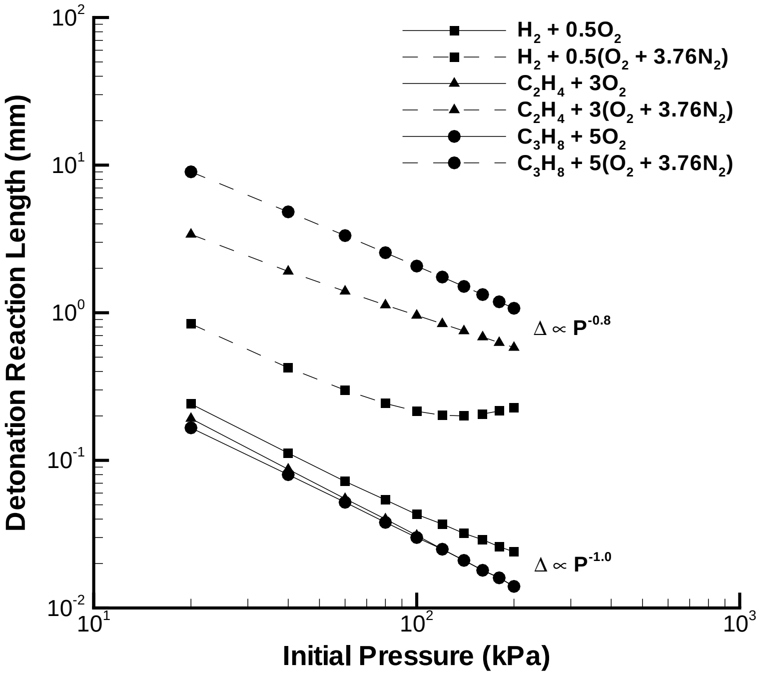

Figure 4.14 Detonation reaction length versus initial pressure for stoichiometric fuel-oxygen and fuel-air mixtures (T_1 = 295 K).

The reaction lengths versus percent diluent data for stoichiometric fuel-oxygen-diluent mixtures with hydrogen, ethylene, and propane fuel are presented in Figs.4.15, 4.16, and 4.17, respectively. Hydrogen is the most sensitive fuel to diluent addition. The argon and helium diluents are chemically inert and, therefore, have a strictly thermal inhibiting effect. Addition of these monatomic gases to a fuel-oxygen mixture decreases the heat capacity, decreases the energy release, and raises the post-shock temperature over a wide range of dilution (Schultz and Shepherd 1999), maintaining relatively constant reaction length over the same range. Argon and helium are quantitatively identical in their effect on the reaction time, and the reaction lengths for helium are greater due to increased shock velocities relative to argon-diluted mixtures. Carbon dioxide increases the reaction length most significantly for all fuels, followed by nitrogen; this order is given by the

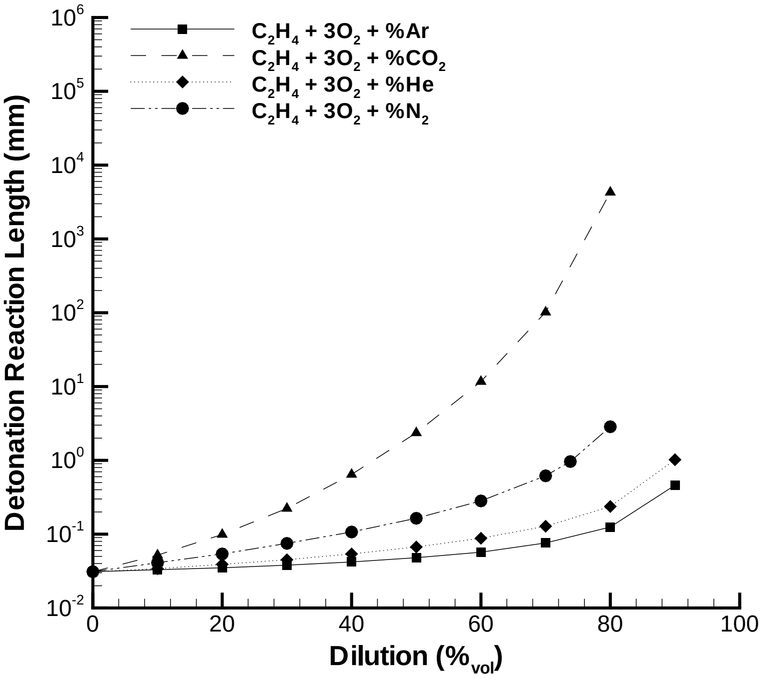

Figure 4.16 Detonation reaction length versus dilution for stoichiometric ethylene-oxygen mixtures (P_1 = 100 kPa, T_1 = 295 K).

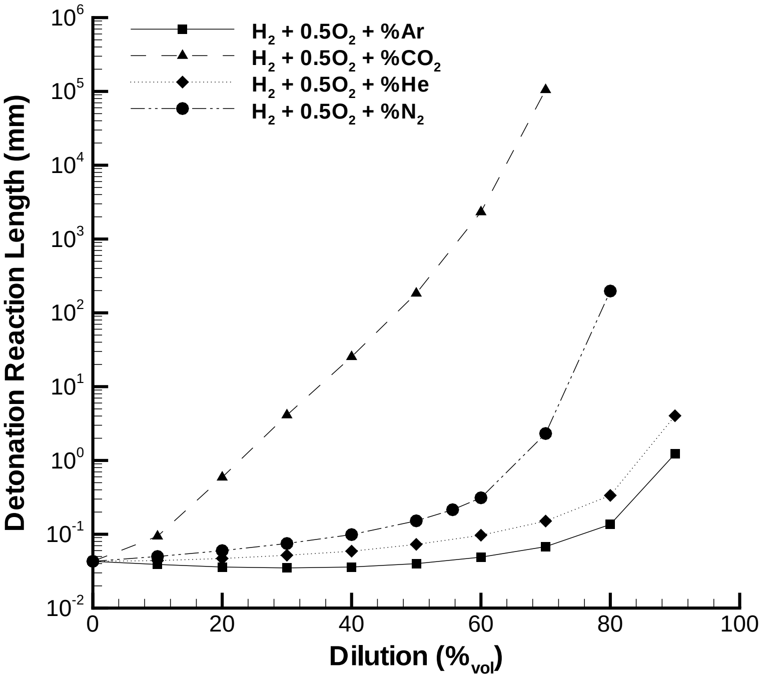

Figure 4.15 Detonation reaction length versus dilution for stoichiometric hydrogen-oxygen mixtures (P_1 = 100 kPa, T_1 = 295 K).

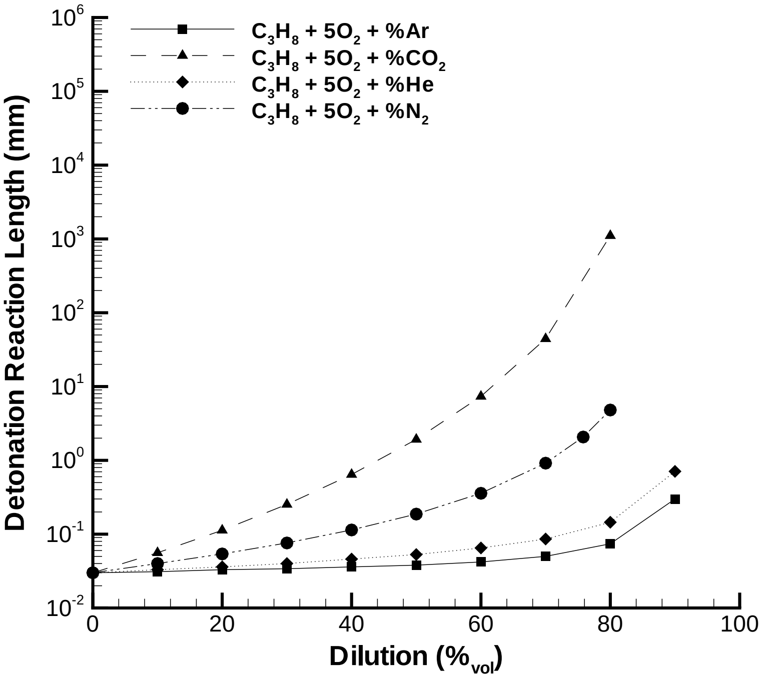

Figure 4.17 Detonation reaction length versus dilution for stoichiometric propane-oxygen mixtures (P_1 = 100 kPa, T_1 = 295 K).

effect of these diluents on the post-shock temperature (Schultz and Shepherd 1999). The effect of carbon dioxide is primarily thermal for hydrogen mixtures as shown by Shepherd (1986b) in which the thermal and kinetic effects of this diluent were investigated. Excellent agreement between constant-volume explosion induction times for mechanisms with and without nitrogen as a chemically active species indicates that nitrogen also has primarily a thermal effect (Schultz and Shepherd 1999).

4.2.2 Disturbance propagation

ZND detonation simulations were also used to investigate the variation of the characteristic disturbance velocity through the reaction zone, which determines the disturbance propagation angle along with the detonation velocity (E qn.3.2, Fi g.3.3). The disturbance velocity versus time for a detonation in stoichiometric propane-oxygen at

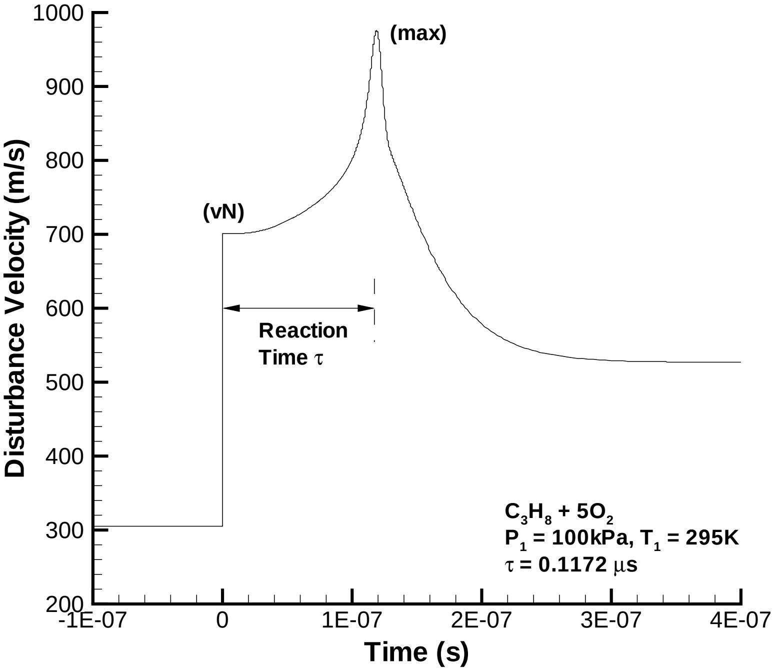

Figure 4.18 Disturbance propagation velocity versus time for a representative ZND reaction zone computation.

atmospheric initial conditions is presented in Fig.4.18. A significant increase is observed beyond the post-shock state, with a maximum closely corresponding to the maximum temperature gradient point. The relative increase in disturbance velocity from the post-shock state to the maximum is highly dependent upon the mixture under consideration. Experimental results in Section 5.3 are used to determine whether the disturbance propagation velocities characteristic of the post-shock state or reaction zone maximum are more accurate for modeling purposes.

Disturbance propagation angles calculated from the post-shock and maximum reaction zone disturbance velocities for varying equivalence ratio in fuel-oxygen and fuel-air mixtures are presented in Figs. 4.19 and 4.20, respectively. These angles are presented

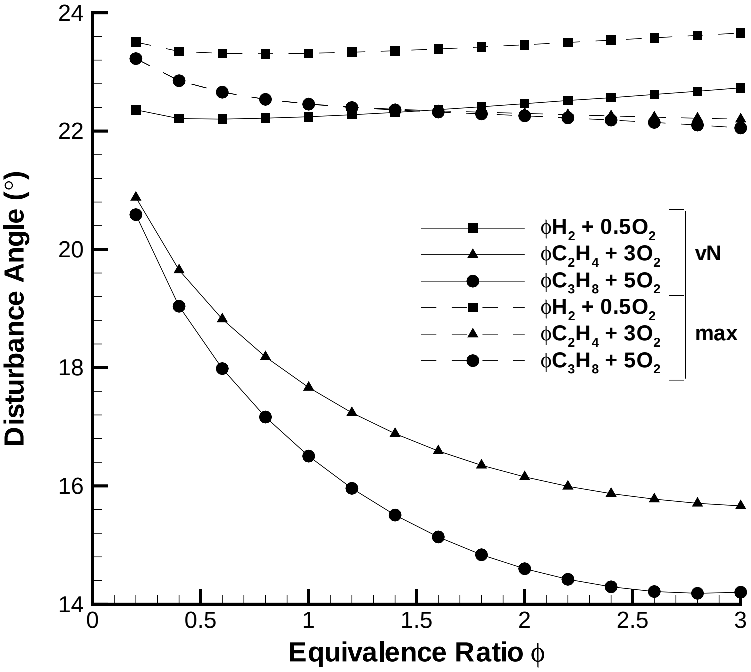

Figure 4.19 Disturbance propagation angle versus equivalence ratio for fuel-oxygen mixtures (P_1 = 100 kPa, T_1 = 295 K).

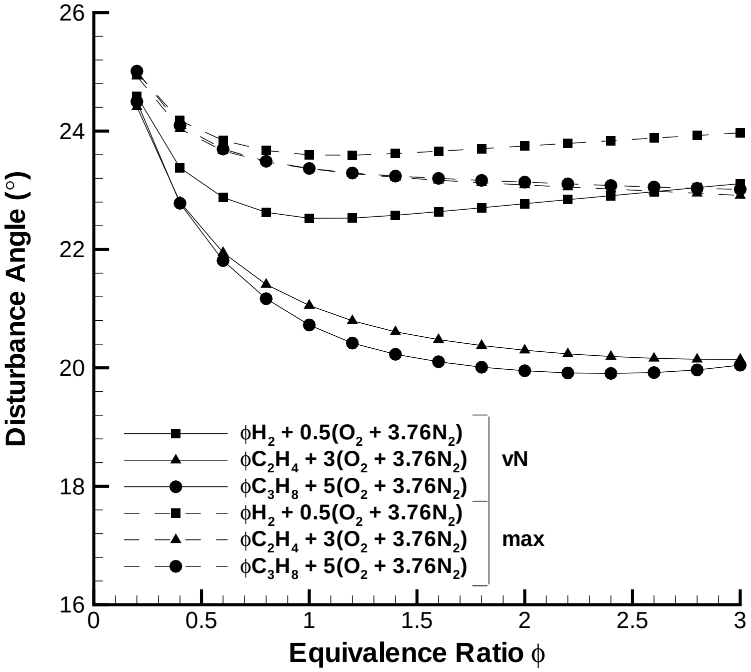

Figure 4.20 Disturbance propagation angle versus equivalence ratio for fuel-air mixtures (P_1 = 100 kPa, T_1 = 295 K).

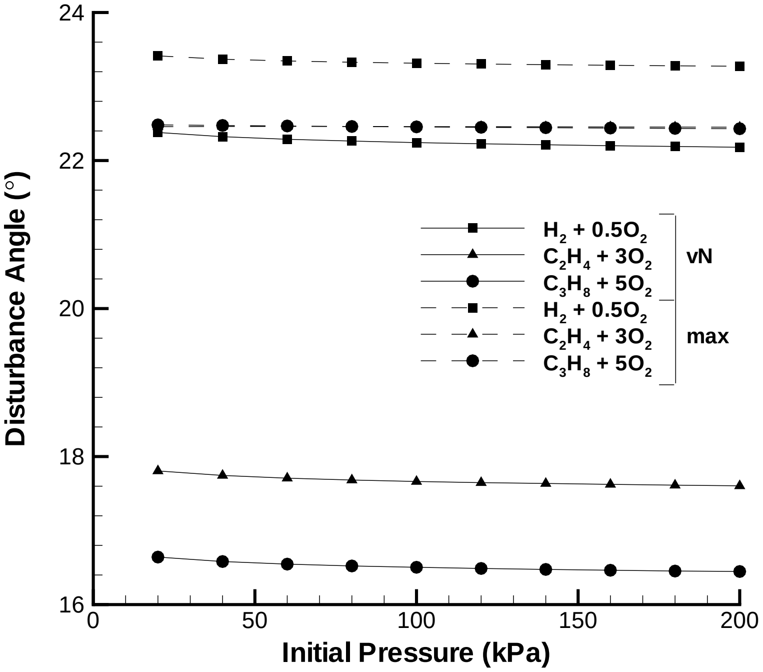

Figure 4.21 Disturbance propagation angle versus initial pressure for stoichiometric fuel-oxygen mixtures (T_1 = 295 K).

for stoichiometric fuel-oxygen and fuel-air mixtures with varying initial pressure in Figs. 4.21 and 4.22, respectively. Dilution effects are presented in Figs .4.23, 4.24, and 4.25 for hydrogen, ethylene, and propane mixtures, respectively.

The disturbance propagation angles for hydrocarbon mixtures based on the maximum disturbance velocity, and hydrogen mixtures based on either the post-shock or maximum reaction zone velocity, lie primarily between 22° and 26°. Angles for the hydrogen mixtures are insensitive to the choice of reaction zone disturbance velocity because it does not vary much through the reaction zone (< 10%). Significantly greater variation occurs for the hydrocarbon mixtures when the post-shock disturbance velocity is used to calculate the disturbance propagation angle because the disturbance velocity increases for these mixtures by up to 50% through the reaction zone.

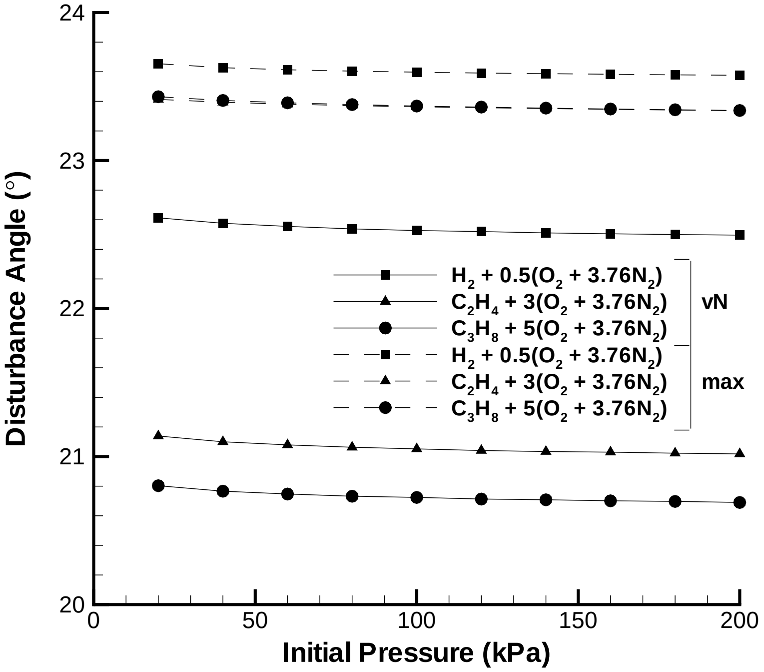

Figure 4.22 Disturbance propagation angle versus initial pressure for stoichiometric fuel-air mixtures (T_1 = 295 K).

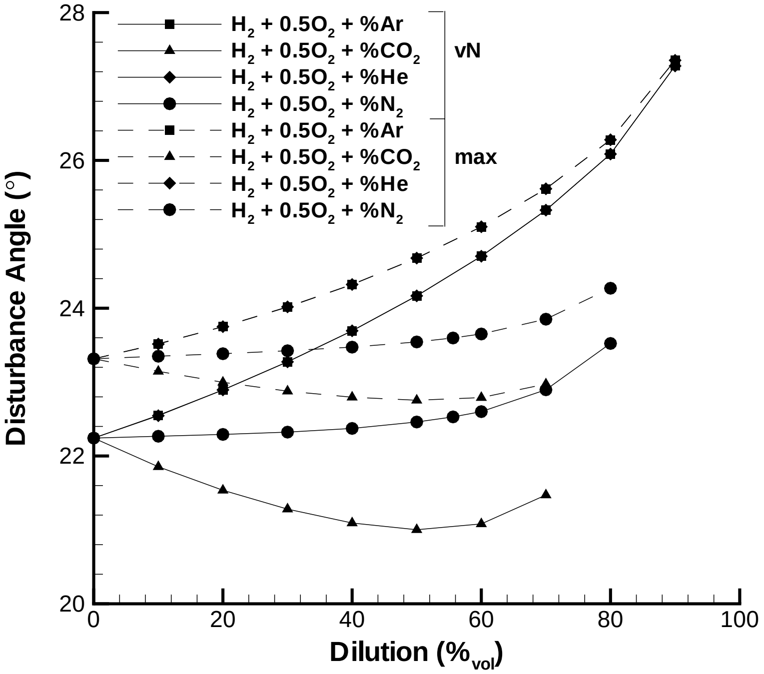

Figure 4.23 Disturbance propagation angle versus dilution for stoichiometric hydrogen-oxygen mixtures (P_1 = 100 kPa, T_1 = 295 K).

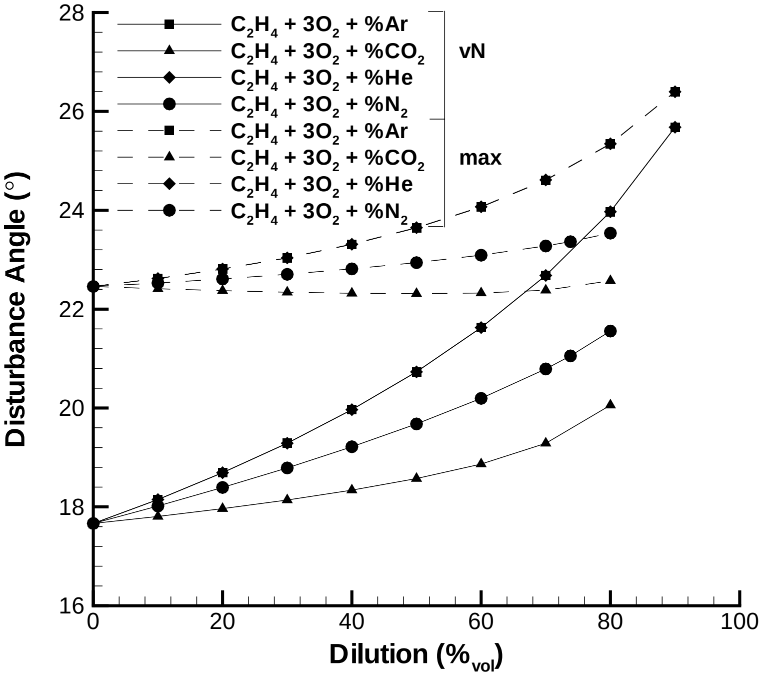

Figure 4.24 Disturbance propagation angle versus dilution for stoichiometric ethylene-oxygen mixtures (P_1 = 100 kPa, T_1 = 295 K).

4.3 Constant-volume explosion simulations

Constant-volume explosion simulations were carried out (Schultz and Shepherd 1999) with a computer program utilizing the same chemical kinetics package and stiff, ordinary differential equation solver as the ZND detonation simulations. The program evolves the energy and species equations through time for an adiabatic, fixed-volume fluid particle:

$$\frac{de}{dt} = 0 \tag{4.7}$$

$$\frac{dy_i}{dt} = \Omega_i \tag{4.8}$$

The internal energy for an ideal gas is related to the temperature and species through a

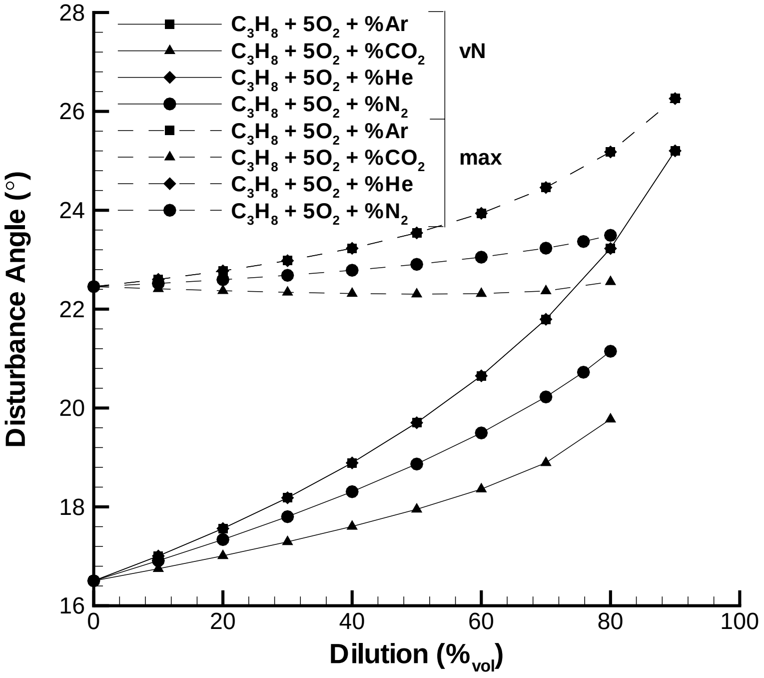

Figure 4.25 Disturbance propagation angle versus dilution for stoichiometric propane-oxygen mixtures (P_1 = 100 kPa, T_1 = 295 K).

caloric equation of state

$$e = e(T,\hat{y}) = \sum_{i=1}^{K} y_i e_i(T) \tag{4.9}$$

The internal energy of each species as a function of temperature is calculated with NASA polynomial functions from the thermodynamic database supplied with Chemkin (Kee et al. 1989). Taking the differential of this expression gives

$$\begin{aligned} de &= \sum_{i=1}^{K} dy_i e_i + dT \sum_{i=1}^{K} y_i \frac{de_i}{dT} = \\ &\sum_{i=1}^{K} dy_i e_i + dT \sum_{i=1}^{K} y_i C_{v,\,i} = \sum_{i=1}^{K} dy_i e_i + C_v dT \end{aligned} \tag{4.10}$$

Substituting into the original energy equation for the internal energy differential, the energy equation is re-formulated in terms of temperature

$$C_v\frac{dT}{dt} = -\sum_{i=1}^{K}\frac{dy_i}{dt}e_i = -\sum_{i=1}^{K}\Omega_i e_i \tag{4.11}$$

The species mass fraction production rate is calculated through Chemkin subroutines with the reaction mechanism providing the reaction rate constants in the standard form of

$$k_i = A_i T^{n_i}\exp\left(-\frac{E_i}{R_g T}\right) \tag{4.12}$$

Detailed discussion on the various forms of reaction rate expressions is provided by Kee et al. (1989).

The evolution of temperature, temperature rate of change, and some species for a representative constant-volume explosion simulation are presented in Fi g 4.26. Hydrogen and oxygen are consumed through the reaction zone while hydroxyl is the intermediate radical species and formation of the water product is the primary exothermic reaction. The high level of argon dilution limits the temperature rise to within 1.5% of the initial values. The reaction time is defined as the time corresponding to the maximum rate of temperature change, which is very close to the maximum rate of OH production time.

4.3.1 Effective activation energy (CJ shock velocity)

Effective activation energies are calculated with constant-volume explosion simulations by assuming that the global chemical behavior can be represented by an Arrhenius

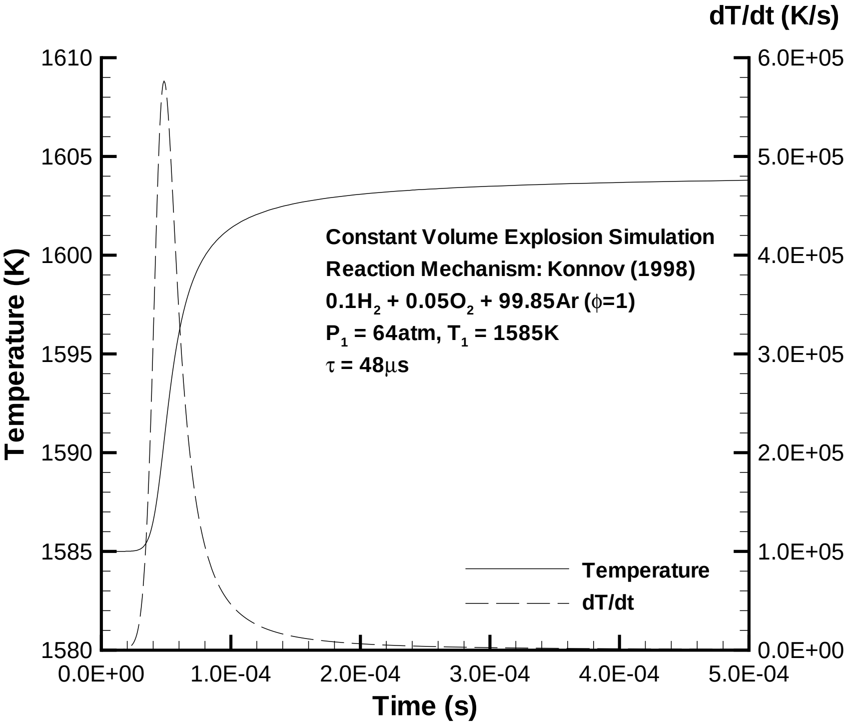

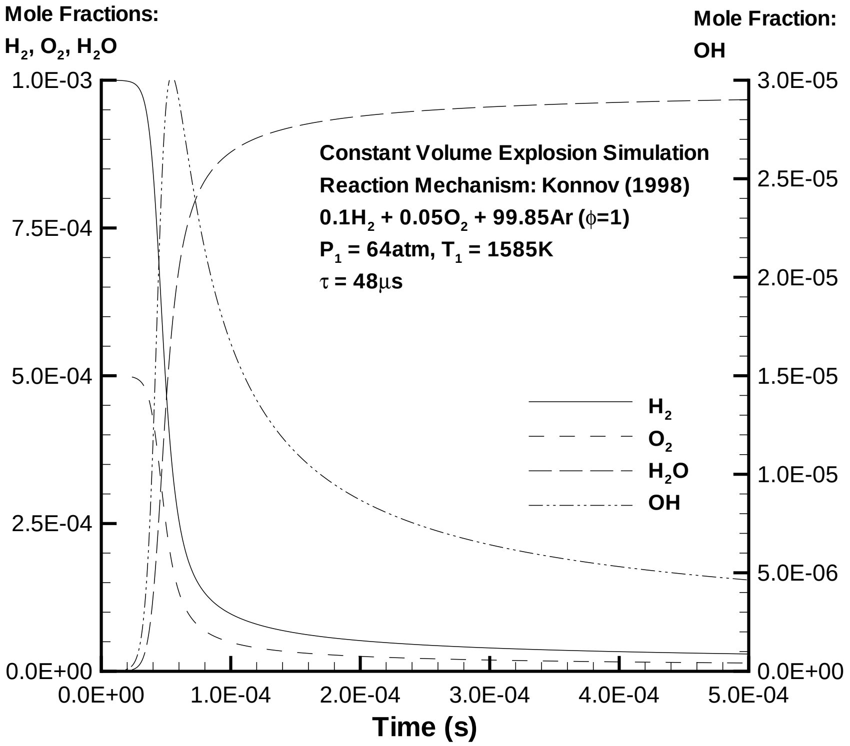

Figure 4.26 Representative constant-volume explosion simulation results.

reaction time of (Schultz and Shepherd 1999)

$$\tau = \frac{k}{\rho_{vN}} \exp\left(\frac{E_a}{R_g T_{vN}}\right) \tag{4.13}$$

The end of the reaction time is defined as the time corresponding to the maximum rate of temperature change. The perfect gas shock jump expression for density is given by

$$\frac{\rho_{vN}}{\rho_0} = \frac{(\gamma+1)M_{CJ}^2}{(\gamma-1)M_{CJ}^2+2} \tag{4.14}$$

In the strong-shock limit appropriate for detonation Mach numbers, this reduces to

$$\left.\frac{\rho_{vN}}{\rho_0}\right|_{M_{CJ}\to\infty} = \frac{\gamma+1}{\gamma-1} \tag{4.15}$$

The perfect gas shock jump expression for temperature is given by

$$\frac{T_{vN}}{T_0} = \left[1+\frac{2\gamma}{\gamma+1}(M_{CJ}^2-1)\right]\left[\frac{(\gamma-1)M_{CJ}^2+2}{(\gamma+1)M_{CJ}^2}\right] \tag{4.16}$$

which retains a squared dependence on the detonation Mach number in the strong-shock limit. Therefore, the post-shock density is nearly a constant when varying the shock velocity relative to the significant temperature variation due to the squared Mach number and Arrhenius induction time dependence on the post-shock temperature. Hence, consideration is given only to the temperature dependence of the reaction time when considering how the thermodynamic state affects the reaction time. The effective activation energy parameter is defined by

$$\theta = \frac{E}{RT_{vN}} = \frac{1}{T_{vN}}\left(\frac{\ln\tau_2 - \ln\tau_1}{\frac{1}{T_2}-\frac{1}{T_1}}\right) \tag{4.17}$$

where two constant-volume explosion simulations corresponding to (T_1,τ_1) and (T_2,τ_2) are run for each activation energy data point. Initial conditions for states one and two are generated by varying the shock velocity by ±1% V_{CJ}. The jump conditions were solved with these perturbed velocities to obtain the post-shock conditions used as initial conditions in the constant-volume explosion simulations.

The sensitivity of the calculated activation energy parameters to the choice of shock velocity perturbation was investigated by running all cases with shock velocities differing from V_{CJ} by factors of 10^{-2}, 10^{-3}, 10^{-4}, and 10^{-5}. Simulations performed with the 10^{-4} and 10^{-5} factors produced very erratic activation energy parameters. In some cases, the values converged to those obtained with 10^{-2} and 10^{-3} factors but in many other cases, the values were abnormally high, low, or even negative. The reason for these observations is the very small shock velocity perturbation which produces variations in induction time on the order of the numerical accuracy of the constant-volume explosion simulations. Consequently, activation energy parameters obtained with the 10^{-2} (±1%) variation factor are presented here.

All propane activation energy parameters obtained with 10^{-2} and 10^{-3} variation factors agree to within 3% (most within 1%) with the exception of the two greatest argon dilution mixtures simulated. For these two cases, the 10^{-2} results matched the corresponding helium dilution activation energy parameters as expected, whereas the 10^{-3} results did not (providing confidence in the 10^{-2} values). All ethylene activation energy parameters obtained with 10^{-2} and 10^{-3} variation factors agree to within 4% (most within 1%). Significantly greater changes in the activation energy parameter with different shock velocity variation factors were observed for the hydrogen mixtures. Most of the hydrogen activation energy parameters obtained with 10^{-2} and 10^{-3} variation factors agree to within 5%, although one quarter of the cases have discrepancies of up to 20% between the values. The calculated hydrogen-air activation parameters are in good agreement with the activation energy data presented by Shepherd (1986b). In addition, all of the calculated values are in reasonable agreement with activation energies corresponding to experimental shock tube induction time data (Schultz and Shepherd 1999).

The activation energy parameters are plotted versus equivalence ratio for fuel-oxygen and fuel-air mixtures in Fig. 4.27. Activation parameters are generally greater for fuel-air mixtures relative to the corresponding fuel-oxygen mixture indicating greater reaction zone sensitivity to temperature perturbations for fuel-air mixtures. Minimum

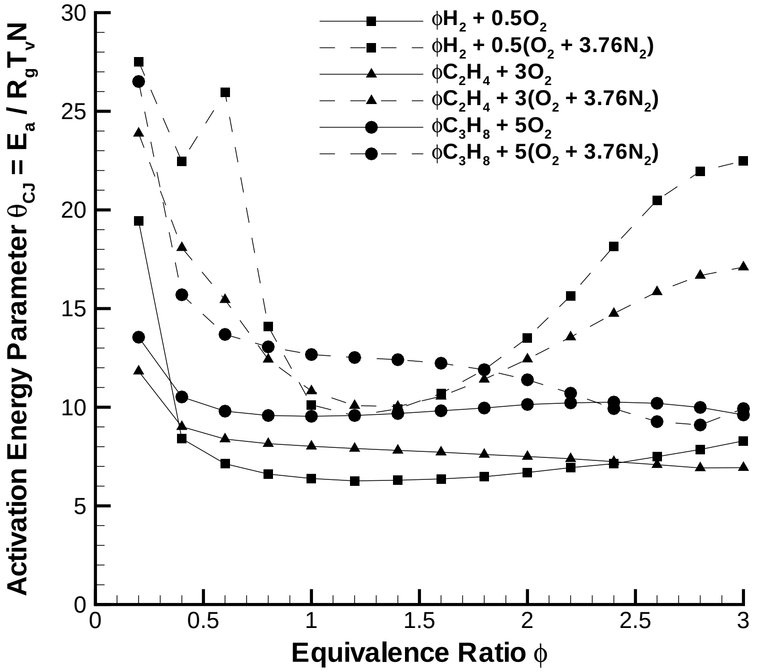

Figure 4.27 Activation energy parameter (CJ velocity) versus equivalence ratio for fuel-oxygen and fuel-air mixtures (P_1 = 100 kPa, T_1 = 295 K).

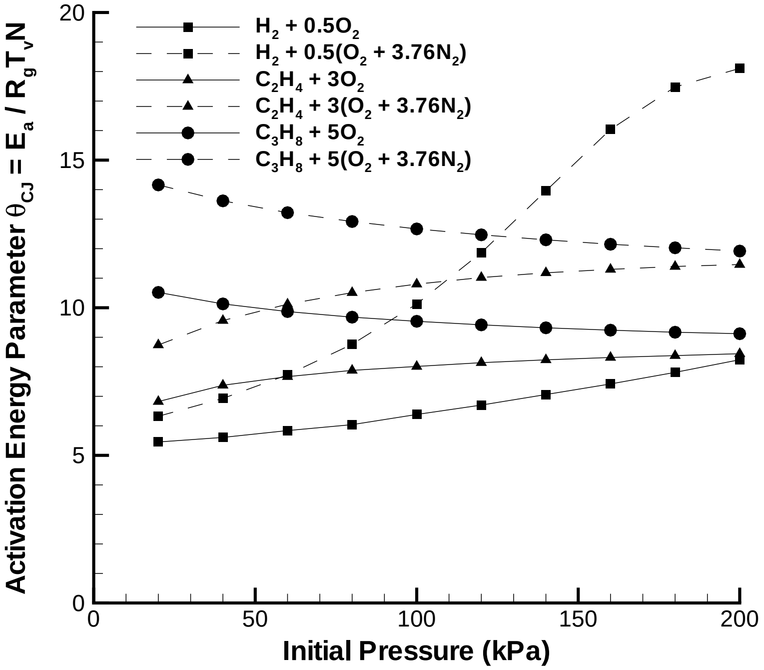

Figure 4.28 Activation energy parameter (CJ velocity) versus initial pressure for stoichiometric fuel-oxygen and fuel-air mixtures (T_1 = 295 K).

activation parameters are generally found near the stoichiometric condition, with the exception of ethylene-oxygen and propane-air mixtures.

Activation energy parameters for stoichiometric fuel-oxygen and fuel-air mixtures with varying initial pressure are presented in Fig.4.28. Increasing the initial pressure increases the activation parameter for hydrogen and ethylene mixtures but decreases the parameter for propane mixtures. Activation parameters for the fuel-air mixtures are always greater than those for the corresponding fuel-oxygen mixtures.

The activation energy parameter versus percent diluent data for stoichiometric fuel-oxygen-diluent mixtures with hydrogen, ethylene, and propane fuel are presented in Figs. 4.29, 4.30, and 4.31, respectively. Dilution of these mixtures with argon or helium

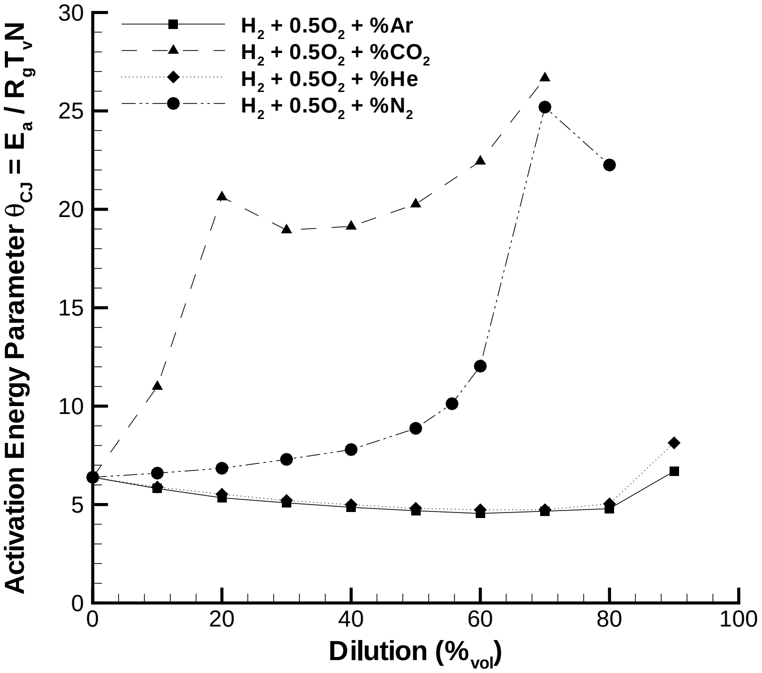

Figure 4.29 Activation energy parameter (CJ velocity) versus dilution for stoichiometric hydrogen-oxygen mixtures (P_1 = 100 kPa, T_1 = 295 K).

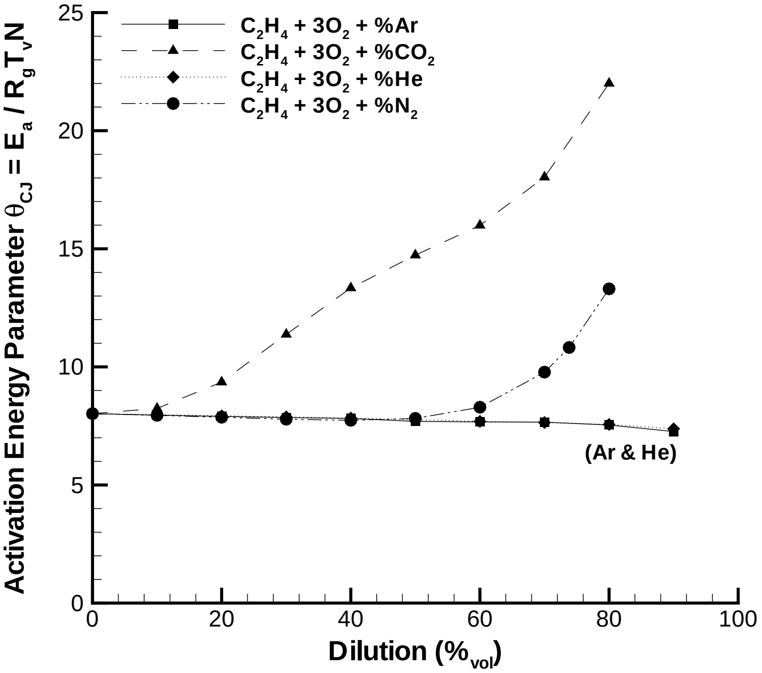

Figure 4.30 Activation energy parameter (CJ velocity) versus dilution for stoichiometric ethylene-oxygen mixtures (P_1 = 100 kPa, T_1 = 295 K).

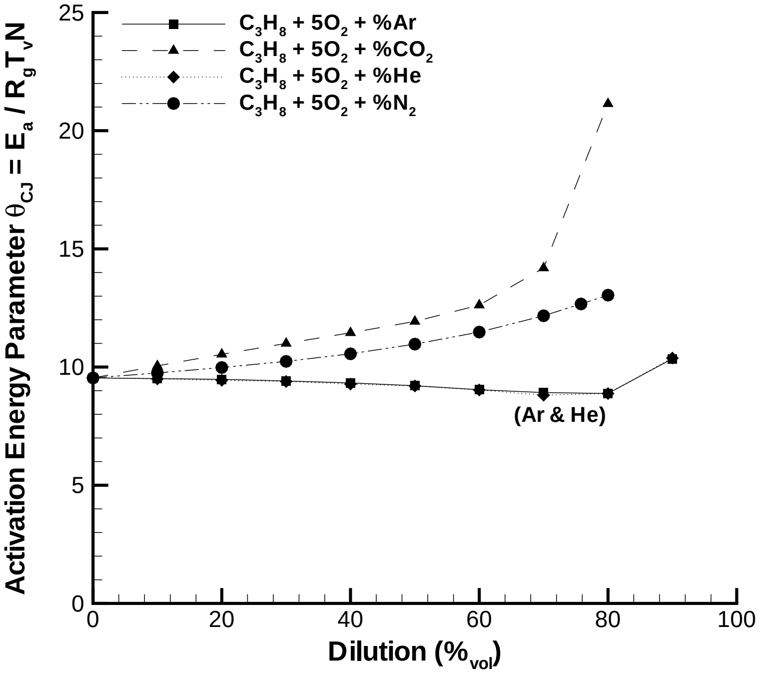

Figure 4.31 Activation energy parameter (CJ velocity) versus dilution for stoichiometric propane-oxygen mixtures (P_1 = 100 kPa, T_1 = 295 K).

has quantitatively the same effect and results in a slight decrease of the activation parameter, up to a maximum of 10% relative to the undiluted cases (Sections 2.2.2 and 2.2.4). Carbon dioxide and nitrogen diluents increase the activation parameter of all mixtures primarily due to post-shock temperature variations with diluent type and amount (Schultz and Shepherd 1999). The concentration of diluent required to raise the activation parameter and the magnitude by which it is increased varies greatly between the three fuels. Note that these two diluents result in complex variations in activation parameter behavior and do not always monotonously increase the activation parameter.

4.3.2 Critical shock velocity

The shock velocity along the tube axis at which the critical diffraction model is evaluated can be determined by experimental observations (Section 5.4) or the analytical

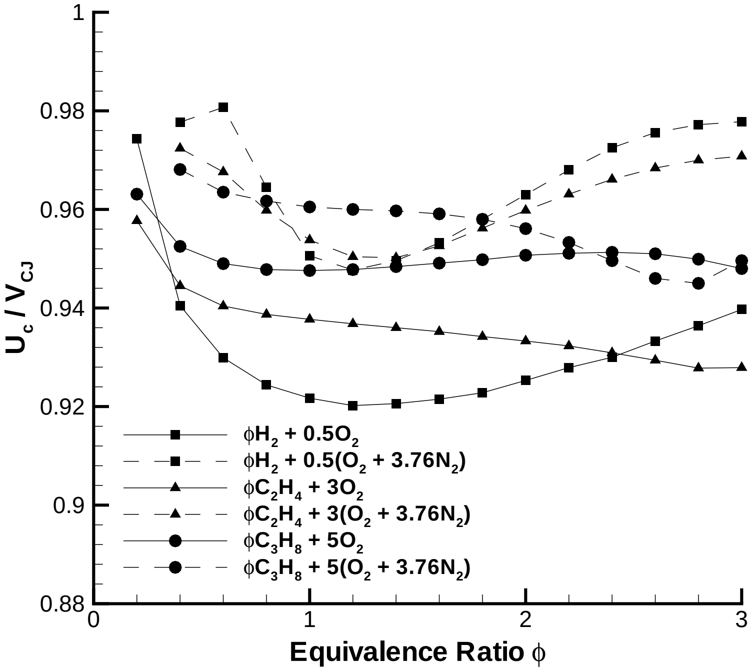

Figure 4.32 Critical shock velocity (He and Clavin 1994) versus equivalence ratio (P_1 = 100 kPa, T_1 = 295 K).

expression (Eqn. 3.44) derived from high activation energy asymptotics by He and Clavin (1994). Plots of their critical shock velocity using the CJ velocity calculations from Section 4.1.2 and the CJ effective activation energy calculations from Section 4.3.1 are presented in Figs. 4.32 - 4.36. Most of the critical velocities are within 10% of the CJ velocity, with all U_c / V_{CJ} ratios between 0.89 and 0.98. Clear trends are observed only for the mixtures with variable dilution. Argon and helium dilution causes a decrease in the critical velocity until relatively high concentration levels and carbon dioxide dilution increases the critical velocity for all fuels. Dilution with nitrogen increases the critical velocity for hydrogen and propane mixtures, and decreases the critical velocity for ethylene mixtures up to 50% dilution. Critical velocities for the hydrogen mixtures are the most sensitive to composition changes.

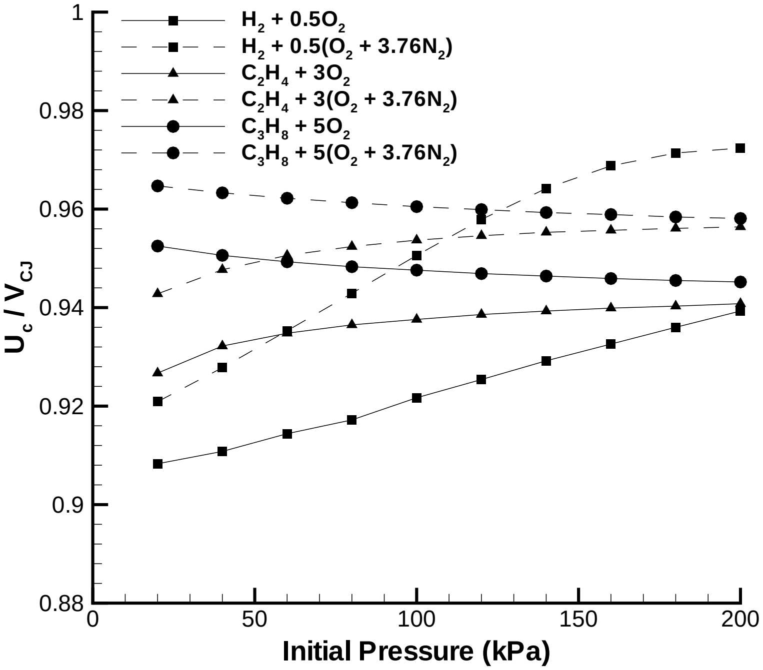

Figure 4.33 Critical shock velocity (He and Clavin 1994) versus initial pressure (T_1 = 295 K).

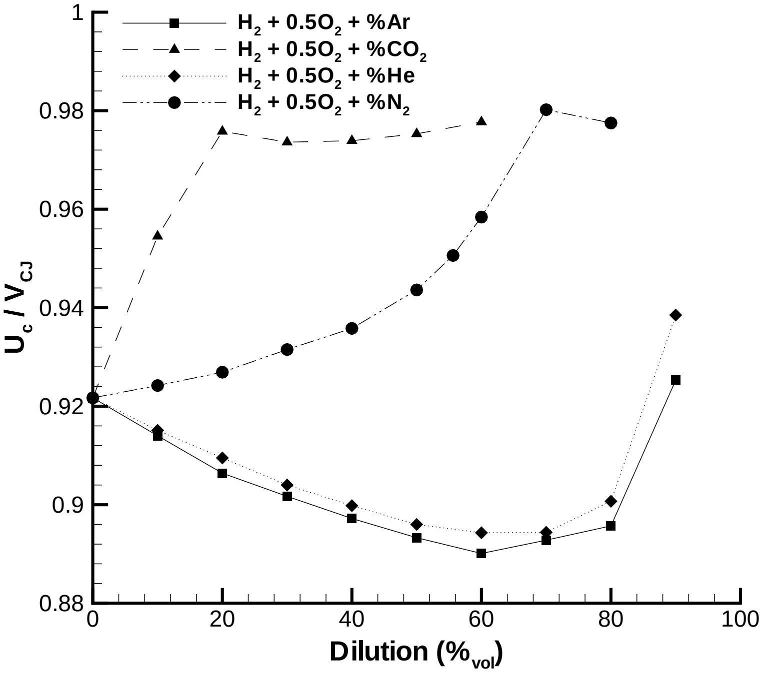

Figure 4.34 Critical shock velocity (He and Clavin 1994) versus dilution for hydrogen mixtures (P_1 = 100 kPa, T_1 = 295 K).

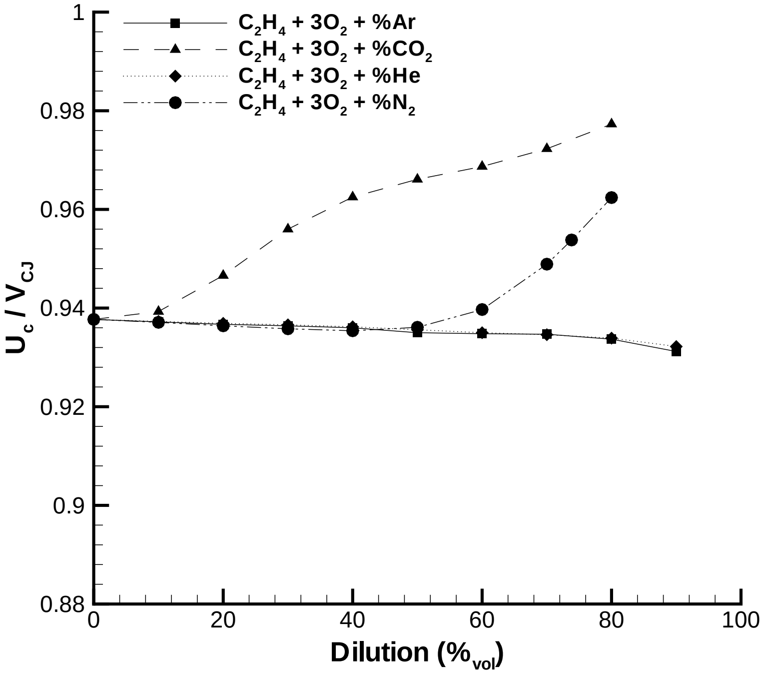

Figure 4.35 Critical shock velocity (He and Clavin 1994) versus dilution for ethylene mixtures (P_1 = 100 kPa, T_1 = 295 K).

4.3.3 Reaction time

Reaction times were calculated with constant-volume explosion simulations for shock velocities corresponding to the He and Clavin (1994) critical shock velocities of Section 4.3.2 and for arbitrary $0.9V_{CJ}$ shock velocities. The reaction times for hydrogen, ethylene, and propane mixtures with varying equivalence ratio, initial pressure, and dilution are presented in Figs. 4.37 - 4.39, 4.40 - 4.42, and 4.4 3 -4.45, respectively. Similar trends are observed with variations in mixture composition as discussed for the detonation reaction lengths in Section 4.2.1, with the exception of the reaction time behavior at $0.9V_{CJ}$ shock velocity with initial pressure variation for hydrogen mixtures in which the reaction time does not decrease monotonously with increasing initial pressure.

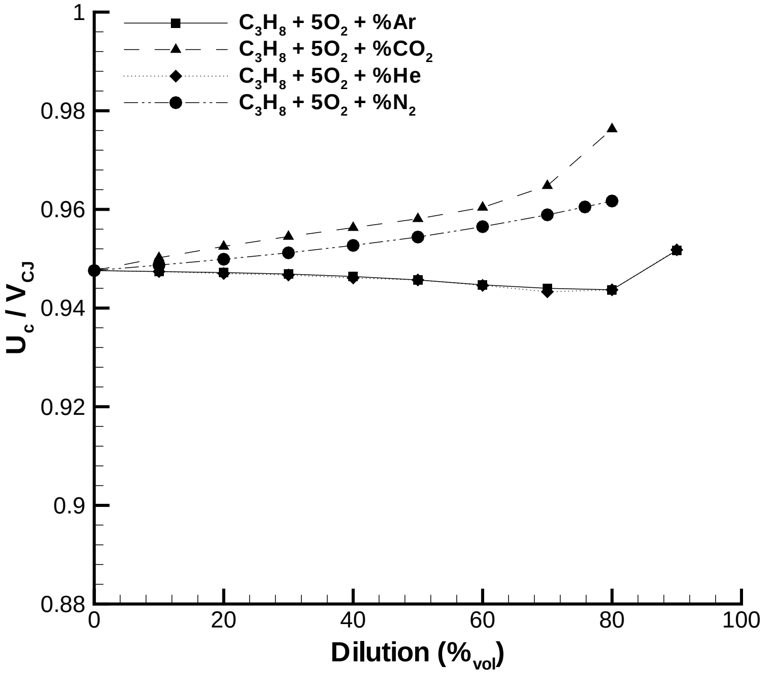

Figure 4.36 Critical shock velocity (He and Clavin 1994) versus dilution for propane mixtures (P_1 = 100 kPa, T_1 = 295 K).

Reaction times are greater for the $0.9V_{CJ}$ shock velocities versus those calculated with the He and Clavin (1994) critical shock velocities which are typically around $0.95V_{CJ}$ (Section 4.3.2). The differences are significant because of the exponential dependence of reaction time on shock velocity through the post-shock temperature. The only exception is for argon and helium diluted hydrogen mixtures for which U_c / V_{CJ} is slightly less than 0.9.

4.3.4 Effective activation energy (critical shock velocity)

Effective activation energy parameters were also calculated with constant-volume explosion simulations for shock velocities corresponding to the He and Clavin (1994) critical shock velocities of Section 4.3.2 and for arbitrary $0.9V_{CJ}$ shock velocities. The procedure used is described in Section 4.3.1 except now the shock velocity is perturbed by ±1%

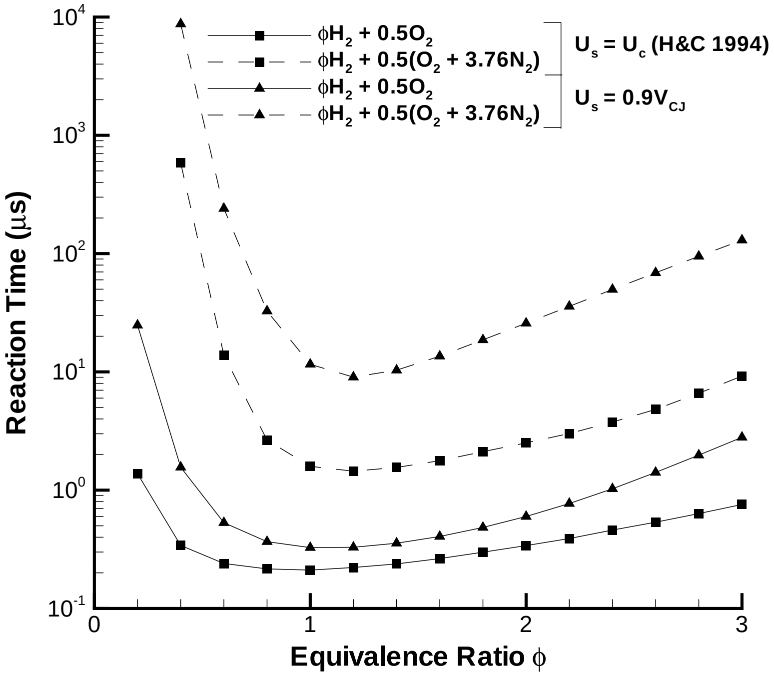

Figure 4.37 Reaction time versus equivalence ratio for hydrogen-oxygen and hydrogen-air mixtures (P_1 = 100 kPa, T_1 = 295 K).

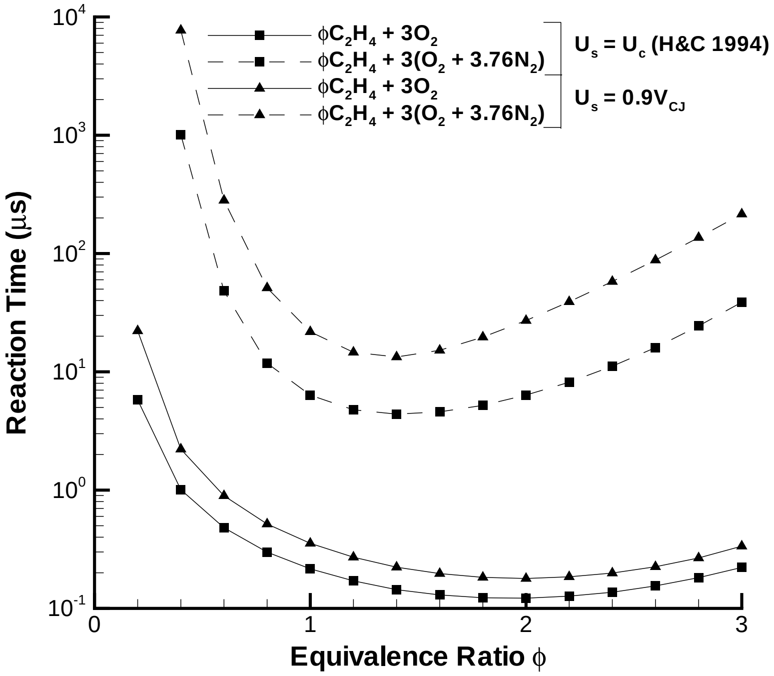

Figure 4.38 Reaction time versus equivalence ratio for ethylene-oxygen and ethylene-air mixtures (P_1 = 100 kPa, T_1 = 295 K).

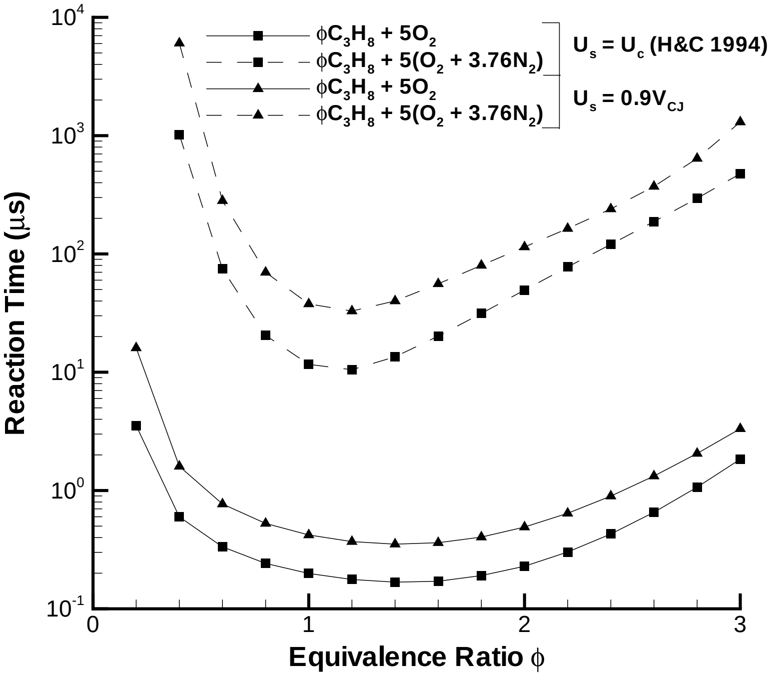

Figure 4.39 Reaction time versus equivalence ratio for propane-oxygen and propane-air mixtures (P_1 = 100 kPa, T_1 = 295 K).

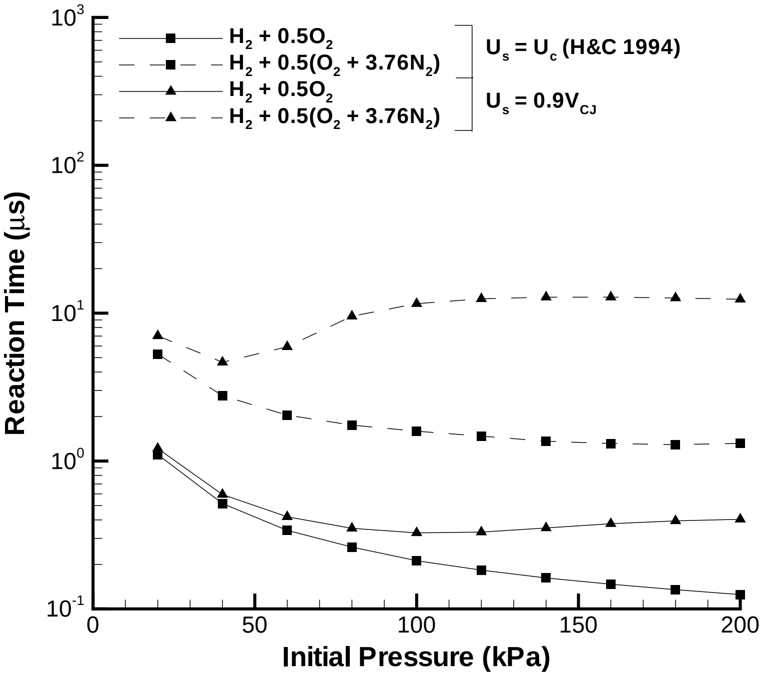

Figure 4.40 Reaction time versus initial pressure for hydrogen-oxygen and hydrogen-air mixtures (T_1 = 295 K).

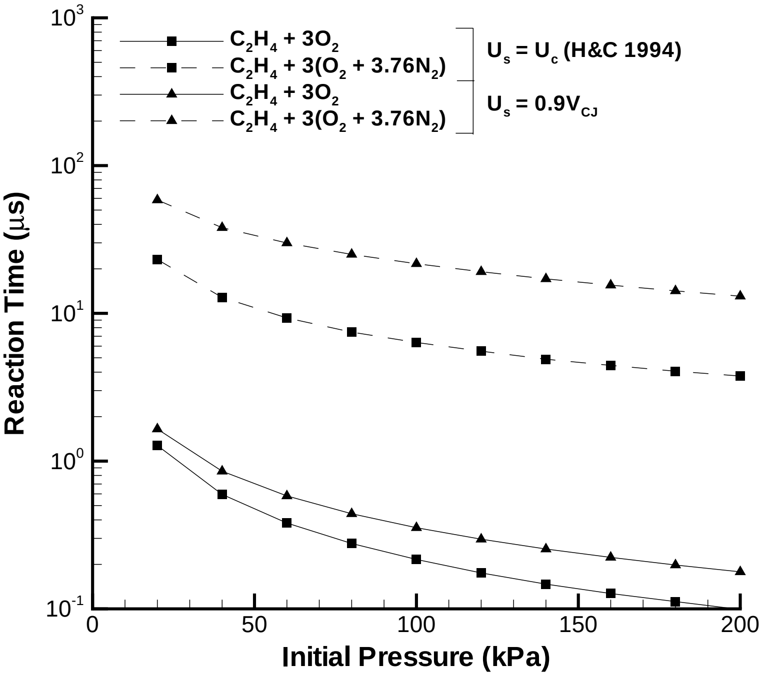

Figure 4.41 Reaction time versus initial pressure for ethylene-oxygen and ethylene-air mixtures (T_1 = 295 K).

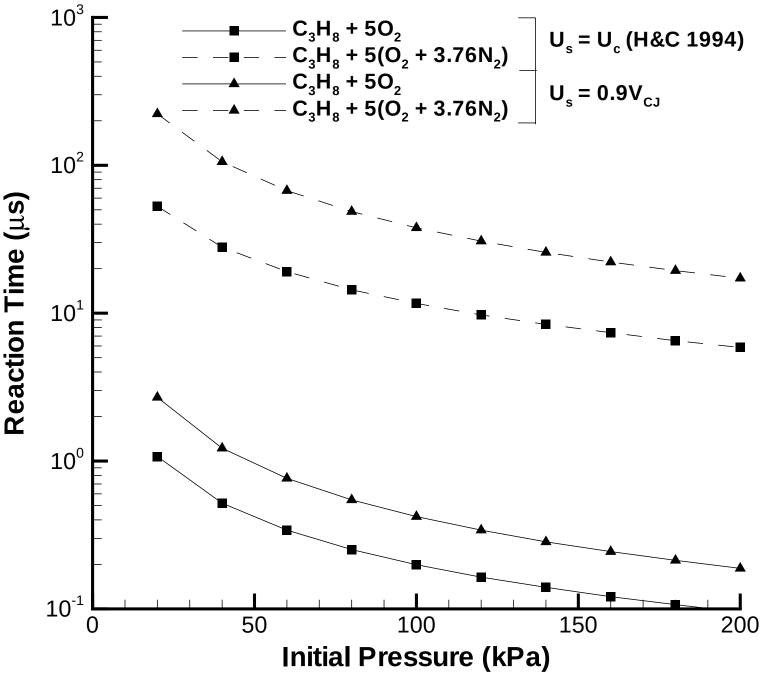

Figure 4.42 Reaction time versus initial pressure for propane-oxygen and propane-air mixtures (T_1 = 295 K).

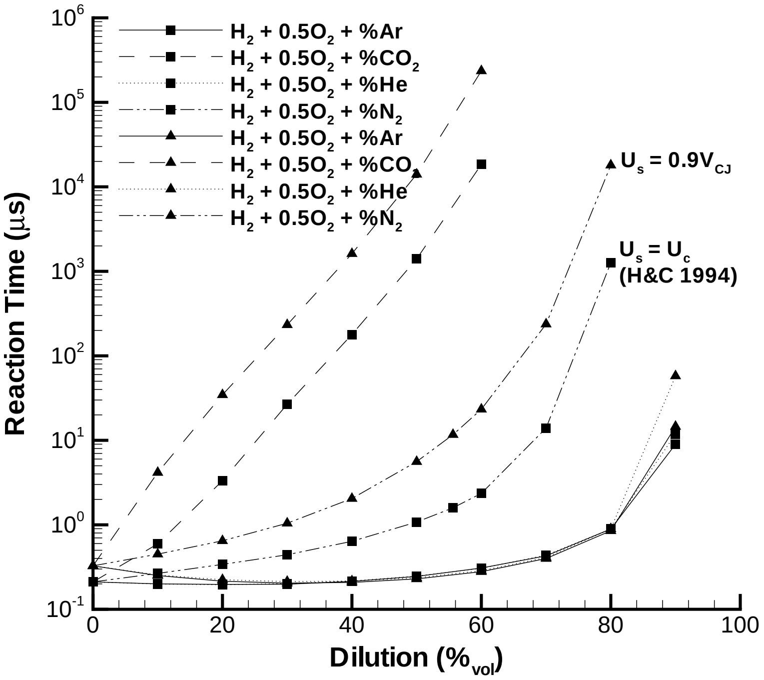

Figure 4.43 Reaction time versus dilution for hydrogen mixtures (P_1 = 100 kPa, T = 295 K).

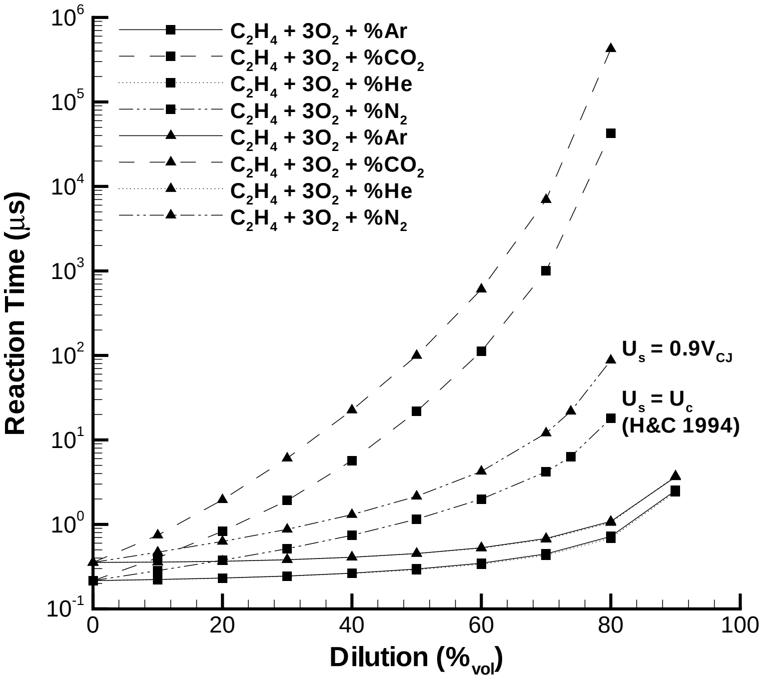

Figure 4.44 Reaction time versus dilution for ethylene mixtures (P_1 = 100 kPa, T = 295 K).

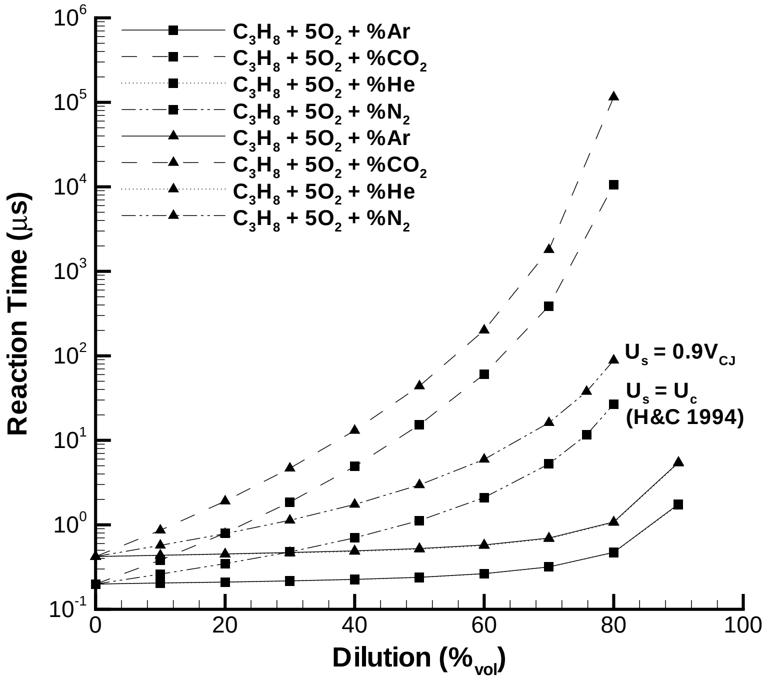

Figure 4.45 Reaction time versus dilution for propane mixtures (P_1 = 100 kPa, T_1 = 295 K).

around these two shock velocity definitions. The activation energy parameters for hydrogen, ethylene, and propane mixtures with varying equivalence ratio, initial pressure, and dilution are presented in Figs. 4.46 - 4.48, 4.49 - 4.51, and 4.5 2 -4.54, respectively. Critical shock velocities from He and Clavin (1994) typically result in lower activation energy parameters, indicating that the chemical reactions are more sensitive to temperature perturbations at reduced ($0.9V_{CJ}$) shock velocities. Argon and helium diluents tend to decrease the activation energy until relatively high diluent concentration and carbon dioxide significantly increases the activation energy. Hydrogen mixtures are the most sensitive to mixture composition changes. Varying the initial pressure has little effect on the activation energy of the hydrocarbon mixtures.

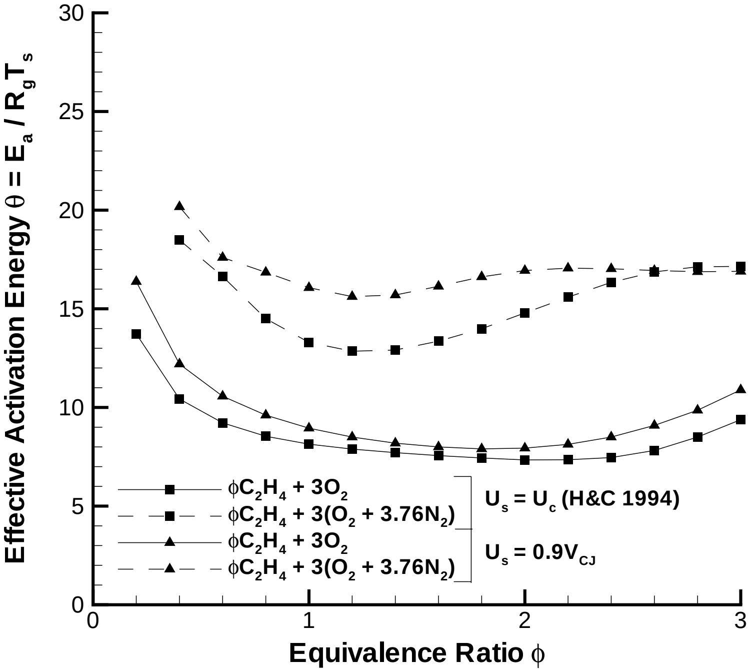

Figure 4.47 Activation energy parameter (critical velocity) versus equivalence ratio for ethylene-oxygen and ethylene-air mixtures (P_1 = 100 kPa, T_1 = 295 K).

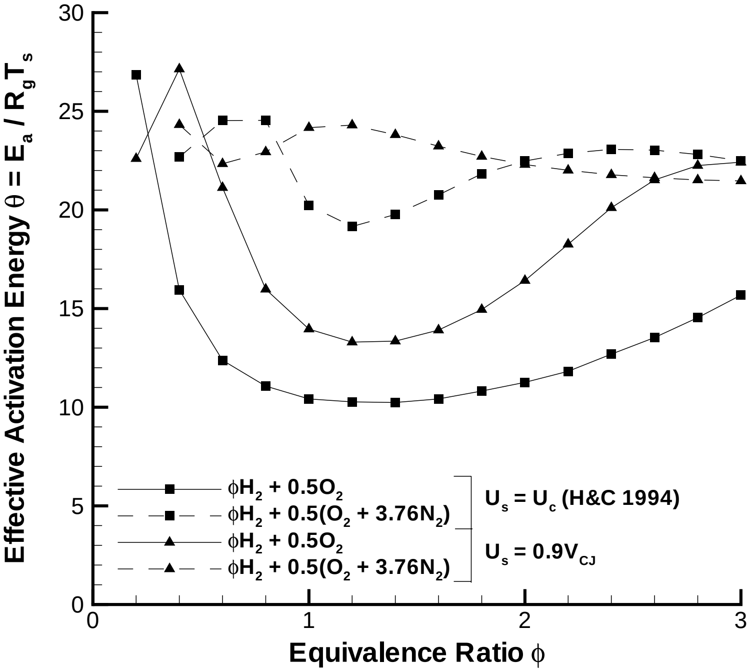

Figure 4.46 Activation energy parameter (critical velocity) versus equivalence ratio for hydrogen-oxygen and hydrogen-air mixtures (P_1 = 100 kPa, T_1 = 295 K).

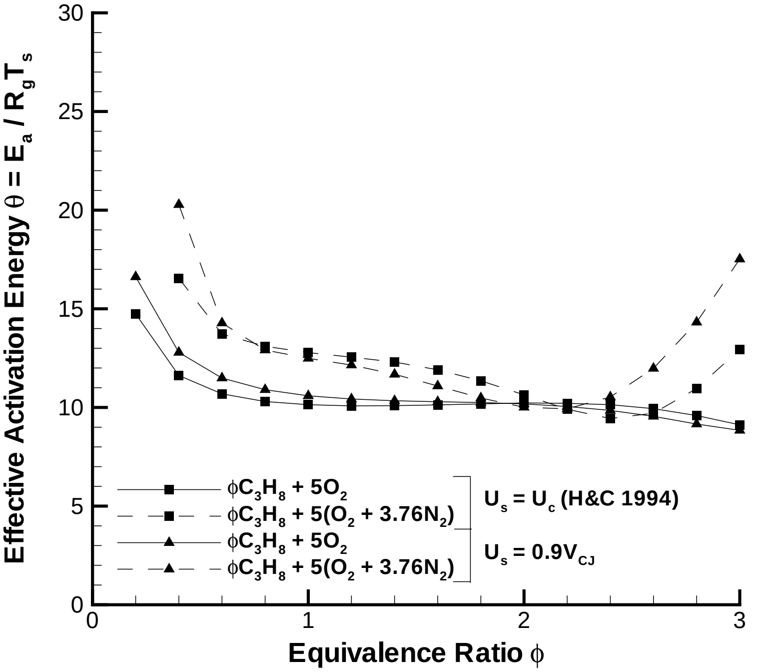

Figure 4.48 Activation energy parameter (critical velocity) versus equivalence ratio for propane-oxygen and propane-air mixtures (P_1 = 100 kPa, T_1 = 295 K).

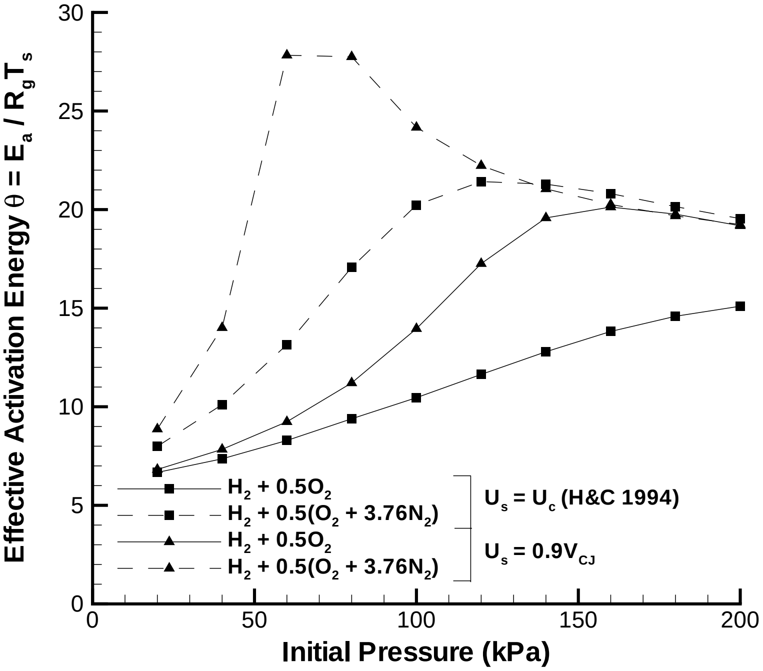

Figure 4.49 Activation energy parameter (critical velocity) versus initial pressure for hydrogen-oxygen and hydrogen-air mixtures (T_1 = 295 K).

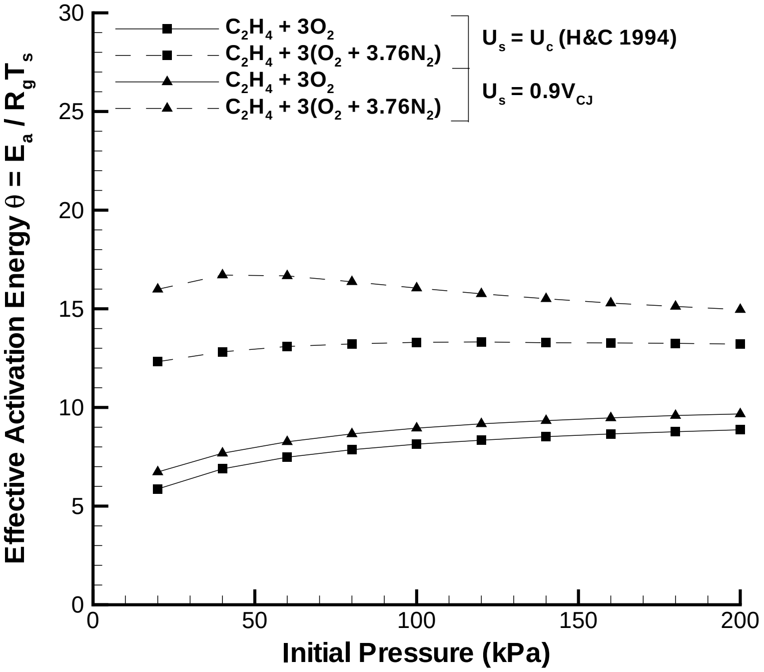

Figure 4.50 Activation energy parameter (critical velocity) versus initial pressure for ethylene-oxygen and ethylene-air mixtures (T_1 = 295 K).

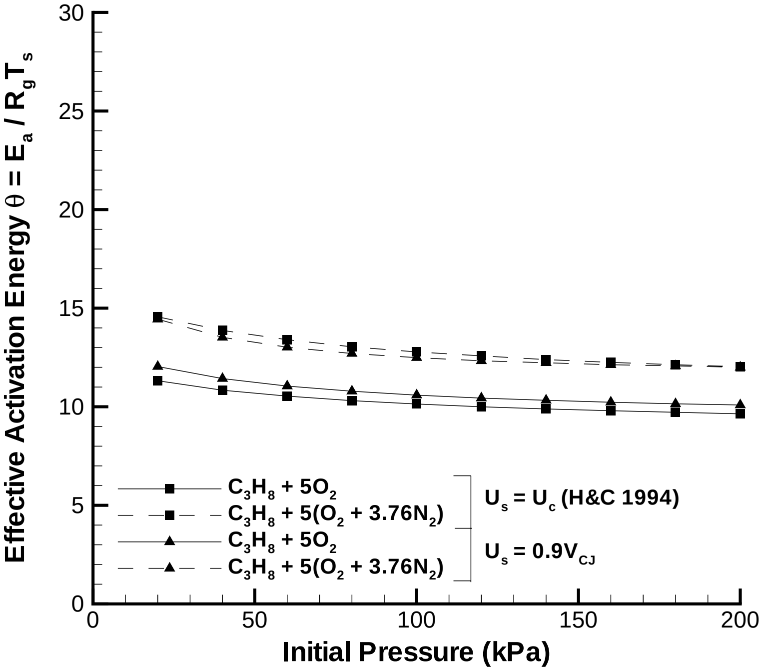

Figure 4.51 Activation energy parameter (critical velocity) versus initial pressure for propane-oxygen and propane-air mixtures (T_1 = 295 K).

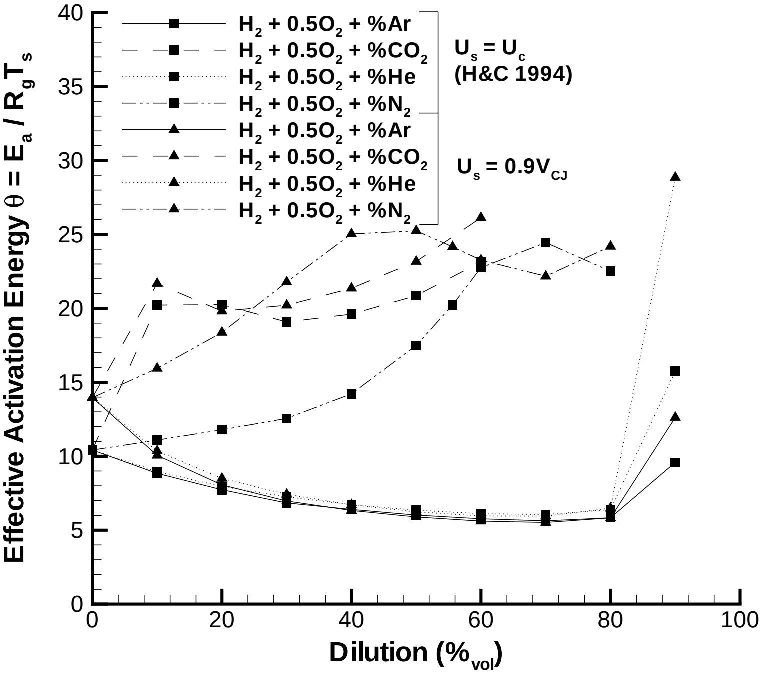

Figure 4.52 Activation energy parameter (critical velocity) versus dilution for hydrogen mixtures (P_1 = 100 kPa, T_1 = 295 K).

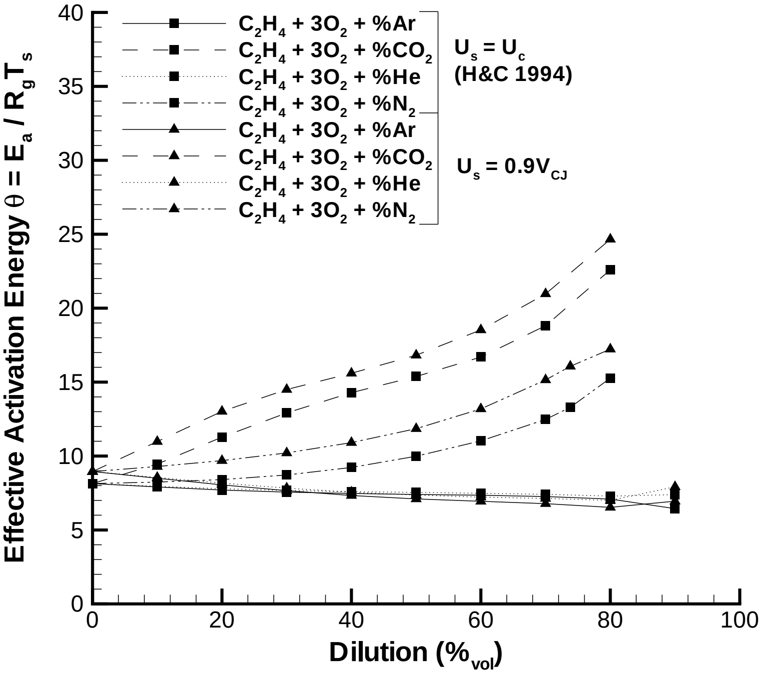

Figure 4.53 Activation energy parameter (critical velocity) versus dilution for ethylene mixtures (P_1 = 100 kPa, T_1 = 295 K).

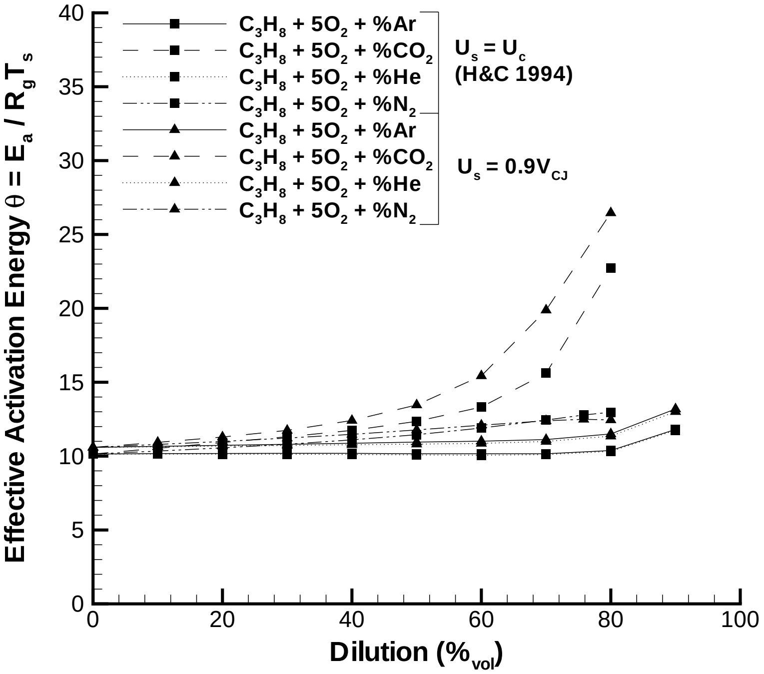

Figure 4.54 Activation energy parameter (critical velocity) versus dilution for propane mixtures (P_1 = 100 kPa, T_1 = 295 K).

4.4 Non-reacting axial shock decay CFD simulations

The decay of the shock wave after the unsteady expansion disturbance reaches the tube axis was investigated with computational fluid dynamic (CFD) simulations (Hornung 2000). The non-reacting, axisymmetric Euler equations were solved within the Amrita CFD environment (Quirk 1998a, 1998b) for a normal shock wave in a constant diameter tube diffracting through an abrupt area change with 90° divergence angle. Specified initial conditions included a constant specific heat ratio of 1.4, uniform pre-shock and post-shock fluid states, and incident shock Mach numbers from two to eight. An extrapolation inflow boundary condition was imposed at the tube end behind the shock wave to simulate an infinite test time shock tube.

Pseudo-Schlieren simulation images at various stages in the diffraction process are presented in Fig. 4.55 for an incident shock Mach number of six. All of the flowfield fea-

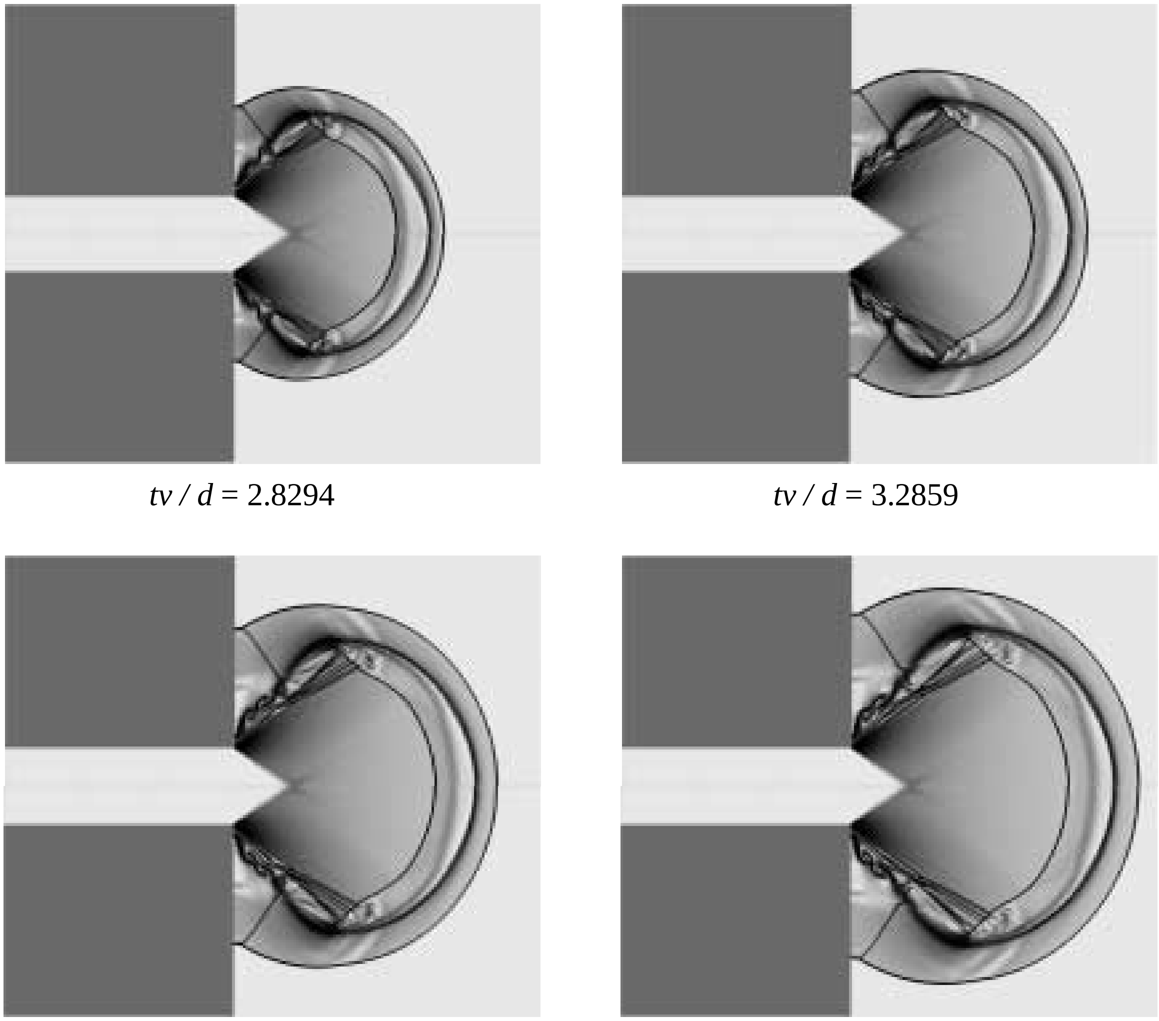

$tv / d = 2.8294$ $tv / d = 3.2859$

$tv / d = 3.7424$ $tv / d = 4.1989$

Figure 4.30 (cont.) Pseudo-Schlieren images from a non-reacting, axisymmetric diffraction simulation with an incident shock Mach number of 6.

tures present have already been observed by previous researchers (Section 2.1). The second and third images of the shock diffracting from the tube are before the critical time ($tv / d = 1.0$); the planar portion of the shock front has not yet been disturbed and the unsteady expansion head is moving towards the tube axis. Supersonic flow is following the incident shock, as indicated by the unsteady expansion head which is being swept entirely downstream from the corner. The third and fourth frames clearly show the establishment

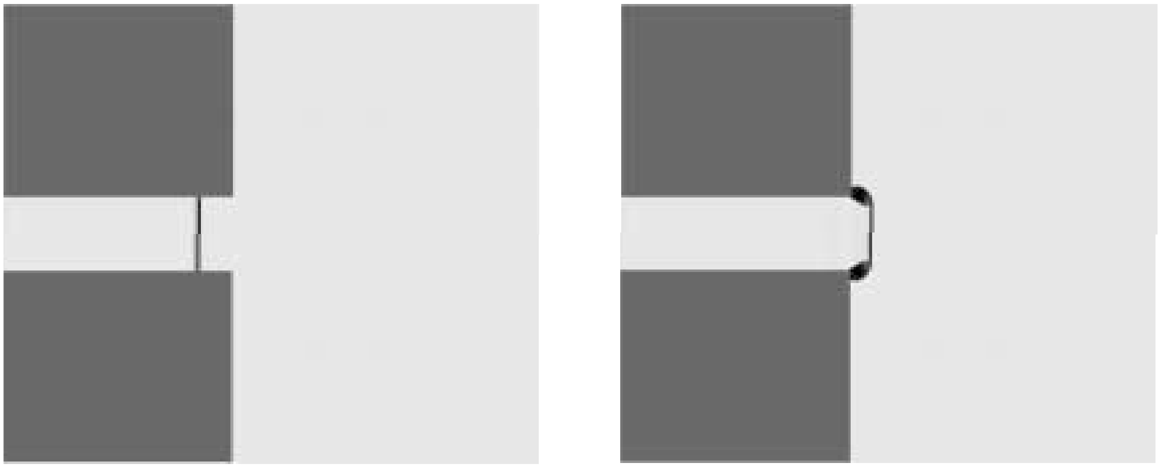

tv / *d* = 0.0421

tv / *d* = 0.548

tv / *d* = 1.0035

tv / *d* = 1.4599

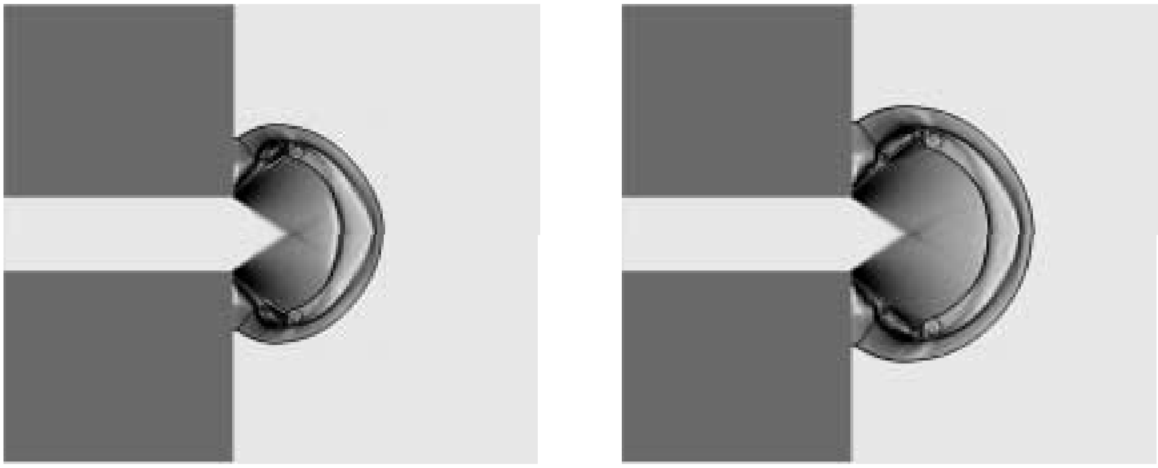

tv / *d* = 1.9164

tv / *d* = 2.3729

Figure 4.55 Pseudo-Schlieren images from a non-reacting, axisymmetric diffraction simulation with an incident shock Mach number of 6.

of the steady expansion fan at the tube edge, the contact surface separating fluid processed by the incident and diffracted shock, and the secondary shock closing in on the tube axis. The secondary shock matches the pressure and velocity of the fluid behind the contact surface with that entering the expansion fan. The wall shock has obviously formed a Mach stem configuration by frame five and the shear layer near the corner is rolling up due to Kelvin-Helmholtz instabilities. The remaining images illustrate the flowfield progression as the shock decays, with an axial shock Mach number approaching three in the last frame. Separation of the tube wall boundary layer occurs near the corner in reality, but the simulation is inviscid and the shear layer appearance with vortical structures is a result of the finite computational grid.

The Mach number of the shock along the tube axis is plotted versus a non-dimensional time for incident shock Mach numbers of two, four, six, and eight in Fig.4.56.

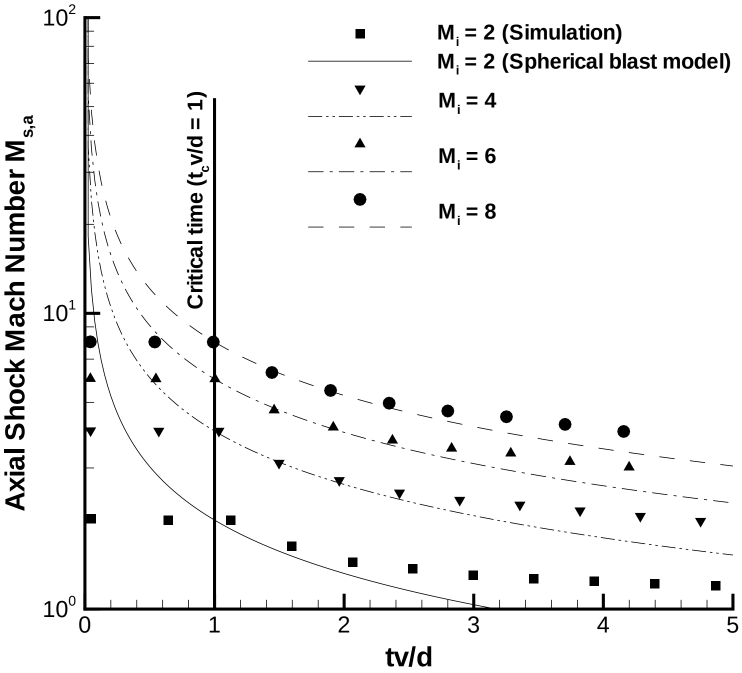

Figure 4.56 Simulation and modeling calculations of non-reacting axial shock decay following diffraction from an abrupt area change.

Time has been non-dimensionalized by the ratio of post-shock transverse disturbance velocity (Section 3.2) and the tube diameter. Therefore, the non-dimensional time of one corresponds to the time at which the unsteady expansion disturbance reaches the tube axis, i.e., the critical time t_c. As expected from the work of Skews (1967a), the simulated axial shock Mach number remains constant until approximately the critical time and decays rapidly thereafter. The axial shock decay does not appear to begin exactly at the critical time in all cases (notably at low incident shock Mach numbers) due to the numerical solver and grid resolution used in these particular simulations.

The curves on Fig.4.56 represent Taylor (1950a, 1950b) and Sedov (1959) similarity solutions for the spherical decay of a strong blast from a concentrated point source energy release located at the tube exit (Section 3.3). The energy constant (Eqn.3.40) for each blast decay curve is defined such that the blast shock Mach number is equal to the incident shock Mach number at the critical time. The Taylor-Sedov blast decay solution represents the simulation data of axial shock decay reasonably well for strong incident shocks ($M_i > 4$) and early times ($1 < tv/d < 2$). The agreement is worse at lower incident shock Mach numbers and longer times corresponding to low axial shock Mach number, which is to be expected for a strong blast approximation solution.

5 Experimental

Experiments were conducted to verify approximations made in the critical diffraction model derivation and to determine critical diffraction conditions with which to validate the model results. The mixtures investigated were comprised of either hydrogen, ethylene, or propane fuel, oxygen, and diluents including argon, carbon dioxide, helium, and nitrogen. Parameters varied in these experiments were the fuel type, equivalence ratio, initial pressure, diluent type, and diluent concentration. The initial gas mixture temperature was between 293K and 298K in all cases.

Single- and multi-sequence shadowgraph visualization, digital chemiluminescence imaging, and pressure transducer diagnostics were used to document the diffraction regimes and determine critical conditions to supplement the literature data (Section 2.2.2). Trajectories of the unsteady expansion disturbance propagation into the planar detonation front were measured and compared to those calculated from the extension of Skews' construction to diffracting detonations (Section 3.2, Section 4.2.2). The decay of the shock along the tube axis for sub-critical cases was investigated to support the use of the Taylor-Sedov strong blast decay solution in the critical diffraction model. Experimental data are also presented illustrating the axial shock decay below the CJ velocity prior to re-initiating in super-critical cases. Finally, study of the chemiluminescence images provides qualitative insight on the coupling between the shock and the reaction zone in the diffracted region. This supports the model evaluation of the competition between energy release, unsteadiness, and curvature only in the immediate vicinity of the interaction point between the unsteady expansion head and the planar detonation front.

5.1 Facilities

Two facilities were used to investigate detonation diffraction through an abrupt area change. The first experimental configuration is illustrated in Fig. 5.1. The 280 mm diameter stainless steel detonation tube (Akbar 1997) is 7.3m long with a 25mm wall thickness. A 762mm long, 152mm square stainless steel test section (Kaneshige 1999) is mated to the end of the detonation tube. A 610 mm long, 25.4 mm diameter aluminum tube is sandwiched between the detonation tube and test section so that one end protrudes into the 165 mm diameter test section window. Piezoelectric pressure transducers located in the 280 mm detonation tube and test section walls recorded shock wave time-of-arrival and pressure data. A ruby laser shadowgraph system (Akbar 1997) was used to image the diffraction of detonations from the 25mm tube into the test section (Section 5.2.2). This

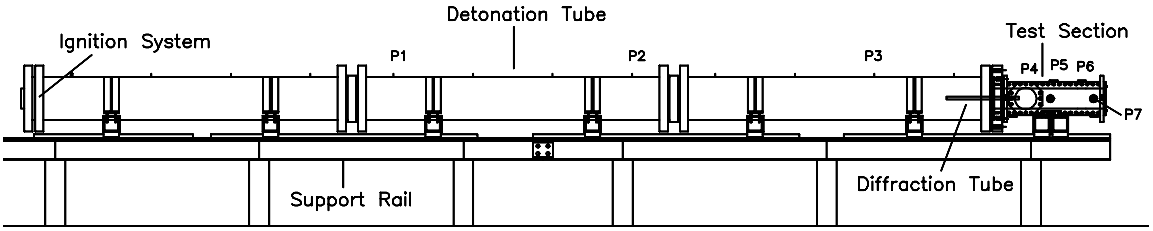

(a) Schematic of facility.

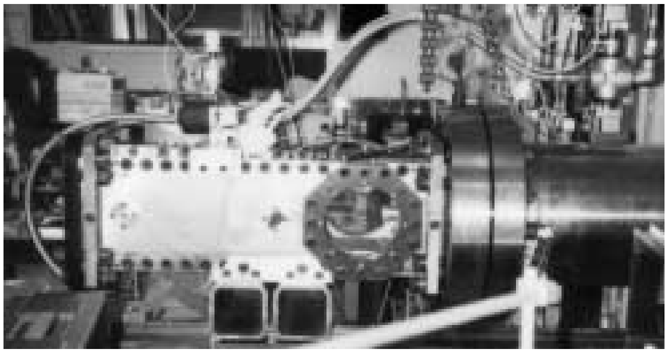

(b) Test section with diffraction tube installed.

Figure 5.1 Experimental configuration with 280mm detonation tube, 25mm diffraction tube, and test section.

facility was used in an initial series of experiments to document the diffraction regimes (Section 5.3).

Prior to an experiment, the entire assembly is evacuated to a pressure level below 7 Pa and then the desired gas mixture composition is filled via the partial pressure technique. The concentration accuracy of each mixture constituent is limited to the electronic Heise 901a gauge accuracy of ±0.18 kPa. After filling, the mixture is circulated through the tubes and test section for 5minutes to ensure mixture homogeneity. The ignition system utilizes an oxygen-acetylene driver injected into the end of the 280mm detonation tube where a 30mm long copper wire is located. The copper wire is exploded through a 2 μF, 9 kV capacitor discharge which causes direct initiation of the driver gas. The driver detonation, with an equivalent energy of approximately 50kJ, transmits a detonation into the test mixture. The detonation propagates in the test mixture down the 280mm tube, into and through the 25 mm tube, and then expands into the test section.

The second facility, used for all other experiments, consisted of a stand-alone detonation diffraction tube mated to the aforementioned test section. The diffraction tube is constructed from 2024-T3 aluminum and is 1.5 m long with a 38.1 mm internal diameter (Fig. 5.2). The ignition source consists of a spark plug mounted in a Teflon end cap, followed by a Schelkin spiral which enhances transition of the spark-induced deflagration to a detonation (Zeldovich and Kompaneets 1960, Shepherd and Lee 1992). The spark system consists of a 5 μF capacitor at 300 V (total stored energy of 225mJ) discharged through a 163:1 trigger transformer to a piston-engine spark plug. The Schelkin spiral is 305 mm long, 38mm outside diameter, has a wire diameter of 4mm, and 11mm distance between coils. A flange is fixed to the opposite end of the tube and the entire assembly is

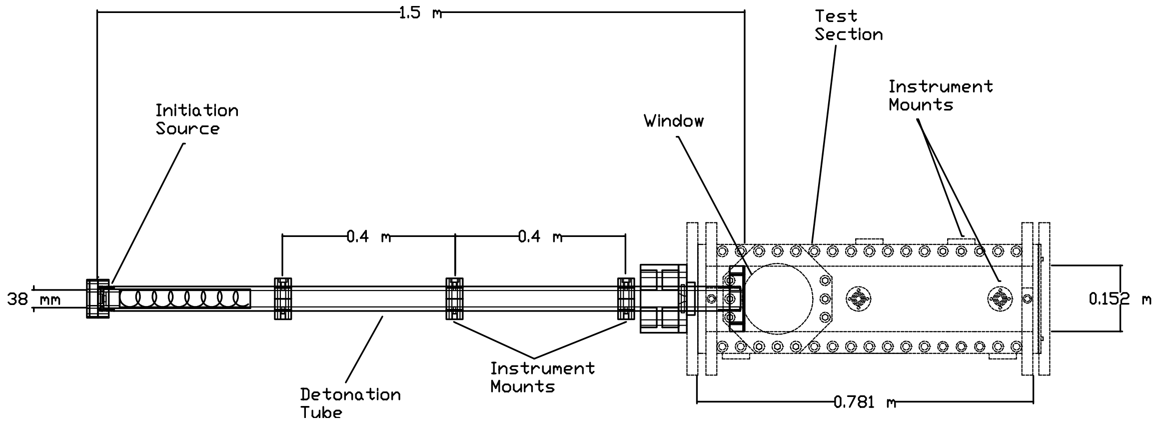

Figure 5.2 38 mm diffraction tube and test section.

connected to the 762 mm long, 152mm square stainless steel test section into which the detonation diffracts. The flange face is 15mm from the centerline edge of the 165mm diameter test section window, affording flow visualization of the diffraction process. Pressure transducers are mounted flush to the wall along the diffraction tube and in the test section. This facility was evacuated to between 5Pa and 25Pa prior to an experiment. Constituent gases were filled via the partial pressure technique and the final test mixture was circulated by a pump for 10 minutes. Detonations were initiated at the end of the diffraction tubes with the spark plug and spiral, and propagated through the diffraction tube towards the test section.

5.2 Diagnostics

Pressure transducers mounted flush to the tube and test section walls provided time-of-arrival and pressure data. Flow visualization was acquired through single- and multi-sequence shadowgraph cameras and digital chemiluminescence imaging. Note that all of the visualization diagnostics were integrating through the test section flowfield to acquire a two-dimensional image, and therefore, it is often difficult to discern the depth at which various flowfield features are located.

5.2.1 Pressure transducers

PCB 113A26 piezoelectric pressure transducers mounted flush to apparatus walls were used for recording time-of-arrival and pressure history data on a digital acquisition system sampling at 1 MHz. Three pressure transducers were in the 280 mm detonation tube, spaced 1.83m apart beginning 2.7m from the exploding wire. The 38mm diffraction tube pressure transducers were 40cm apart and began 43cm from the spark plug. Test section pressure transducers were located at the window center, and 190mm and 430 mm downstream of this location.

Wave velocity measurements derived from pressure transducer time-of-arrival data have uncertainties dependent upon the distance between pressure transducers, transducer response time, data acquisition sampling rate, and the wave velocity. For example, a detonation wave propagating at 2000 m/s will transit the 40cm distance between diffraction tube pressure transducers in 200 μs. The transducers have a 1 μs response time which is matched by the 1 MHz data sampling rate, and so the typical time-of-arrival measurement error is ±1 μs. The measured transit time for this hypothetical detonation could be 198 μs or 202 μs, resulting in apparent velocities of 1980 m/s and 2020m/s, respectively. Therefore, for this configuration, the pressure transducers system has a velocity measurement uncertainty of ±1%.

Calculated detonation velocities (Section 4.1.2) were compared to the pressure transducer velocity measurements to deduce whether or not a CJ detonation wave was initiated prior to diffracting through the area expansion. A successful experiment was considered to have occurred if the wave propagated within +1% and -3% of V_{CJ} from the first pressure transducer down the remainder of the detonation tube. This velocity criteria is consistent with the initiation of a CJ detonation wave given the aforementioned ±1% velocity measurement uncertainty and momentum and energy losses to the boundary layers for relatively small tube diameters (Murray and Lee 1986).

5.2.2 Ruby laser shadowgraph

The ruby laser shadowgraph constructed by Akbar (1997) acquires one high-resolution image per experiment and is illustrated in Fig. 5.3. This device is sensitive to the second density derivative through index of refraction changes in the flowfield and consequently records the presence of shocks and contact surfaces (Goldstein and Kuehn 1996). The ruby rod is pumped with a helical flashlamp and Q-switching via a Pockels cell permits high energies (up to 1 J) to be delivered under flexible timing conditions with approximately a 40 ns pulse width. After the beam is expanded, collimated, and passed through the test section, the image is focused onto a 3.25x4.25inch black-and-white 3000 speed Polaroid 667 film. The collimated beam is approximately 100mm diameter for experiment shot numbers below 714, and 150mm diameter for shot numbers above.

5.2.3 Framing camera shadowgraph

A Beckman and Whitley model 189 framing camera is used to acquire multiple shadowgraph images per experiment and shares much of the same collimating and imaging optics with the ruby laser shadowgraph (Fig.5.4). The ruby laser is replaced by a linear flashlamp light source, supplying up to 100J of energy over a 25-10 μs pulse width. A variable speed rotating mirror in the camera rapidly re-directs incoming light through a set of lenses onto a strip of Kodak TMAX 400 black-and-white 35mm film. The 25 images acquired during one experiment have a minimum of 416ns between frames and 76 ns exposure time per frame. For the experiments conducted in this investigation, the

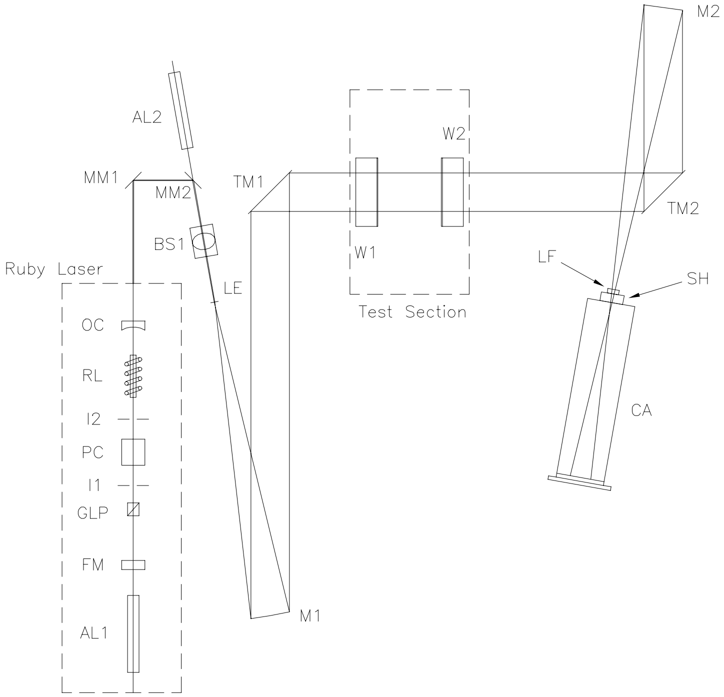

AL1	He-Ne Alignment Laser
FM	Rear Cavity Mirror
GLP	Glan Laser Polarizing Beam Splitter
I1	Iris
PC	Pockels Cell
I2	Iris
RL	Ruby Rod & Flashlamp
OC	Output Coupler
MM1	Turning Mirror
MM2	Turning Mirror
AL2	He-Ne Alignment Laser
BS1	Beam Stearing Mirror Pair
LE	Beam Expanding Lens
M1	Concave Mirror
TM1	Input Turning Mirror
W1	Input Test Section Window
W2	Output Test Section Window
TM2	Output Turning Mirror
M2	Concave Mirror
LF	Laser Line Filter
SH	Capping Shutter
CA	Camera Box (with 4”x5” back)

(a) System schematic.

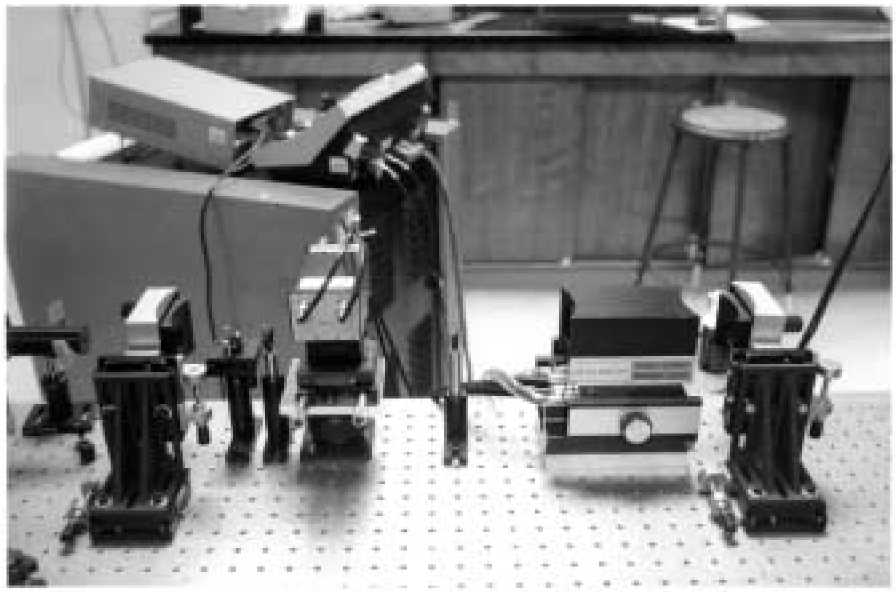

(b) Photograph of laser cavity.

Figure 5.3 Ruby laser shadowgraph.

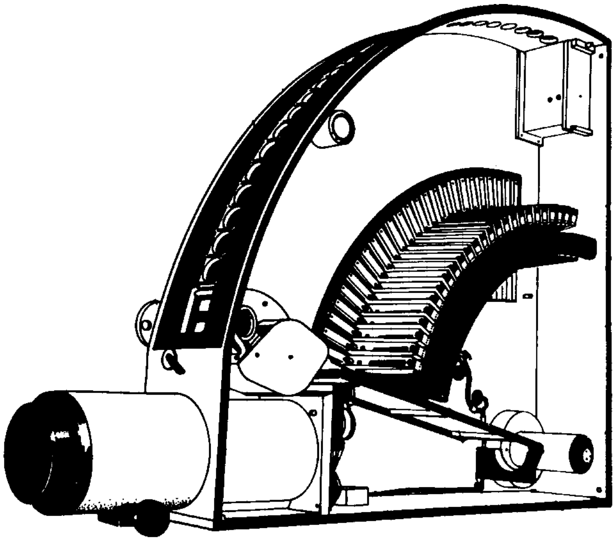

Figure 5.4 Beckman and Whitley 189 framing camera used in shadowgraph system.

camera was configured such that the time between frames and exposure time per frame were 832 ns and 152ns, respectively. While the images obtained are lower resolution than those provided by the ruby laser shadowgraph due to the greater exposure time, the multiple frame capability allows visualization of the temporal and spatial evolution of a diffracting detonation. The collimated beam is approximately 150mm diameter for all experiments with the framing camera.

5.2.4 Digital chemiluminescence imaging

A Princeton Instruments ITE/ICCD-576 intensified CCD detector was used to acquire digital images of chemiluminescent emission on a 5 7 6 x384 pixel array. Imaging optics included a Nikon UV-Nikkor 105 mm f / 4.5 camera lens which transmits throughout the ultraviolet and visible spectrum and various filters for imaging of desired wavelengths. The camera system includes a high-voltage pulse generator capable of detector gate widths down to 3 nsec, although most images were acquired with gate widths between 50ns and 100ns. One image was acquired per experiment and the typical field of view was 100 x 145 mm, for a spatial resolution of approximately 0. 25mm/pixel. Specific filter arrangement, gate width, spatial resolution, depth-of-field, and intensifier gain are provided where appropriate.

5.3 Regime documentation

An initial series of experiments was conducted with the 280 mm detonation tube, 25 mm diffraction tube, and test section facility with pressure transducer and laser shadowgraph diagnostics to document the diffraction regimes. Appendix B contains a summary of the experimental conditions, and all laser shadowgraph images acquired are presented in Appendix C. Representative images and pressure data are presented below, highlighting the criteria by which the diffraction regime is identified in the experiments which follow. Note that the sequences of laser shadowgraphs illustrating the evolution of each regime are from different experiments under the same conditions. The diffraction tube at the left of each image has a 25mm inner diameter and 6mm w all thickness. The scale at the top of the diffraction tube is 10 mm in the horizontal direction. Some of the pressure traces decay below zero after passage of the detonation wave, indicative of thermal effects on the transducer.

Ruby laser shadowgraphs representative of the super-critical case are presented in Fig. 5.5. There is no evidence of reaction zone decoupling from the shock wave, and the detonation is able to continuously transit the area change without failure. Pressure data from a super-critical diffraction experiment are presented in Fig. 5.6. The first three pressure signals show a detonation wave propagating at the CJ velocity through the 280mm tube, and the reflected shock from the tube end wall is visible in the third pressure trace. The last four signals contain high peak pressures indicative of successful detonation trans-

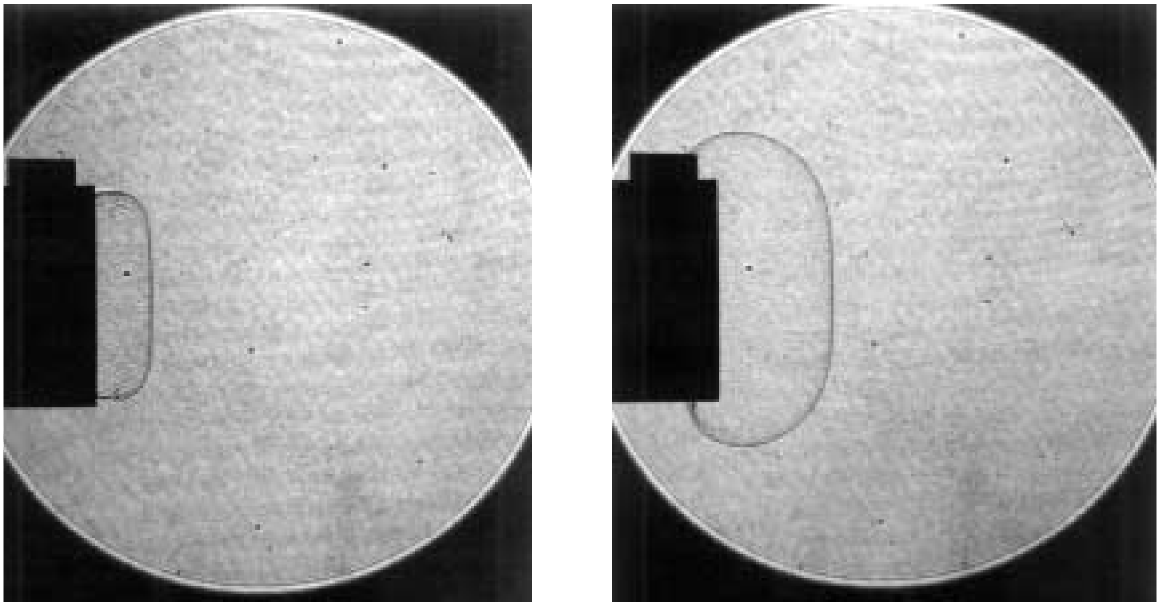

(a) 3177 μsec, Shot 510

(b) 3181 μsec, Shot 509

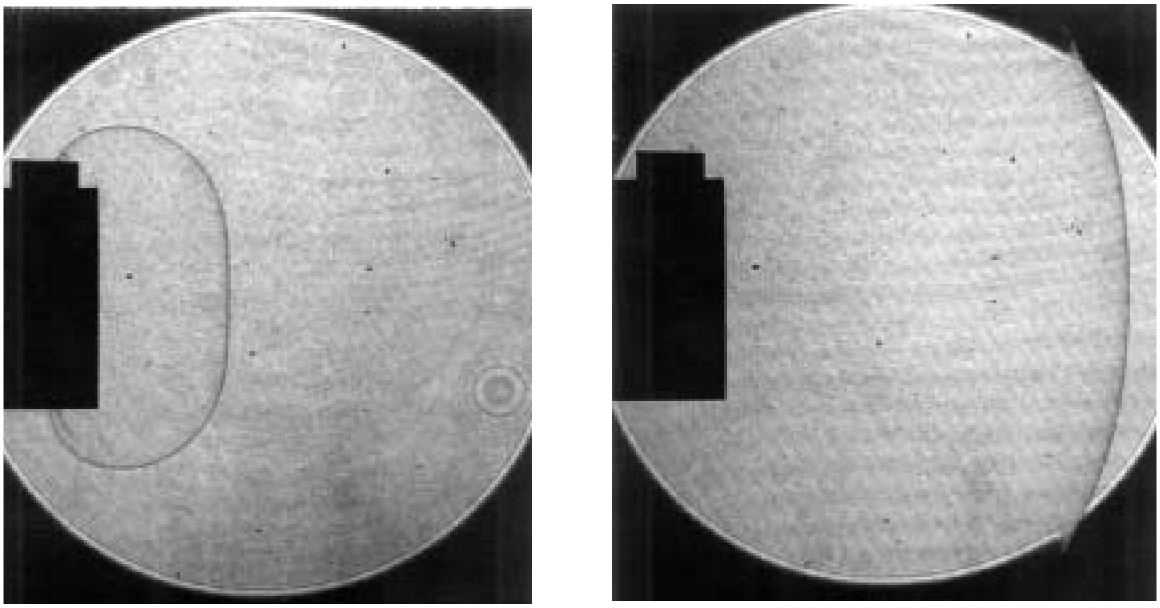

(c) 3185 μsec, Shot 508

(d) 3200 μsec, Shot 511

Figure 5.5 Shadowgraphs of super-critical detonation diffraction (30kPa $C_2H_2+2.5O_2$).

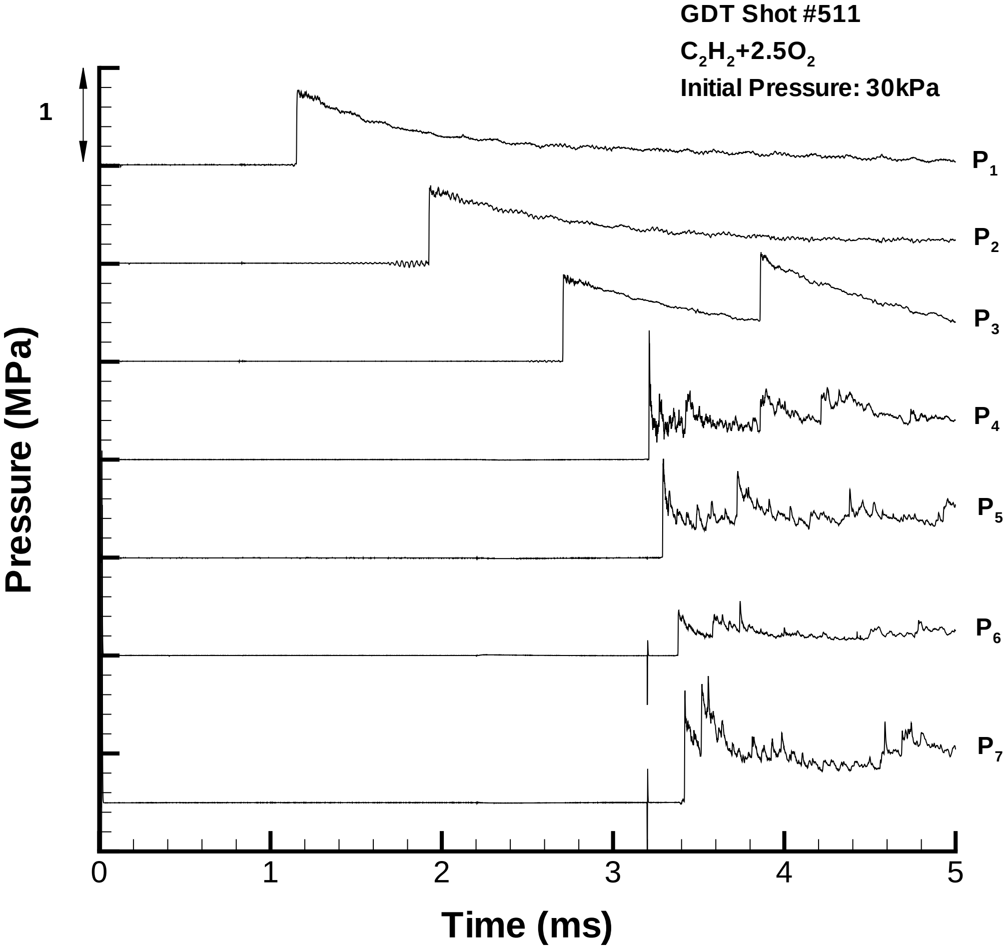

Figure 5.6 Pressure versus time data for super-critical detonation diffraction.

mission into the test section and are complex in nature due to various wave reflections off the test section side and end walls. Note that the pressure amplitude from transducer six was lower than expected during all of the experiments, indicating a recalibration is necessary. The spike in the last two pressure traces just prior to the arrival of the detonation wave is a result of the capacitor discharge through the ruby laser flashlamp.

The sudden expansion from the confinement of the small tube results in complete failure of the detonation wave in the sub-critical regime. As shown in the laser shadowgraphs of Fig. 5.7, the shock wave separates from the reaction zone and rapidly decelerates. The contact surface which follows the decaying shock wave separates the products from shocked reactants, but it is not clear whether the contact surface is a deflagration or the expansion has completed quenched the reactions. Pressure data from a sub-critical diffraction experiment are presented in Fig. 5.8. A detonation was clearly established in the 280 mm tube, but the low initial pressure rise in the test section is indicative of detonation failure due to diffraction. The relatively weak shock observed in the test section pressure traces reflects from the end wall and initiates a detonation which propagates back towards the diffraction tube. Note that the experiment shown had a bad signal from pressure transducer six and therefore, its data trace has been omitted.

Near-critical conditions are characterized by partial failure of the diffracting wave followed by re-initiation leading to the detonation propagating throughout the unconfined volume. The shadowgraphs of Fig. 5.9 illustrate various stages of the re-initiation process. Localized explosions occur between the shocked reactants and that portion of the detonation not yet affected by the expansion to begin the re-initiation process (Fig.5.9b). The blast waves and energy release from these discrete sites couple into a detonation front

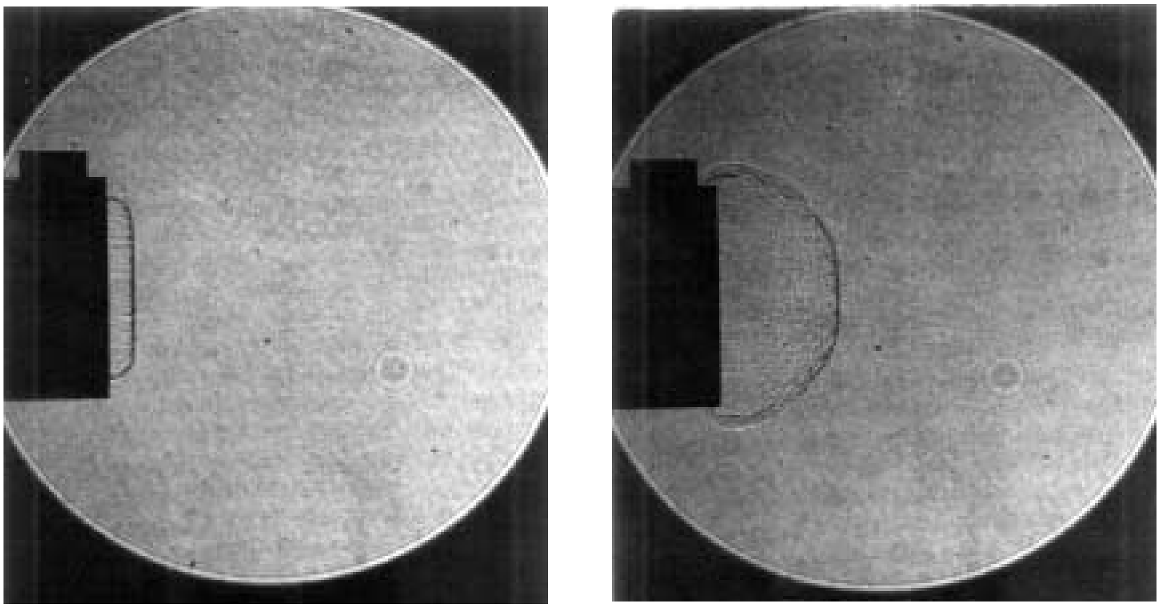

(a) 2656 μsec, Shot 497 (b) 2660 μsec, Shot 496

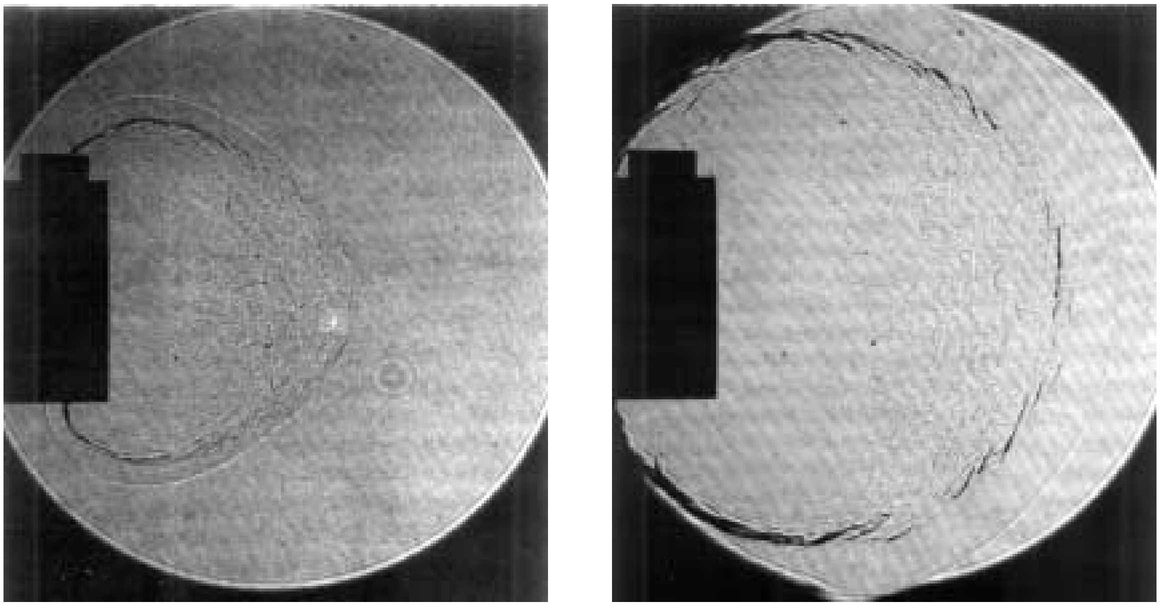

(c) 2670 μsec, Shot 495 (d) 2690 μsec, Shot 494

Figure 5.7 Shadowgraphs of sub-critical detonation diffraction (70kPa $2H_2$+O_2).

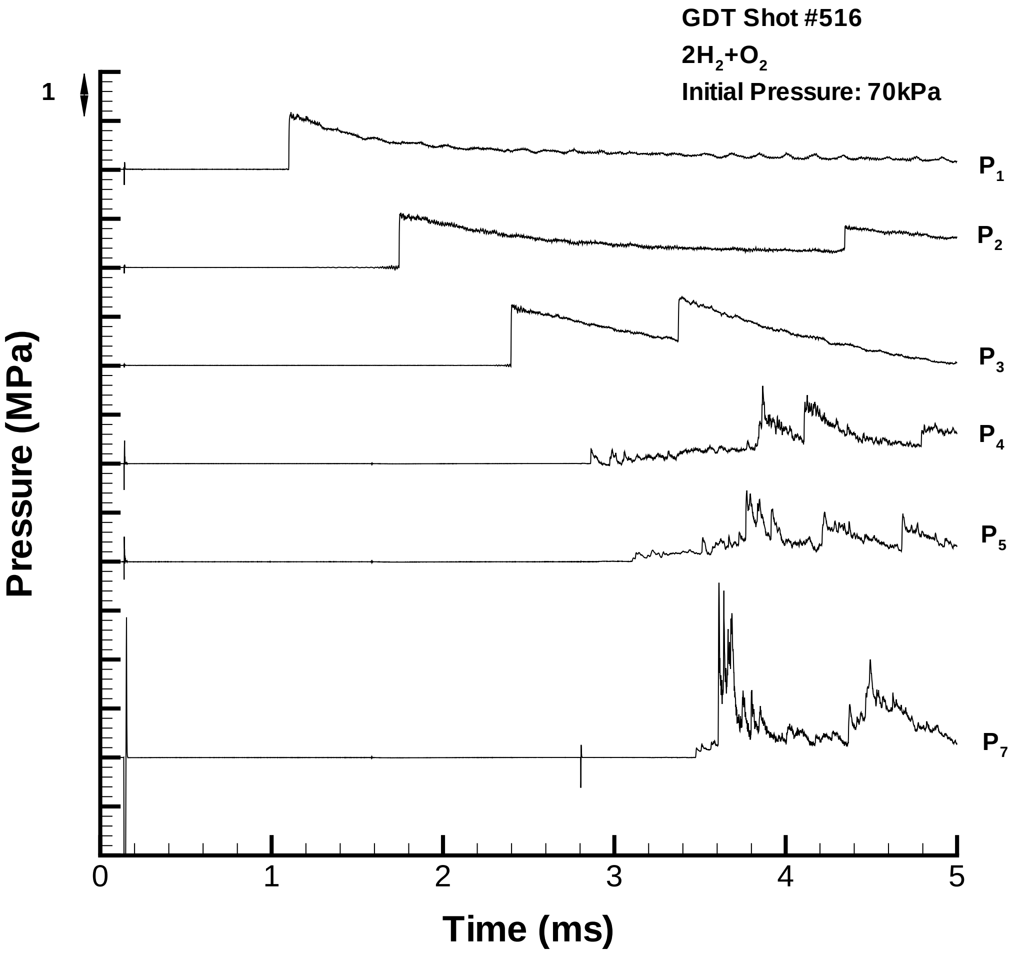

Figure 5.8 Pressure versus time data for sub-critical detonation diffraction.

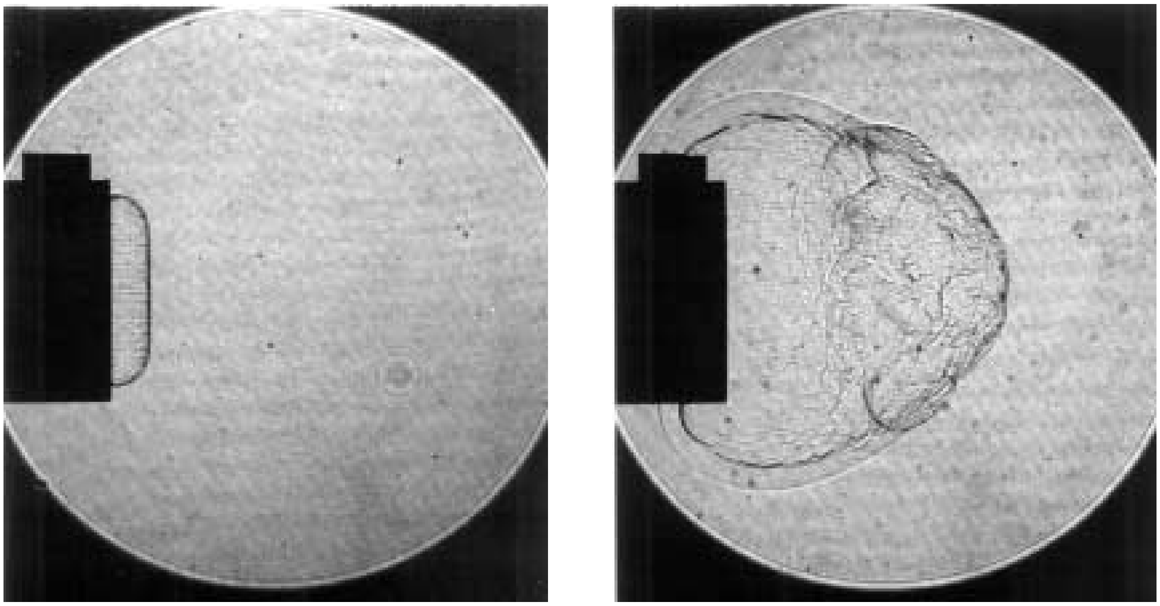

(a) 2635 μsec, Shot 500

(b) 2649 μsec, Shot 520

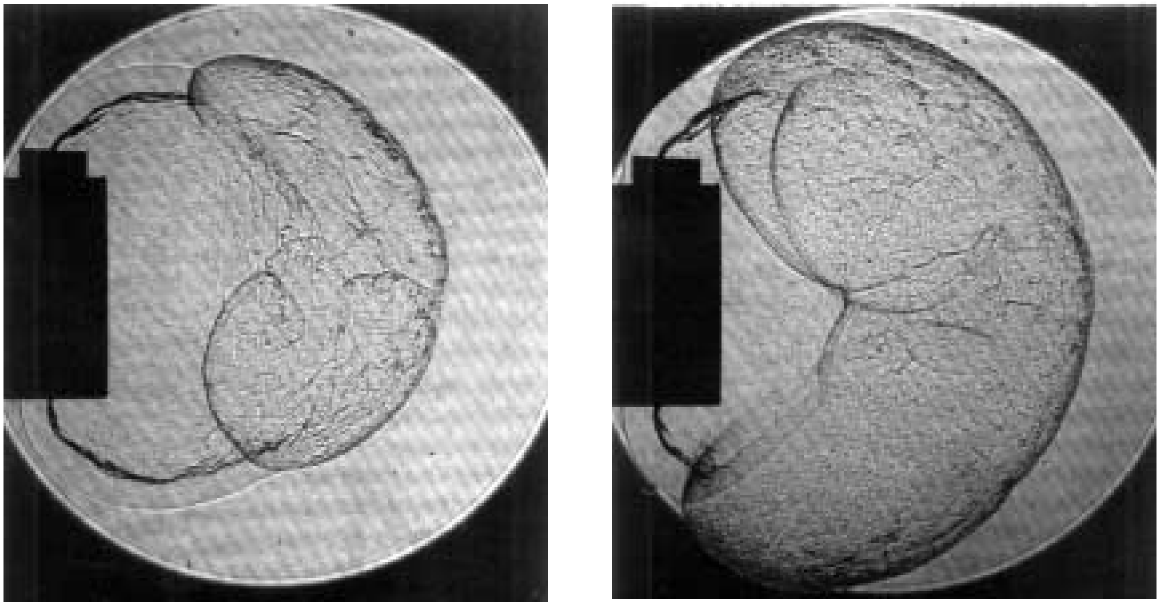

(c) 2650 μsec, Shot 498

(d) 2655 μsec, Shot 502

Figure 5.9 Shadowgraphs of near-critical detonation diffraction (100kPa 2H $_2$+O$_2$).

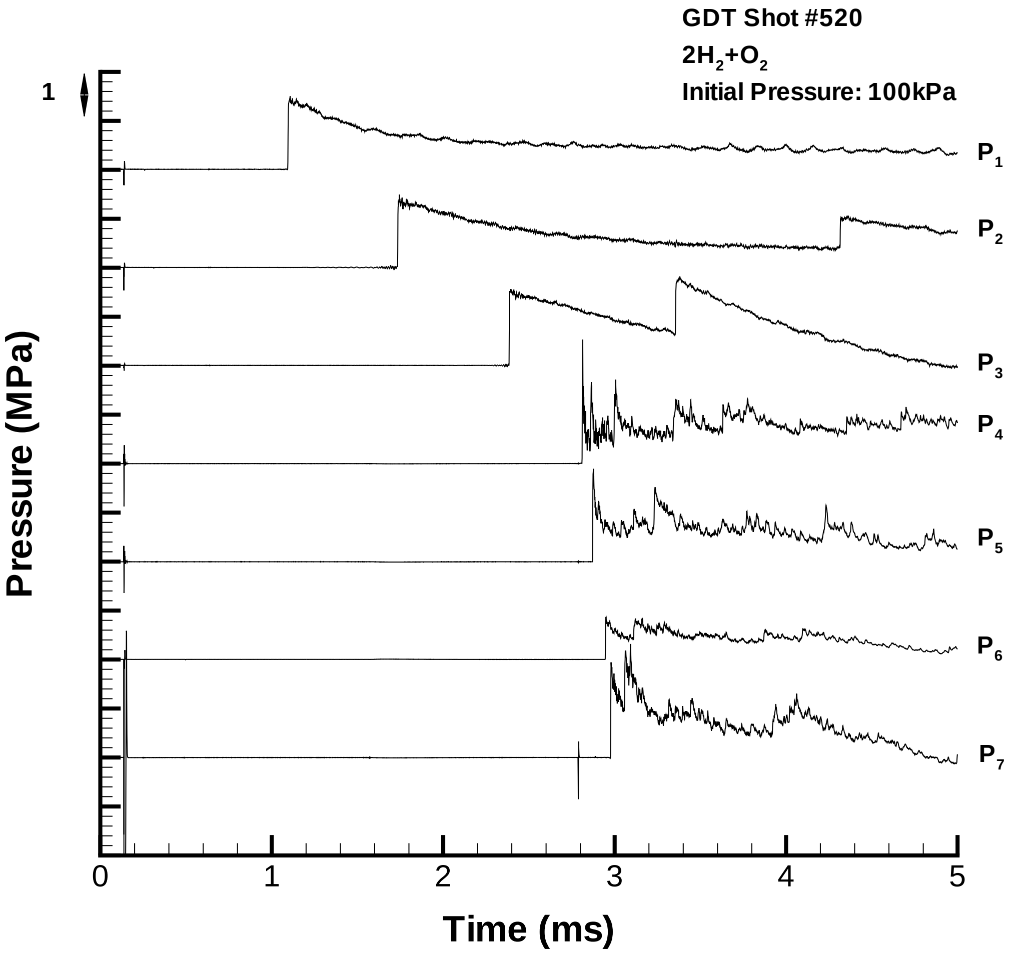

Figure 5.10 Pressure versus time data for near-critical detonation diffraction.

propagating spherically outward and sweeping back into the shocked reactants (Fig. 5.9c,d). The highly non-uniform flowfield is a result of the random, stochastic nature of explosion center formation. Pressure data from a critical diffraction experiment are presented in Fig. 5.10. The signals are very similar to those observed in the super-critical case because the detonation has been re-initiated by the time it reaches the pressure transducers at the test section wall. The shock reflections are evident as in the other experiments and the amplitude from pressure transducer six is low as mentioned above.

In most cases, both pressure data and imagery were obtained during experiments to determine the critical diffraction conditions (Section 5.7). In situations for which no pressure data were obtained, the experiment was not used to determine the diffraction regime unless an image was obtained at relatively late time clearly indicating a sub-critical or super-critical event. When only pressure data was obtained, the diffraction regime was determined based on the initial pressure rise at the fourth (first in the test section) pressure transducer. It is possible that in some cases, a pressure signal which appears to indicate a super-critical diffraction could be a result of a sub-critical experiment in which the decaying shock reflected off the test section side wall and formed a detonation induced by confinement. In fact, a few experiments were conducted in which the imagery clearly illustrated a fully decoupled shock wave but the pressure signal was indicative of a detonation at the test section wall. However, experiments at nearly the same initial conditions led to the conclusion that this phenomenon only occurred near criticality and did not change the identified critical condition by more than a few percent. As discussed in Chapter 2, this type of confinement-induced re-initiation is expected to play a more dominant role as the expansion ratio through which the detonation diffracts becomes smaller.

5.4 Disturbance propagation

Framing camera shadowgraph movies, such as the example of a detonation diffracting from the 3 8mm tube shown in Fig.5.11, were used to measure the unsteady expansion disturbance propagation into the planar detonation front for comparison against the calculations of Section 4.5. Other framing camera movies are presented in Appendix E. The undisturbed detonation was taken as that portion of the wave remaining perpendicular to the tube axis, and so only movies capturing the early time and non-reinitiating diffraction history were applicable. The distance from the tube exit plane (flange edge on the left side) to this wave front and the length of the planar front were recorded from each image frame (Fig. 5.12). An assumption of axisymmetry then provided the experimental

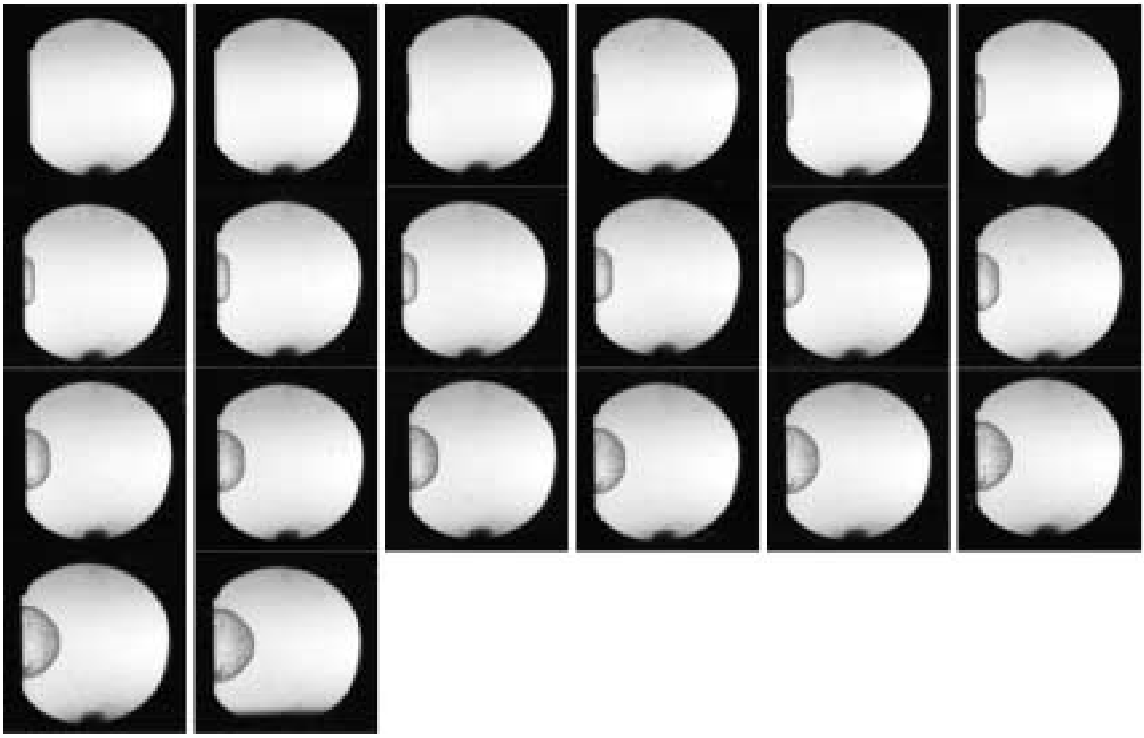

Figure 5.11 Representative framing camera movie of disturbance propagating into planar detonation in $H_2 + 0.5O_2 + 0.5N_2$ 100 kPa mixture (Shot 1093).

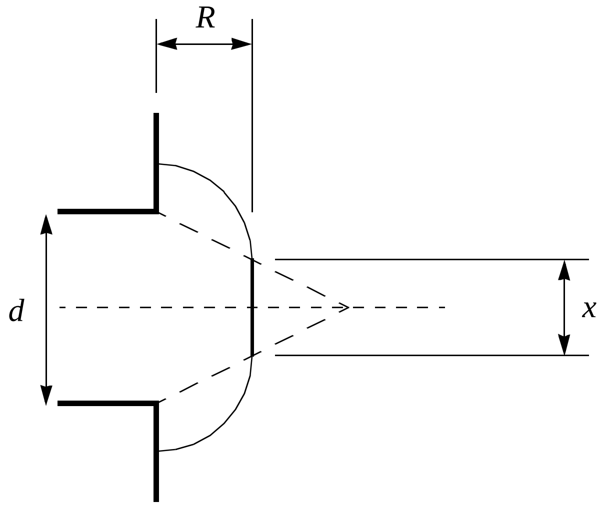

$$\tan\alpha = \frac{d - x}{2R}$$

Figure 5.12 Illustration of disturbance propagation measurements from framing camera shadowgraph images.

disturbance propagation angle. The spatial resolution of these measurements was ± 2mm, corresponding to an angular resolution of approximately ±3°.

Figure 5.13 contains disturbance position data for the experiment with the greatest departure from the calculations based on extending Skews (1967) disturbance propagation construction to steady, one-dimensional detonation waves (Section 4.5). At zero axial distance, the radial distance corresponds to the tube radius, and at zero radial distance, the data intersects the x-axis at the critical distance x_c. An experimental disturbance propagation angle of 27.9° is obtained from a linear fit through the data, which is 5.6° greater than the angle calculated using the von Neumann conditions and 4.5° greater than the angle corresponding to the greatest disturbance velocity in the reaction zone. A best-case example of agreement between the experimental and calculated disturbance is presented in Fig. 5.14.

The angular differences between experimental and calculated disturbance propagation angles are presented in Fig. 5.15. Most of the discrepancy falls within the ±3° exper-

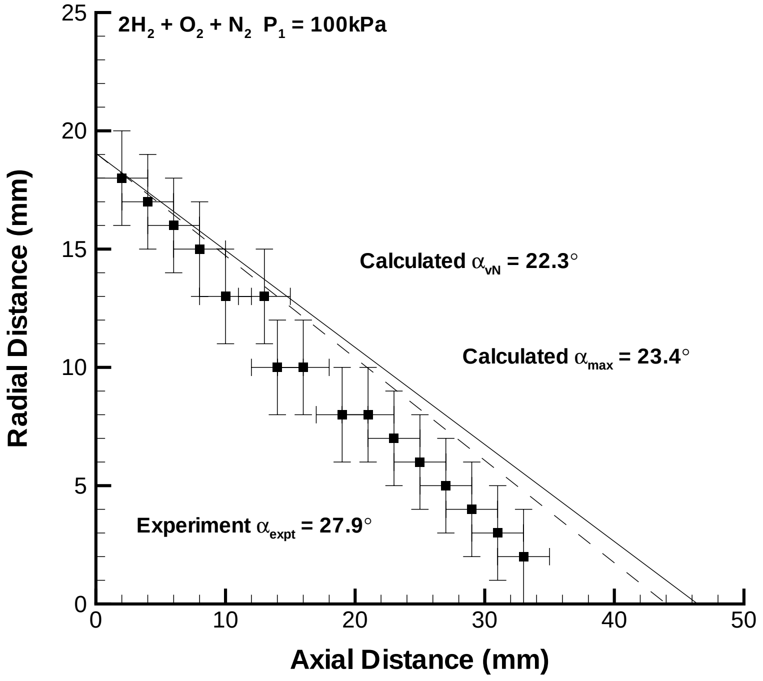

Figure 5.13 Worst case disturbance propagation calculations and experimental measurements.

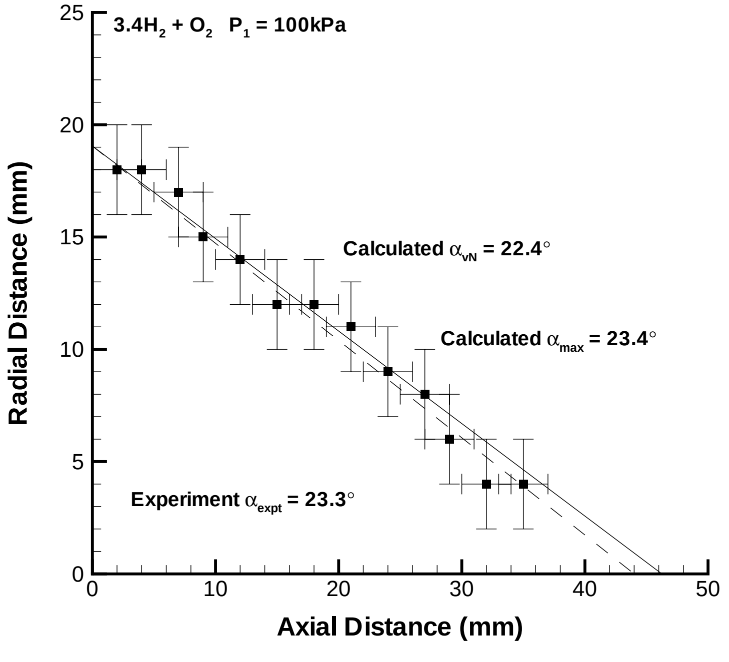

Figure 5.14 Best case disturbance propagation calculations and experimental measurements.

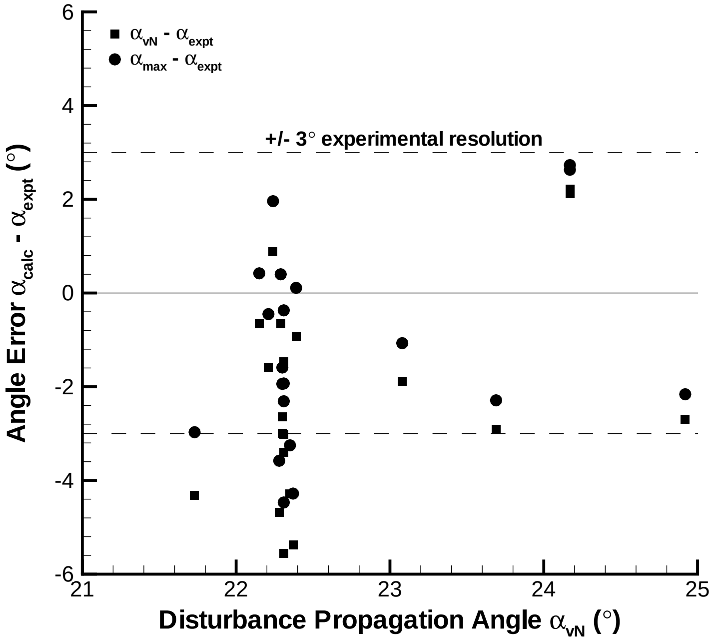

Figure 5.15 Difference between calculated and experimental disturbance propagation angle.

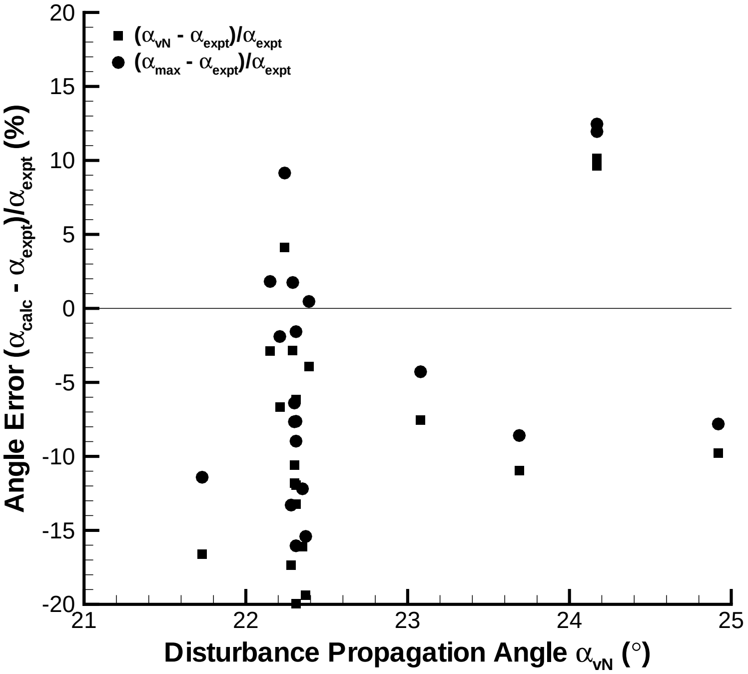

Figure 5.16 Percentage difference between calculated and experimental disturbance propagation angle.

imental measurement resolution, although a few cases exist in which the experimental disturbance propagation angle was greater than the calculated angle by more than 3°. The same data is plotted in percentage error format in Fig.5.16. In most cases the calculations underpredict the experimental angle, with deviations up to a maximum of 20%. This is in general agreement with the soot foil experiment observations by Borisov and Mikhalkin (1989) in which the disturbance propagated into the detonation core at velocities 3% to 30% faster than that expected from a von Neumann state evaluation of Skews' (1967) expression. The disturbance propagation angles corresponding to the maximum reaction zone disturbance velocity are in better agreement with the experimental values. The detonation cellular structure causes widely varying post-shock and reaction zone conditions as the shock velocity varies from approximately 60% to 140% of the CJ velocity (Schultz and Shepherd 1999). This has not been accounted for in the present analytical treatment and is a likely source of difference between the calculated and experimental disturbance propagation angles.

5.5 Axial shock decay

The measurements taken from framing camera images by Mitrofanov and Soloukhin (1965), Soloukhin and Ragland (1969), and the present investigation are not sufficient to determine whether or not the decay of the shock along the tube axis after the critical time can be modeled adequately by the Taylor-Sedov spherical strong blast decay similarity solution. The degree of resolution necessary can be provided by streak camera data, and Edwards et al. (1979, 1981) presents some data for the axial shock decay. The detonation diffraction experiment of Edwards et al. (1979, 1981) for which data is available was conducted in a thin, rectangular channel and the exact mixture is not identified.

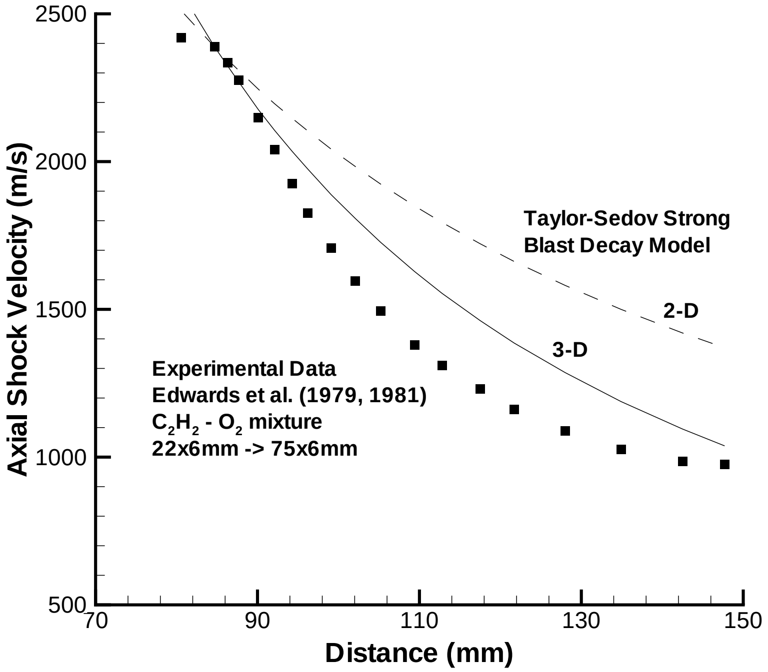

Figure 5.17 Axial shock decay measurements from Edwards et al. (1979, 1981) detonation diffraction experiments.

Their axial shock decay data are presented in Fi g.5.17 along with cylindrical and spherical Taylor-Sedov blast solutions matching the experimental axial shock velocity at the onset of decay. The cylindrical solution might be expected to best match the decay of Edwards' et al. experiment, but it grossly underpredicts the axial shock decay rate. In fact, even the spherical decay solution does not capture the high rate at which the experimental shock decays. The thin channel experiment is influenced by boundary layer effects and the associated viscous losses are probably causing the shock to decay more rapidly than it would in a more unconfined environment.

Ungut et al. (1984) collected shock decay data during detonation diffraction experiments with a laser Schlieren time-of-flight technique. They include little description of this technique and the experimental configuration in general, although they do note that the device has a spatial resolution of ±2 8mm which is approximately 25% of the tube diameter. It also appears that the shock decay measurements were taken somewhat off-axis because a plate with a soot foil attached was located along the axis during the same experiments. The shock decay data from Ungut et al. (1984) for propane mixtures are presented in Fig. 5.18 along with two Taylor-Sedov spherical blast decay solutions. The solution denoted by the solid line is that which corresponds to a blast velocity of V_{CJ} at the

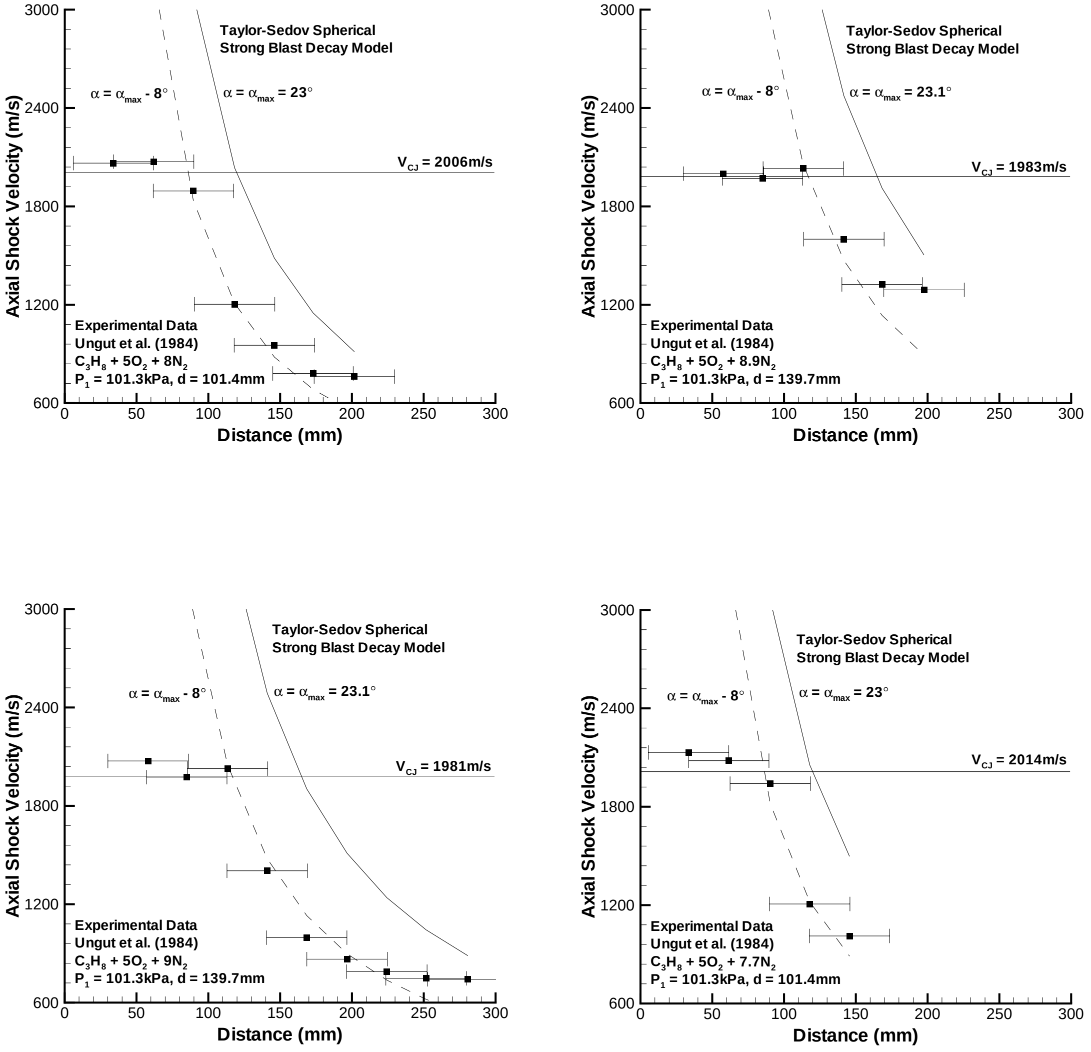

Figure 5.18 Axial shock decay measurements from Ungut et al. (1984) detonation diffraction experiments.

critical distance given by the calculated disturbance propagation angle (Section 4.5). The dashed line solution corresponds to a blast velocity of V_{CJ} at a pseudo-critical distance obtained if the disturbance propagation angle were 8° less than that calculated in Section 4.5. Both solutions match the experimental shock decay rate fairly well, but the critical distance for the onset of shock decay is greatly overpredicted by the calculated disturbance propagation angle. At low shock velocities, the experimental shock decay rate is reduced relatively to the Taylor-Sedov solution because the strong shock condition is violated. The 8° solution case was chosen arbitrarily to illustrate the good agreement between the Taylor-Sedov solution and the experimental data. These results indicate that the measurements of Ungut et al. (1984) were taken off-axis where the shock begins to decay earlier and that this portion of the shock also decays approximately as a spherical strong blast soon after the critical time.

Analysis of the data of Ungut et al. (1984) provides some support for the critical diffraction model assumption that the shock decay along the tube axis can be modeled accurately by the Taylor-Sedov blast decay spherical similarity solution immediately after the critical time. The non-reacting axisymmetric simulations of Section 4.6 also lend support to this assumption. Further confirmation of the applicability of the Taylor-Sedov model within the context of the critical diffraction model must come from streak camera measurements along the tube axis of detonations diffracting through an abrupt area expansion into an unconfined region.

Shock velocity measurements from Edwards et al. (1979, 1981) and Ungut et al. (1984) for re-initiating super-critical diffractions are presented in Fig.5.19. The shock velocity decays significantly before accelerating back to the CJ velocity. These observa-

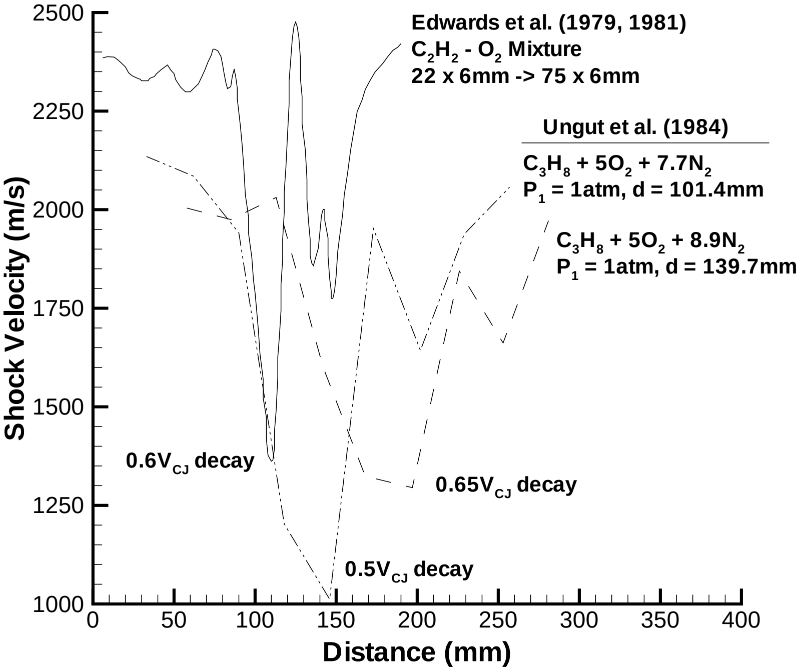

Figure 5.19 Axial shock velocity decay measurements prior to re-initiation.

tions lend support to the use of a sub-V_{CJ} critical shock velocity at which to evaluate the critical diffraction model. As previously mentioned, the Edwards et al. (1979, 1981) data were obtained in a thin, two-dimensional channel with probable boundary layer influence and the Ungut et al. (1984) data were obtained off-axis and with possible influence from a sooted plate reflecting surface. Therefore, the magnitude of the velocity decrease is not necessarily representative of the axial shock decay before critical re-initiation in detonation diffraction into an unconfined space.

5.6 Shock-reaction zone coupling

A digital chemiluminescence image, ruby laser shadowgraph, and framing camera shadowgraphs of super-critical detonation diffractions are presented in Fig.5.20. Note that the digital image is a double exposure and therefore, shows the intense luminosity of

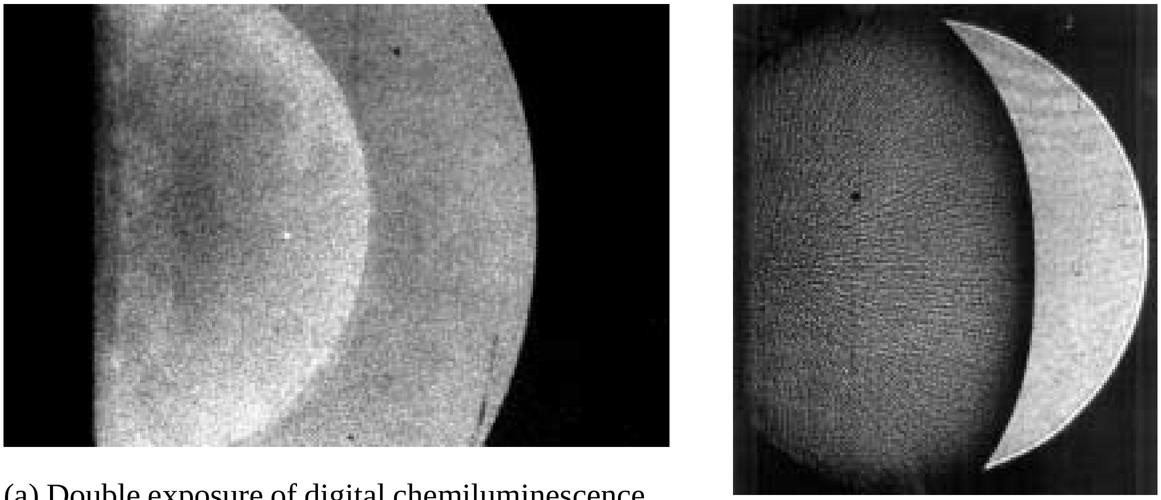

(a) Double exposure of digital chemiluminescence image (Shot 1240).

(b) Laser shadowgraph (Shot 753).

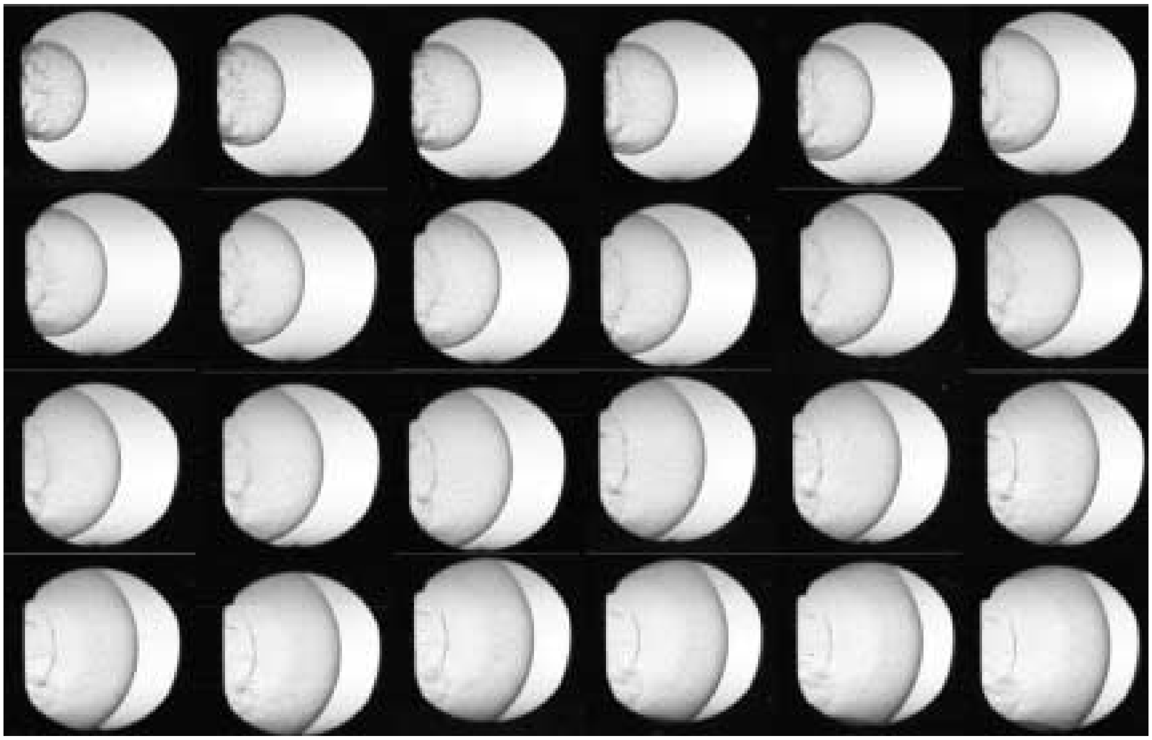

(c) Framing camera shadowgraphs (Shot 1079).

Figure 5.20 Super-critical images.

the detonation at two times during its spherical expansion. These images are in contrast to the sub-critical images presented in Fig.5.21. The chemiluminosity is very weak and the decoupled shock front is barely visible due to light scattering off the post-shock reactants. The vortex ring forming from the jet of hot products being expelled from the tube has relatively high luminosity and there is no noticeable sign of post-shock reactant combustion.

Images acquired during experiments near the critical conditions are presented in Fig. 5.22. The chemiluminescence image clearly highlights the regions in which re-initiation is taking place through re-coupling of the shock and reaction zone. The vortex ring formation is only faintly visible because it is overshadowed by the emission intensity from the re-initiation region. The framing camera movie depicts a localized explosion originating near the tube axis which is subsequently able to amplify and re-initiates the super-critical detonation diffraction. This process was qualitatively similar for re-initiations observed in all mixtures. Two other framing camera movies are shown in Fig.5.23 which give a sense of the re-initiation process at relatively early and late times. Multiple explosion centers give rise to an overall re-initiation of the spherically expanding detonation.

Several chemiluminescence images are presented in Fig. 5.24, along with lines marking the tube axis and unsteady expansion head disturbance propagation trajectory calculated in Section 4.5. The intensity of the luminosity in the detonation core from the coupled shock and reaction zone supports the extension of Skews’ (1967) construction for disturbance propagation through the detonation reaction zone (Section 3.2). Chemiluminescent emission decays rapidly in the diffracted region, confirming the critical diffraction model assumption of the primary competition between energy release and quenching

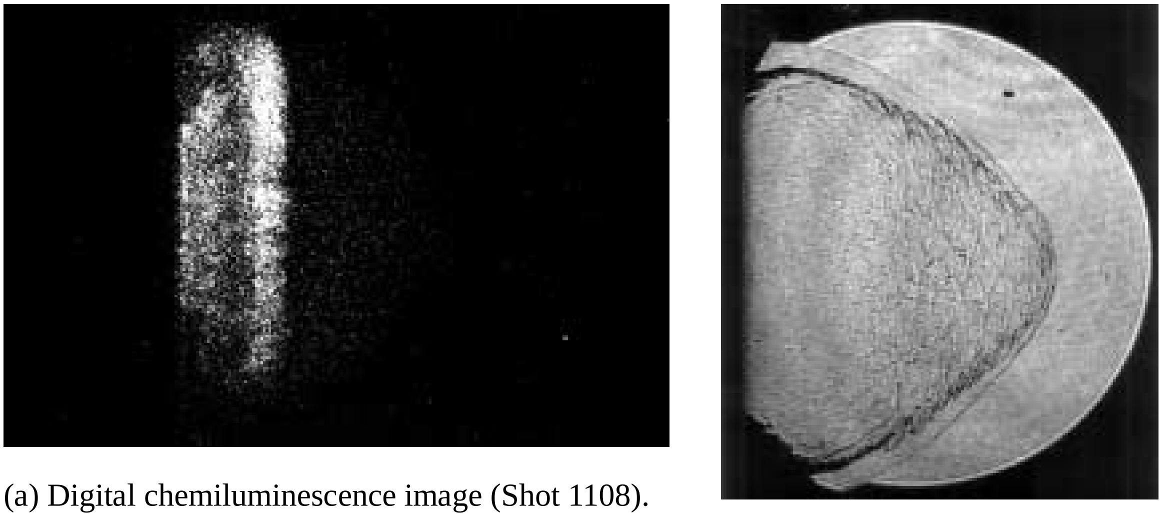

(a) Digital chemiluminescence image (Shot 1108).

(b) Laser shadowgraph (Shot 721).

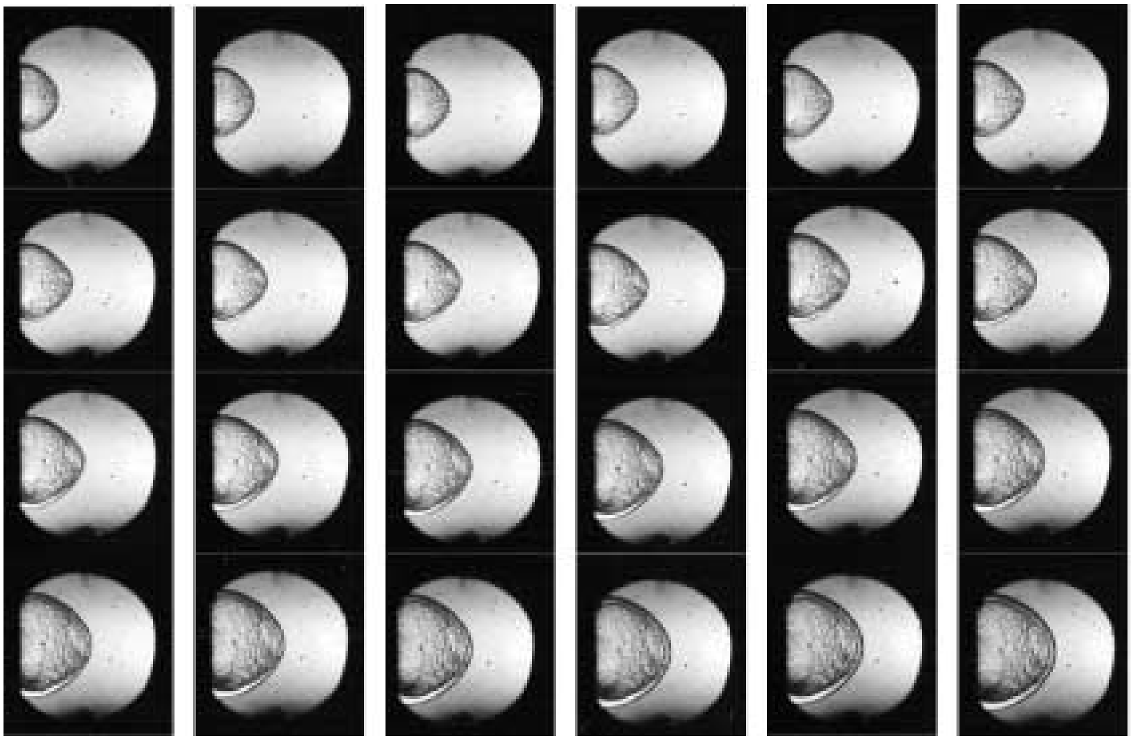

(c) Framing camera shadowgraphs (Shot 1116).

Figure 5.21 Sub-critical images.

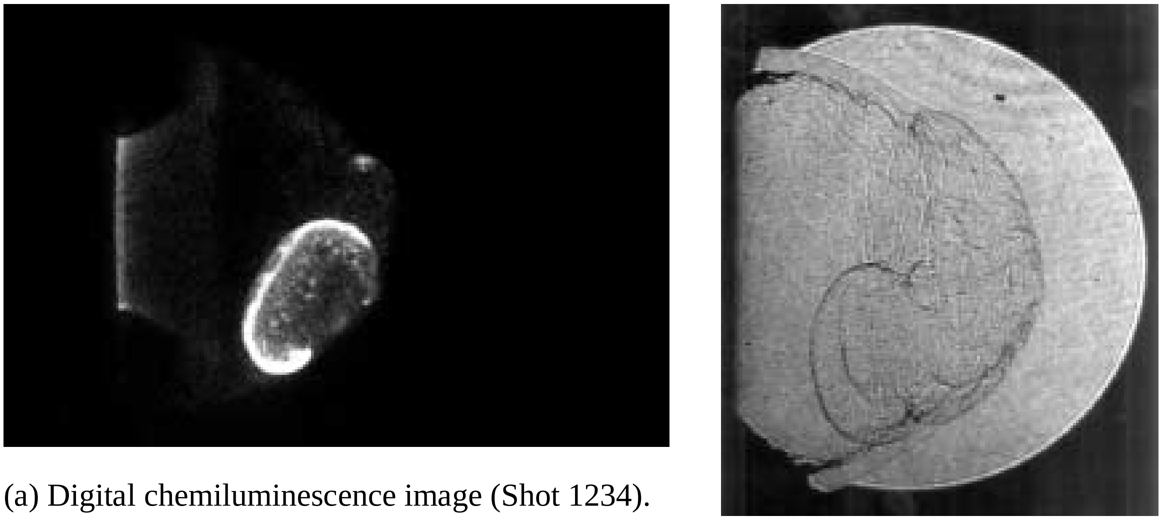

(a) Digital chemiluminescence image (Shot 1234).

(b) Laser shadowgraph (Shot 725).

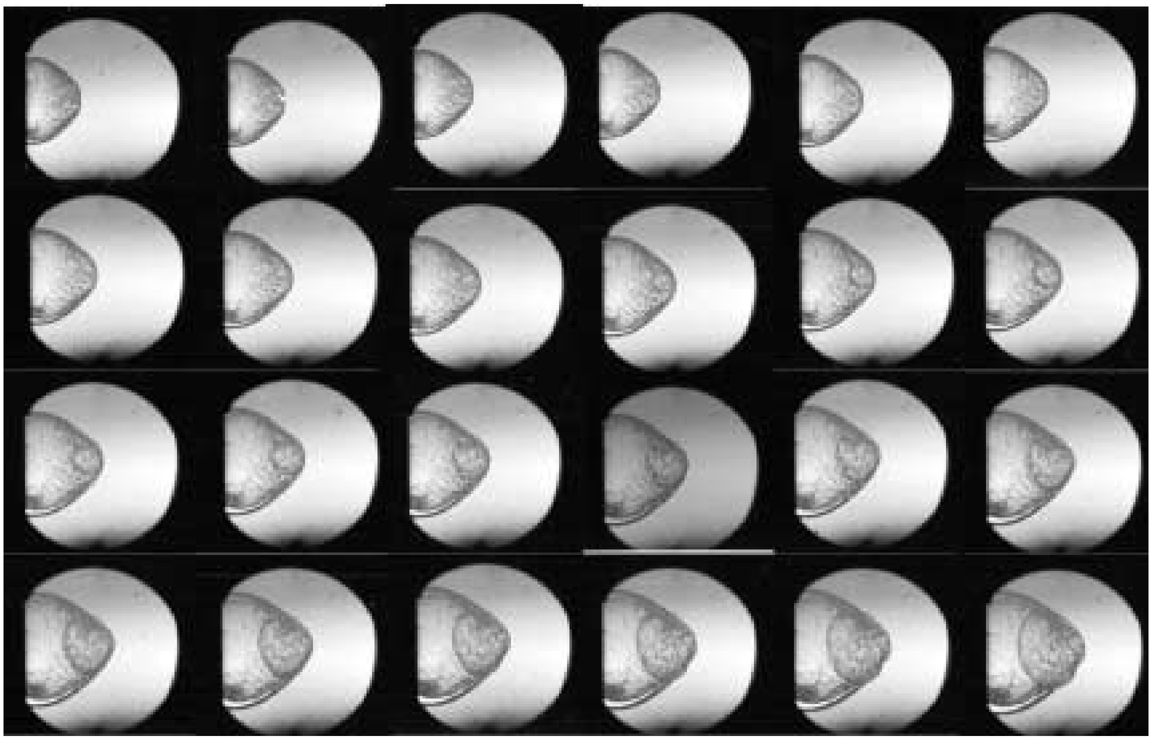

(c) Framing camera shadowgraphs (Shot 1090).

Figure 5.22 Near-critical images.

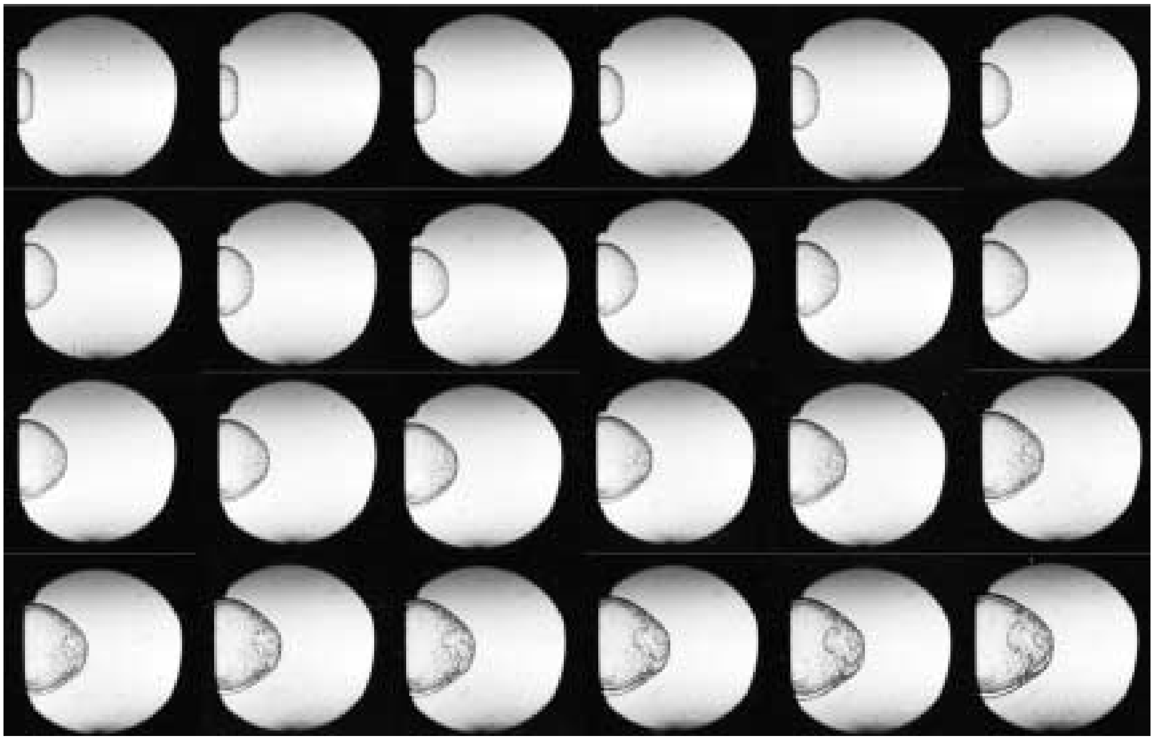

(a) Early time (Shot 1078).

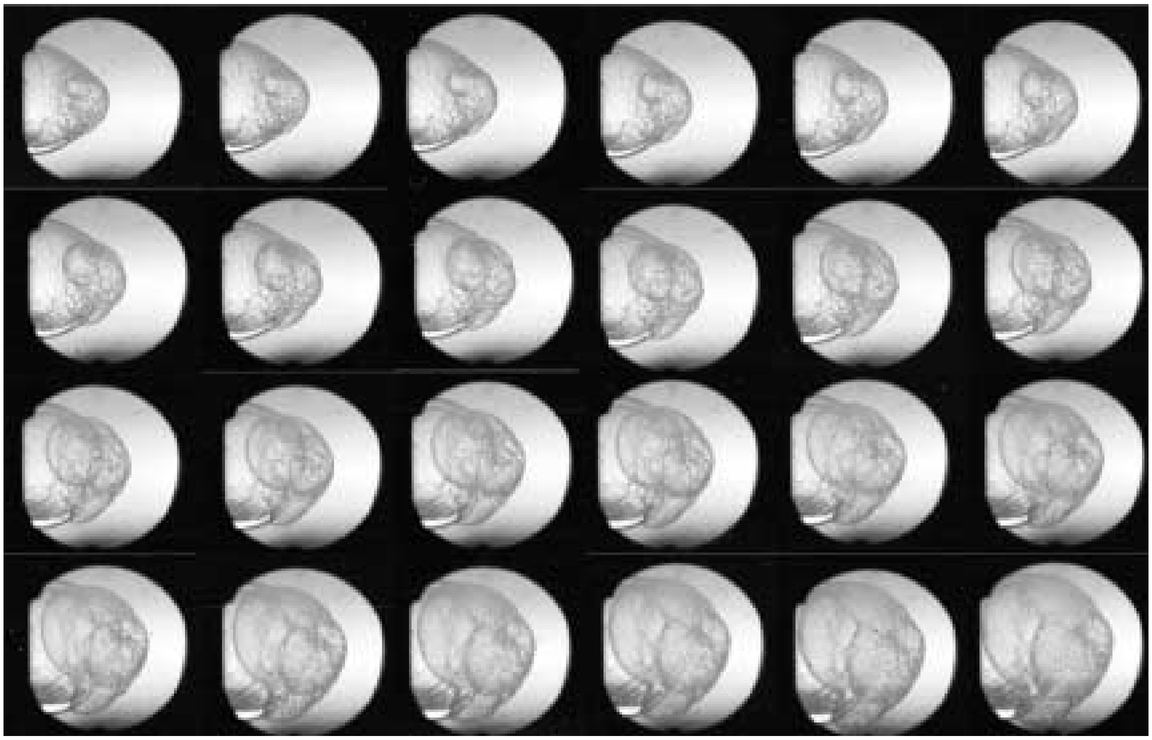

(b) Late time (Shot 1088).

Figure 5.23 Framing camera shadowgraphs of critical detonation diffraction.

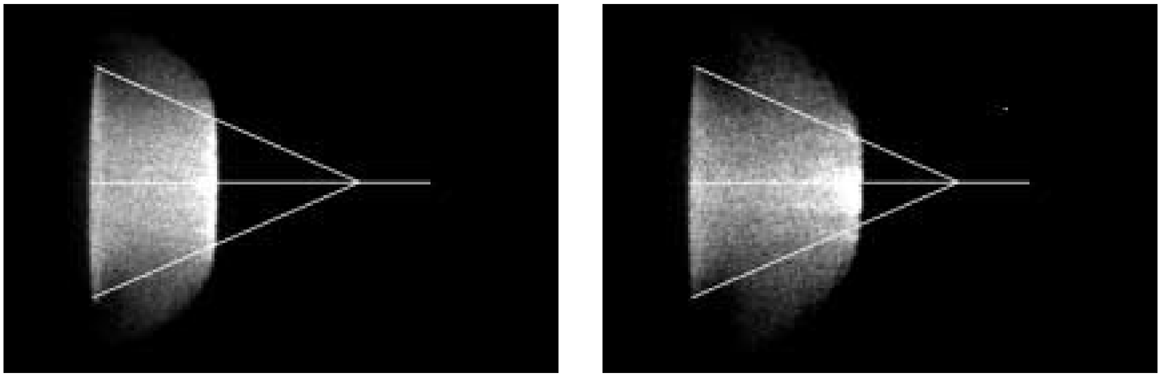

(a) Shot 1276.

(b) Shot 1273.

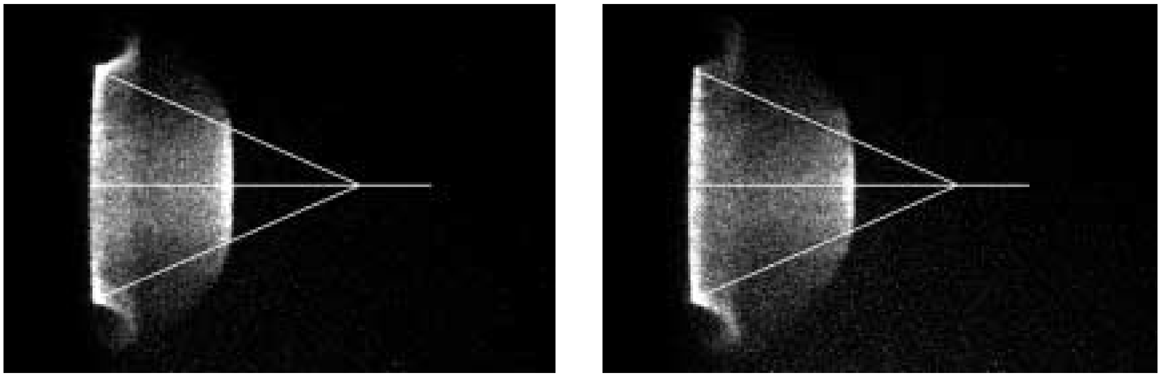

(c) Shot 1281.

(d) Shot 1282.

Figure 5.24 Digital chemiluminescence images near the critical time.

effects occurring in the immediate vicinity of the disturbance interaction point with the detonation core.

5.7 Critical conditions

The 38 mm diffraction tube and test section facility was used to determine the critical conditions for hydrogen, ethylene, and propane mixtures with varying stoichiometry, initial pressure, and dilution by argon, carbon dioxide, helium, and nitrogen. Initial temperatures were always between 2 9 3K and 298K and the initial pressure was 100kPa except for the initial pressure variation series of experiments. Stoichiometric proportions of fuel and oxidizer were used except for the stoichiometry variation series of experiments. All of the experimental conditions are tabulated in Appendix D and imagery from the ruby laser shadowgraph, ICCD digital camera, and framing camera shadowgraph systems is presented in Appendix E.

Determination of whether or not a given experiment was sub-critical or super-critical was made based on the regime documentation discussion of Section 5.3. The critical condition is defined as the average condition of the two limiting sub-critical and super-critical cases. In some cases near criticality, repeat experiments resulted in both sub-critical and super-critical diffractions. As discussed in Chapter 2, this has been observed by other researchers and the detailed evaluation by Higgins and Lee (1998) suggests that the range of conditions under which both regimes can be observed is relatively small. This phenomena is probably a manifestation of the stochastic nature of the re-initiation process, its sensitivity to small perturbations in the initial conditions which are beyond experimental control, and the non-reproducible nature of the transverse wave structure.

The critical conditions identified during the present investigation as well as the relevant critical data from Zeldovich et al. (1956), Matsui and Lee (1979), Moen et al. (1981, 1982, 1984a, 1984b), Guirao et al. (1982), Knystautas et al. (1982), Rinnan (1982), Liu et al. (1984), Ungut et al. (1984), Shepherd et al. (1986a), Makris et al. (1994), and Higgins and Lee (1998) are tabulated in Appendix F. Only data from experiments with circular tube and orifice geometries were included. Note that some duplicate data are reported in the literature, and every effort has been made to verify that redundant data are not presented here. The critical conditions are plotted in Section 5.8 along with results from the critical diffraction model. Data from all researchers have been treated equally in the sense that no relevant data have been discarded and no data are preferentially weighted in comparison with the model results.

5.8 Evaluation of the critical diffraction model

Critical diameters calculated with the diffraction model (Eqn. 3.46) and the computational results of Chapter 4 are compared with the experimental critical diameter data from Section 5.7 in this section. The disturbance propagation angle corresponding to the maximum reaction zone disturbance velocity was used based on the disturbance propagation measurements of Section 5.4. Critical diameters were calculated with the critical shock velocity of He and Clavin (1994) (Section 4.3.2) and a critical shock velocity of $0.9V_{CJ}$, along with the corresponding reaction times (Section 4.3.3) and effective activation energies (Section 4.3.4).

The experimental and analytical critical diffraction conditions for fuel-oxygen and fuel-air mixtures with varying stoichiometry for hydrogen, ethylene, and propane fuels are presented in Figs. 5.25, 5.26, and 5.27, respectively. Only fuel-lean experimental data are available for ethylene-air mixtures, and very few data exist (all near stoichiometric) for propane-air mixtures. In general, the critical diameter is minimized near stoichiometric conditions (usually slightly fuel-rich, especially for the hydrocarbon mixtures) and increases monotonically in the lean and rich directions to form the familiar U-shaped curves. Critical diameters are one order of magnitude less for fuel-oxygen relative to fuel-air mixtures for hydrogen fuel and two orders of magnitude less for the hydrocarbon fuels. The analytical model results are in qualitative agreement with the experimentally determined critical conditions; the level of quantitative agreement between experimental and calculated critical diameter data is considered below.

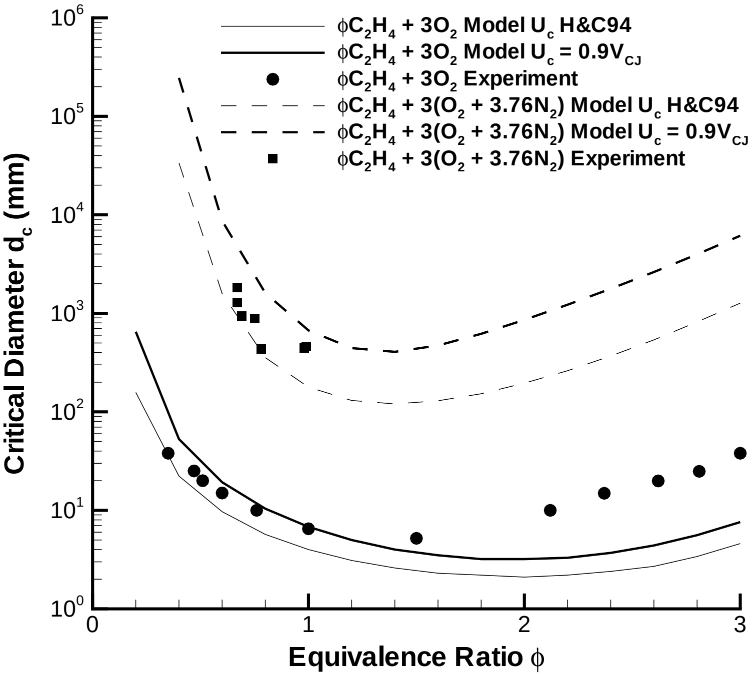

Figure 5.26 Critical diameter versus equivalence ratio model and experimental data for ethylene-oxygen and ethylene-air mixtures (P_1 = 100 kPa).

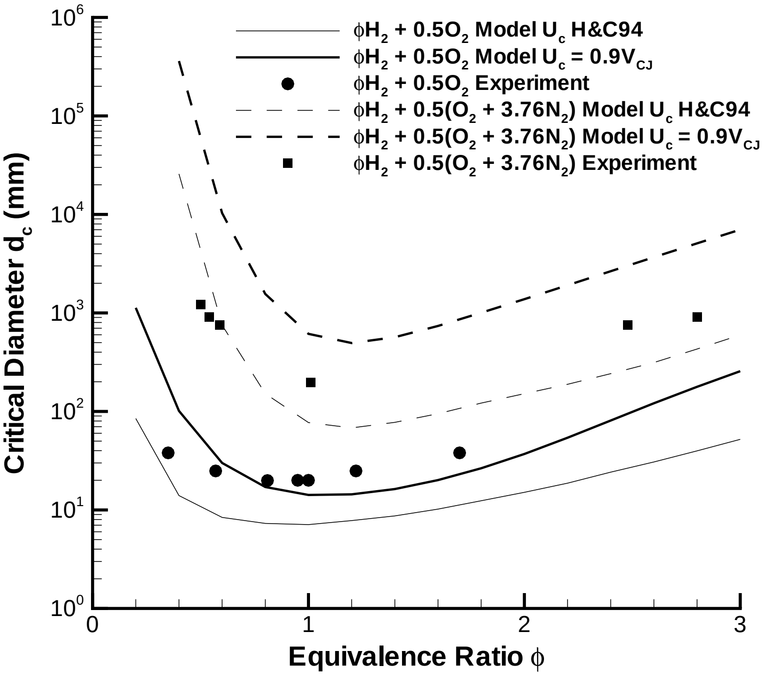

Figure 5.25 Critical diameter versus equivalence ratio model and experimental data for hydrogen-oxygen and hydrogen-air mixtures (P_1 = 100 kPa).

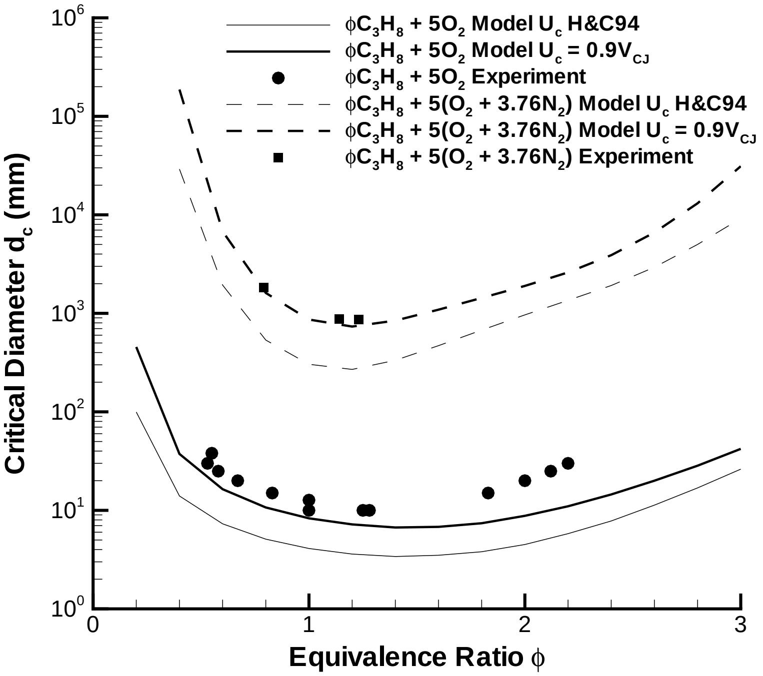

Figure 5.27 Critical diameter versus equivalence ratio model and experimental data for propane-oxygen and propane-air mixtures (P_1 = 100 kPa).

The experimental and analytical critical diffraction conditions for stoichiometric fuel-oxygen mixtures with varying initial pressure for hydrogen, ethylene, and propane fuels are presented in Figs. 5.28, 5.29, and 5.30, respectively. Experimental data do not exist for initial pressures much above atmospheric, and no data are available for fuel-air mixtures of varying initial pressure. Increasing initial pressure leads to a monotonic decrease in the critical diameter except for the hydrogen mixtures. The non-monotone behavior of the calculated critical diameter for hydrogen mixtures with 0.9 V_{CJ} critical shock velocity is related to similar reaction length (Section 4.2.1) and reaction time (Section 4.3.3) behavior with varying initial pressure. This is an artifact of the Konnov (1998) reaction mechanism because reaction time calculations with other mechanisms did not reproduce this behavior (Schultz and Shepherd 1999). With the noted exception of hydro-

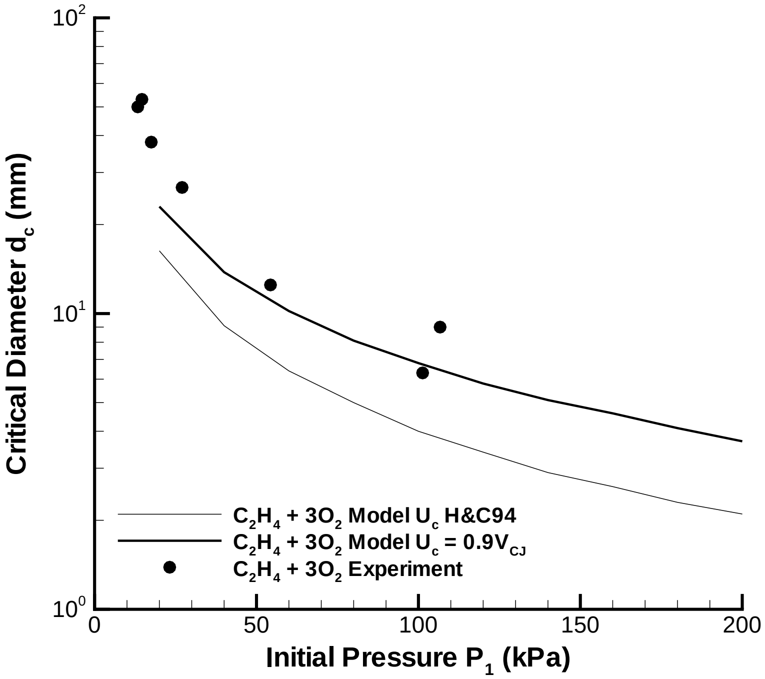

Figure 5.29 Critical diameter versus initial pressure model and experimental data for stoichiometric ethylene-oxygen and ethylene-air mixtures.

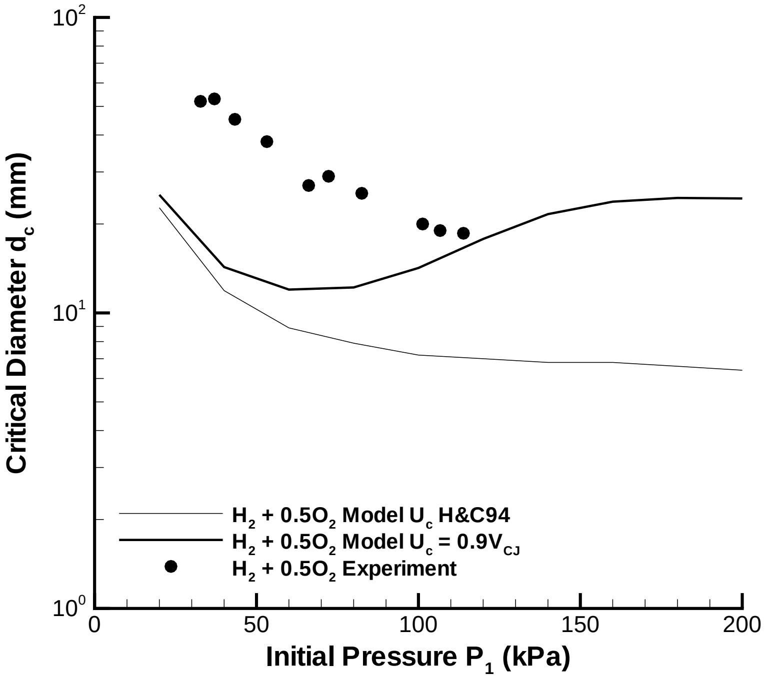

Figure 5.28 Critical diameter versus initial pressure model and experimental data for stoichiometric hydrogen-oxygen and hydrogen-air mixtures.

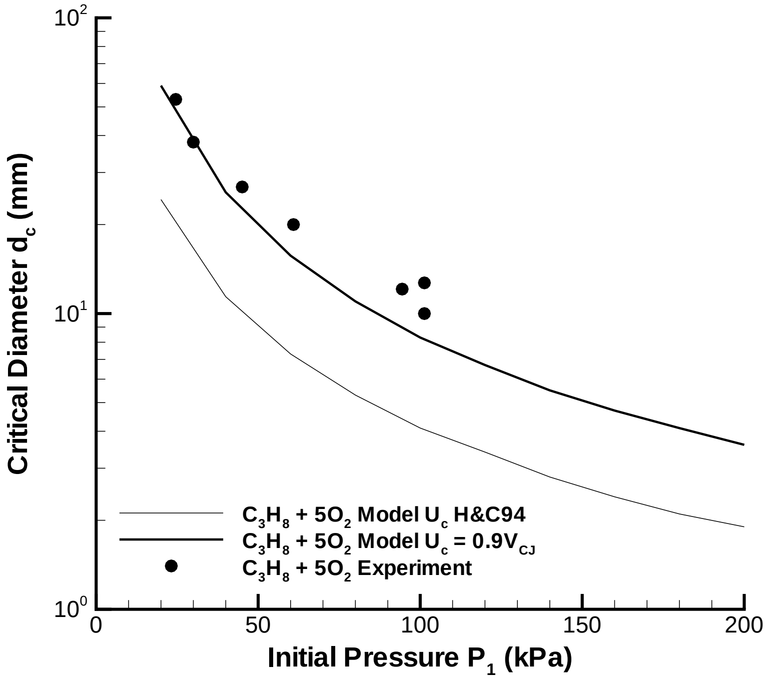

Figure 5.30 Critical diameter versus initial pressure model and experimental data for stoichiometric propane-oxygen and propane-air mixtures.

gen mixtures, the analytical model results are in qualitative agreement with the experimentally determined critical conditions; the level of quantitative agreement is considered below.

The experimental and analytical critical diffraction conditions for stoichiometric fuel-oxygen-nitrogen mixtures for hydrogen, ethylene, and propane fuels are presented in Figs. 5.31, 5.32, and 5.33, respectively. Note that the argon, carbon dioxide, and helium dilution data are not plotted here because of the limited experimental data for stoichiometric fuel-oxygen-diluent mixtures at 100kPa initial pressure. However, the calculated and experimental critical diameter data available are tabulated in Appendices A andF, respectively. Low concentration of argon and helium slightly reduces or has no appreciable effect on the critical diameter, which does not increase until significant levels (greater than

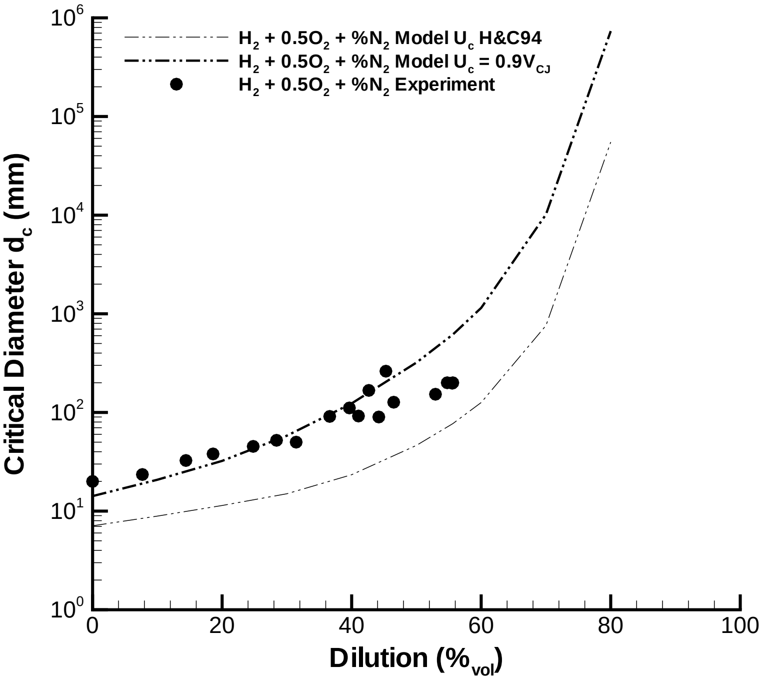

Figure 5.31 Critical diameter versus dilution model and experimental data for stoichiometric hydrogen-oxygen-nitrogen mixtures (P_1 = 100 kPa).

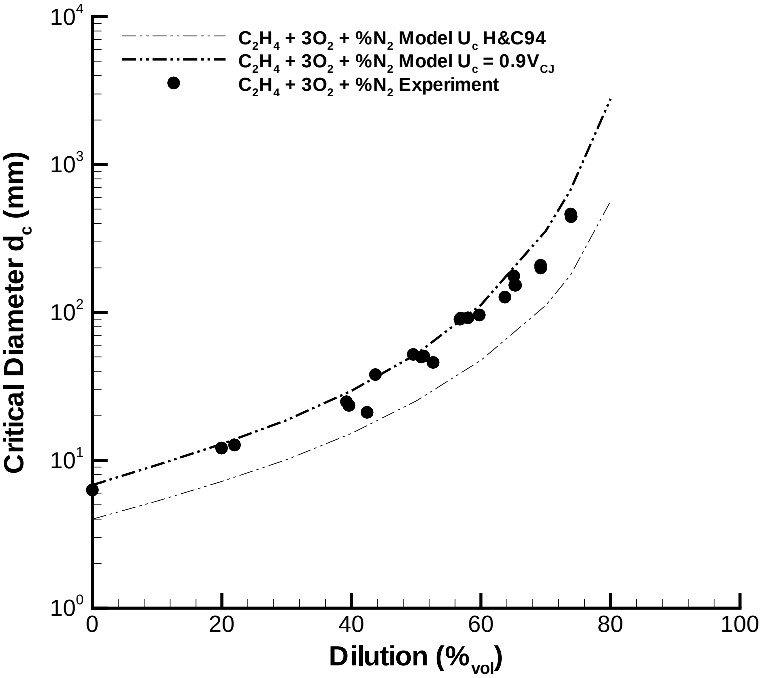

Figure 5.32 Critical diameter versus dilution model and experimental data for stoichiometric ethylene-oxygen-nitrogen mixtures (P_1 = 100 kPa).

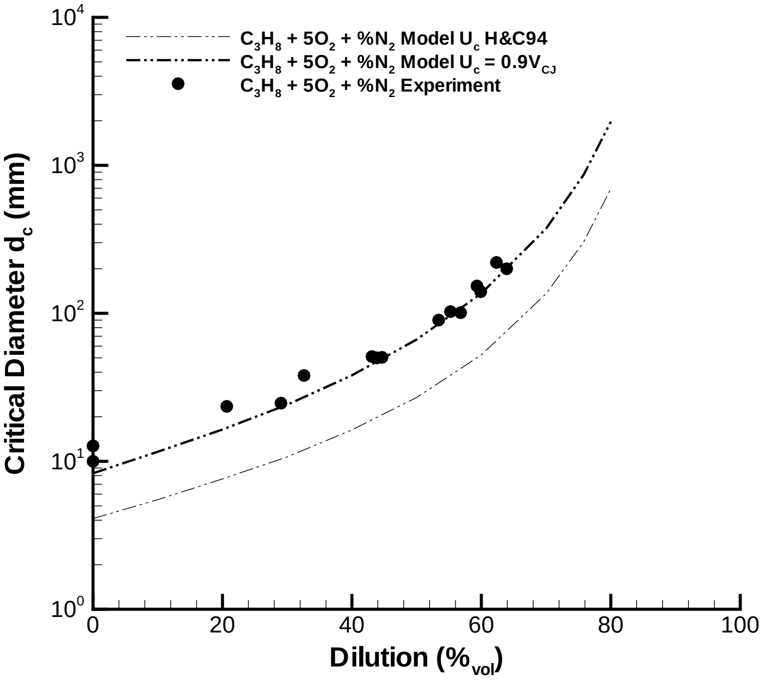

Figure 5.33 Critical diameter versus dilution model and experimental data for stoichiometric propane-oxygen-nitrogen mixtures (P_1 = 100 kPa).

60%) of dilution are reached (Appendices A and F). Carbon dioxide (Appendices A and F) and nitrogen (Figs .5.3 1 -5.33) dilution monotonically increase the critical diameter, with carbon dioxide having a much more pronounced effect. Once again, the analytical model results are in qualitative agreement with the experimentally determined critical conditions; the level of quantitative agreement is considered now.

Experimental critical diameter data are plotted versus values calculated with the critical shock velocity of He and Clavin (1994) in Fig. 5.34. The critical diffraction model evaluated with their analytical critical shock velocity expression underpredicts the experimental results in most cases, but the data collapses into banded form fairly well which lends support to the physical model. The experimental data are plotted versus critical

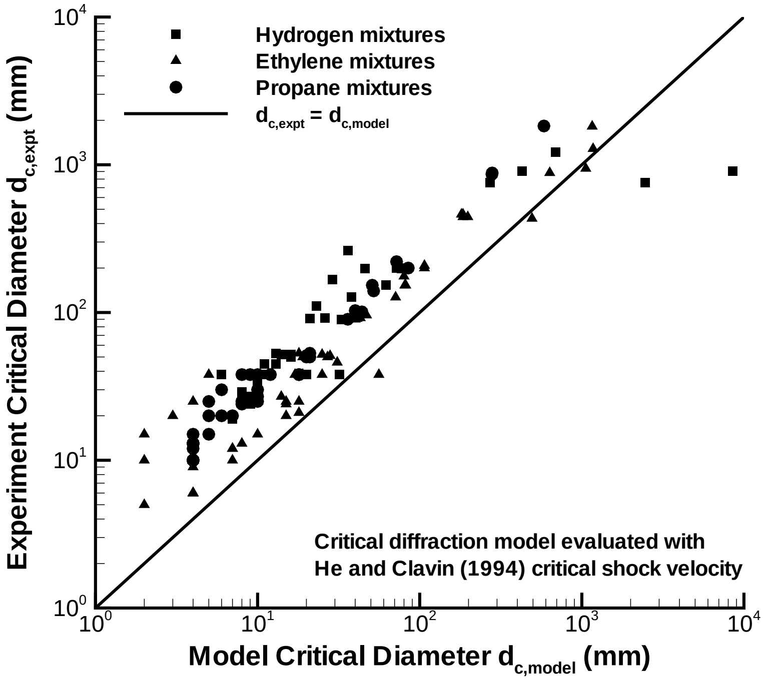

Figure 5.34 Experimental critical diameter versus model critical diameter evaluated with He and Clavin (1994) critical shock velocity.

diameters calculated with $0.9V_{CJ}$ critical shock velocity in Fig .5.35. The agreement between calculated and experimental values is substantially improved. However, the data do not collapse as well because the physical model is altered by imposing a critical shock velocity which is independent of the detailed chemistry important in the re-initiation process.

In order to obtain a quantitative measure of the discrepancy between the experimental critical conditions and critical diffraction model results, the experimental critical diameter values were compared to the calculated values through a logarithmic ratio

$$\log\left[\frac{d_{c,\,i,\,model}}{d_{c,\,i,\,\exp t}}\right]$$

The logarithmic ratio is zero when the calculated and experimental data are equal, nega-

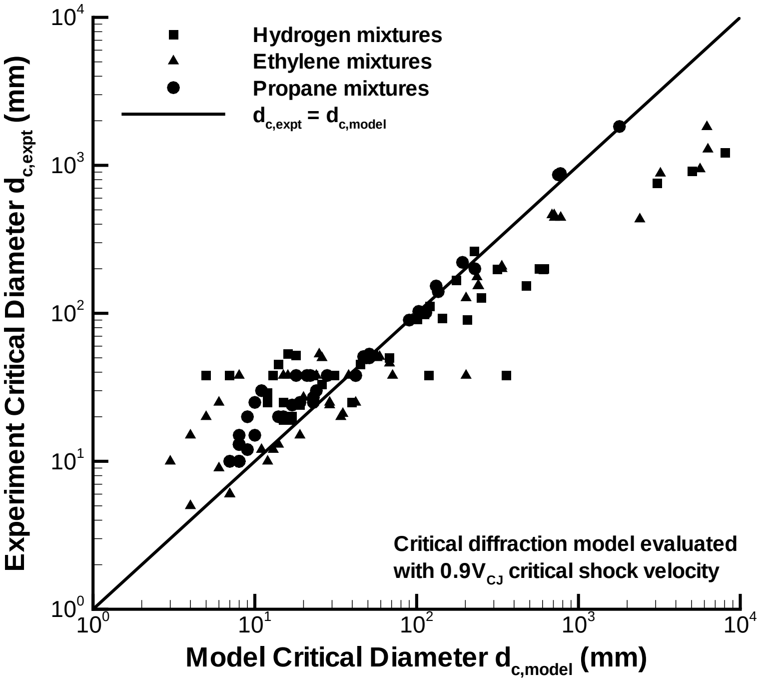

Figure 5.35 Experimental critical diameter versus model critical diameter evaluated with 0.9 V_{CJ} critical shock velocity.

tive when the model underpredicts the critical diameter, and positive for overpredicted values. Logarithmic ratios of ±0.3 correspond to calculated values within a factor of two of the experimental critical diameter. These ratios were averaged for a given mixture series of data and are presented in Table s5.1 and 5.2 for critical diameters evaluated with

Table 5.1: Logarithmic error between diffraction model evaluated with He and Clavin (1994) critical shock velocity and experimental critical diameter data.

Mixture Variable		Fuel		
		Hydrogen	Ethylene	Propane
Equivalence Ratio	Oxygen	-0.41	-0.66	-0.57
	Air	0.15	-0.15	-0.49
Initial Pressure	Oxygen	-0.49	-0.33	-0.41
	Air	No Expts	No Expts	No Expts

Table 5.1: Logarithmic error between diffraction model evaluated with He and Clavin (1994) critical shock velocity and experimental critical diameter data.

Mixture Variable		Fuel		
		Hydrogen	Ethylene	Propane
Dilution	Argon	-0.63	-0.35	-0.51
	Carbon Dioxide	-0.36	-0.19	-0.40
	Helium	-0.57	-0.35	-0.49
	Nitrogen	-0.53	-0.32	-0.42

$$\frac{1}{N}\sum_{i=1}^{N}\log\left[\frac{d_{c,\,i,\,model}}{d_{c,\,i,\,\exp t}}\right]$$

Table 5.2: Logarithmic error between diffraction model evaluated with $0.9V_{CJ}$ critical shock velocity and experimental critical diameter data.

Mixture Variable		Fuel		
		Hydrogen	Ethylene	Propane
Equivalence Ratio	Oxygen	0.06	-0.46	-0.28
	Air	1.23	0.53	-0.04
Initial Pressure	Oxygen	-0.26	-0.16	-0.08
	Air	No Expts	No Expts	No Expts
Dilution	Argon	-0.50	-0.18	-0.19
	Carbon Dioxide	0.17	0.15	-0.07
	Helium	-0.44	-0.17	-0.17
	Nitrogen	0.32	0.19	0.00

$$\frac{1}{N}\sum_{i=1}^{N}\log\left[\frac{d_{c,\,i,\,model}}{d_{c,\,i,\,\exp t}}\right]$$

the He and Clavin (1994) and $0.9V_{CJ}$ critical shock velocities, respectively. No comparison is possible for fuel-air mixtures with varying initial pressure because no experimental data exist. Also note that the comparisons for fuel-oxygen-diluent mixtures with argon, carbon dioxide, and helium dilution are based on few experimental data.

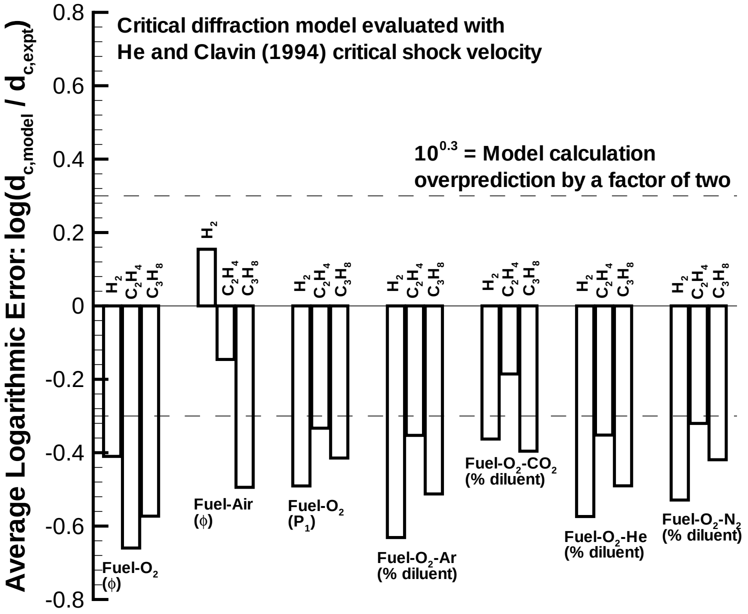

Figure 5.36 Logarithmic error between model evaluated with He and Clavin (1994) critical shock velocity and experimental critical diameter data.

The tabulated data are plotted in the corresponding bar charts of F ig.5.36 and 5.37, with factor of two agreement between calculated and experimental critical diameters indicated by the horizontal dashed lines. Critical diameters calculated with the He and Clavin (1994) critical shock velocity almost always underpredict the experimental results by more than a factor of two, with a maximum error of approximately a factor of four. In general, the critical diameter data calculated with $0.9V_{CJ}$ critical shock velocity are in better agreement with experimental results than the calculations with the He and Clavin (1994) critical shock velocity. Critical diameters calculated with the $0.9V_{CJ}$ critical shock velocity typically agree with the experimental results to within a factor of two, with the primary exception of hydrogen-air mixtures of varying equivalence ratio. This exception

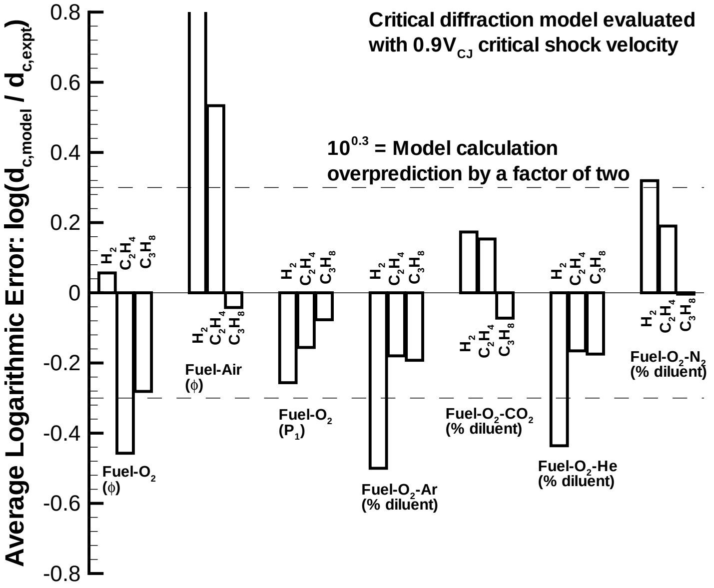

Figure 5.37 Logarithmic error between model evaluated with 0.9V_{CJ} critical shock velocity and experimental critical diameter data.

stems from the sensitivity of lean hydrogen-air conditions to the critical shock velocity (Figs. 5.25).

The selection of critical shock velocity at which to evaluate the diffraction model is clearly important, as the characteristic reaction time is highly sensitive to this parameter (Section 4.3.3). Unfortunately, the only analytical expression available for a critical shock velocity is that of He and Clavin (1994) which seems to underpredict the critical shock velocity based on the experimental observations discussed in Section 5.5, resulting in up to an average factor of four underprediction of the critical diameter. Insufficient experimental data of the shock decay along the tube axis exist with which to empirically determine critical shock velocities (Section 5.5). Fixed critical shock velocities of 0.8, 0.85, 0.9, and 0.9 5V_{CJ} were also used to calculate critical diameters. The critical diameters calculated with the imposed critical shock velocity of 0.9V_{CJ} exhibit the best overall agreement with the experimental critical diameters, especially in light of the other model uncertainties discussed below. However, the selection of this critical velocity is not rigorous and physically questionable because of the likelihood that the critical shock velocity varies with the chemical composition of these mixtures.

Other sources of model uncertainty exist in the calculated model parameters, aside from the approximations made in deriving the analytical expression (Eqn.3.46) itself.

$$d_c = 18\left(\frac{\gamma-1}{\gamma+1}\right)\left(\frac{U_c}{V_{CJ}}\right)^{\frac{2}{3}} U_c \tau\theta \tan\alpha \qquad (3.46)$$

Perfect gas behavior was assumed for analytical simplicity, and the specific heat ratio function in parentheses varies by an average of 20% depending on whether the pre-shock or post-shock state is chosen (Section 4.1.1). The CJ velocity is obtained through thermochemical equilibrium calculations (Section 4.1.2) and is within a few percent of the experimental data. Calculations of the disturbance propagation angle were found to be accurate to within 5%, corresponding to a 5% to 10% effect on the calculated critical diameter for disturbance propagation angles between 15° and 25°.

The reaction mechanism validation study summarized in Chapter 4 places confidence in calculated reaction times to within a factor of 2.5 for the post-shock temperature ranges found under most of the conditions considered, so this is a relatively large source of uncertainty. Some uncertainty also exists within the calculation of the effective activation energy parameters (Sections 4.3.1 and 4.3.4), with calculated parameters varying by 50% or more depending upon the reaction mechanism used (Schultz and Shepherd 1999). In addition, Schultz and Shepherd (1999) noted that effective activation energy parameters for hydrogen mixtures are very sensitive to the shock velocity perturbation used in the parameter calculation. Furthermore, there are insufficient experimental data with which to determine effective activation energies for comparison with calculated values.

The experimental measurements of critical diameter were found to be very well defined during this investigation, but there exists variation in the results obtained by different researchers. For example, there are experimental data for ethylene-air presented in Fig. 5.26 which vary by almost a factor of two for similar equivalence ratios and stoichiometric propane-oxygen data at atmospheric initial pressure (Fig.5.30) which differ by 30%. Some of the hydrogen-oxygen-nitrogen experimental data (Fig. 5.31) around 40% dilution also differ by up to a factor of two.

The calculated critical conditions are satisfactory given the uncertainties in the calculated parameters entering into the analytical expression for critical diameter, the discrepancies in experimental data between different researchers, and also the numerous simplifying assumptions required in the analytical derivation of the critical diffraction model. Recommendations for future work expected to improve the quantitative agreement between experimental and calculated data are presented in Chapter 7. The qualitative agreement between the model and experimental results indicates that detonation diffraction through an abrupt area expansion is dominated by a competition between energy release and the quenching effect of unsteadiness. The analytical model which has been derived and validated against experimental data provides a useful tool for engineering analysis situations in which the success or failure of a diffracting detonation must be considered. The observations of critical condition independence of divergence angle beyond a certain angular limit by Thomas et al. (1986) and Vasileev (1988) indicate that the critical diffraction model is applicable for divergence angles greater than approxi-

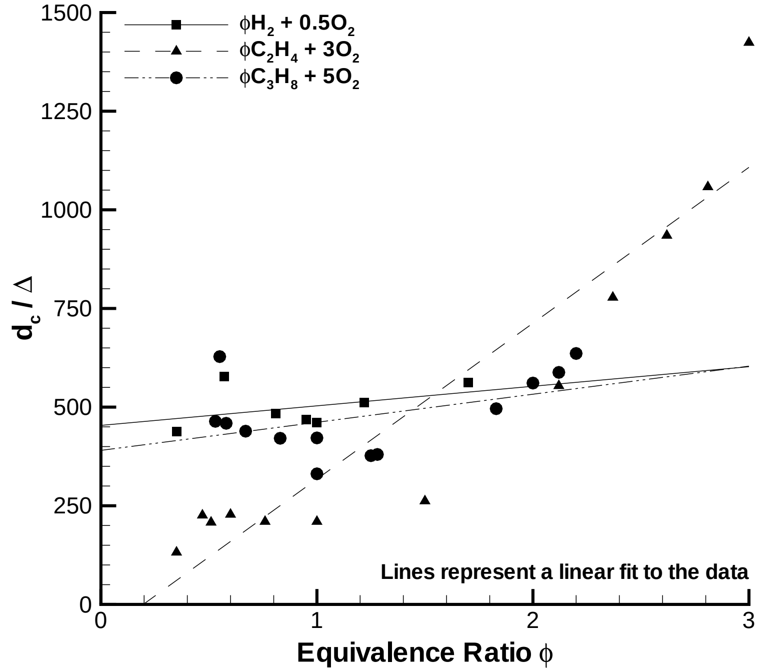

Figure 5.38 Critical diameter versus reaction length correlation for fuel-oxygen mixtures with varying equivalence ratio (P_1 = 100 kPa, T_1 = 295 K).

mately 50°. In addition, the experiments of Liu et al. (1984) suggest that calculated critical diameters can be applied to square, triangular, and elliptical tube and orifice geometries provided that the diameter is defined as the average of the circles inscribing and circumscribing the geometry.

5.9 Critical diameter correlation with reaction length

Several researchers have considered the correlation between the critical tube diameter and detonation reaction length with varying degrees of success in identifying a constant proportionality factor (Section 2.2.3). Ratios of experimental critical diameter to calculated detonation reaction length are plotted in Figs .5.38 - 5.43 for mixtures with varying equivalence ratio, initial pressure, and dilution. The detonation reaction length data are from Section 4.2.1.

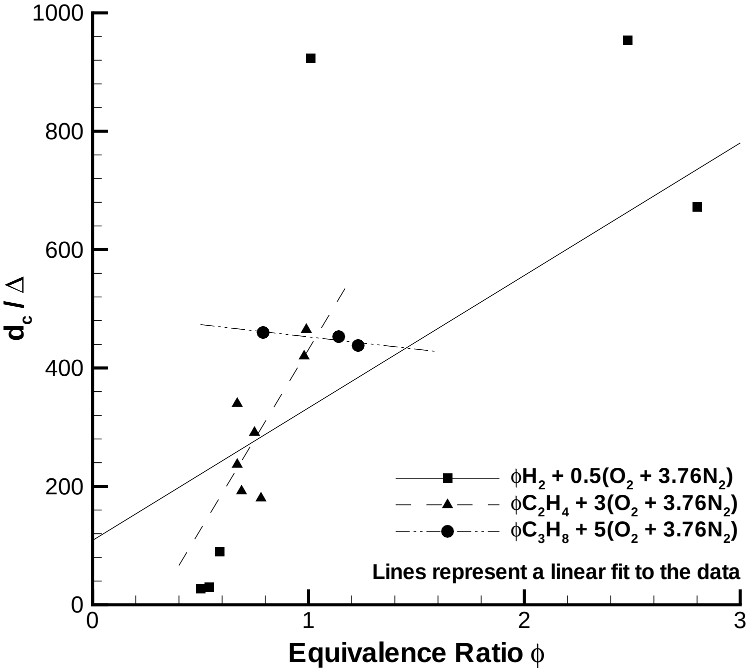

Figure 5.39 Critical diameter versus reaction length correlation for fuel-air mixtures with varying equivalence ratio (P_1 = 100 kPa, T_1 = 295 K).

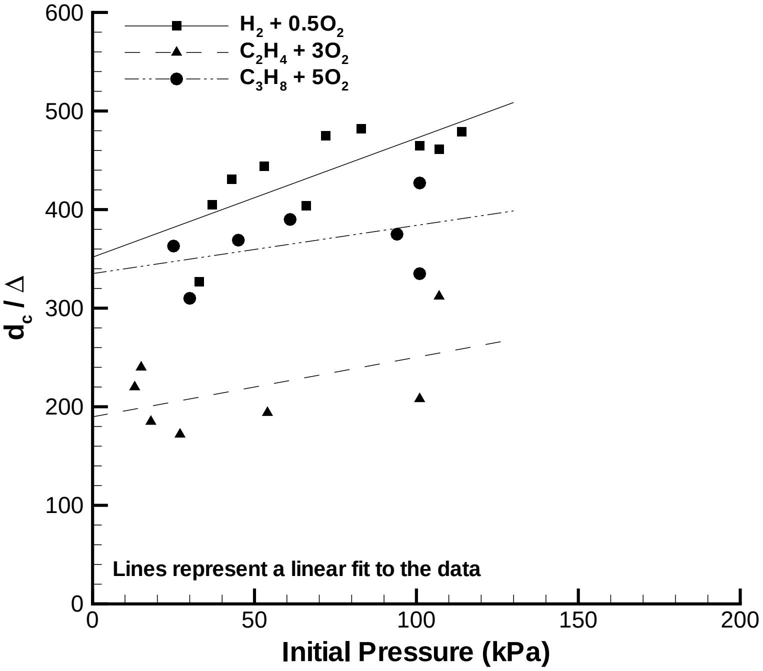

Figure 5.40 Critical diameter versus reaction length correlation for fuel-oxygen mixtures with varying initial pressure (T_1 = 295 K).

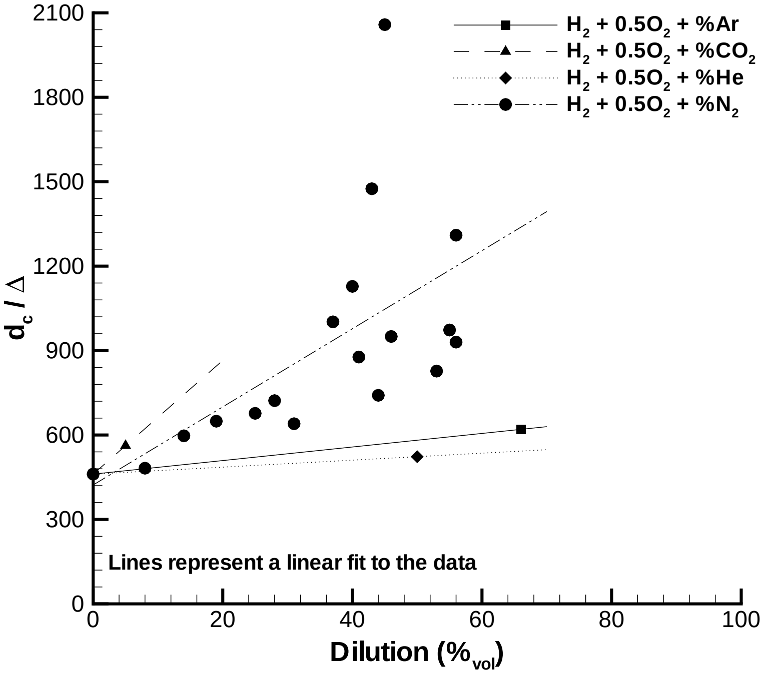

Figure 5.41 Critical diameter versus reaction length correlation for hydrogen mixtures with varying dilution (P_1 = 100 kPa, T_1 = 295 K).

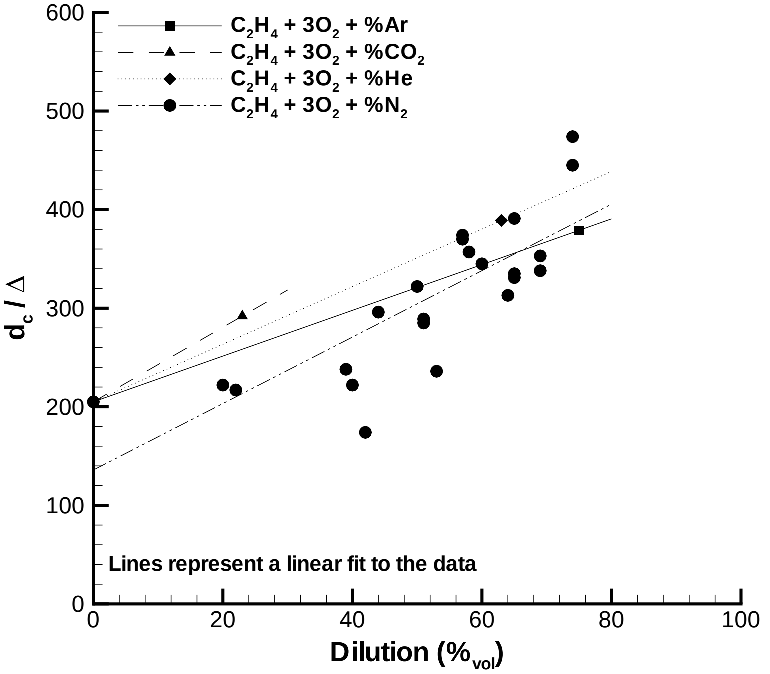

Figure 5.42 Critical diameter versus reaction length correlation for ethylene mixtures with varying dilution (P_1 = 100 kPa, T_1 = 295 K).

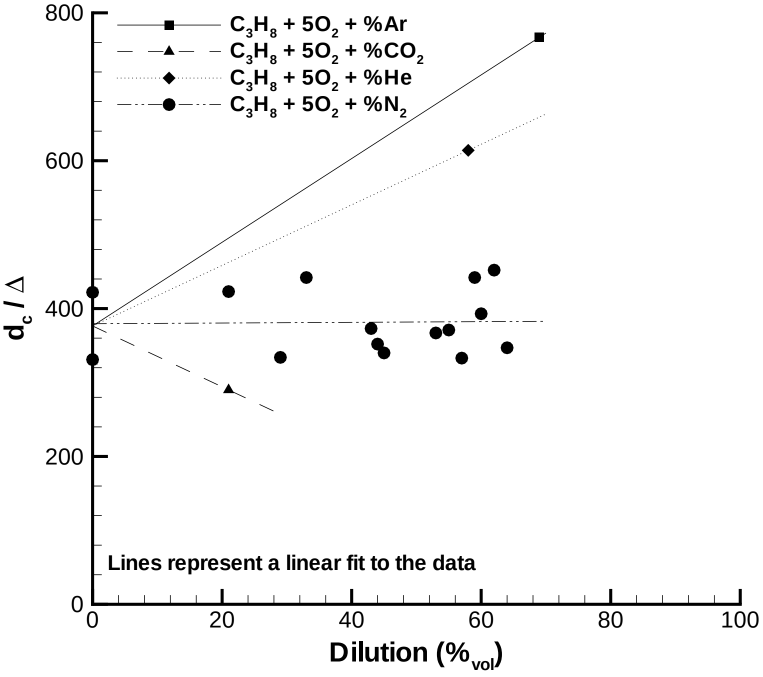

Figure 5.43 Critical diameter versus reaction length correlation for propane mixtures with varying dilution (P_1 = 100 kPa, T_1 = 295 K).

In general, the critical tube diameter can not be related to the reaction length by a single proportionality constant. Critical diameter to reaction length ratios for ethylene-oxygen mixtures with varying equivalence ratio vary by an order of magnitude (Fig. 5.38), as does the data for hydrogen-air mixtures (Fig. 5.39). The ratios increase by up to 40% with increasing initial pressure (Fig. 5.40). The experimental data are insufficient to assess trends for the hydrocarbon-air mixtures of varying equivalence ratio and fuel-oxygen-diluent mixtures of varying dilution other than nitrogen. Hydrogen-oxygen-nitrogen (Fig. 5.41) and ethylene-oxygen-nitrogen (Fig. 5.42) mixtures exhibit increasing critical diameter to reaction length ratios with increasing dilution, while the ratio is approximately constant around 400 for propane-oxygen-nitrogen mixtures (Fig. 5.43). This ratio is close to the constant proportionality factor of 380 identified by Westbrook (1982) and Westbrook and Urtiew (1982). In most cases, d_c / Δ lies between 100 and 1000 except for rich

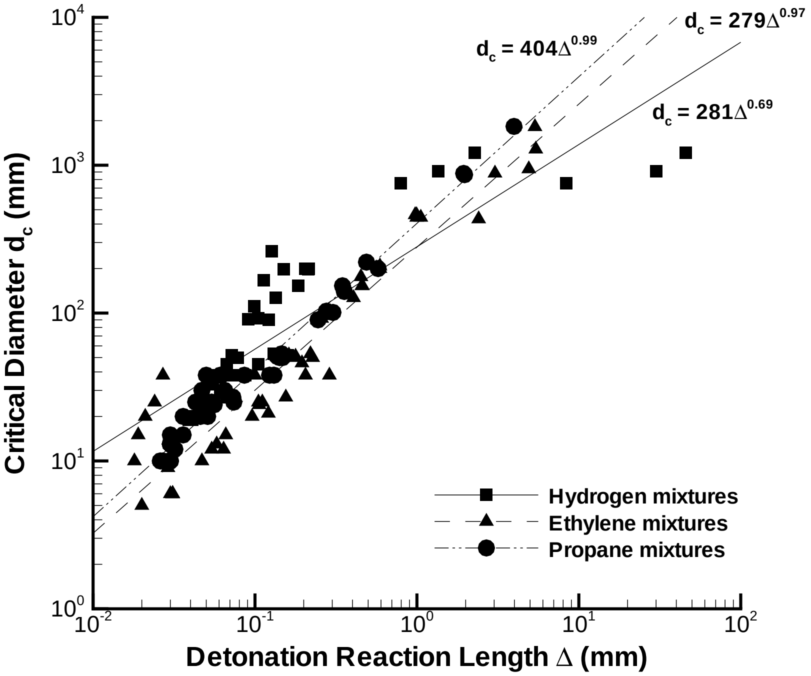

Figure 5.44 Experimental critical diameter versus detonation reaction length for all mixtures.

ethylene-air mixtures and hydrogen-oxygen-nitrogen mixtures with relatively high nitrogen dilution.

The experimental critical diameter data are plotted versus detonation reaction length for all mixtures with power law curve fits for each fuel in F ig.5.44. The hydrocarbon mixtures closely follow a linear proportionality between the critical diameter and reaction length, although with different proportionality constants. The hydrogen mixtures tend to follow a $d_c \sim \Delta^{0.7}$ power law. Variation in the proportionality constant and power in these curve fits further supports the conclusion that the ratio of critical diameter to reaction length is not a constant and the relation between the two is dependent upon the chemistry.

6 Conclusions

A comprehensive survey of the literature on detonation diffraction reveals an extensive degree of empirical work but no means by which the critical conditions can be calculated from first principles. In the present investigation, an analytical expression has been derived from a model of detonation diffraction through an abrupt area expansion which permits the calculation of critical conditions which separate the sub-critical and super-critical regimes. This critical diffraction model is based on the spherically symmetric reacting Euler equations in which the diffraction regime is governed by a competition between the sustaining effect of energy release and the quenching effect of unsteadiness. Assumptions regarding the unsteady expansion propagation into the detonation core and the shock decay along the tube axis after the critical time have been supported by computations and experiments. The parameters necessary for evaluation of the analytical expression were obtained with thermochemical equilibrium calculations, ZND detonation simulations, and constant-volume explosion simulations with validated detailed reaction mechanisms.

The critical diffraction conditions were calculated for fuel-oxygen and fuel-air mixtures with varying stoichiometry, initial pressure, and diluent type (argon, carbon dioxide, helium, nitrogen) and concentration for hydrogen, ethylene, and propane fuels. Results from the critical diffraction model were compared against experimentally-determined critical conditions for diffraction from a circular cross section and found to be in qualitative agreement. The quantitative agreement obtained is very sensitive to the critical shock velocity at which the diffraction model is evaluated. The analytical expression for critical shock velocity from He and Clavin (1994) results in underprediction of the critical diameter by up to a factor of four. Insufficient experimental data of the axial shock decay prior to re-initiation exist with which to empirically determine critical shock velocities. An arbitrary critical velocity of $0.9V_{CJ}$ resulted in critical diameter calculations which were typically within the uncertainty (factor of two) associated with the model parameters and simplifications made to facilitate derivation of an analytical model. Experimental results from other researchers support the validity of this model for divergence angles greater than approximately 50°, as well as extending the validity to square, triangular, and elliptical geometries in which the effective diameter is defined as the average of the inscribed and circumscribed circles. This critical diffraction model can readily be extended to systems of other chemical composition given an appropriate validated reaction mechanism.

7 Recommendations

The efforts of the present investigation can be augmented and extended in a number of ways. Additional experimental critical diameter data are necessary for adequate validation of the critical diffraction model for fuel-air mixtures of varying stoichiometry and initial pressure, and fuel-oxygen-diluent mixtures with dilution by argon, carbon dioxide, and helium. The model calculations could easily be extended to other chemical systems once appropriate detailed reaction mechanisms are validated. Candidate fuels for which adequate shock tube data exist to validate reaction mechanisms include acetylene, methane, and ethane. Streak camera visualization of the shock decay along the tube axis after the critical time would be useful to support the use of the Taylor-Sedov spherical strong blast decay solution in the critical diffraction model and assist the development of a new analytical expression for the critical shock velocity. The Taylor-Sedov solution could be augmented by the work of Korobeinikov (1991) in which the strong blast decay is modified by post-shock energy release as in Eckett et al. (2000). Numerical solutions of the differential equations which lead to the analytical model are possible at various levels of approximation, and could serve to improve predictions of the critical diffraction conditions as well as testing assumptions made in derivation of the analytical model.

Independence of the critical conditions on divergence angles greater than 50° is an interesting experimental observation which should be further investigated, perhaps leading to a generalization of the critical diffraction model presented here to cover less abrupt area expansions. Other diffraction geometries might also be an area to explore to further generalize the model. The basic notions of competition between energy release, unsteadiness, and curvature should still apply with modifications to accommodate unsteady expansion propagation in non-circular geometries. An improved understanding of detonation behavior as it propagates through a mixture gradient could extend the model to situations in which diffraction through an area expansion and a mixture gradient are encountered simultaneously. The existing model can provide bounds for these situations by considering the two cases of detonation diffraction through the most sensitive and least sensitive mixture present in the gradient.

The details of the mechanism by which a failing detonation wave re-initiates itself are not addressed by the critical diffraction model. This mechanism probably involves the detonation cellular structure and the interaction of transverse waves with unreacted mixture pockets which explode and strengthen the wave front such that the shock-reaction zone structure recouples. Given the spectrum of wavelengths which characterize the cellular structure of detonations and the lack of understanding of the importance of the spectrum characteristics in all detonation-related phenomena, it is obvious that future research efforts in this area will supplement detonation diffraction research.

One clue to a process playing a role in this mechanism might be found by considering the difference which has been identified in the critical diffraction conditions for argon and helium dilution as well as substantially different deflagration to detonation transition limits for these two monatomic diluents (Schultz et al. 1999). Planar laser induced fluorescence (PLIF), simultaneous PLIF-shadowgraph, or simultaneous chemiluminescence-shadowgraph visualization experiments will greatly assist in deducing decoupling and recoupling phenomena between the shocks and reaction zones. Analytical efforts in this area would form a logical sub-model for the present critical diffraction model, perhaps resulting in an accurate expression for the critical shock velocity, and would also lend insight to the problems of direct detonation initiation and deflagration to detonation transition. Confinement-induced re-initiations are also of scientific and practical interest to study and are directly related to detonation initiation by shock reflection and focusing.

Bibliography

Akbar R (1991) On the application of Whitham theory to gaseous detonations. Rensselaer Polytechnic Institute Master of Science Thesis.

Akbar R, Kaneshige M, Schultz E, Shepherd J (1997) Detonations in H_2-N_2O-CH_4-NH_3-O_2-N_2 mixtures. Graduate Aeronautical Laboratories of the California Institute of Technology Technical Report FM97-3.

Akbar R (1997) Mach reflection of gaseous detonations. Ph.D. Dissertation. Rensselaer Polytechnic Institute.

Bartlma F, Schroder K (1986) The diffraction of a plane detonation wave at a convex corner. Combustion and Flame, 66:237-248.

Bazhenova TV, Gvozdeva LG, Lobastov YS, Naboko IM, Nemkov RG, Predvoditeleva OA (1969) Shock waves in real gases. NASA Technical Translation TT-F-585, 109-113.

Bazhenova TV, Gvozdeva LG, Komarov VS, Suchov BG (1971) Diffraction of strong shock waves in a shock tube. Proceedings of the 8th International Shock Tube Symposium, Shock Tube Research, Chapman and Hall, London.

Bazhenova TV, Gvozdeva LG, Komarov VS, Suchov BG (1972) Pressure and temperature change in the wall surface in strong shock wave diffraction. Astronautica Acta, 17:659-666.

Bazhenova TV, Gvozdeva LG, Zhilin YuV (1979) Change in the shape of the diffracting shock wave at a convex corner. Acta Astronautica, 6:401-412.

Bdzil JB, Stewart DS (1986) Time-dependent two-dimensional detonation: the interaction of edge rarefactions with finite-length reaction zones. Journal of Fluid Mechanics, 171:1-26.

Bdzil JB, Stewart DS (1989) Modeling two-dimensional detonations with detonation shock dynamics. Physics of Fluids A, 1(7):1261-1267.

Benedick WB, Knystautas R, Lee JH (1984) Large scale experiments on the transmission of fuel-air detonations from two-dimensional channels. Progress in Astronautics and Aeronautics, 94:546-555.

Borisov AA, Mikhalkin VN (1989) Diffraction of a multifront detonation wave. Combustion, Explosions, and Shock Waves, 25(5):645-649.

Campbell AW, Engelke R (1976) The diameter effect in high density heterogeneous explosives. Proceedings of the 6th Detonation Symposium, 642-652.

Chester W (1953) The propagation of shock waves in a channel of non-uniform width. Quarterly Journal of Mechanics and Applied Mathematics, 6(4):440-452.

Chisnell RF (1957) The motion of a shock wave in a channel, with applications to cylindrical and spherical shock waves. Journal of Fluid Mechanics, 2:286-298.

Davies POAL, Guy TB (1971) Shock wave propagation in ducts with abrupt area expansions. Symposium on Internal Flows, University of Salford, D46-D52.

Deckker BEL, Gururaja J (1970) An investigation of shock wave behaviour in ducts with a gradual or sudden enlargement in cross-sectional area. Proceedings of the Institute of Mechanical Engineers, 184(3G):17-27.

Desbordes D, Vachon M (1986) Critical diameter of diffraction for strong plane detonations. Dynamics of Explosions, Progress in Astronautics and Aeronautics, 106:131-143.

Desbordes D (1988) Transmission of overdriven plane detonations: critical diameter as a function of cell regularity and size. Progress in Astronautics and Aeronautics, 114:170-185.

Desbordes D, Guerraud C, Hamada L, Presles HN (1993) Failure of the classical dynamic parameters relationships in highly regular cellular detonation systems. Progress in Astronautics and Aeronautics, 153:347-359.

Desbordes D (1995) Critical initiation conditions for gaseous diverging spherical detonations. Journal de Physique IV, 5(C4):155-162.

Dremin AN (1962) The critical detonation diameter of liquid explosives. Doklady Physical Chemistry 147:845-847.

Dremin AN, Tofimov VA (1965) On the nature of the critical diameter. 10th Combustion Symposium, 839-843.

Dumitrescu LZ, Predas (1975) Some new results concerning the diffraction of shock wave around a convex corner. Modern developments in shock tube research, Kyoto Japan, 369-377.

Eckett CA, Quirk JJ, Shepherd JE (1997) An analytical model for direct initiation of gaseous detonations. Proceedings of the 21st International Symposium on Shock Waves, Paper 2100.

Eckett CA, Quirk JJ, Shepherd JE (2000) The role of unsteadiness in direct initiation of gaseous detonations. Submitted to the Journal of Fluid Mechanics.

Edwards DH, Thomas GO, Nettleton MA (1979) The diffraction of a planar detonation wave at an abrupt area change. Journal of Fluid Mechanics, 95:79-96.

Edwards DH, Thomas GO, Nettleton MA (1981) Diffraction of a planar detonation in various fuel-oxygen mixtures at an area change. Progress in Astronautics and Aeronautics, 76:341-357.

Fickett W, Davis WC (1979) Detonation. University of California Press.

Freiwald H, Koch HW (1963) Spherical detonations of acetylene-oxygen-nitrogen mixtures as a function of nature and strength of initiation. 9th Combustion Symposium, 275-281.

Glassman I (1996) Combustion, 3rd ed. Academic Press.

Goldstein RJ, Kuehn TH (1996) Fluid Mechanics Measurements, 2nd edition. Taylor and Francis Publishers, Editor R. Goldstein, 7:451-508.

Gubin SA, Kogarko SM, Mikhalkin VN (1982) Experimental study of gas detonation in conical tubes. Combustion, Explosion, and Shock Waves, 18(5):592-597.

Guirao CH, Knystautas R, Lee J, Benedick W, Berman M (1982) Hydrogen-air detonations. 19th Symposium (International) on Combustion, 583-590.

Guy TB (1969) The propagation of shock waves in discontinuous ducts. PhD Thesis, University of Southampton.

Guy TB, Davies POAL (1970) The shape and strength distribution of blast waves. Journal of Sound and Vibration, 12:254-256.

Gvozdeva LG (1961) On the diffraction of a detonation wave. Prykladnaya Mekhanika, 33:731-739.

He L, Clavin P (1994) On the direct initiation of gaseous detonations by an energy source. Journal of Fluid Mechanics, 277:227-248.

Higgins AJ, Lee JHS (1998) A quantitative measurement of detonation wave irregularity. Combustion Institute Spring Technical Meeting, Canadian Section.

Higgins AJ (1999) Personal communication.

Hornung H (2000) Personal communication.

James DJ (1965) An investigation of the pressure wave propagated from the open end of a 30 x 18 in shock tube. United Kingdom Atomic Weapons Research Establishment Report Number 0-60/65.

Jones DA, Kemister G, Oran ES, Sichel M (1996) The influence of cellular structure on detonation transmission. Shock Waves, 6:119-129.

Jones DM, Moria P, Martin E, Thornhill CK (1951) A note on the pseudo-stationary flow behind a strong shock diffracted or reflected at a corner. Proceedings of the Royal Society A, 238-248.

Kahane A, Warren WR, Griffith WC, Marino AA (1954) A theoretical and experimental study of finite amplitude wave interactions with channels of varying area. Journal of the Aeronautical Sciences, 21(8):505-524.

Kaneshige M (1999) Detonation initiation by hypervelocity projectiles. Ph.D. Dissertation. Graduate Aeronautical Laboratories, California Institute of Technology.

Kee R, Rupley F, Miller J (1989) Chemkin II: A fortran chemical kinetics package for the analysis of gas-phase chemical kinetics. Sandia National Laboratory Technical Report SAND89-8009.

Knystautas R, Lee JH, Guirao CM (1982) The critical tube diameter for detonation failure in hydrocarbon-air mixtures. Combustion and Flame, 48:63-83.

Knystautas R, Guirao C, Lee JH, Sulmistras A (1984) Measurements of cell size in hydrocarbon-air mixtures and prediction of critical tube diameter, critical initiation energy, and detonability limits. Progress in Astronautics and Aeronautics, 94:23-37.

Konnov AA (1998) Detailed reaction mechanism for small hydrocarbons combustion. Release 0.4. http://homepages.vub.ac.be/~akonnov/

Korobeinikov VP (1968) Point explosion in a detonating gas. Soviet Phys Doklady 12:1003-1005.

Korobeinikov VP (1991) Problems of point-blast theory. American Institute of Physics.

Lee JH, Matsui H (1977) A comparison of the critical energies for direct initiation of spherical detonations in acetylene-oxygen mixtures. Combustion and Flame, 28:61-66.

Lee JHS, Knystautas R, Guirao C (1982) The link between cell size, critical tube diameter, initiation energy, and detonability limits. Fuel-Air Explosions, ed JHS Lee and C Guirao, University of Waterloo Press, 157-187.

Lee JHS (1984) Dynamic parameters of gaseous detonations. Annual Review of Fluid Mechanics, 16:311-336.

Lee JH (1996) On the critical diameter problem. Dynamics of Exothermicity, ed Bowen JR. Gordon and Breech Publishers, Netherlands. 321-336.

Li H, Ben-Dor G (1998) A modified CCW theory for detonation waves. Combustion and Flame, 113:1-12.

Lighthill MJ (1949) The diffraction of a blast. Proceedings of the Royal Society A, 198:454-470.

Liu YK, Lee JH, Knystautas R (1984) Effect of geometry on the transmission of detonation through an orifice. Combustion and Flame, 56:215-225.

Makris A, Oh TJ, Lee JHS, Knystautas R (1994) Critical diameter for the transmission of a detonation wave into a porous medium. 25th Combustion Symposium, 65-71.

Matsui H, Lee JH (1979) On the measure of the relative detonation hazards of gaseous fuel-oxygen and air mixtures. 17th Combustion Symposium, 1269-1280.

Mitrofanov VV, Soloukhin RI (1965) The diffraction of multifront detonation waves. Soviet Physics - Doklady, 9(12):1055-1058.

Moen IO, Donato M, Knystautas R, Lee JH (1981) The influence of confinement on the propagation of detonations near the detonability limits. 18th Combustion Symposium, 1615-1622.

Moen IO, Murray SB, Bjerketvedt D, Rinnan A, Knystautas R, Lee JH (1982) Diffraction of detonation from tubes into a large fuel-air explosive cloud. 19th Combustion Symposium, 635-644.

Moen IO, Funk JW, Ward SA, Rude GM, Thibault PA (1984a) Detonation length scales for fuel-air explosives. Progress in Astronautics and Aeronautics, 94:55-79.

Moen IO, Ward SA, Thibault PA, Lee JH, Knystautas R, Dean T, Westbrook CK (1984b) The influence of diluents and inhibitors on detonations. 20th Combustion Symposium, 1717-1726.

Moen IO, Sulmistras A, Thomas GO, Bjerketvedt D, Thibault PA (1986) Influence of cellular regularity on the behavior of gaseous detonations. Progress in Astronautics and Aeronautics, 106:220-243.

Murray SB, Lee JH (1983) On the transformation of planar detonation to cylindrical detonation. Combustion and Flame, 52:269-289.

Murray SB, Lee JH (1986) The influence of physical boundaries on gaseous detonation waves. Dynamics of Explosions, Progress in Astronautics and Aeronautics, 106:329-355.

Nettleton MA (1973) Shock attenuation in a gradual area expansion. Journal of Fluid Mechanics, 60(2):209-223.

Oppenheim AK, Soloukhin RI (1973) Experiments in gasdynamics of explosions. Annual Review of Fluid Mechanics, 5:31-58.

Oshima K, Sugaya K, Yamamoto M, Totoki T (1965) Diffraction of a plane shock wave around a corner. Institute of Space and Aeronautical Science, University of Tokyo, Report No 393, 51-82.

Pantow EG, Fischer M, Kratzel Th (1996) Decoupling and recoupling of detonation waves associated with sudden expansion. Shock Waves, 6:131-137.

Price D (1967) Contrasting patterns in the behavior of high explosives. 11th Combustion Symposium, 693-701.

Quirk JJ (1994) Godunov-type schemes applied to detonation flows. Combustion in High-Speed Flows, Kluwer Academic Publishers, 575-596.

Quirk JJ (1998a) Amrita: a computational facility for CFD modeling. 29th Computational Fluid Dynamics Lecture Series, ed H. Deconinck, von Karman Institute. Available at http://www.amrita-cfd.org/doc.

Quirk JJ (1998b) Amr_sol: design principles and practice. 29th Computational Fluid Dynamics Lecture Series, ed H. Deconinck, von Karman Institute. Available at http://www.amrita-cfd.org/doc.

Reynolds WC (1986) The element potential method for chemical equilibrium analysis: implementation in the interactive program STANJAN (3rd ed.). Mechanical Engineering Department, Stanford University.

Rinnan A (1982) Transmission of detonation through tubes and orifices. Fuel-Air Explosions, University of Waterloo Press, 553-564.

Schultz E, Shepherd J (1999) Validation of detailed reaction mechanisms for detonation simulation. Graduate Aeronautical Laboratories of the California Institute of Technology Technical Report FM99-5.

Schultz E, Wintenberger E, Shepherd J (1999) Investigation of deflagration to detonation transition for application to pulse detonation engine ignition systems. 36th JANNAF Combustion and Airbreathing Propulsion Subcommittees Meeting. Cocoa Beach, Florida.

Schultz E, Shepherd J (2000) Detonation diffraction through a mixture gradient. Graduate Aeronautical Laboratories of the California Institute of Technology Technical Report FM00-1.

Sedov LI (1959) Similarity and dimensional methods in mechanics, 4th edition. Academic Press.

Shampine LF, Watts HA (1979) DEPAC - Design of a user oriented package of ODE solvers. Sandia National Laboratory Technical Report SAND79-2374.

Shchelkin KI (1959) Two cases of unstable combustion. Soviet Phys JETP, 9:416.

Shepherd JE, Moen IO, Murray SB, Thibault PA (1986a) Analysis of the cellular structure of detonations. 21st Combustion Symposium, 1649-1658.

Shepherd JE (1986b) Chemical kinetics of hydrogen-air-diluent detonations. Progress in Astronautics and Aeronautics, 106:263-293.

Shepherd JE, Lee JHS (1992) On the transition from deflagration to detonation. Major Topics in Combustion, Springer-Verlag, 439-487.

Skews BW (1966) Profiles of diffracting shock waves. University of Witwatersrand, Department of Mechanical Engineering Report number 35.

Skews BW (1967a) The shape of a diffracting shock wave. Journal of Fluid Mechanics, 29:297-304.

Skews BW (1967b) The perturbed region behind a diffracting shock wave. Journal of Fluid Mechanics, 29:705-719.

Sloan SA, Nettleton MA (1975) A model for the axial decay of a shock wave in a large abrupt area change. Journal of Fluid Mechanics, 71:769-784.

Sloan SA, Nettleton MA (1978) A model for the decay of a wall shock in a large abrupt area change. Journal of Fluid Mechanics, 88:259-272.

Sochet I, Lamy T, Brossard J, Vaglio C, Cayzac R (1999) Critical tube diameter for detonation transmission and critical initiation energy of spherical detonation. Shock Waves, 9:113-123.

Soloukhin RI, Ragland KW (1969) Ignition processes in expanding detonations. Combustion and Flame, 13:295-302.

Strehlow RA (1968) Gas phase detonations: recent developments. Combustion and Flame, 12:81-101

Strehlow RA (1970) Multi-dimensional detonation wave structure. Astronautica Acta, 15:345-357.

Strehlow RA, Salm RJ (1976) The failure of marginal detonations in expanding channels. Acta Astronautica, 3:983-994.

Strehlow RA (1984) Combustion fundamentals. McGraw-Hill.

Sugimura (1995) Behavior of detonations passing through reflection nozzles. JSME International Journal B, 38(3):353-359.

Taylor GI (1950a) The formation of a blast wave by a very intense explosion 1: theoretical discussion. Proceedings of the Royal Society of London A, 201:159-174.

Taylor GI (1950b) The formation of a blast wave by a very intense explosion 2: the atomic explosion of 1945. Proceedings of the Royal Society of London A, 201:175-186.

Thibault PA (1985) Numerical modeling of transmission phenomena in gaseous detonations. Paper at the 11th IMACS World Congress on System Simulation and Scientific Computation, Oslo, Norway.

Thomas GO (1979) Gasdynamic studies of diverging detonations. PhD dissertation, University of Wales.

Thomas GO, Edwards DH, Lee JH, Knystautas R, Moen IO, Wei YM (1986) Detonation diffraction by divergent channels. Dynamics of Explosions, Progress in Astronautics and Aeronautics, 106:144-154.

Thompson PA (1988) Compressible-Fluid Dynamics. McGraw-Hill, New York. pp. 347-358.

Tyler LD (1968) Numerical results of blast wave propagation in tunnel intersections. Sandia Laboratory Report SC-RR-68-430.

Ungut A, Shuff PJ, Eyre JA (1984) Initiation of unconfined gaseous detonation by diffraction of a detonation front emerging from a pipe. Progress in Astronautics and Aeronautics, 94:523-545.

Urtiew PA (1975) From cellular structure to failure waves in liquid detonations. Combustion and Flame, 25:241-245.

Urtiew PA, Tarver CM (1981) Effects of cellular structure on the behavior of gaseous detonation waves under transient conditions. Progress in Astronautics and Aeronautics, 76:371-384.

Vasileev AA, Grigoriev VV (1980) Critical conditions for gas detonation in sharply expanding channels. Combustion, Explosion, and Shock Waves, 16:579-585.

Vasileev AA (1988) Diffraction of multifront detonation. Combustion, Explosions, and Shock Waves, 24(1):92-99.

Westbrook CK (1982) Chemical kinetics of hydrocarbon oxidation in gaseous detonations. Combustion and Flame, 46:191-210.

Westbrook CK, Urtiew PA (1982) Chemical kinetics prediction of critical parameters in gaseous detonations. 19th Combustion Symposium, 615-623.

Whitham GB (1957) A new approach to problems of shock dynamics: Part I, two-dimensional problems. Journal of Fluid Mechanics, 2:145-171.

Whitham GB (1959) A new approach to the problems of shock dynamics: Part II, three-dimensional problems. Journal of Fluid Mechanics, 5:369-386.

Yao J, Stewart DS (1995) On the normal shock velocity-curvature relationship for materials with large activation energy. Combustion and Flame, 100:519-528.

Zeldovich IaB, Kogarko SM, Simonov NN (1956) An experimental investigation of spherical detonation in gases. Soviet Phys Tech Phys, 1(8):1689-1713.

Zeldovich IB, Kompaneets AS (1960) Theory of Detonation. Academic Press, 185-191.

Appendix A: Calculated diffraction model parameters

The diffraction model parameters calculated in Chapter 4 are presented in the following tables along with the critical tube diameters calculated with Eqn. 3.46 and presented in Section 5.8.

Table A.1: Diffraction model parameters for hydrogen-oxygen mixtures with varying equivalence ratio (P_1 = 100 kPa).

						He and Clavin (1994) $U_c = V_{CJ}[1-(1/2\theta_{CJ})]$				$U_c = 0.9V_{CJ}$		
ϕ	γ	V_{CJ} (m/s)	Δ (mm)	α_{max} (°)	θ_{CJ}	U_c/V_{CJ}	τ (µs)	θ	d_c (mm)	τ (µs)	θ	d_c (mm)
0.2	1.403	1826	0.193	23.5	19.43	0.97	1.38	26.86	84.8	24.82	22.60	1126.8
0.4	1.403	2187	0.051	23.3	8.41	0.94	0.34	15.95	14.0	1.56	27.14	101.3
0.6	1.404	2447	0.042	23.3	7.13	0.93	0.24	12.38	8.4	0.53	21.13	30.0
0.8	1.404	2661	0.041	23.3	6.61	0.92	0.22	11.07	7.3	0.37	15.98	17.1
1	1.404	2842	0.043	23.3	6.39	0.92	0.21	10.42	7.1	0.33	13.96	14.2
1.2	1.404	2995	0.048	23.3	6.27	0.92	0.22	10.27	7.8	0.33	13.30	14.4
1.4	1.405	3125	0.054	23.4	6.30	0.92	0.24	10.24	8.7	0.36	13.35	16.3
1.6	1.405	3235	0.062	23.4	6.37	0.92	0.26	10.42	10.2	0.41	13.91	20.1
1.8	1.405	3329	0.073	23.4	6.48	0.92	0.30	10.82	12.4	0.48	14.95	26.5
2	1.405	3409	0.085	23.5	6.69	0.93	0.34	11.26	15.1	0.60	16.42	37.0
2.2	1.405	3478	0.100	23.5	6.94	0.93	0.39	11.82	18.7	0.77	18.26	54.1
2.4	1.405	3537	0.118	23.5	7.14	0.93	0.46	12.69	24.2	1.03	20.11	80.9
2.6	1.405	3588	0.140	23.6	7.49	0.93	0.54	13.53	30.7	1.41	21.52	121.1
2.8	1.405	3631	0.166	23.6	7.86	0.94	0.63	14.54	39.8	1.98	22.25	177.9
3	1.405	3669	0.198	23.7	8.29	0.94	0.76	15.68	52.1	2.80	22.42	256.4

Table A.2: Diffraction model parameters for hydrogen-air mixtures with varying equivalence ratio (P_1 = 100 kPa).

						He and Clavin (1994) $U_c = V_{CJ}[1-(1/2\theta_{CJ})]$				$U_c = 0.9V_{CJ}$		
ϕ	γ	V_{CJ} (m/s)	Δ (mm)	α_{max} (°)	θ_{CJ}	U_c/V_{CJ}	τ (μs)	θ	d_c (mm)	τ (μs)	θ	d_c (mm)
0.2	1.403	1164	171500.	25.0	27.52	0.98						
0.4	1.404	1491	91.730	24.2	22.46	0.98	583.35	22.68	25789.0	8737.17	24.32	360699.
0.6	1.404	1710	2.307	23.8	25.96	0.98	13.84	24.53	751.6	240.45	22.34	10307.1
0.8	1.404	1866	0.349	23.7	14.10	0.96	2.65	24.54	151.6	32.69	22.94	1557.2
1	1.405	1971	0.215	23.6	10.12	0.95	1.59	20.23	77.1	11.60	24.17	613.3
1.2	1.404	2034	0.201	23.6	9.57	0.95	1.45	19.16	68.1	9.03	24.30	494.9
1.4	1.405	2073	0.221	23.6	9.92	0.95	1.56	19.77	77.5	10.34	23.81	567.2
1.6	1.405	2102	0.259	23.7	10.70	0.95	1.78	20.76	94.9	13.57	23.23	737.8
1.8	1.405	2126	0.316	23.7	11.90	0.96	2.12	21.83	121.6	18.66	22.71	1005.4
2	1.404	2147	0.395	23.7	13.51	0.96	2.51	22.48	151.5	25.79	22.30	1379.4
2.2	1.405	2165	0.510	23.8	15.65	0.97	3.01	22.87	188.6	35.80	22.01	1910.4
2.4	1.405	2181	0.684	23.8	18.16	0.97	3.76	23.07	241.9	49.73	21.78	2652.2
2.6	1.405	2196	0.951	23.9	20.49	0.98	4.82	23.03	313.7	68.84	21.63	3679.7
2.8	1.405	2210	1.356	23.9	21.95	0.98	6.60	22.81	430.2	94.86	21.52	5086.5
3	1.405	2222	1.948	24.0	22.49	0.98	9.21	22.49	597.2	130.03	21.47	7009.6

Table A.3: Diffraction model parameters for stoichiometric hydrogen-oxygen mixtures with varying initial pressure.

						He and Clavin (1994) $U_c = V_{CJ}[1-(1/2\theta_{CJ})]$				$U_c = 0.9V_{CJ}$		
P_1 (kPa)	γ	V_{CJ} (m/s)	Δ (mm)	α_{max} (°)	θ_{CJ}	U_c/V_{CJ}	τ (μs)	θ	d_c (mm)	τ (μs)	θ	d_c (mm)
20	1.404	2753	0.241	23.4	5.45	0.91	1.11	6.67	22.7	1.22	6.82	25.1
40	1.404	2791	0.112	23.4	5.61	0.91	0.52	7.36	11.9	0.59	7.84	14.3
60	1.404	2814	0.072	23.3	5.84	0.91	0.34	8.29	8.9	0.42	9.24	12.0
80	1.404	2830	0.054	23.3	6.04	0.92	0.26	9.39	7.9	0.35	11.21	12.2
100	1.404	2842	0.043	23.3	6.38	0.92	0.21	10.46	7.2	0.33	13.96	14.2
120	1.404	2852	0.037	23.3	6.70	0.93	0.18	11.64	7.0	0.33	17.26	17.8
140	1.404	2861	0.032	23.3	7.06	0.93	0.16	12.79	6.8	0.35	19.58	21.6
160	1.404	2868	0.029	23.3	7.42	0.93	0.15	13.82	6.8	0.38	20.13	23.8
180	1.404	2875	0.026	23.3	7.81	0.94	0.14	14.59	6.6	0.39	19.77	24.5
200	1.404	2880	0.024	23.3	8.24	0.94	0.13	15.10	6.4	0.40	19.18	24.4

Table A.4: Diffraction model parameters for stoichiometric hydrogen-air mixtures with varying initial pressure.

						He and Clavin (1994) $U_c = V_{CJ}[1-(1/2\theta_{CJ})]$				$U_c = 0.9V_{CJ}$		
P_1 (kPa)	γ	V_{CJ} (m/s)	Δ (mm)	α_{max} (°)	θ_{CJ}	U_c/V_{CJ}	τ (μs)	θ	d_c (mm)	τ (μs)	θ	d_c (mm)
20	1.405	1935	0.840	23.7	6.32	0.92	5.29	7.99	94.5	7.03	8.87	134.2
40	1.405	1951	0.424	23.6	6.93	0.93	2.77	10.11	63.8	4.66	14.01	141.5
60	1.405	1960	0.299	23.6	7.73	0.94	2.04	13.15	62.4	5.93	27.83	359.1
80	1.405	1967	0.243	23.6	8.76	0.94	1.75	17.07	70.5	9.54	27.75	577.9
100	1.405	1971	0.215	23.6	10.12	0.95	1.59	20.23	77.1	11.60	24.17	613.3

Table A.4: Diffraction model parameters for stoichiometric hydrogen-air mixtures with varying initial pressure.

						He and Clavin (1994) $U_c = V_{CJ}[1-(1/2\theta_{CJ})]$				$U_c = 0.9V_{CJ}$		
P_1 (kPa)	γ	V_{CJ} (m/s)	Δ (mm)	α_{max} (°)	θ_{CJ}	U_c/V_{CJ}	τ (μs)	θ	d_c (mm)	τ (μs)	θ	d_c (mm)
120	1.405	1975	0.202	23.6	11.86	0.96	1.47	21.42	76.8	12.51	22.23	609.5
140	1.405	1978	0.200	23.6	13.96	0.96	1.36	21.29	71.3	12.83	21.05	592.6
160	1.405	1981	0.206	23.6	16.04	0.97	1.31	20.81	67.9	12.84	20.26	571.3
180	1.405	1984	0.216	23.6	17.48	0.97	1.29	20.15	65.0	12.67	19.68	548.4
200	1.405	1986	0.228	23.6	18.11	0.97	1.32	19.54	64.5	12.42	19.24	526.1

Table A.5: Diffraction model parameters for stoichiometric hydrogen-oxygen-argon mixtures with varying dilution (P_1 = 100 kPa).

						He and Clavin (1994) $U_c = V_{CJ}[1-(1/2\theta_{CJ})]$				$U_c = 0.9V_{CJ}$		
% diluent	γ	V_{CJ} (m/s)	Δ (mm)	α_{max} (°)	θ_{CJ}	U_c/V_{CJ}	τ (μs)	θ	d_c (mm)	τ (μs)	θ	d_c (mm)
0	1.404	2842	0.043	23.3	6.39	0.92	0.21	10.42	7.1	0.33	13.96	14.2
10	1.424	2567	0.039	23.5	5.82	0.91	0.20	8.84	5.4	0.25	10.06	7.4
20	1.441	2357	0.036	23.7	5.34	0.91	0.20	7.73	4.4	0.22	8.06	4.9
30	1.460	2190	0.035	24.0	5.09	0.90	0.20	6.84	3.7	0.20	6.97	3.9
40	1.484	2049	0.036	24.3	4.86	0.90	0.21	6.40	3.7	0.21	6.33	3.6
50	1.509	1926	0.040	24.7	4.69	0.89	0.25	6.02	4.0	0.23	5.89	3.7
60	1.537	1812	0.049	25.1	4.55	0.89	0.31	5.77	4.7	0.28	5.61	4.2
70	1.568	1694	0.068	25.6	4.66	0.89	0.43	5.63	6.5	0.40	5.52	6.0
80	1.603	1545	0.136	26.3	4.79	0.90	0.89	5.84	13.8	0.85	5.83	13.2

Table A.5: Diffraction model parameters for stoichiometric hydrogen-oxygen-argon mixtures with varying dilution (P_1 = 100 kPa).

						He and Clavin (1994) $U_c = V_{CJ}[1-(1/2\theta_{CJ})]$				$U_c = 0.9V_{CJ}$		
% diluent	γ	V_{CJ} (m/s)	Δ (mm)	α_{max} (°)	θ_{CJ}	U_c/V_{CJ}	τ (μs)	θ	d_c (mm)	τ (μs)	θ	d_c (mm)
90	1.643	1236	1.230	27.4	6.69	0.93	8.99	9.59	211.9	14.58	12.62	432.2

Table A.6: Diffraction model parameters for stoichiometric hydrogen-oxygen-carbon dioxide mixtures with varying dilution (P_1 = 100 kPa).

						He and Clavin (1994) $U_c = V_{CJ}[1-(1/2\theta_{CJ})]$				$U_c = 0.9V_{CJ}$		
% diluent	γ	V_{CJ} (m/s)	Δ (mm)	α_{max} (°)	θ_{CJ}	U_c/V_{CJ}	τ (μs)	θ	d_c (mm)	τ (μs)	θ	d_c (mm)
0	1.404	2842	0.043	23.3	6.39	0.92	0.21	10.42	7.1	0.33	13.96	14.2
10	1.391	2438	0.094	23.1	10.99	0.95	0.60	20.22	34.2	4.16	21.68	232.2
20	1.374	2137	0.591	23.0	20.62	0.98	3.33	20.25	166.5	34.58	19.81	1478.7
30	1.359	1900	4.117	22.9	18.95	0.97	26.73	19.08	1072.3	232.95	20.21	8679.8
40	1.349	1703	25.380	22.8	19.13	0.97	178.85	19.61	6415.4	1616.34	21.36	55383.2
50	1.337	1528	183.500	22.8	20.26	0.98	1403.83	20.86	46695.5	14066.4	23.17	454460.
60	1.326	1355	2323.000	22.8	22.44	0.98	18444.55	23.14	589945.5	235416.	26.13	7407106
70	1.316	1165	105000.0	23.0	26.67	0.98	876306.6	27.43	28211040			

Table A.7: Diffraction model parameters for stoichiometric hydrogen-oxygen-helium mixtures with varying dilution (P_1 = 100 kPa).

						He and Clavin (1994) $U_c = V_{CJ}[1-(1/2\theta_{CJ})]$				$U_c = 0.9V_{CJ}$		
% diluent	γ	V_{CJ} (m/s)	Δ (mm)	α_{max} (°)	θ_{CJ}	U_c/V_{CJ}	τ (μs)	θ	d_c (mm)	τ (μs)	θ	d_c (mm)
0	1.404	2842	0.043	23.3	6.39	0.92	0.21	10.42	7.1	0.33	13.96	14.2
10	1.421	2949	0.044	23.5	5.89	0.92	0.20	8.97	6.2	0.26	10.35	8.9
20	1.440	3065	0.047	23.7	5.52	0.91	0.20	7.95	5.8	0.22	8.50	7.0
30	1.462	3190	0.052	24.0	5.21	0.90	0.20	7.25	5.9	0.21	7.42	6.4
40	1.484	3325	0.059	24.3	4.99	0.90	0.22	6.72	6.4	0.22	6.71	6.4
50	1.509	3470	0.073	24.7	4.81	0.90	0.25	6.35	7.6	0.24	6.24	7.2
60	1.537	3620	0.097	25.1	4.73	0.89	0.31	6.11	10.0	0.29	5.96	9.3
70	1.568	3761	0.151	25.6	4.74	0.89	0.44	6.05	15.8	0.41	5.95	14.7
80	1.603	3826	0.336	26.3	5.04	0.90	0.89	6.39	37.6	0.90	6.48	38.4
90	1.642	3437	4.032	27.4	8.13	0.94	11.86	15.75	1307.8	57.78	28.85	10880.4

Table A.8: Diffraction model parameters for stoichiometric hydrogen-oxygen-nitrogen mixtures with varying dilution (P_1 = 100 kPa).

						He and Clavin (1994) $U_c = V_{CJ}[1-(1/2\theta_{CJ})]$				$U_c = 0.9V_{CJ}$		
% diluent	γ	V_{CJ} (m/s)	Δ (mm)	α_{max} (°)	θ_{CJ}	U_c/V_{CJ}	τ (μs)	θ	d_c (mm)	τ (μs)	θ	d_c (mm)
0	1.404	2842	0.043	23.3	6.39	0.92	0.21	10.42	7.1	0.33	13.96	14.2
10	1.405	2645	0.050	23.3	6.59	0.92	0.27	11.09	8.9	0.45	15.94	20.8
20	1.405	2475	0.060	23.4	6.84	0.93	0.34	11.79	11.4	0.65	18.37	32.3
30	1.404	2325	0.075	23.4	7.29	0.93	0.44	12.56	15.0	1.04	21.78	58.2

Table A.8: Diffraction model parameters for stoichiometric hydrogen-oxygen-nitrogen mixtures with varying dilution (P_1 = 100 kPa).

						He and Clavin (1994) $U_c = V_{CJ}[1-(1/2\theta_{CJ})]$				$U_c = 0.9V_{CJ}$		
% diluent	γ	V_{CJ} (m/s)	Δ (mm)	α_{max} (°)	θ_{CJ}	U_c/V_{CJ}	τ (μs)	θ	d_c (mm)	τ (μs)	θ	d_c (mm)
40	1.405	2188	0.099	23.5	7.79	0.94	0.64	14.22	23.4	2.05	25.03	123.6
50	1.405	2051	0.152	23.5	8.87	0.94	1.08	17.49	46.4	5.59	25.24	320.6
55.62	1.405	1971	0.215	23.6	10.12	0.95	1.59	20.23	77.1	11.68	24.16	617.2
60	1.404	1905	0.312	23.7	12.03	0.96	2.36	22.76	126.2	23.32	23.26	1149.6
70	1.404	1723	2.317	23.9	25.20	0.98	13.98	24.45	761.5	237.37	22.17	10172.4
80	1.404	1469	197.500	24.3	22.25	0.98	1269.11	22.51	55132.2	18060.8	24.19	734784.

Table A.9: Diffraction model parameters for ethylene-oxygen mixtures with varying equivalence ratio (P_1 = 100 kPa).

						He and Clavin (1994) $U_c = V_{CJ}[1-(1/2\theta_{CJ})]$				$U_c = 0.9V_{CJ}$		
ϕ	γ	V_{CJ} (m/s)	Δ (mm)	α_{max} (°)	θ_{CJ}	U_c/V_{CJ}	τ (μs)	θ	d_c (mm)	τ (μs)	θ	d_c (mm)
0.2	1.383	1719	0.749	23.2	11.82	0.96	5.78	13.73	157.5	22.19	16.38	650.7
0.4	1.369	1974	0.134	22.9	9.01	0.94	1.01	10.43	22.3	2.22	12.20	52.9
0.6	1.356	2138	0.066	22.7	8.38	0.94	0.48	9.22	9.7	0.90	10.57	19.3
0.8	1.346	2268	0.042	22.5	8.15	0.94	0.30	8.54	5.7	0.52	9.61	10.4
1	1.338	2376	0.031	22.5	8.02	0.94	0.22	8.14	4.0	0.36	8.95	6.8
1.2	1.330	2467	0.024	22.4	7.91	0.94	0.17	7.89	3.1	0.27	8.50	5.0
1.4	1.324	2543	0.021	22.4	7.81	0.94	0.14	7.71	2.6	0.22	8.19	4.0

Table A.9: Diffraction model parameters for ethylene-oxygen mixtures with varying equivalence ratio (P_1 = 100 kPa).

						He and Clavin (1994) $U_c = V_{CJ}[1-(1/2\theta_{CJ})]$				$U_c = 0.9V_{CJ}$		
ϕ	γ	V_{CJ} (m/s)	Δ (mm)	α_{max} (°)	θ_{CJ}	U_c/V_{CJ}	τ (μs)	θ	d_c (mm)	τ (μs)	θ	d_c (mm)
1.6	1.318	2604	0.019	22.3	7.72	0.94	0.13	7.56	2.3	0.20	8.00	3.5
1.8	1.312	2650	0.018	22.3	7.60	0.93	0.12	7.44	2.2	0.18	7.90	3.2
2	1.308	2682	0.018	22.3	7.50	0.93	0.12	7.34	2.1	0.18	7.94	3.2
2.2	1.303	2699	0.018	22.3	7.39	0.93	0.13	7.35	2.2	0.19	8.13	3.3
2.4	1.300	2703	0.019	22.3	7.24	0.93	0.14	7.46	2.4	0.20	8.50	3.7
2.6	1.296	2697	0.021	22.2	7.09	0.93	0.16	7.82	2.7	0.23	9.09	4.4
2.8	1.294	2682	0.023	22.2	6.92	0.93	0.18	8.50	3.4	0.27	9.86	5.6
3	1.291	2657	0.027	22.2	6.94	0.93	0.22	9.38	4.6	0.34	10.89	7.6

Table A.10: Diffraction model parameters for ethylene-air mixtures with varying equivalence ratio (P_1 = 100 kPa).

						He and Clavin (1994) $U_c = V_{CJ}[1-(1/2\theta_{CJ})]$				$U_c = 0.9V_{CJ}$		
ϕ	γ	V_{CJ} (m/s)	Δ (mm)	α_{max} (°)	θ_{CJ}	U_c/V_{CJ}	τ (μs)	θ	d_c (mm)	τ (μs)	θ	d_c (mm)
0.2	1.399	1119	121700.0	24.9	23.88	0.98	805254.7	24.61	29814103			
0.4	1.395	1423	149.000	24.0	18.09	0.97	1011.49	18.49	33622.1	7709.50	20.17	245783.
0.6	1.391	1623	7.271	23.7	15.45	0.97	48.25	16.64	1591.8	281.74	17.60	8708.8
0.8	1.387	1749	1.799	23.5	12.43	0.96	11.83	14.50	355.3	51.21	16.85	1606.8
1	1.384	1824	0.963	23.4	10.82	0.95	6.35	13.30	178.2	21.81	16.07	671.3
1.2	1.381	1868	0.724	23.3	10.08	0.95	4.78	12.85	130.5	14.63	15.62	443.8
1.4	1.377	1886	0.665	23.2	10.03	0.95	4.39	12.91	120.3	13.35	15.70	406.7

Table A.10: Diffraction model parameters for ethylene-air mixtures with varying equivalence ratio (P_1 = 100 kPa).

						He and Clavin (1994) $U_c = V_{CJ}[1-(1/2\theta_{CJ})]$				$U_c = 0.9V_{CJ}$		
ϕ	γ	V_{CJ} (m/s)	Δ (mm)	α_{max} (°)	θ_{CJ}	U_c/V_{CJ}	τ (μs)	θ	d_c (mm)	τ (μs)	θ	d_c (mm)
1.6	1.374	1887	0.703	23.2	10.55	0.95	4.59	13.36	129.6	15.21	16.14	472.0
1.8	1.372	1877	0.809	23.1	11.41	0.96	5.20	13.99	152.7	19.66	16.62	619.9
2	1.369	1862	0.983	23.1	12.44	0.96	6.36	14.79	195.6	27.13	16.94	858.1
2.2	1.366	1844	1.256	23.1	13.55	0.96	8.17	15.59	261.5	39.11	17.06	1223.3
2.4	1.363	1823	1.686	23.0	14.75	0.97	11.16	16.34	368.9	58.00	17.03	1776.3
2.6	1.361	1800	2.390	23.0	15.85	0.97	16.02	16.87	537.7	88.04	16.94	2626.4
2.8	1.359	1775	3.563	22.9	16.68	0.97	24.43	17.13	817.8	136.45	16.88	3973.1
3	1.356	1747	5.533	22.9	17.10	0.97	38.76	17.15	1270.3	215.49	16.90	6136.7

Table A.11: Diffraction model parameters for stoichiometric ethylene-oxygen mixtures with varying initial pressure.

						He and Clavin (1994) $U_c = V_{CJ}[1-(1/2\theta_{CJ})]$				$U_c = 0.9V_{CJ}$		
P_1 (kPa)	γ	V_{CJ} (m/s)	Δ (mm)	α_{max} (°)	θ_{CJ}	U_c/V_{CJ}	τ (μs)	θ	d_c (mm)	τ (μs)	θ	d_c (mm)
20	1.338	2299	0.192	22.5	6.82	0.93	1.28	5.87	16.3	1.65	6.73	23.0
40	1.338	2332	0.087	22.5	7.37	0.93	0.60	6.89	9.1	0.85	7.68	13.8
60	1.338	2351	0.055	22.5	7.67	0.93	0.38	7.48	6.4	0.58	8.26	10.2
80	1.338	2365	0.040	22.5	7.88	0.94	0.28	7.86	5.0	0.44	8.66	8.1
100	1.338	2376	0.031	22.5	8.01	0.94	0.22	8.14	4.0	0.35	8.95	6.8
120	1.338	2385	0.025	22.5	8.14	0.94	0.18	8.34	3.4	0.30	9.17	5.8
140	1.338	2393	0.021	22.5	8.24	0.94	0.15	8.52	2.9	0.25	9.33	5.1

Table A.11: Diffraction model parameters for stoichiometric ethylene-oxygen mixtures with varying initial pressure.

						He and Clavin (1994) $U_c = V_{CJ}[1-(1/2\theta_{CJ})]$				$U_c = 0.9V_{CJ}$		
P_1 (kPa)	γ	V_{CJ} (m/s)	Δ (mm)	α_{max} (°)	θ_{CJ}	U_c/V_{CJ}	τ (μs)	θ	d_c (mm)	τ (μs)	θ	d_c (mm)
160	1.338	2399	0.018	22.5	8.31	0.94	0.13	8.66	2.6	0.22	9.47	4.6
180	1.338	2405	0.016	22.5	8.38	0.94	0.11	8.77	2.3	0.20	9.59	4.1
200	1.338	2410	0.014	22.4	8.44	0.94	0.10	8.87	2.1	0.18	9.67	3.7

Table A.12: Diffraction model parameters for stoichiometric ethylene-air mixtures with varying initial pressure.

						He and Clavin (1994) $U_c = V_{CJ}[1-(1/2\theta_{CJ})]$				$U_c = 0.9V_{CJ}$		
P_1 (kPa)	γ	V_{CJ} (m/s)	Δ (mm)	α_{max} (°)	θ_{CJ}	U_c/V_{CJ}	τ (μs)	θ	d_c (mm)	τ (μs)	θ	d_c (mm)
20	1.384	1792	3.394	23.4	8.74	0.94	23.14	12.32	581.0	58.52	15.99	1765.5
40	1.384	1807	1.907	23.4	9.57	0.95	12.81	12.82	340.2	38.01	16.71	1207.0
60	1.384	1815	1.397	23.4	10.12	0.95	9.31	13.09	254.7	29.95	16.67	952.5
80	1.384	1821	1.127	23.4	10.51	0.95	7.46	13.22	207.4	25.06	16.37	785.0
100	1.384	1825	0.959	23.4	10.80	0.95	6.35	13.30	178.2	21.67	16.05	666.9
120	1.384	1828	0.841	23.4	11.02	0.95	5.54	13.32	156.4	19.13	15.76	579.0
140	1.384	1831	0.752	23.4	11.18	0.96	4.89	13.28	137.9	17.12	15.51	510.6
160	1.384	1834	0.684	23.3	11.30	0.96	4.44	13.27	125.4	15.52	15.29	456.8
180	1.384	1836	0.627	23.3	11.40	0.96	4.06	13.25	114.6	14.19	15.12	413.3
200	1.384	1838	0.581	23.3	11.46	0.96	3.76	13.21	106.0	13.07	14.96	377.0

Table A.13: Diffraction model parameters for stoichiometric ethylene-oxygen-argon mixtures with varying dilution (P_1 = 100 kPa).

						He and Clavin (1994) $U_c = V_{CJ}[1-(1/2\theta_{CJ})]$				$U_c = 0.9V_{CJ}$		
% diluent	γ	V_{CJ} (m/s)	Δ (mm)	α_{max} (°)	θ_{CJ}	U_c/V_{CJ}	τ (μs)	θ	d_c (mm)	τ (μs)	θ	d_c (mm)
0	1.338	2376	0.031	22.5	8.02	0.94	0.22	8.14	4.0	0.36	8.95	6.8
10	1.355	2296	0.033	22.6	7.96	0.94	0.22	7.91	4.1	0.36	8.50	6.6
20	1.375	2216	0.035	22.8	7.90	0.94	0.23	7.70	4.2	0.37	8.05	6.6
30	1.398	2137	0.038	23.0	7.86	0.94	0.25	7.56	4.5	0.38	7.66	6.7
40	1.424	2056	0.042	23.3	7.82	0.94	0.27	7.47	4.9	0.41	7.33	7.0
50	1.453	1974	0.048	23.6	7.69	0.94	0.30	7.40	5.6	0.45	7.10	7.8
60	1.486	1888	0.057	24.1	7.67	0.93	0.35	7.35	6.8	0.53	6.94	9.1
70	1.524	1794	0.076	24.6	7.66	0.93	0.45	7.26	8.9	0.68	6.78	11.9
80	1.570	1681	0.125	25.3	7.54	0.93	0.72	7.09	14.5	1.09	6.53	18.9
90	1.622	1493	0.460	26.4	7.26	0.93	2.53	6.44	45.7	3.65	6.95	67.4

Table A.14: Diffraction model parameters for stoichiometric ethylene-oxygen-carbon dioxide mixtures with varying dilution (P_1 = 100 kPa).

						He and Clavin (1994) $U_c = V_{CJ}[1-(1/2\theta_{CJ})]$				$U_c = 0.9V_{CJ}$		
% diluent	γ	V_{CJ} (m/s)	Δ (mm)	α_{max} (°)	θ_{CJ}	U_c/V_{CJ}	τ (μs)	θ	d_c (mm)	τ (μs)	θ	d_c (mm)
0	1.338	2376	0.031	22.5	8.02	0.94	0.22	8.14	4.0	0.36	8.95	6.8
10	1.332	2228	0.052	22.4	8.24	0.94	0.40	9.46	8.1	0.75	10.98	16.2
20	1.326	2083	0.099	22.4	9.36	0.95	0.83	11.28	18.5	1.96	13.02	46.2
30	1.321	1945	0.223	22.3	11.38	0.96	1.92	12.92	45.8	6.08	14.50	147.0

Table A.14: Diffraction model parameters for stoichiometric ethylene-oxygen-carbon dioxide mixtures with varying dilution (P_1 = 100 kPa).

						He and Clavin (1994) $U_c = V_{CJ}[1-(1/2\theta_{CJ})]$				$U_c = 0.9V_{CJ}$		
% diluent	γ	V_{CJ} (m/s)	Δ (mm)	α_{max} (°)	θ_{CJ}	U_c/V_{CJ}	τ (μs)	θ	d_c (mm)	τ (μs)	θ	d_c (mm)
40	1.315	1811	0.644	22.3	13.34	0.96	5.71	14.29	139.4	22.52	15.60	537.2
50	1.311	1679	2.355	22.3	14.73	0.97	21.73	15.38	526.1	99.64	16.82	2344.1
60	1.306	1544	11.680	22.3	15.99	0.97	111.97	16.70	2685.0	607.26	18.53	14294.4
70	1.302	1395	101.700	22.4	18.03	0.97	1003.44	18.82	24417.1	6962.40	20.97	166046.
80	1.297	1200	4280.000	22.6	22.00	0.98	42735.30	22.60	1079179.	425358.	24.66	10214168

Table A.15: Diffraction model parameters for stoichiometric ethylene-oxygen-helium mixtures with varying dilution (P_1 = 100 kPa).

						He and Clavin (1994) $U_c = V_{CJ}[1-(1/2\theta_{CJ})]$				$U_c = 0.9V_{CJ}$		
% diluent	γ	V_{CJ} (m/s)	Δ (mm)	α_{max} (°)	θ_{CJ}	U_c/V_{CJ}	τ (μs)	θ	d_c (mm)	τ (μs)	θ	d_c (mm)
0	1.338	2376	0.031	22.5	8.02	0.94	0.22	8.14	4.0	0.36	8.95	6.8
10	1.355	2437	0.034	22.6	7.98	0.94	0.22	7.95	4.4	0.36	8.55	7.1
20	1.375	2508	0.039	22.8	7.93	0.94	0.23	7.79	4.8	0.37	8.17	7.6
30	1.398	2590	0.045	23.0	7.88	0.94	0.24	7.67	5.5	0.38	7.83	8.3
40	1.424	2690	0.054	23.3	7.83	0.94	0.26	7.59	6.5	0.41	7.55	9.5
50	1.453	2810	0.067	23.6	7.77	0.94	0.29	7.54	8.0	0.45	7.36	11.4
60	1.486	2959	0.088	24.1	7.69	0.93	0.34	7.48	10.5	0.52	7.22	14.8
70	1.524	3148	0.128	24.6	7.64	0.93	0.43	7.41	15.4	0.67	7.13	21.5
80	1.569	3386	0.237	25.3	7.56	0.93	0.69	7.29	28.6	1.05	7.00	39.5

Table A.15: Diffraction model parameters for stoichiometric ethylene-oxygen-helium mixtures with varying dilution (P_1 = 100 kPa).

						He and Clavin (1994) $U_c = V_{CJ}[1-(1/2\theta_{CJ})]$				$U_c = 0.9V_{CJ}$		
% diluent	γ	V_{CJ} (m/s)	Δ (mm)	α_{max} (°)	θ_{CJ}	U_c/V_{CJ}	τ (μs)	θ	d_c (mm)	τ (μs)	θ	d_c (mm)
90	1.623	3603	1.020	26.4	7.38	0.93	2.43	7.39	122.3	3.75	7.92	190.2

Table A.16: Diffraction model parameters for stoichiometric ethylene-oxygen-nitrogen mixtures with varying dilution (P_1 = 100 kPa).

						He and Clavin (1994) $U_c = V_{CJ}[1-(1/2\theta_{CJ})]$				$U_c = 0.9V_{CJ}$		
% diluent	γ	V_{CJ} (m/s)	Δ (mm)	α_{max} (°)	θ_{CJ}	U_c/V_{CJ}	τ (μs)	θ	d_c (mm)	τ (μs)	θ	d_c (mm)
0	1.338	2376	0.031	22.5	8.02	0.94	0.22	8.14	4.0	0.36	8.95	6.8
10	1.343	2317	0.041	22.5	7.95	0.94	0.28	8.24	5.3	0.47	9.29	9.3
20	1.349	2259	0.054	22.6	7.87	0.94	0.38	8.41	7.2	0.63	9.69	12.9
30	1.355	2198	0.075	22.7	7.78	0.94	0.52	8.72	10.1	0.88	10.21	18.7
40	1.361	2132	0.107	22.8	7.74	0.94	0.74	9.23	15.2	1.31	10.91	29.5
50	1.368	2060	0.164	22.9	7.82	0.94	1.16	9.99	25.2	2.15	11.85	52.2
60	1.375	1977	0.282	23.1	8.29	0.94	2.00	11.03	47.5	4.25	13.19	112.5
70	1.381	1874	0.617	23.3	9.78	0.95	4.20	12.48	111.6	12.04	15.15	355.6
73.82	1.385	1824	0.963	23.4	10.82	0.95	6.35	13.30	178.5	21.81	16.07	672.5
80	1.388	1723	2.853	23.5	13.30	0.96	17.95	15.27	564.8	87.61	17.23	2782.7

Table A.17: Diffraction model parameters for propane-oxygen mixtures with varying equivalence ratio (P_1 = 100 kPa).

						He and Clavin (1994) $U_c = V_{CJ}[1-(1/2\theta_{CJ})]$				$U_c = 0.9V_{CJ}$		
ϕ	γ	V_{CJ} (m/s)	Δ (mm)	α_{max} (°)	θ_{CJ}	U_c/V_{CJ}	τ (μs)	θ	d_c (mm)	τ (μs)	θ	d_c (mm)
0.2	1.369	1692	0.542	23.2	13.55	0.96	3.54	14.74	99.6	16.05	16.62	455.7
0.4	1.344	1958	0.091	22.9	10.52	0.95	0.60	11.62	14.0	1.60	12.79	37.4
0.6	1.323	2123	0.050	22.7	9.80	0.95	0.33	10.69	7.3	0.77	11.49	16.4
0.8	1.306	2253	0.037	22.5	9.58	0.95	0.24	10.30	5.1	0.53	10.90	10.7
1	1.291	2361	0.030	22.5	9.54	0.95	0.20	10.14	4.1	0.42	10.59	8.3
1.2	1.279	2449	0.027	22.4	9.58	0.95	0.18	10.08	3.6	0.37	10.43	7.2
1.4	1.269	2520	0.026	22.4	9.68	0.95	0.17	10.09	3.4	0.35	10.34	6.7
1.6	1.259	2571	0.026	22.3	9.82	0.95	0.17	10.13	3.5	0.36	10.29	6.8
1.8	1.251	2602	0.029	22.3	9.96	0.95	0.19	10.18	3.8	0.40	10.25	7.4
2	1.244	2612	0.036	22.3	10.14	0.95	0.23	10.23	4.5	0.49	10.18	8.8
2.2	1.237	2603	0.047	22.2	10.22	0.95	0.30	10.21	5.8	0.64	10.05	11.0
2.4	1.231	2576	0.067	22.2	10.26	0.95	0.43	10.14	7.8	0.90	9.85	14.5
2.6	1.226	2532	0.103	22.1	10.20	0.95	0.66	9.94	11.3	1.33	9.55	20.0
2.8	1.221	2471	0.167	22.1	9.99	0.95	1.07	9.59	16.9	2.06	9.16	28.4
3	1.217	2394	0.285	22.1	9.61	0.95	1.84	9.12	26.2	3.33	8.84	42.1

Table A.18: Diffraction model parameters for propane-air mixtures with varying equivalence ratio (P_1 = 100 kPa).

						He and Clavin (1994) $U_c = V_{CJ}[1\text{-}(1/2\theta_{CJ})]$				$U_c = 0.9V_{CJ}$		
ϕ	γ	V_{CJ} (m/s)	Δ (mm)	α_{max} (°)	θ_{CJ}	U_c/V_{CJ}	τ (μs)	θ	d_c (mm)	τ (μs)	θ	d_c (mm)
0.2	1.396	1091	134900.0	25.0	26.51	0.98	875313.7	27.25	34981461			
0.4	1.389	1388	173.000	24.1	15.70	0.97	1020.28	16.55	29104.8	6049.78	20.28	187252.
0.6	1.382	1588	13.340	23.7	13.69	0.96	74.68	13.72	1935.6	281.81	14.28	6787.8
0.8	1.375	1722	3.637	23.5	13.06	0.96	20.49	13.10	535.4	69.91	12.91	1611.0
1	1.370	1801	2.072	23.4	12.67	0.96	11.64	12.78	304.0	37.78	12.49	865.1
1.2	1.364	1836	1.889	23.3	12.52	0.96	10.50	12.55	269.6	32.90	12.15	734.3
1.4	1.358	1834	2.427	23.2	12.41	0.96	13.50	12.30	333.7	40.03	11.68	844.1
1.6	1.353	1813	3.629	23.2	12.23	0.96	20.17	11.91	469.9	55.89	11.09	1089.7
1.8	1.348	1785	5.674	23.2	11.90	0.96	31.40	11.35	676.1	80.07	10.48	1433.8
2	1.343	1752	8.958	23.1	11.39	0.96	49.48	10.64	964.4	114.55	10.01	1898.4
2.2	1.338	1716	14.080	23.1	10.71	0.95	77.63	9.91	1355.0	163.92	9.93	2603.0
2.4	1.333	1676	21.800	23.1	9.93	0.95	120.48	9.44	1916.5	239.98	10.53	3893.3
2.6	1.329	1633	32.920	23.1	9.27	0.95	187.71	9.71	2937.6	372.12	11.98	6613.0
2.8	1.326	1586	49.450	23.0	9.10	0.95	295.06	10.96	5004.4	641.25	14.32	13095.0
3	1.321	1536	76.020	23.0	9.93	0.95	476.60	12.94	9197.1	1303.20	17.52	31128.8

Table A.19: Diffraction model parameters for stoichiometric propane-oxygen mixtures with varying initial pressure.

						He and Clavin (1994) $U_c = V_{CJ}[1-(1/2\theta_{CJ})]$				$U_c = 0.9V_{CJ}$		
P_1 (kPa)	γ	V_{CJ} (m/s)	Δ (mm)	α_{max} (°)	θ_{CJ}	U_c/V_{CJ}	τ (μs)	θ	d_c (mm)	τ (μs)	θ	d_c (mm)
20	1.291	2288	0.166	22.5	10.52	0.95	1.07	11.32	24.3	2.70	12.04	59.0
40	1.291	2319	0.080	22.5	10.13	0.95	0.52	10.84	11.4	1.22	11.43	25.7
60	1.291	2337	0.052	22.5	9.87	0.95	0.34	10.54	7.3	0.76	11.05	15.7
80	1.291	2351	0.038	22.5	9.68	0.95	0.25	10.31	5.3	0.55	10.79	11.0
100	1.291	2361	0.030	22.5	9.54	0.95	0.20	10.14	4.1	0.42	10.59	8.3
120	1.291	2369	0.025	22.4	9.42	0.95	0.16	10.00	3.4	0.34	10.44	6.7
140	1.291	2376	0.021	22.4	9.32	0.95	0.14	9.89	2.8	0.28	10.33	5.5
160	1.291	2382	0.018	22.4	9.24	0.95	0.12	9.80	2.4	0.24	10.23	4.7
180	1.291	2387	0.016	22.4	9.17	0.95	0.11	9.72	2.1	0.21	10.15	4.1
200	1.291	2392	0.014	22.4	9.12	0.95	0.10	9.64	1.9	0.19	10.09	3.6

Table A.20: Diffraction model parameters for stoichiometric propane-air mixtures with varying initial pressure.

						He and Clavin (1994) $U_c = V_{CJ}[1-(1/2\theta_{CJ})]$				$U_c = 0.9V_{CJ}$		
P_1 (kPa)	γ	V_{CJ} (m/s)	Δ (mm)	α_{max} (°)	θ_{CJ}	U_c/V_{CJ}	τ (μs)	θ	d_c (mm)	τ (μs)	θ	d_c (mm)
20	1.370	1772	9.009	23.4	14.16	0.96	52.78	14.56	1560.7	222.79	14.44	5817.1
40	1.370	1785	4.823	23.4	13.62	0.96	27.94	13.87	789.8	105.71	13.52	2600.0
60	1.370	1792	3.332	23.4	13.22	0.96	19.11	13.40	522.7	67.43	13.02	1603.0
80	1.370	1797	2.551	23.4	12.92	0.96	14.39	13.04	383.3	48.67	12.70	1131.6
100	1.370	1801	2.071	23.4	12.67	0.96	11.64	12.78	304.0	37.78	12.49	865.1

Table A.20: Diffraction model parameters for stoichiometric propane-air mixtures with varying initial pressure.

						He and Clavin (1994) $U_c = V_{CJ}[1-(1/2\theta_{CJ})]$				$U_c = 0.9V_{CJ}$		
P_1 (kPa)	γ	V_{CJ} (m/s)	Δ (mm)	α_{max} (°)	θ_{CJ}	U_c/V_{CJ}	τ (μs)	θ	d_c (mm)	τ (μs)	θ	d_c (mm)
120	1.370	1804	1.745	23.4	12.47	0.96	9.73	12.58	250.1	30.72	12.33	695.4
140	1.370	1807	1.507	23.4	12.30	0.96	8.41	12.39	212.8	25.77	12.23	578.9
160	1.370	1809	1.328	23.3	12.15	0.96	7.39	12.25	185.0	22.17	12.13	494.5
180	1.370	1811	1.186	23.3	12.03	0.96	6.52	12.13	161.6	19.40	12.07	430.9
200	1.370	1813	1.072	23.3	11.92	0.96	5.87	12.03	144.4	17.23	12.00	381.1

Table A.21: Diffraction model parameters for stoichiometric propane-oxygen-argon mixtures with varying dilution (P_1 = 100 kPa).

						He and Clavin (1994) $U_c = V_{CJ}[1-(1/2\theta_{CJ})]$				$U_c = 0.9V_{CJ}$		
% diluent	γ	V_{CJ} (m/s)	Δ (mm)	α_{max} (°)	θ_{CJ}	U_c/V_{CJ}	τ (μs)	θ	d_c (mm)	τ (μs)	θ	d_c (mm)
0	1.291	2361	0.030	22.5	9.54	0.95	0.20	10.14	4.1	0.42	10.59	8.3
10	1.310	2286	0.031	22.6	9.51	0.95	0.21	10.17	4.4	0.44	10.66	8.9
20	1.329	2211	0.033	22.8	9.48	0.95	0.21	10.18	4.6	0.45	10.73	9.6
30	1.353	2134	0.034	23.0	9.41	0.95	0.22	10.19	4.9	0.47	10.80	10.4
40	1.379	2056	0.036	23.2	9.33	0.95	0.23	10.19	5.3	0.49	10.87	11.3
50	1.409	1975	0.038	23.5	9.21	0.95	0.24	10.16	5.8	0.52	10.95	12.7
60	1.445	1889	0.042	23.9	9.04	0.94	0.26	10.16	6.7	0.58	11.01	14.7
70	1.489	1795	0.050	24.5	8.92	0.94	0.32	10.16	8.4	0.70	11.12	18.8
80	1.540	1681	0.074	25.2	8.88	0.94	0.47	10.38	13.4	1.08	11.50	31.5

Table A.21: Diffraction model parameters for stoichiometric propane-oxygen-argon mixtures with varying dilution (P_1 = 100 kPa).

						He and Clavin (1994) $U_c = V_{CJ}[1-(1/2\theta_{CJ})]$				$U_c = 0.9V_{CJ}$		
% diluent	γ	V_{CJ} (m/s)	Δ (mm)	α_{max} (°)	θ_{CJ}	U_c/V_{CJ}	τ (μs)	θ	d_c (mm)	τ (μs)	θ	d_c (mm)
90	1.605	1494	0.299	26.3	10.35	0.95	1.76	11.81	58.9	5.48	13.19	187.1

Table A.22: Diffraction model parameters for stoichiometric propane-oxygen-carbon dioxide mixtures with varying dilution (P_1 = 100 kPa).

						He and Clavin (1994) $U_c = V_{CJ}[1-(1/2\theta_{CJ})]$				$U_c = 0.9V_{CJ}$		
% diluent	γ	V_{CJ} (m/s)	Δ (mm)	α_{max} (°)	θ_{CJ}	U_c/V_{CJ}	τ (μs)	θ	d_c (mm)	τ (μs)	θ	d_c (mm)
0	1.291	2361	0.030	22.5	9.54	0.95	0.20	10.14	4.1	0.42	10.59	8.3
10	1.291	2224	0.056	22.4	10.05	0.95	0.38	10.53	7.7	0.86	10.93	16.6
20	1.291	2092	0.113	22.4	10.54	0.95	0.80	10.92	15.8	1.91	11.29	35.5
30	1.291	1961	0.253	22.3	11.00	0.95	1.86	11.31	35.8	4.67	11.74	84.6
40	1.290	1831	0.643	22.3	11.45	0.96	4.90	11.74	91.5	13.05	12.41	232.6
50	1.290	1701	1.922	22.3	11.93	0.96	15.25	12.35	279.0	43.89	13.46	788.7
60	1.289	1565	7.353	22.3	12.62	0.96	60.61	13.32	1103.0	200.60	15.43	3793.2
70	1.289	1413	44.340	22.4	14.19	0.96	388.56	15.61	7553.4	1801.81	19.88	39737.2
80	1.289	1215	1106.000	22.6	21.14	0.98	10609.42	22.74	265562.7	115320.	26.46	2933615

Table A.23: Diffraction model parameters for stoichiometric propane-oxygen-helium mixtures with varying dilution (P_1 = 100 kPa).

						He and Clavin (1994) $U_c = V_{CJ}[1-(1/2\theta_{CJ})]$				$U_c = 0.9V_{CJ}$		
% diluent	γ	V_{CJ} (m/s)	Δ (mm)	α_{max} (°)	θ_{CJ}	U_c/V_{CJ}	τ (μs)	θ	d_c (mm)	τ (μs)	θ	d_c (mm)
0	1.291	2361	0.030	22.5	9.54	0.95	0.20	10.14	4.1	0.42	10.59	8.3
10	1.309	2415	0.033	22.6	9.50	0.95	0.20	10.14	4.6	0.43	10.63	9.4
20	1.329	2478	0.036	22.8	9.44	0.95	0.21	10.13	5.1	0.45	10.68	10.6
30	1.352	2553	0.040	23.0	9.39	0.95	0.22	10.13	5.8	0.46	10.72	12.2
40	1.378	2644	0.046	23.2	9.28	0.95	0.23	10.11	6.7	0.48	10.77	14.2
50	1.409	2755	0.053	23.5	9.20	0.95	0.24	10.08	8.0	0.52	10.81	17.1
60	1.445	2894	0.065	23.9	9.03	0.94	0.26	10.06	10.1	0.57	10.86	21.8
70	1.488	3075	0.086	24.5	8.81	0.94	0.32	10.10	14.4	0.69	10.99	31.2
80	1.540	3308	0.145	25.2	8.88	0.94	0.47	10.32	26.2	1.07	11.35	60.4
90	1.605	3540	0.709	26.3	10.38	0.95	1.73	11.75	136.5	5.38	13.01	428.7

Table A.24: Diffraction model parameters for stoichiometric propane-oxygen-nitrogen mixtures with varying dilution (P_1 = 100 kPa).

						He and Clavin (1994) $U_c = V_{CJ}[1-(1/2\theta_{CJ})]$				$U_c = 0.9V_{CJ}$		
% diluent	γ	V_{CJ} (m/s)	Δ (mm)	α_{max} (°)	θ_{CJ}	U_c/V_{CJ}	τ (μs)	θ	d_c (mm)	τ (μs)	θ	d_c (mm)
0	1.291	2361	0.030	22.5	9.54	0.95	0.20	10.14	4.1	0.42	10.59	8.3
10	1.300	2306	0.040	22.5	9.75	0.95	0.26	10.34	5.5	0.57	10.79	11.6
20	1.309	2252	0.054	22.6	9.98	0.95	0.35	10.56	7.6	0.79	10.99	16.4
30	1.318	2195	0.076	22.7	10.24	0.95	0.48	10.80	10.7	1.13	11.22	24.1

Table A.24: Diffraction model parameters for stoichiometric propane-oxygen-nitrogen mixtures with varying dilution (P_1 = 100 kPa).

						He and Clavin (1994) $U_c = V_{CJ}[1-(1/2\theta_{CJ})]$				$U_c = 0.9V_{CJ}$		
% diluent	γ	V_{CJ} (m/s)	Δ (mm)	α_{max} (°)	θ_{CJ}	U_c/V_{CJ}	τ (μs)	θ	d_c (mm)	τ (μs)	θ	d_c (mm)
40	1.328	2132	0.114	22.8	10.56	0.95	0.70	11.10	16.3	1.74	11.47	38.1
50	1.339	2062	0.187	22.9	10.97	0.95	1.12	11.45	27.0	2.97	11.77	66.5
60	1.350	1981	0.358	23.1	11.48	0.96	2.10	11.90	52.4	5.95	12.09	136.3
70	1.362	1879	0.916	23.2	12.17	0.96	5.25	12.44	135.6	16.16	12.39	374.0
75.81	1.370	1801	2.072	23.4	12.67	0.96	11.64	12.78	304.0	37.78	12.49	865.1
80	1.375	1728	4.809	23.5	13.04	0.96	26.81	12.97	695.3	88.54	12.45	1973.3

Appendix B: Conditions from diffraction regime documentation experiments

The following experimental data were obtained through the initial series of detonation diffraction experiments with a 2 5mm tube used to document the subcritical and supercritical regimes (Section 5.3). The average experimental detonation velocity prior to diffraction is indicated, and the discrepancy from the CJ velocity was almost always within ±1% (Section 5.2.1). The ‘image’ column indicates whether or not a ruby laser shadowgraph image was obtained, and if so the image is presented in Appendix C. An experiment was identified as sub- or super-critical based upon the observations summarized in Section 5.3.

Table B.1: Conditions from diffraction regime documentation experiments with stoichiometric acetylene-oxygen mixtures.

Shot #	P_1 (kPa)	V_{CJ} (m/s)	V_{avg} (m/s)	% V_{CJ} deficit	Image	Critical
514	5	2264	2208	-1.66	ruby	super
513	10	2300	2305	-0.82	ruby	super
512	20	2337	2350	0.35	ruby	super
507	30	2358	2359	-0.07	ruby	super
508	30	2358	2364	0.18	ruby	super
509	30	2358	2365	0.18	ruby	super
510	30	2358	2368	0.31	ruby	super
511	30	2358	2365	0.18	ruby	super

Table B.2: Conditions from diffraction regime documentation experiments with stoichiometric acetylene-oxygen-argon mixtures.

Shot #	P_1 (kPa)	V_{CJ} (m/s)	V_{avg} (m/s)	% V_{CJ} deficit	Image	Critical
504	50	1691	1683	-0.54	ruby	sub
505	70	1703	1697	-0.53	none	sub
506	90	1711	1707	-0.37	none	sub

Table B.3: Conditions from diffraction regime documentation experiments with stoichiometric hydrogen-oxygen mixtures.

Shot #	P_1 (kPa)	V_{CJ} (m/s)	V_{avg} (m/s)	% V_{CJ} deficit	Image	Critical
491	70	2822	2824	-0.05	none	sub
492	70	2822	2818	-0.35	ruby	sub
493	70	2822	2833	0.26	ruby	sub
494	70	2822	2831	0.10	ruby	sub
495	70	2822	2831	0.10	ruby	sub
496	70	2822	2829	0.10	ruby	sub
497	70	2822	2831	0.26	ruby	sub
516	80	2829	2842	0.45	ruby	sub
517	85	2832	2846	0.33	ruby	super
515	90	2836	2848	0.38	ruby	super
498	100	2841	2855	0.17	ruby	super
499	100	2841	2855	0.32	ruby	super
500	100	2841	2851	0.01	ruby	super
501	100	2841	2853	0.17	ruby	super
502	100	2841	2855	0.17	ruby	super
503	100	2841	2855	0.17	ruby	super
518	100	2841	2853	0.17	ruby	super
519	100	2841	2853	0.17	ruby	super
520	100	2841	2853	0.17	ruby	super

Table B.4: Conditions from diffraction regime documentation experiments with stoichiometric hydrogen-oxygen-nitrogen mixtures (P_1 = 100 kPa).

Shot #	% N_2	V_{CJ} (m/s)	V_{avg} (m/s)	% V_{CJ} deficit	Image	Critical
521	55.6	1971	1980	0.27	ruby	sub

Appendix C: Images from diffraction regime documentation

The following images were obtained with the ruby laser shadowgraph system described in Section 5.2.2, and were used as an initial series of detonation diffraction experiments to visually document the subcritical and supercritical regimes (Section 5.3). The images are organized following the experiment sequence which was presented in Appendix B. The diffraction tube at the left of each image has a 25 mm inner diameter and 6mm wall thickness. The scale at the top of the diffraction tube is 10 mm in the horizontal direction.

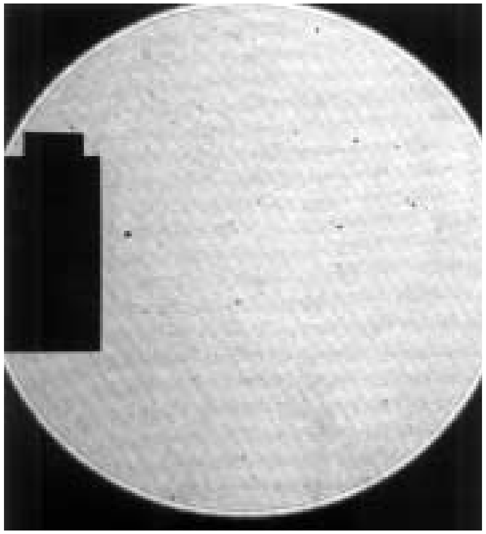

Shot 514, $C_2H_2 + 2.5O_2$, $P_1 = 5$ kPa

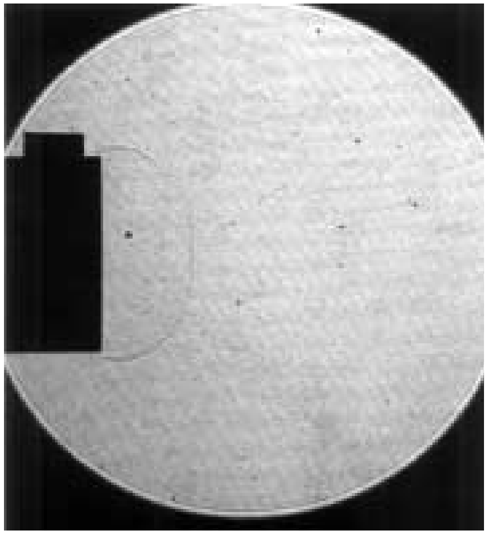

Shot 513, $C_2H_2 + 2.5O_2$, $P_1 = 10$ kPa

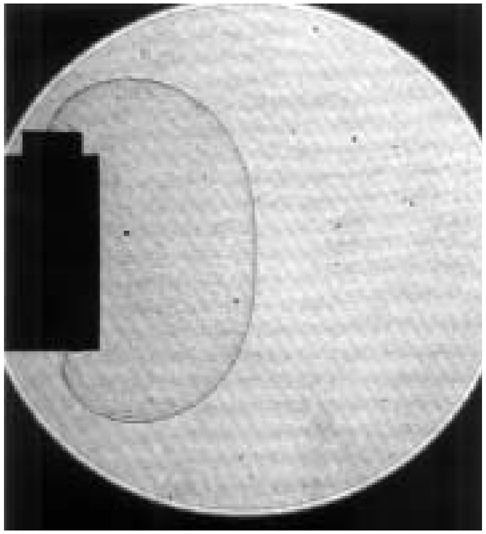

Shot 512, $C_2H_2 + 2.5O_2$, $P_1 = 20$ kPa

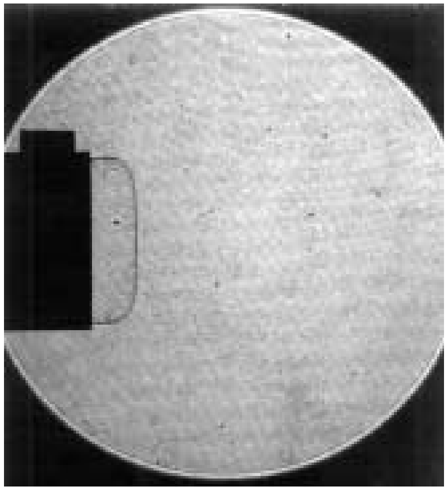

Shot 510, $C_2H_2 + 2.5O_2$, P_1 = 30 kPa

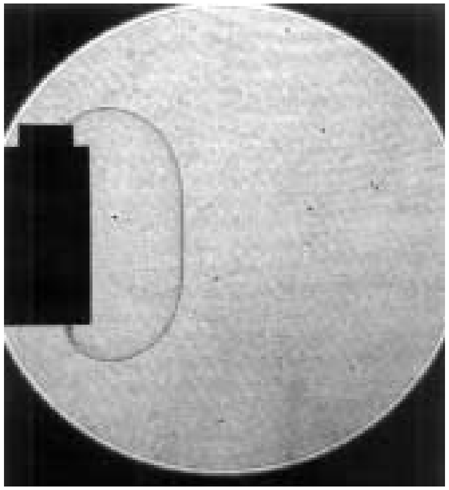

Shot 509, $C_2H_2 + 2.5O_2$, P_1 = 30 kPa

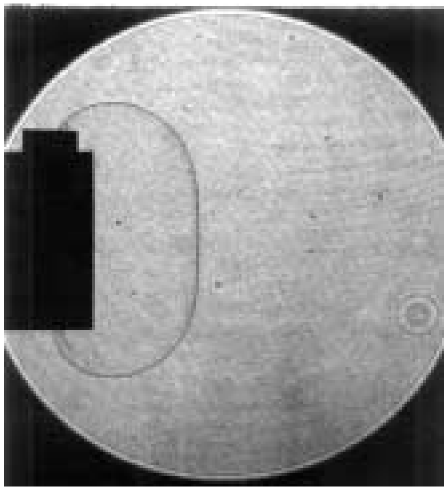

Shot 508, $C_2H_2 + 2.5O_2$, P_1 = 30 kPa

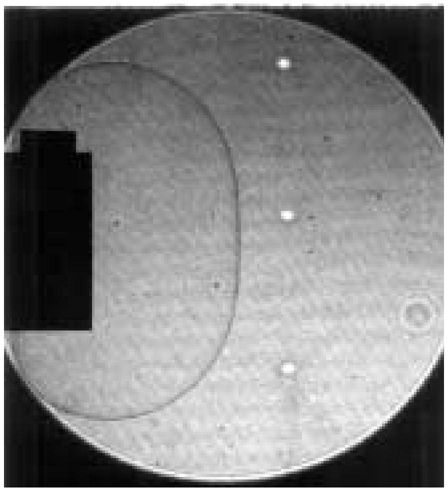

Shot 507, $C_2H_2 + 2.5O_2$, P_1 = 30 kPa

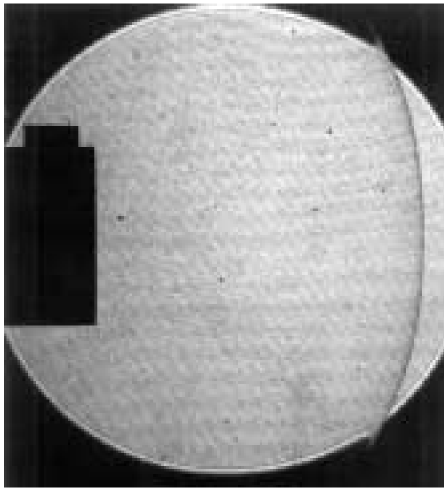

Shot 511, $C_2H_2 + 2.5O_2$, P_1 = 30 kPa

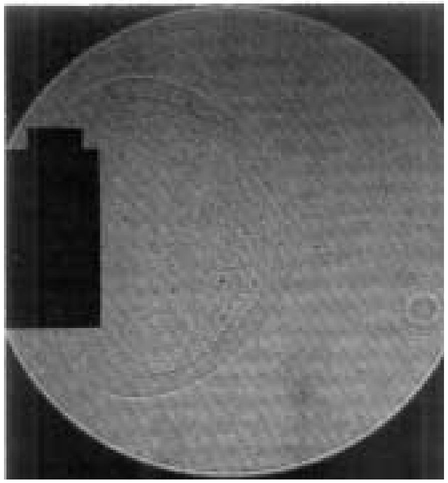

Shot 504, $C_2H_2 + 2.5O_2 + 14Ar$, P_1 = 50 kPa

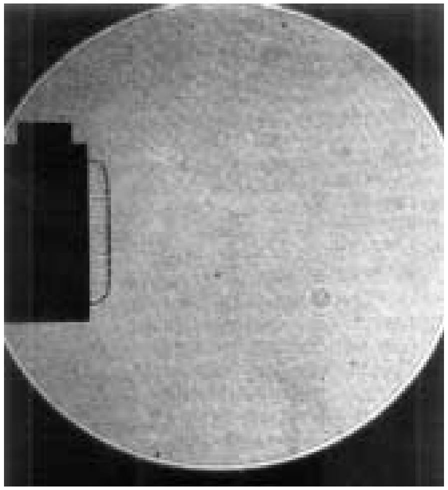

Shot 497, $H_2 + 0.5O_2$, $P_1 = 70$ kPa

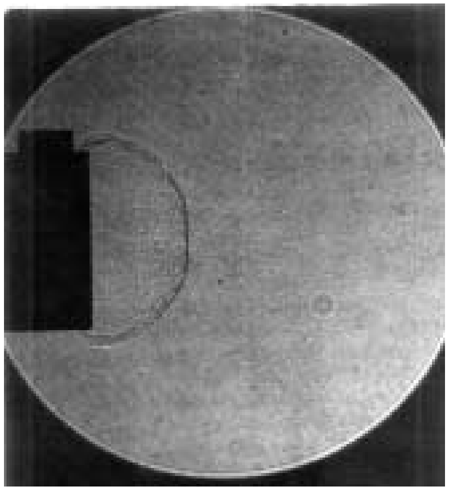

Shot 496, $H_2 + 0.5O_2$, $P_1 = 70$ kPa

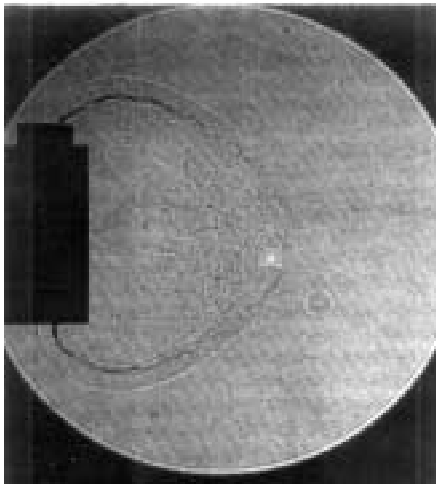

Shot 495, $H_2 + 0.5O_2$, $P_1 = 70$ kPa

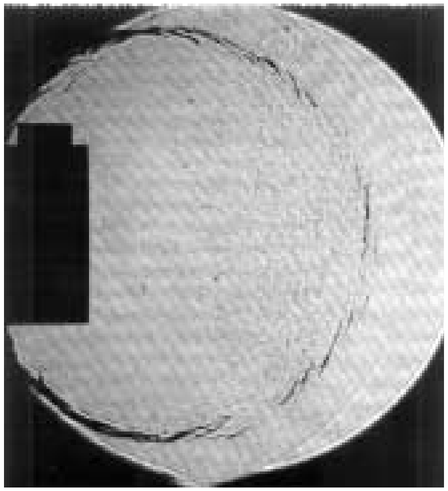

Shot 494, $H_2 + 0.5O_2$, $P_1 = 70$ kPa

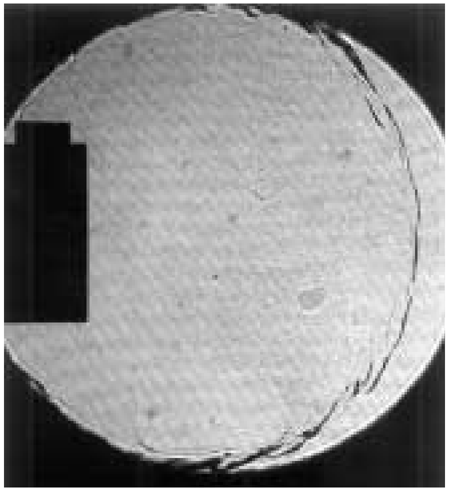

Shot 492, $H_2 + 0.5O_2$, $P_1 = 70$ kPa

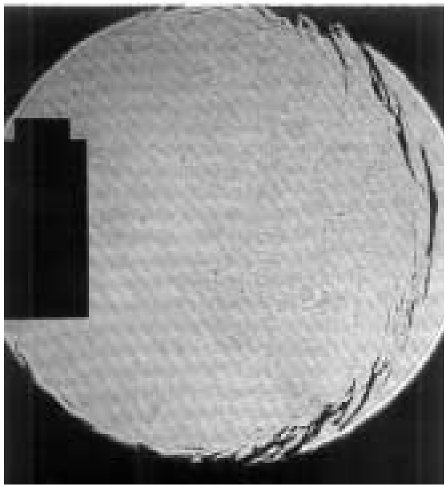

Shot 493, $H_2 + 0.5O_2$, $P_1 = 70$ kPa

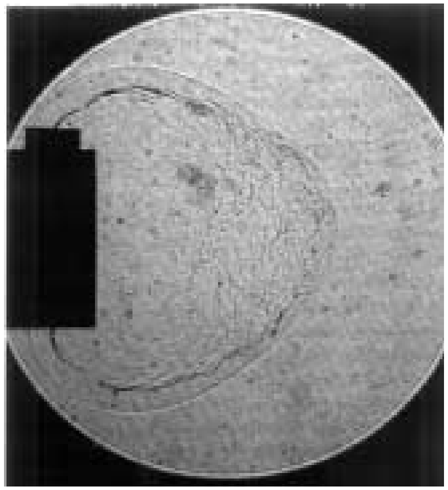

Shot 516, $H_2 + 0.5O_2$, $P_1 = 80$ kPa

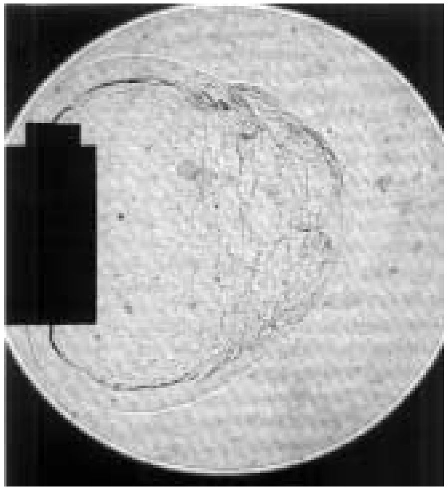

Shot 517, $H_2 + 0.5O_2$, $P_1 = 85$ kPa

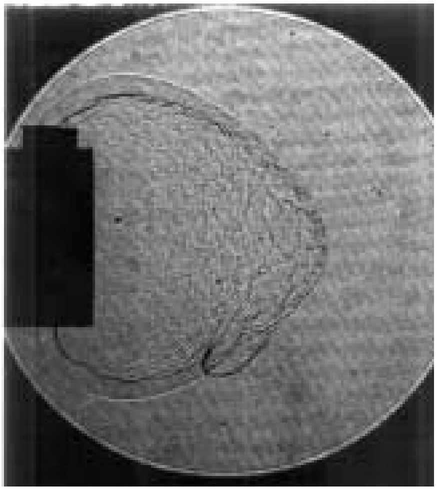

Shot 515, $H_2 + 0.5O_2$, $P_1 = 90$ kPa

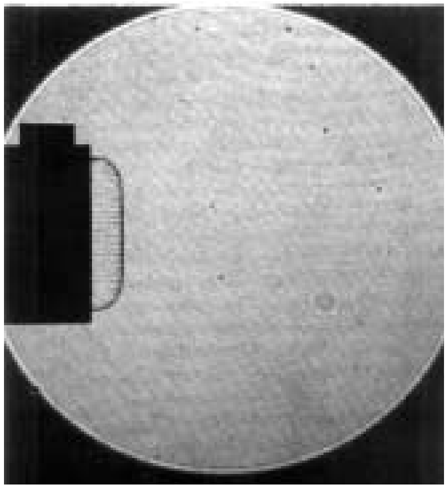

Shot 500, $H_2 + 0.5O_2$, $P_1 = 100$ kPa

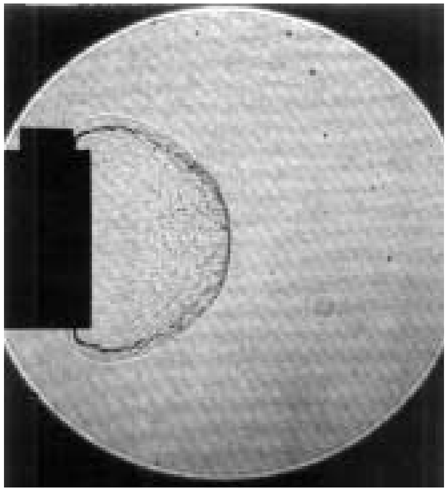

Shot 499, $H_2 + 0.5O_2$, $P_1 = 100$ kPa

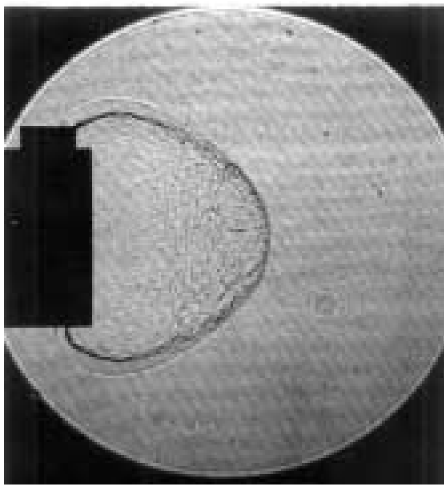

Shot 501, $H_2 + 0.5O_2$, $P_1 = 100$ kPa

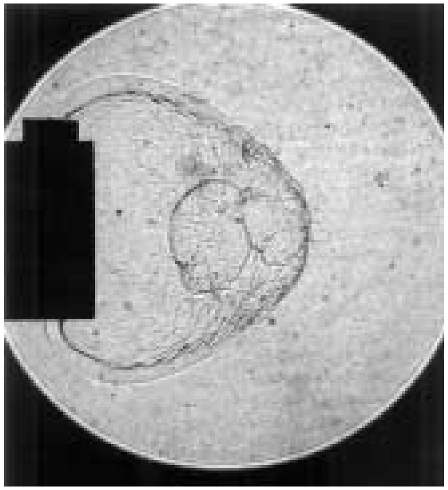

Shot 518, H_2 + $0.5O_2$, P_1 = 100 kPa

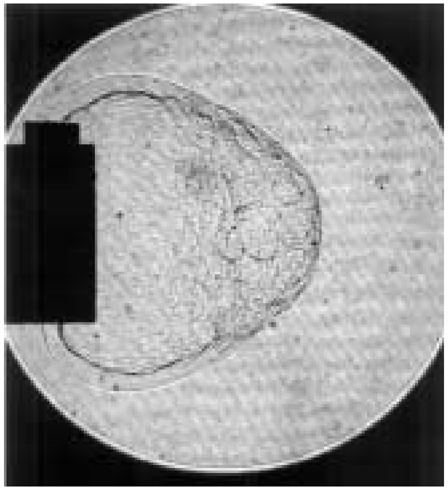

Shot 519, H_2 + $0.5O_2$, P_1 = 100 kPa

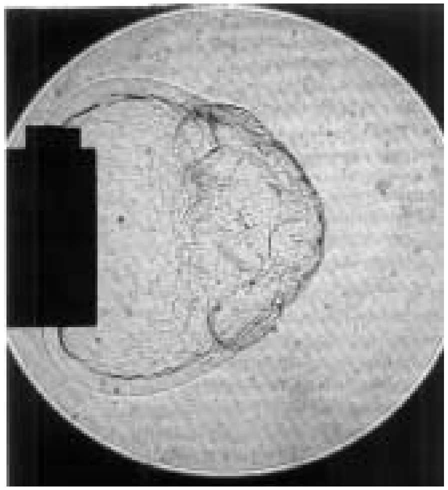

Shot 520, H_2 + $0.5O_2$, P_1 = 100 kPa

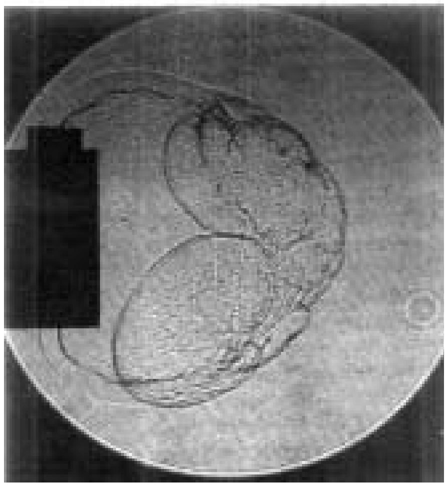

Shot 503, H_2 + $0.5O_2$, P_1 = 100 kPa

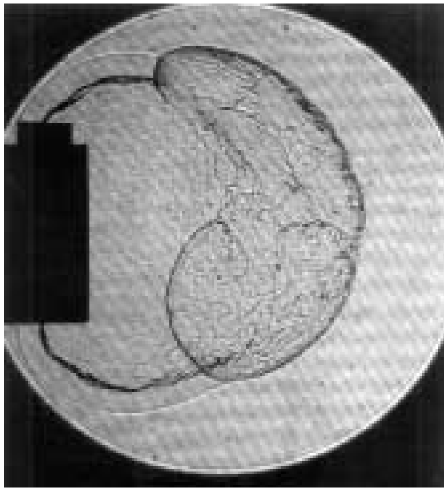

Shot 498, H_2 + $0.5O_2$, P_1 = 100 kPa

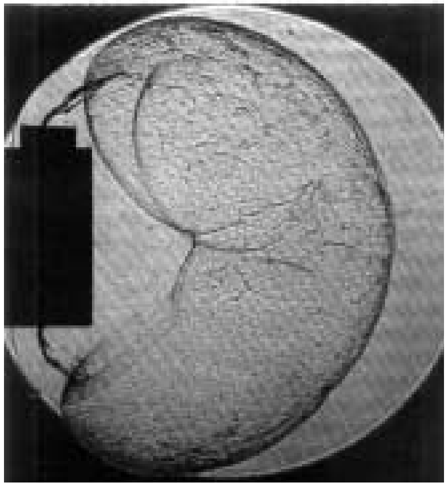

Shot 502, H_2 + $0.5O_2$, P_1 = 100 kPa

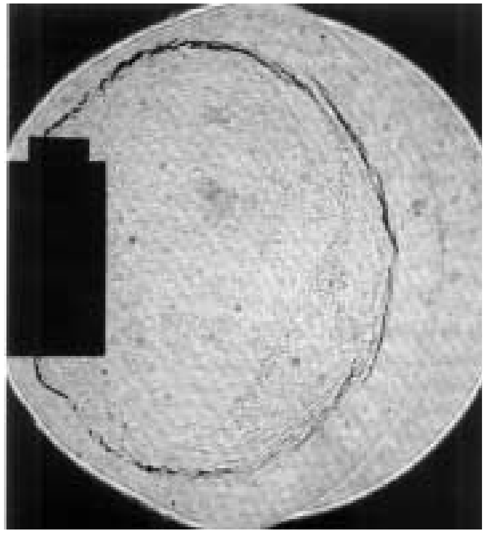

Shot 521, $H_2 + 0.5O_2 + 3.76N_2$,
P_1 = 100 kPa

Appendix D: Conditions from critical condition experiments

The following experimental data were obtained with the 38 mm diffraction tube facility to identify critical conditions (Section 5.7). The average experimental detonation velocity prior to diffraction is indicated, and the discrepancy from the CJ velocity was almost always within +1% and -3% (Section 5.2.1). The few experiments with velocities outside these limits were not a factor in determining the critical conditions. The 'image' column indicates whether or not a ruby laser shadowgraph image, ICCD digital chemiluminescence image, or framing camera shadowgraph images were obtained, and if so the image(s) are presented in Appendix E. An experiment was identified as sub- or super-critical based upon the criteria summarized in Section 5.3. Several stoichiometric hydrogen-oxygen and propane-oxygen experiments with an initial pressure of 100kPa are tabulated separately as "common experiments" because they apply to the respective fuel-oxygen stoichiometry variation series, initial pressure variation series, and dilution series of experiments.

Table D.1: Conditions from critical condition experiments with stoichiometric hydrogen-oxygen mixtures, P_1 = 100 kPa (common experiments).

Shot #	P_1 (kPa)	ϕ	% diluent	V_{CJ} (m/s)	V_{avg} (m/s)	% V_{CJ} deficit	Critical	Image
738	100	1.0	0.0	2842	2847	0.18	super	ruby
741	100	1.0	0.0	2842	2837	-0.18	super	ruby
743	100	1.0	0.0	2842	2827	-0.53	super	ruby
1045	100	1.0	0.0	2843	2817	-0.91	super	none
1046	100	1.0	0.0	2843	2817	-0.91	super	iccd
1047	100	1.0	0.0	2843	2827	-0.56	super	none
1079	100	1.0	0.0	2843	2837	-0.21	super	framer
1191	100	1.0	0.0	2843	2847	0.14	super	framer
1194	100	1.0	0.0	2843	2847	0.14	super	framer
1199	100	1.0	0.0	2843	2857	0.49	super	framer

Table D.2: Conditions from critical condition experiments with hydrogen-oxygen mixtures with varying equivalence ratio.

Shot #	P_1 (kPa)	ϕ	% diluent	V_{CJ} (m/s)	V_{avg} (m/s)	% V_{CJ} deficit	Critical	Image
1082	100	0.3	0.0	2085	2073	-0.58	sub	iccd
1083	100	0.4	0.0	2212	2198	-0.63	super	iccd
1088	100	0.4	0.0	2212	2204	-0.36	super	framer
1091	100	0.4	0.0	2212	2204	-0.36	super	framer
1081	100	0.5	0.0	2325	2312	-0.56	super	iccd
1080	100	0.7	0.0	2524	2508	-0.63	super	none
1109	100	1.5	0.0	3183	3163	-0.64	super	iccd
1110	100	1.7	0.0	3285	3252	-1.00	super	iccd
1115	100	1.7	0.0	3285	3252	-1.00	sub	framer
1116	100	1.7	0.0	3285	3265	-0.61	sub	framer
1117	100	1.7	0.0	3285	3252	-1.00	super	framer
1112	100	1.8	0.0	3308	3279	-0.88	sub	iccd
1111	100	1.8	0.0	3330	3306	-0.72	sub	iccd
1108	100	2.0	0.0	3410	3361	-1.44	sub	iccd

Table D.3: Conditions from critical condition experiments with stoichiometric hydrogen-oxygen mixtures with varying initial pressure.

Shot #	P_1 (kPa)	ϕ	% diluent	V_{CJ} (m/s)	V_{avg} (m/s)	% V_{CJ} deficit	Critical	Image
1202	30	1.0	0.0	2776	2740	-1.28	sub	none
1203	30	1.0	0.0	2776	2750	-0.94	sub	framer
1273	30	1.0	0.0	2776	2721	-1.96	sub	iccd
724	50	1.0	0.0	2804	2703	-3.60	sub	ruby
876	50	1.0	0.0	2804	2749	-1.96	sub	ruby
1044	50	1.0	0.0	2804	2769	-1.27	sub	none
1073	50	1.0	0.0	2804	2759	-1.60	sub	framer
1074	50	1.0	0.0	2804	2731	-2.62	sub	none
1075	50	1.0	0.0	2804	2769	-1.27	sub	framer
1076	50	1.0	0.0	2804	2759	-1.60	sub	framer
1077	50	1.0	0.0	2804	2769	-1.27	sub	framer
1192	50	1.0	0.0	2804	2797	-0.25	sub	none
1193	50	1.0	0.0	2804	2797	-0.25	sub	framer
1195	50	1.0	0.0	2804	2797	-0.25	sub	framer
1196	50	1.0	0.0	2804	2797	-0.25	sub	framer

Table D.3: Conditions from critical condition experiments with stoichiometric hydrogen-oxygen mixtures with varying initial pressure.

Shot #	P_1 (kPa)	ϕ	% diluent	V_{CJ} (m/s)	V_{avg} (m/s)	% V_{CJ} deficit	Critical	Image
1275	50	1.0	0.0	2804	2769	-1.27	sub	iccd
1276	50	1.0	0.0	2804	2769	-1.27	sub	iccd
1277	50	1.0	0.0	2804	2778	-0.93	sub	iccd
1278	50	1.0	0.0	2804	2759	-1.60	super	none
1279	50	1.0	0.0	2804	2769	-1.27	sub	none
1280	50	1.0	0.0	2804	2750	-1.94	super	none
726	56.3	1.0	0.0	2811	2712	-3.52	super	ruby
727	56.3	1.0	0.0	2811	2731	-2.86	super	ruby
725	62.5	1.0	0.0	2817	2749	-2.41	super	ruby
1012	62.5	1.0	0.0	2817	2778	-1.38	super	none
1013	62.5	1.0	0.0	2817	2778	-1.38	super	none
1014	62.5	1.0	0.0	2817			super	framer
1015	62.5	1.0	0.0	2817	2788	-1.05	super	framer
1016	62.5	1.0	0.0	2817	2778	-1.38	super	framer
1017	62.5	1.0	0.0	2817	2788	-1.05	super	none
1018	62.5	1.0	0.0	2817	2788	-1.05	super	none
1019	62.5	1.0	0.0	2817	2788	-1.05	super	iccd
1020	62.5	1.0	0.0	2817	2788	-1.05	super	iccd
1021*	62.5	1.0	0.0	2842	2807	-1.23	super	none
1022*	62.5	1.0	0.0	2842	2807	-1.23	super	none
1023*	62.5	1.0	0.0	2842	2817	-0.88	super	none
1024*	62.5	1.0	0.0	2841	2807	-1.20	super	none
1025*	62.5	1.0	0.0	2841	2807	-1.20	super	none
1026	62.5	1.0	0.0	2817	2788	-1.05	super	none
1027	62.5	1.0	0.0	2817	2769	-1.72	super	none
1028*	62.5	1.0	0.0	2841	2807	-1.20	super	iccd
1029*	62.5	1.0	0.0	2840	2817	-0.81	super	iccd
1030*	62.5	1.0	0.0	2842	2817	-0.88	super	iccd
1031	62.5	1.0	0.0	2817	2778	-1.38	super	iccd
1032*	62.5	1.0	0.0	2842	2807	-1.23	super	iccd
1033	62.5	1.0	0.0	2817	no data	no data	super	iccd
1034	62.5	1.0	0.0	2817	2778	-1.38	super	none
1035*	62.5	1.0	0.0	2842	2817	-0.88	super	none

Table D.3: Conditions from critical condition experiments with stoichiometric hydrogen-oxygen mixtures with varying initial pressure.

Shot #	P_1 (kPa)	ϕ	% diluent	V_{CJ} (m/s)	V_{avg} (m/s)	% V_{CJ} deficit	Critical	Image
1036	62.5	1.0	0.0	2817	2778	-1.38	super	iccd
1037	62.5	1.0	0.0	2817	2788	-1.05	super	iccd
1038	62.5	1.0	0.0	2817	2778	-1.38	super	iccd
1039	62.5	1.0	0.0	2817	2778	-1.38	super	iccd
1040	62.5	1.0	0.0	2817	2788	-1.05	super	none
1041	62.5	1.0	0.0	2817	2769	-1.72	super	iccd
1042	62.5	1.0	0.0	2817	2788	-1.05	super	iccd
1043	62.5	1.0	0.0	2817	2750	-2.40	super	none
1048	62.5	1.0	0.0	2817	2788	-1.05	super	none
1049	62.5	1.0	0.0	2817	2788	-1.05	super	none
1050	62.5	1.0	0.0	2817	2788	-1.05	super	none
1051	62.5	1.0	0.0	2817	2788	-1.05	super	none
1052	62.5	1.0	0.0	2817	2788	-1.05	super	framer
1053	62.5	1.0	0.0	2817	2778	-1.38	super	none
1054	62.5	1.0	0.0	2817	2788	-1.05	super	framer
1069	62.5	1.0	0.0	2817	2778	-1.38	super	none
1070	62.5	1.0	0.0	2817	2788	-1.05	super	framer
1071	62.5	1.0	0.0	2817	2788	-1.05	super	framer
1072	62.5	1.0	0.0	2817	2788	-1.05	super	framer

Note: * indicates experiment was performed with approximately 2% C_3H_6O in mixture.

Table D.4: Conditions from critical condition experiments with stoichiometric hydrogen-oxygen-argon mixtures with varying dilution.

Shot #	P_1 (kPa)	ϕ	% diluent	V_{CJ} (m/s)	V_{avg} (m/s)	% V_{CJ} deficit	Critical	Image
1205	100	1.0	40.0	2049	2046	-0.17	super	none
1206	100	1.0	40.0	2049	2051	0.08	super	framer
865	100	1.0	60.0	1813	1798	-0.83	super	none
867	100	1.0	65.3	1751	1759	0.46	sub	none
868	100	1.0	65.3	1751	1751	0.00	super	ruby
1098	100	1.0	65.3	1751	1779	1.57	super	framer
1099	100	1.0	65.3	1751	1767	0.89	super	framer
1103	100	1.0	65.3	1751	1763	0.66	super	framer
869	100	1.0	67.5	1726	1721	-0.32	sub	none

Table D.4: Conditions from critical condition experiments with stoichiometric hydrogen-oxygen-argon mixtures with varying dilution.

Shot #	P_1 (kPa)	ϕ	% diluent	V_{CJ} (m/s)	V_{avg} (m/s)	% V_{CJ} deficit	Critical	Image
1100	100	1.0	67.5	1726	1752	1.48	super	none
1101	100	1.0	67.5	1726	1728	0.09	sub	framer
1102	100	1.0	67.5	1726	1725	-0.09	sub	framer

Table D.5: Conditions from critical condition experiments with stoichiometric hydrogen-oxygen-carbon dioxide mixtures with varying dilution.

Shot #	P_1 (kPa)	ϕ	% diluent	V_{CJ} (m/s)	V_{avg} (m/s)	% V_{CJ} deficit	Critical	Image
1107	100	1.0	3.2	2698	2685	-0.48	super	iccd
1113	100	1.0	3.2	2698	2685	-0.48	super	framer
1106	100	1.0	6.3	2575	2564	-0.43	sub	iccd
1114	100	1.0	6.3	2575	2556	-0.74	sub	framer
1105	100	1.0	9.1	2470	2462	-0.34	sub	iccd
1211	100	1.0	14.3	2299	2306	0.28	sub	none
1212	100	1.0	14.3	2299	2286	-0.57	sub	none
1213	100	1.0	14.3	2299	2293	-0.28	sub	framer
1214	100	1.0	14.3	2299	2299	0.00	sub	framer
1104	100	1.0	14.3	2299	2286	-0.57	sub	iccd

Table D.6: Conditions from critical condition experiments with stoichiometric hydrogen-oxygen-helium mixtures with varying dilution.

Shot #	P_1 (kPa)	ϕ	% diluent	V_{CJ} (m/s)	V_{avg} (m/s)	% V_{CJ} deficit	Critical	Image
1200	100	1.0	25.0	3126	3125	-0.04	super	none
1201	100	1.0	25.0	3126	3113	-0.43	super	framer
1086	100	1.0	45.5	3404	3376	-0.84	super	iccd
1090	100	1.0	45.5	3404	3376	-0.84	super	framer
1084	100	1.0	50.0	3470	3703	6.71	super	iccd
1089	100	1.0	50.0	3470	3448	-0.63	sub	framer
1197	100	1.0	50.0	3470	3463	-0.20	super	framer
1198	100	1.0	50.0	3470	3463	-0.20	sub	framer
1087	100	1.0	53.8	3529	3479	-1.43	sub	iccd

Table D.7: Conditions from critical condition experiments with stoichiometric hydrogen-oxygen-nitrogen mixtures with varying dilution.

Shot #	P_1 (kPa)	ϕ	% diluent	V_{CJ} (m/s)	V_{avg} (m/s)	% V_{CJ} deficit	Critical	Image
719	100	1.0	14.3	2568	2532	-1.40	super	ruby
722	100	1.0	17.2	2520	2500	-0.79	super	ruby
1092	100	1.0	17.2	2520	2516	-0.16	super	framer
1096	100	1.0	17.2	2520	2516	-0.16	super	framer
721	100	1.0	20.0	2476	2454	-0.89	sub	ruby
720	100	1.0	25.0	2400	2381	-0.79	sub	ruby
1093	100	1.0	25.0	2400	2395	-0.21	sub	framer
1094	100	1.0	25.0	2400	2395	-0.21	sub	framer
1095	100	1.0	25.0	2400	2396	-0.19	super	framer
1097	100	1.0	25.0	2400	2395	-0.21	sub	framer
1208	100	1.0	40.0	2188	2192	0.20	sub	none
1209	100	1.0	40.0	2188	2192	0.20	sub	framer
1281	100	1.0	40.0	2188	2186	-0.07	sub	iccd
1282	100	1.0	40.0	2188	2186	-0.07	sub	iccd
1283	100	1.0	40.0	2188	2186	-0.07	sub	iccd
1284	100	1.0	40.0	2188	2186	-0.07	sub	iccd
1285	100	1.0	40.0	2188	2186	-0.07	sub	iccd

Table D.8: Conditions from critical condition experiments with ethylene-oxygen mixtures with varying equivalence ratio.

Shot #	P_1 (kPa)	ϕ	% diluent	V_{CJ} (m/s)	V_{avg} (m/s)	% V_{CJ} deficit	Critical	Image
1238	100	0.3	0.0	1868	1852	-0.90	sub	none
1290	100	0.3	0.0	1868	1878	0.54	sub	framer
1292	100	0.3	0.0	1868	1869	0.05	sub	none
1293	100	0.3	0.0	1868	1856	-0.64	sub	framer
1294	100	0.3	0.0	1868	1869	0.05	sub	framer
1296	100	0.3	0.0	1868	1869	0.05	sub	none
1239	100	0.4	0.0	1975	1966	-0.44	super	iccd
1237	100	0.5	0.0	2062	2057	-0.27	super	iccd
1227	100	1.5	0.0	2576	2581	0.19	super	none
1228	100	1.8	0.0	2651	2658	0.26	super	iccd
1229	100	2.0	0.0	2682	2685	0.13	super	iccd

Table D.8: Conditions from critical condition experiments with ethylene-oxygen mixtures with varying equivalence ratio.

Shot #	P_1 (kPa)	ϕ	% diluent	V_{CJ} (m/s)	V_{avg} (m/s)	% V_{CJ} deficit	Critical	Image
1230	100	2.4	0.0	2704	2703	-0.02	super	iccd
1231	100	2.8	0.0	2682	2658	-0.89	super	iccd
1233	100	2.9	0.0	2671	2641	-1.12	super	iccd
1232	100	3.0	0.0	2658	2632	-0.98	sub	iccd
1234	100	3.0	0.0	2658	2641	-0.66	super	iccd
1270	100	3.1	0.0	2623	2641	0.68	sub	iccd

Table D.9: Conditions from critical condition experiments with stoichiometric ethylene-oxygen mixtures with varying initial pressure.

Shot #	P_1 (kPa)	ϕ	% diluent	V_{CJ} (m/s)	V_{avg} (m/s)	% V_{CJ} deficit	Critical	Image
846	15	1.0	0.0	2286	2216	-3.06	sub	ruby
1289	15	1.0	0.0	2286	2299	0.55	sub	framer
844	20	1.0	0.0	2299	2254	-1.98	super	ruby
1286	20	1.0	0.0	2299	2319	0.87	super	none
1287	20	1.0	0.0	2299	2306	0.28	super	framer
1288	20	1.0	0.0	2299	2319	0.87	super	framer
843	30	1.0	0.0	2319	2286	-1.42	super	none

Table D.10: Conditions from critical condition experiments with stoichiometric ethylene-oxygen-argon mixtures with varying dilution.

Shot #	P_1 (kPa)	ϕ	% diluent	V_{CJ} (m/s)	V_{avg} (m/s)	% V_{CJ} deficit	Critical	Image
848	100	1.0	73.3	1761	1782	1.19	super	none
849	100	1.0	75.0	1742	1739	-0.17	sub	none
850	100	1.0	75.0	1742	1740	-0.14	super	ruby
1291	100	1.0	75.0	1742	1743	0.06	sub	framer
1295	100	1.0	75.0	1742	1743	0.06	super	none
1297	100	1.0	75.0	1742	1743	0.06	super	none
1298	100	1.0	75.0	1742	1747	0.26	super	none

Table D.11: Conditions from critical condition experiments with stoichiometric ethylene-oxygen-carbon dioxide mixtures with varying dilution.

Shot #	P_1 (kPa)	ϕ	% diluent	V_{CJ} (m/s)	V_{avg} (m/s)	% V_{CJ} deficit	Critical	Image
1244	100	1.0	5.0	2300	2312	0.51	super	iccd
1245	100	1.0	10.0	2227	2235	0.36	super	iccd

Table D.11: Conditions from critical condition experiments with stoichiometric ethylene-oxygen-carbon dioxide mixtures with varying dilution.

Shot #	P_1 (kPa)	ϕ	% diluent	V_{CJ} (m/s)	V_{avg} (m/s)	% V_{CJ} deficit	Critical	Image
1246	100	1.0	20.0	2083	2117	1.62	super	iccd
1268	100	1.0	20.0	2083	2041	-2.00	super	iccd
1267	100	1.0	25.0	2013	2006	-0.38	sub	iccd

Table D.12: Conditions from critical condition experiments with stoichiometric ethylene-oxygen-helium mixtures with varying dilution.

Shot #	P_1 (kPa)	ϕ	% diluent	V_{CJ} (m/s)	V_{avg} (m/s)	% V_{CJ} deficit	Critical	Image
1240	100	1.0	50.0	2810	2788	-0.78	super	iccd
1242	100	1.0	60.0	2959	2931	-0.97	super	iccd
1243	100	1.0	65.0	3048	3042	-0.22	sub	iccd

Table D.13: Conditions from critical condition experiments with stoichiometric ethylene-oxygen-nitrogen mixtures with varying dilution.

Shot #	P_1 (kPa)	ϕ	% diluent	V_{CJ} (m/s)	V_{avg} (m/s)	% V_{CJ} deficit	Critical	Image
856	100	1.0	33.3	2178	2180	0.09	super	ruby
857	100	1.0	42.9	2114	2116	0.09	super	ruby
860	100	1.0	44.4	2102	2105	0.14	sub	ruby
859	100	1.0	46.7	2086	2089	0.12	sub	ruby
858	100	1.0	50.0	2061	2062	0.05	sub	ruby

Table D.14: Conditions from critical condition experiments with stoichiometric propane-oxygen mixtures, P_1 = 100 kPa (common experiments).

Shot #	P_1 (kPa)	ϕ	% diluent	V_{CJ} (m/s)	V_{avg} (m/s)	% V_{CJ} deficit	Critical	Image
753	100	1.0	0.0	2362	2360	-0.08	super	ruby

Table D.15: Conditions from critical condition experiments with propane-oxygen mixtures with varying equivalence ratio.

Shot #	P_1 (kPa)	ϕ	% diluent	V_{CJ} (m/s)	V_{avg} (m/s)	% V_{CJ} deficit	Critical	Image
1262	100	0.4	0.0	1958	1947	-0.56	sub	none
1263	100	0.5	0.0	2046	2025	-1.05	sub	none
1264	100	0.6	0.0	2123	2117	-0.32	super	iccd
1265	100	2.4	0.0	2576	2589	0.52	super	iccd
1308	100	2.4	0.0	2576	2573	-0.14	super	none

Table D.15: Conditions from critical condition experiments with propane-oxygen mixtures with varying equivalence ratio.

Shot #	P_1 (kPa)	ϕ	% diluent	V_{CJ} (m/s)	V_{avg} (m/s)	% V_{CJ} deficit	Critical	Image
1309	100	2.4	0.0	2576	2565	-0.45	super	none

Table D.16: Conditions from critical condition experiments with stoichiometric propane-oxygen mixtures with varying initial pressure.

Shot #	P_1 (kPa)	ϕ	% diluent	V_{CJ} (m/s)	V_{avg} (m/s)	% V_{CJ} deficit	Critical	Image
825	30	1.0	0.0	2307	2280	-1.19	sub	ruby
1299	30	1.0	0.0	2307	2319	0.52	super	none
1300	30	1.0	0.0	2307	2326	0.82	super	framer
1301	30	1.0	0.0	2307	2312	0.22	sub	framer
1302	30	1.0	0.0	2307	2319	0.52	super	framer
826	35	1.0	0.0	2314	2286	-1.21	super	ruby
824	40	1.0	0.0	2320	2293	-1.19	super	ruby
823	50	1.0	0.0	2329	2319	-0.43	super	ruby

Table D.17: Conditions from critical condition experiments with stoichiometric propane-oxygen-argon mixtures with varying dilution.

Shot #	P_1 (kPa)	ϕ	% diluent	V_{CJ} (m/s)	V_{avg} (m/s)	% V_{CJ} deficit	Critical	Image
833	100	1.0	40.0	2057	2054	-0.15	super	ruby
834	100	1.0	50.0	1976	1966	-0.53	super	none
835	100	1.0	60.0	1890	1887	-0.16	super	none
837	100	1.0	64.7	1847	1848	0.03	super	ruby
838	100	1.0	67.6	1820	1823	0.14	super	ruby
836	100	1.0	70.0	1796	1794	-0.11	sub	none
1303	100	1.0	70.0	1796	1802	0.33	sub	none
1304	100	1.0	70.0	1796	1802	0.33	sub	framer
1305	100	1.0	70.0	1796	1798	0.11	sub	none
1306	100	1.0	70.0	1796	1798	0.11	sub	none
1307	100	1.0	70.0	1796	1802	0.33	sub	framer

Table D.18: Conditions from critical condition experiments with stoichiometric propane-oxygen-carbon dioxide mixtures with varying dilution.

Shot #	P_1 (kPa)	ϕ	% diluent	V_{CJ} (m/s)	V_{avg} (m/s)	% V_{CJ} deficit	Critical	Image
1257	100	1.0	15.0	2158	2145	-0.61	super	iccd
1258	100	1.0	20.0	2092	2089	-0.17	super	iccd

Table D.18: **Conditions from critical condition experiments with stoichiometric propane-oxygen-carbon dioxide mixtures with varying dilution.**

Shot #	P_1 (kPa)	ϕ	% diluent	V_{CJ} (m/s)	V_{avg} (m/s)	% V_{CJ} deficit	Critical	Image
1259	100	1.0	22.5	2059	2057	-0.13	sub	iccd

Table D.19: **Conditions from critical condition experiments with stoichiometric propane-oxygen-helium mixtures with varying dilution.**

Shot #	P_1 (kPa)	ϕ	% diluent	V_{CJ} (m/s)	V_{avg} (m/s)	% V_{CJ} deficit	Critical	Image
1261	100	1.0	55.0	2820	2807	-0.47	super	iccd
1260	100	1.0	60.0	2894	2899	0.16	sub	none

Table D.20: **Conditions from critical condition experiments with stoichiometric propane-oxygen-nitrogen mixtures with varying dilution.**

Shot #	P_1 (kPa)	ϕ	% diluent	V_{CJ} (m/s)	V_{avg} (m/s)	% V_{CJ} deficit	Critical	Image
818	100	1.0	29.4	2199	2198	-0.05	super	none
821	100	1.0	29.4	2199	2198	-0.07	super	ruby
822	100	1.0	31.8	2185	2192	0.32	super	ruby
820	100	1.0	33.3	2176	2174	-0.09	sub	ruby
819	100	1.0	36.8	2154	2145	-0.42	sub	ruby

Appendix E: Images from critical condition experiments

The images acquired during the critical condition experiments with the 38mm diffraction tube facility are presented in this appendix. They are grouped according to mixture classes as organized in Appendix D, but note that the common experiments from Appendix D (stoichiometric hydrogen-oxygen and propane-oxygen at an initial pressure of 100kPa) are displayed only among the initial pressure variation images.

Exposure time for the ruby laser shadowgraphs was 40 ns (FWHM), and the framing camera shadowgraph images were exposed for approximately 152 ns per frame with 832ns between successive frames. The collimated light beam in experiments with both shadowgraph devices was approximately 150 mm in diameter; in some images a 10 mm black square is present for scale purposes. Window chips and scratches are visible in many of the images due to the harsh experimental environment.

The ICCD digital chemiluminescence rectangular images are approximately 100mm by 145mm, and were acquired under a variety of intensifier gain, gate width (exposure time), and filter conditions. In addition, some ICCD images were acquired while a laser sheet was passing through the test section which is identifiable by intense reflection off of the 38mm diffraction tube flange. The chemiluminescence images are only being interpreted qualitatively in the present investigation, and therefore the use of different electronic settings and the presence or absence of a laser sheet does not impact the results. All ICCD image intensities were individually scaled manually to make qualitatively important features clear, and so rigorous comparison should not be made between the relative intensities present in different images. Note that some ICCD images show the wavefront at two different times because a double exposure was acquired, and background noise and ICCD dark charge pattern is visible in some low signal images.

Hydrogen-oxygen mixtures with varying equivalence ratio (P_1 = 100 kPa)

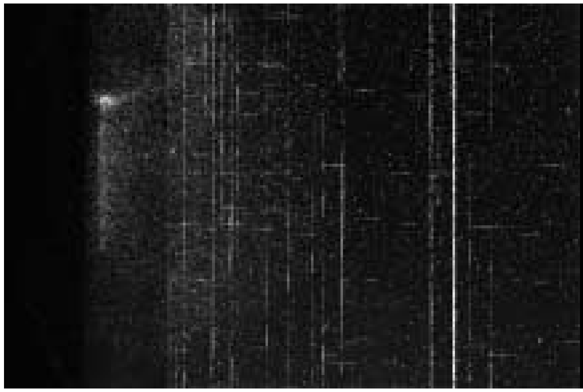

Shot 1082, $\phi = 0.33$

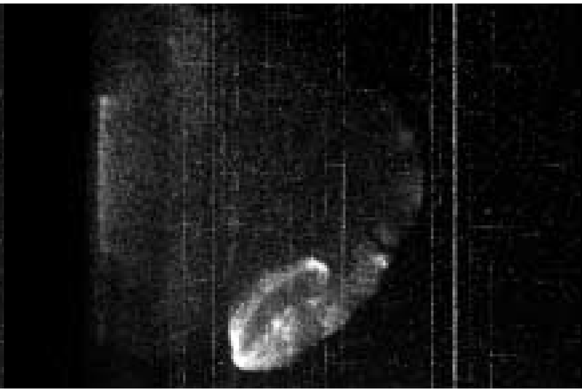

Shot 1083, $\phi = 0.42$

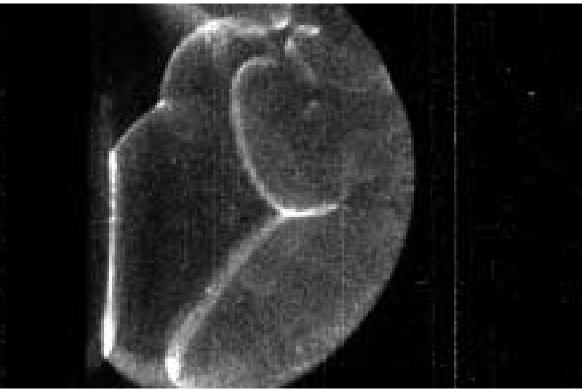

Shot 1081, $\phi = 0.5$

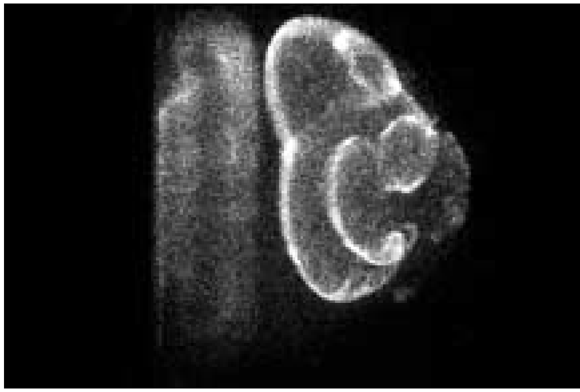

Shot 1109, $\phi = 1.5$

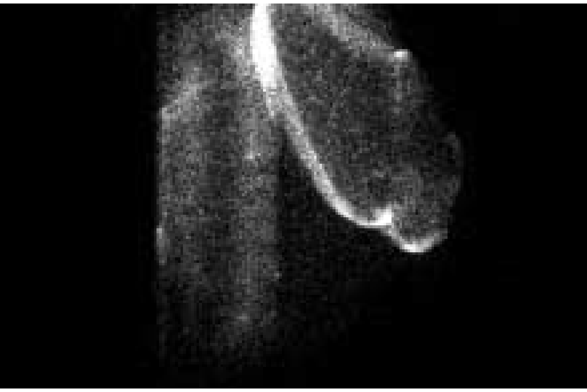

Shot 1110, $\phi = 1.7$

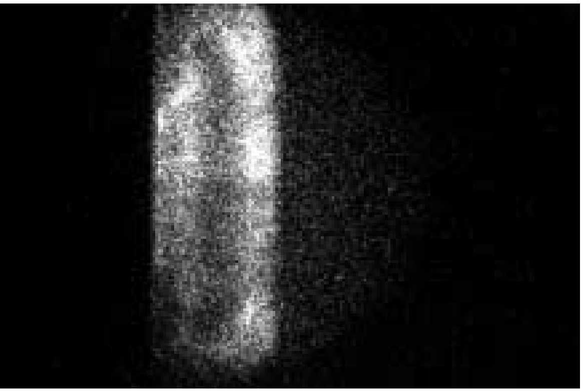

Shot 1112, $\phi = 1.75$

Hydrogen-oxygen mixtures with varying equivalence ratio (P_1 = 100 kPa)

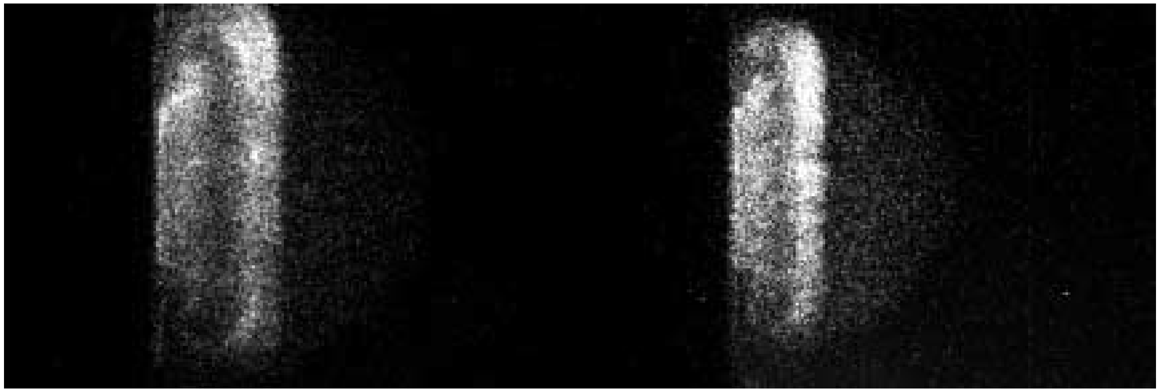

Shot 1111, $\phi = 1.8$ Shot 1108, $\phi = 2.0$

Hydrogen-oxygen mixtures with varying equivalence ratio (P_1 = 100 kPa), Shot 1088, ϕ = 0.42

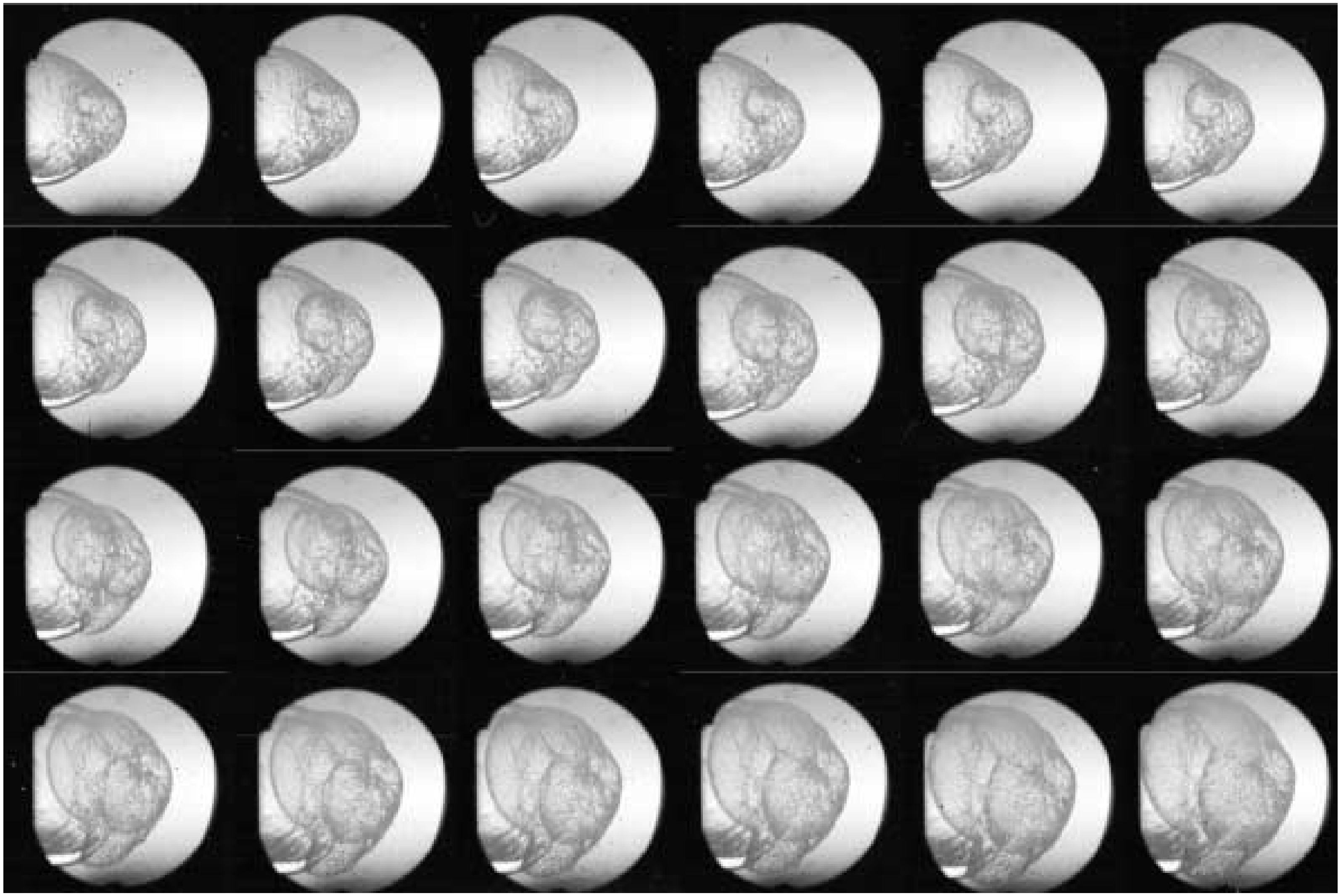

Hydrogen-oxygen mixtures with varying equivalence ratio (P_1 = 100 kPa), Shot 1091, ϕ = 0.42

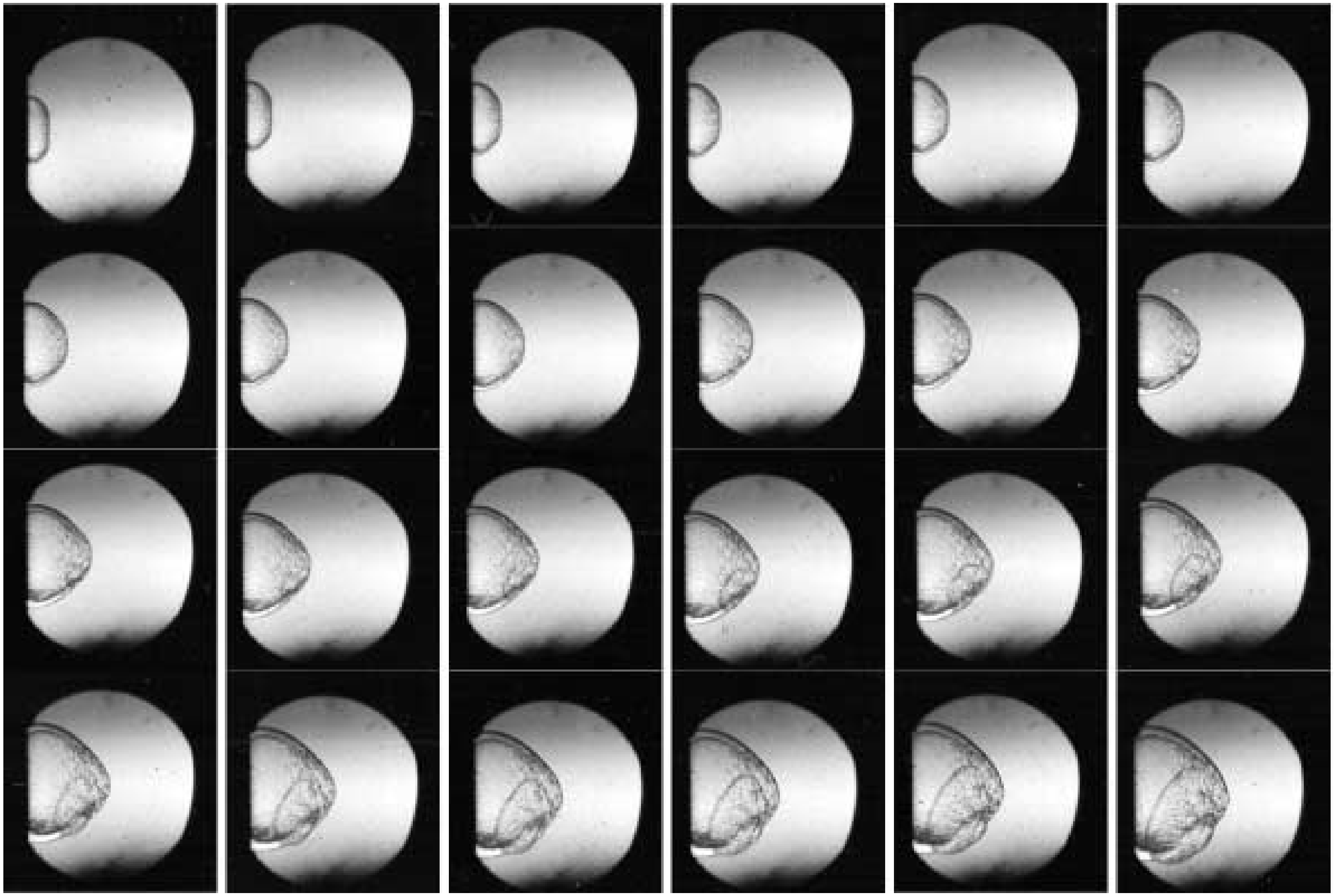

Hydrogen-oxygen mixtures with varying equivalence ratio (P_1 = 100 kPa), Shot 1115, ϕ = 1.7

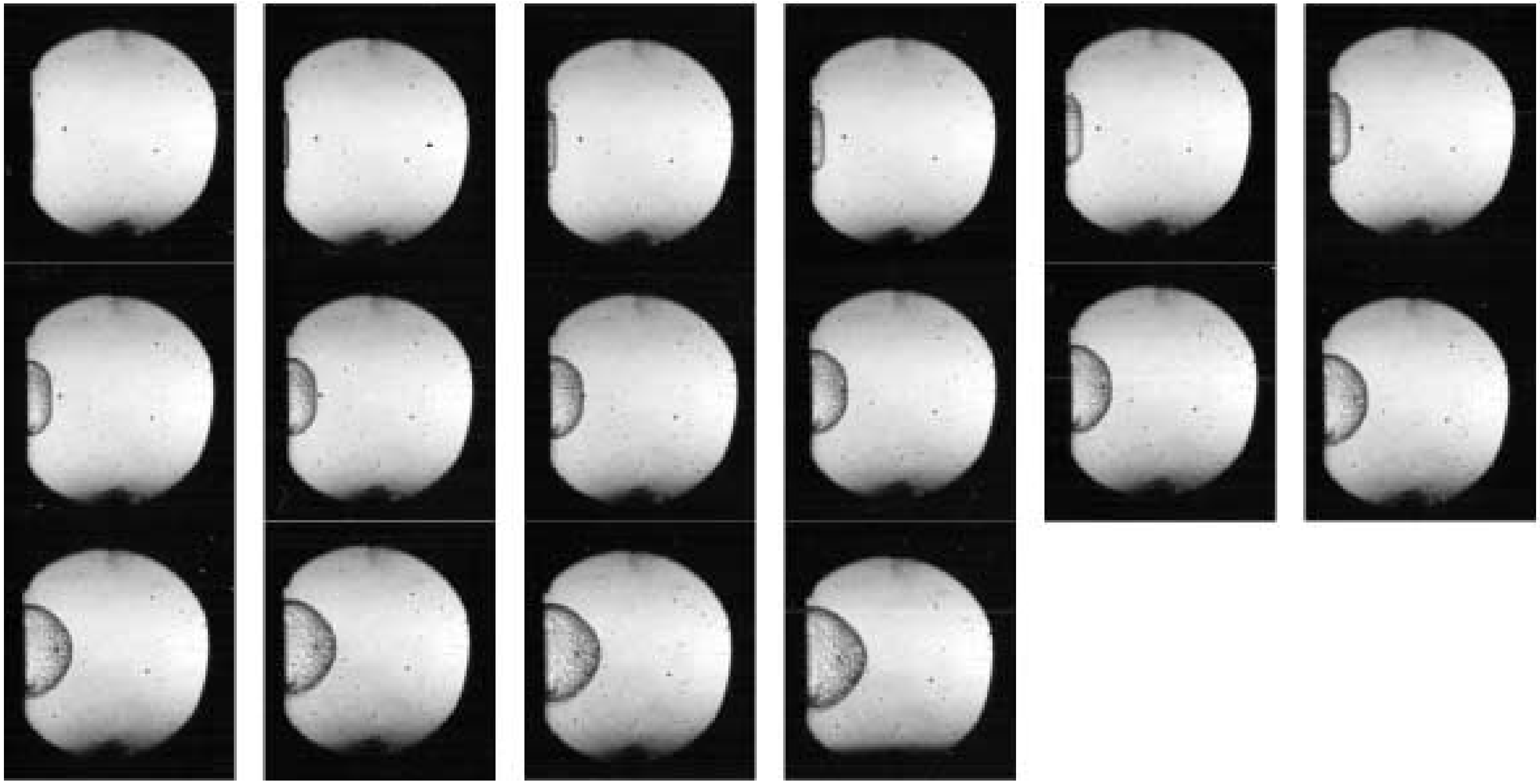

Hydrogen-oxygen mixtures with varying equivalence ratio (P_1 = 100 kPa), Shot 1116, $\phi = 1.7$

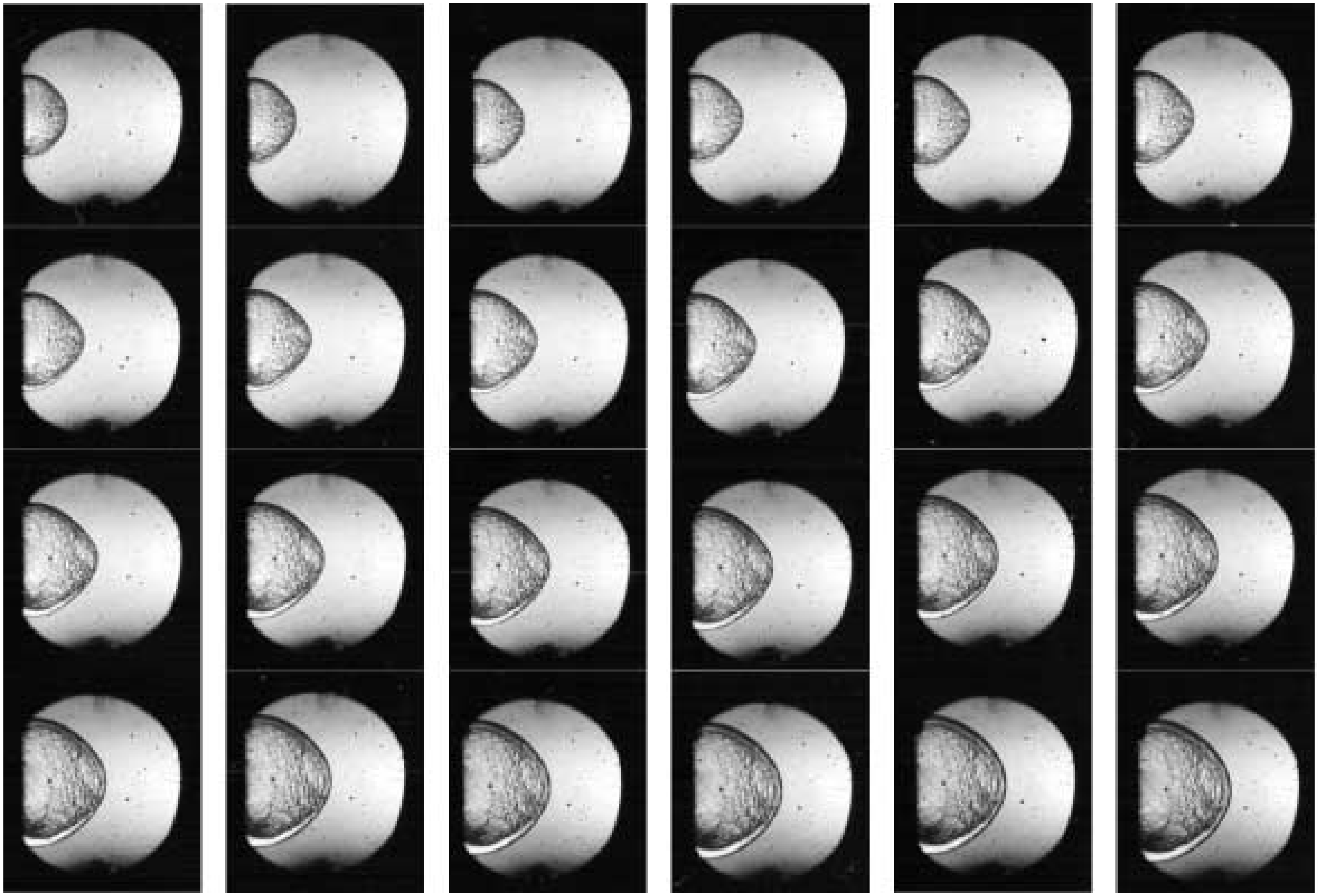

Hydrogen-oxygen mixtures with varying equivalence ratio (P_1 = 100 kPa), Shot 1117, ϕ = 1.7

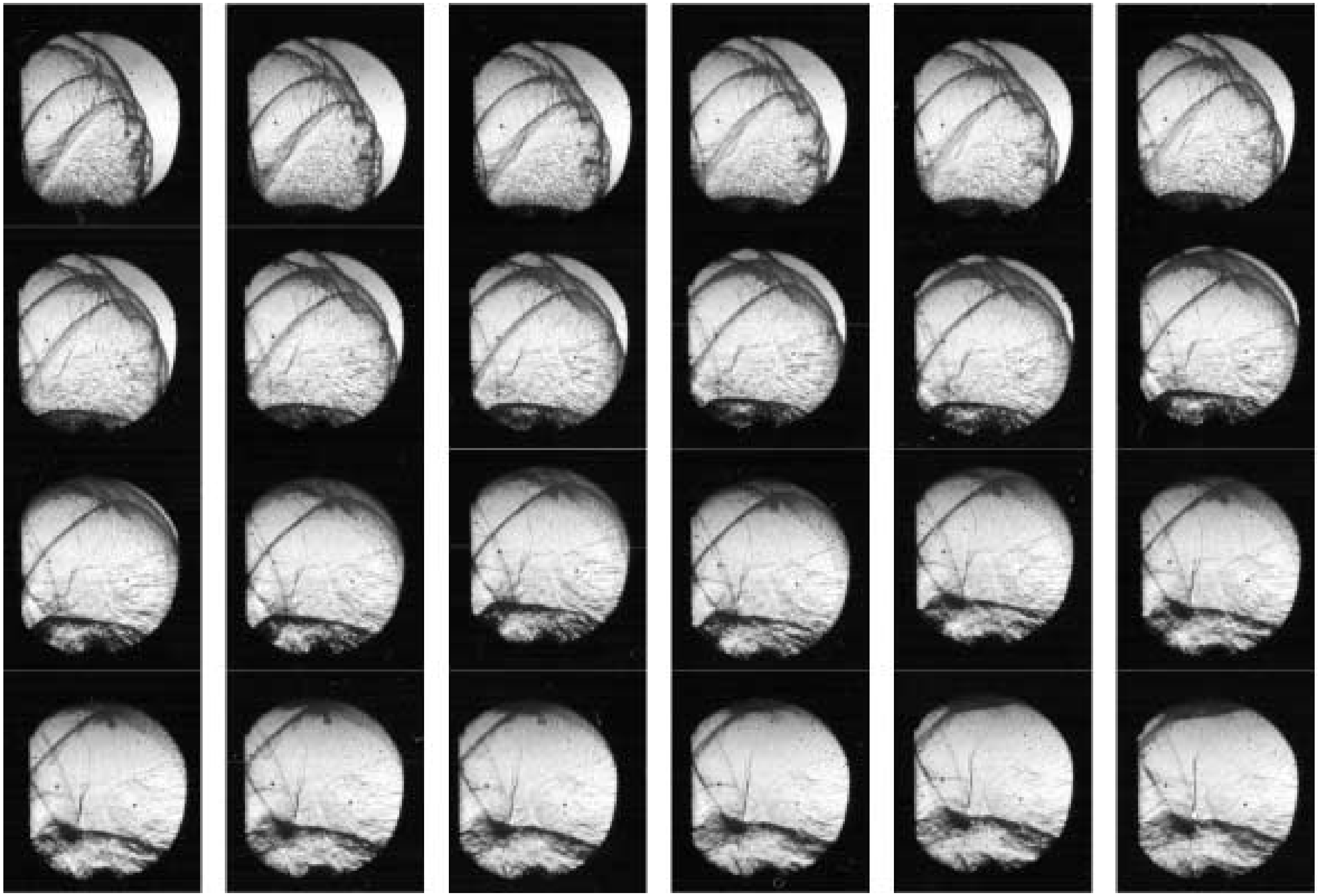

Stoichiometric hydrogen-oxygen mixtures with varying initial pressure

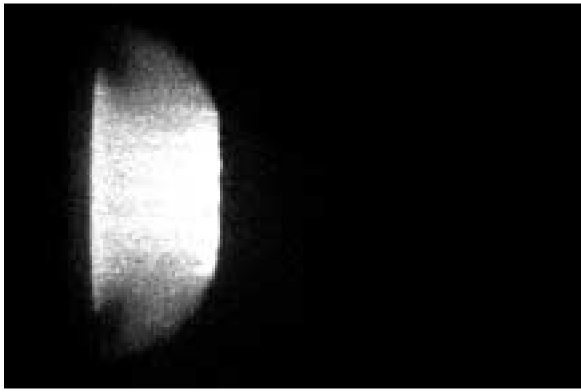
Shot 1272, P_1 = 30 kPa

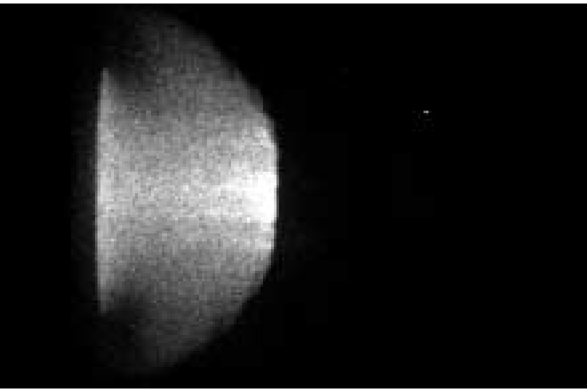
Shot 1273, P_1 = 30 kPa

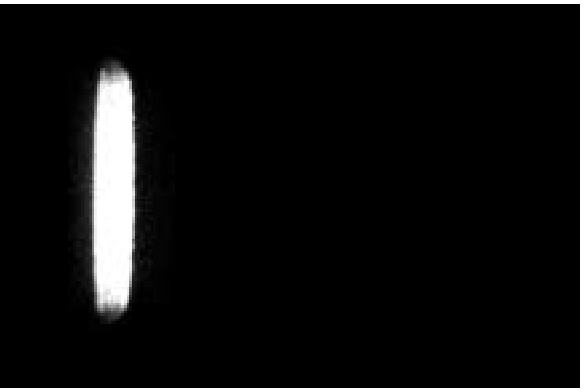
Shot 1275, P_1 = 50 kPa

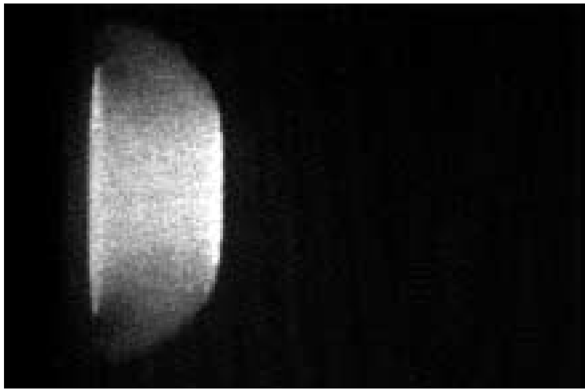
Shot 1277, P_1 = 50 kPa

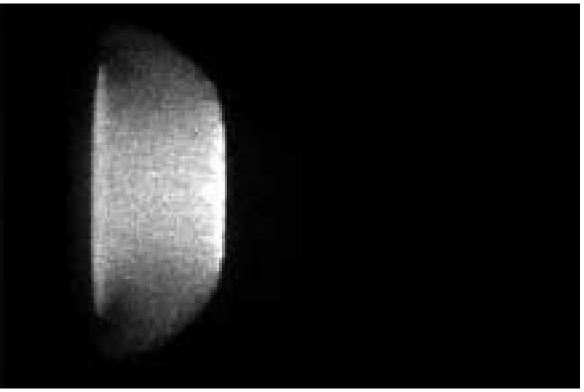
Shot 1276, P_1 = 50 kPa

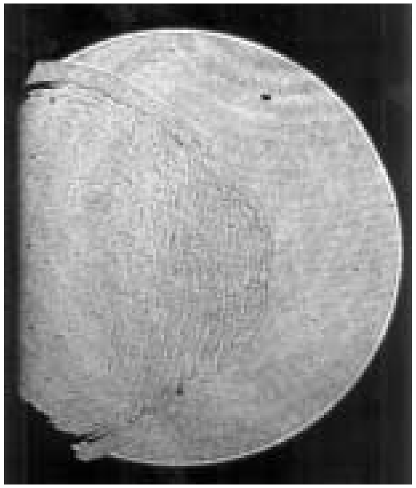
Shot 724, P_1 = 50 kPa

Stoichiometric hydrogen-oxygen mixtures with varying initial pressure

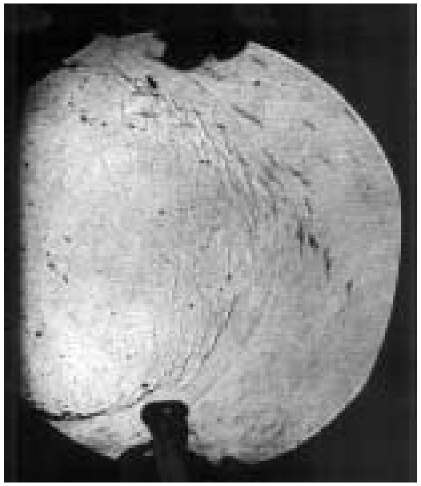

Shot 876, P_1 = 50 kPa

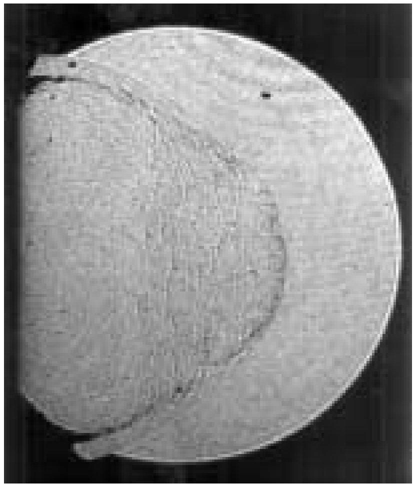

Shot 726, P_1 = 56.25 kPa

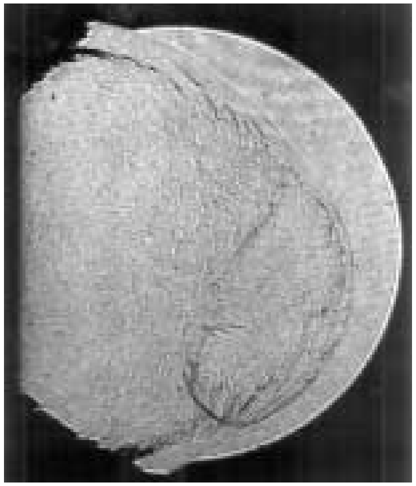

Shot 727, P_1 = 56.25 kPa

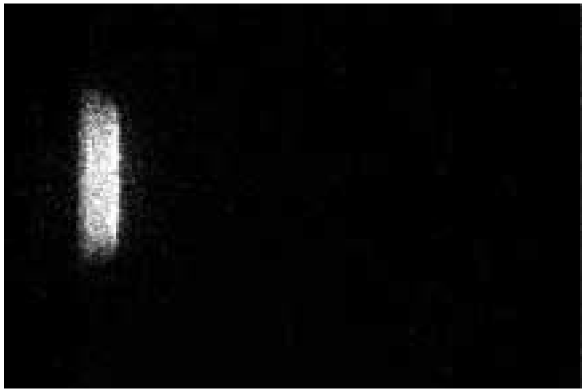

Shot 1020, P_1 = 62.5 kPa

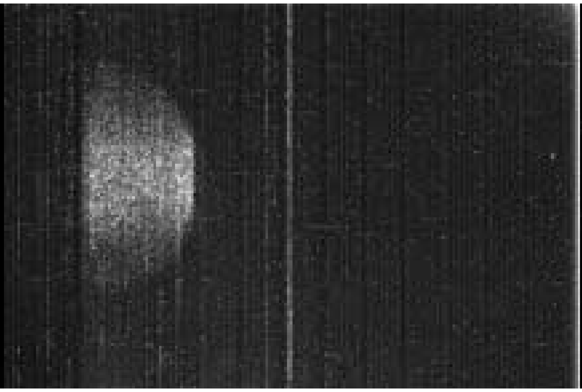

Shot 1019, P_1 = 62.5 kPa

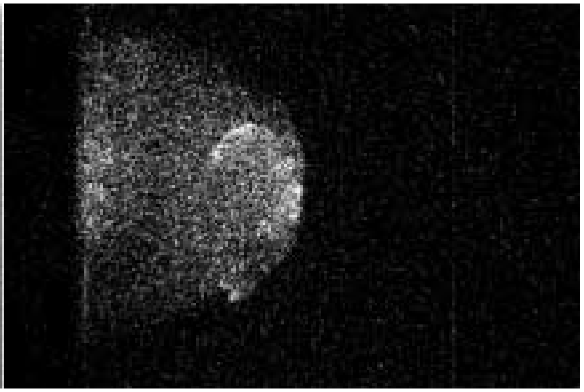

Shot 1031, P_1 = 62.5 kPa

Stoichiometric hydrogen-oxygen mixtures with varying initial pressure

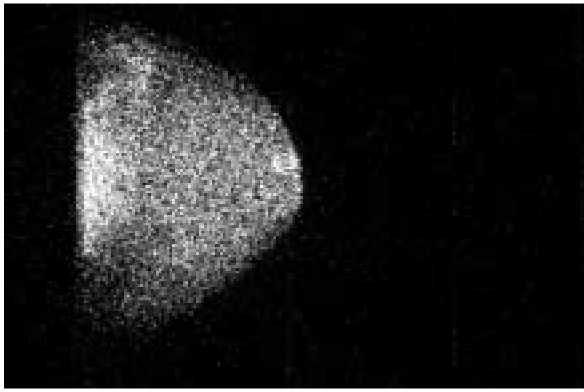
Shot 1029, P_1 = 62.5 kPa
(1.9% C_3H_6O)

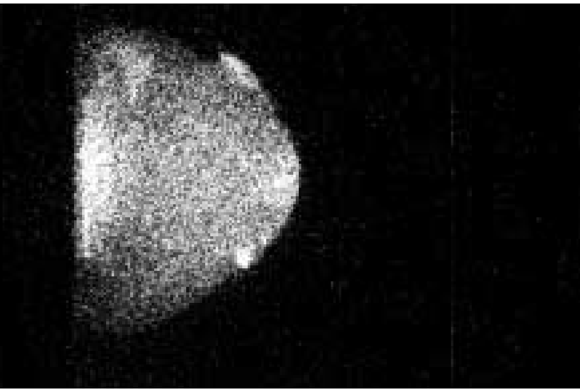
Shot 1028, P_1 = 62.5 kPa
(2.1% C_3H_6O)

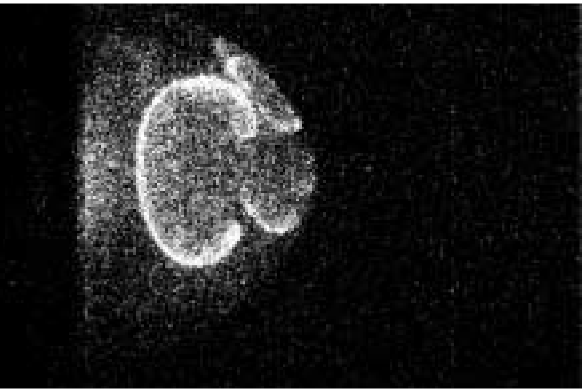
Shot 1030, P_1 = 62.5 kPa
(2.2% C_3H_6O)

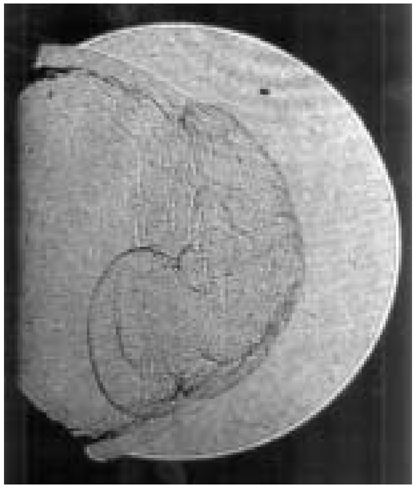
Shot 725, P_1 = 62.5 kPa

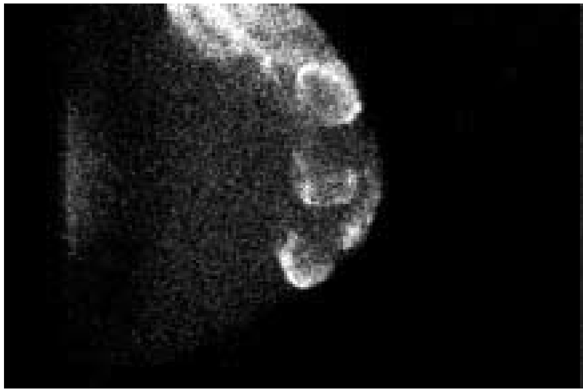
Shot 1038, P_1 = 62.5 kPa

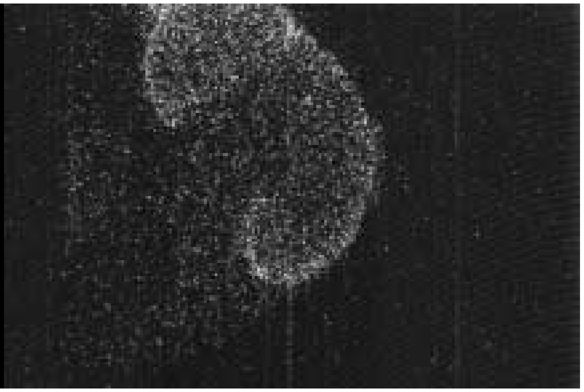
Shot 1039, P_1 = 62.5 kPa

Stoichiometric hydrogen-oxygen mixtures with varying initial pressure


Shot 1041, P_1 = 62.5 kPa

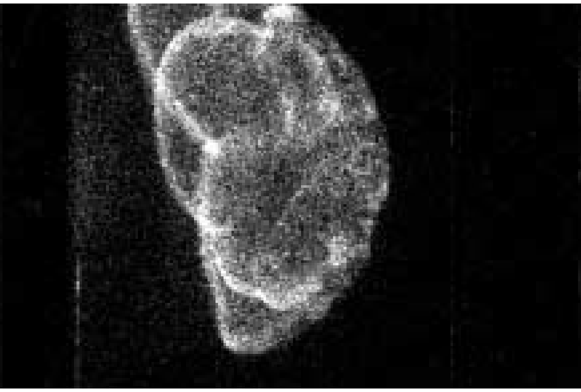
Shot 1033, P_1 = 62.5 kPa

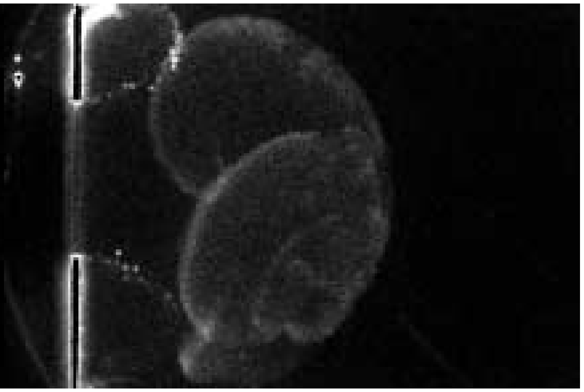
Shot 1037, P_1 = 62.5 kPa

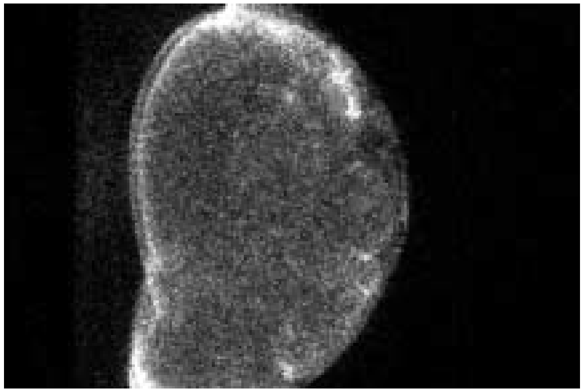
Shot 1032, P_1 = 62.5 kPa
(2.2% C_3H_6O)

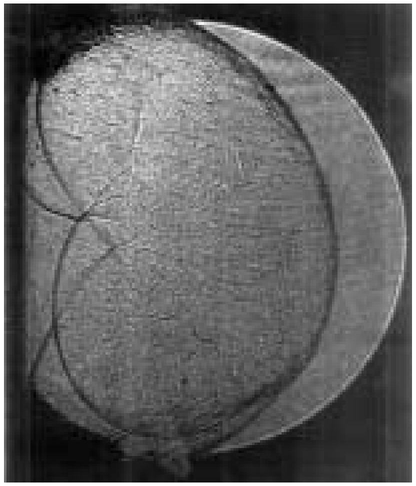
Shot 723, P_1 = 75 kPa

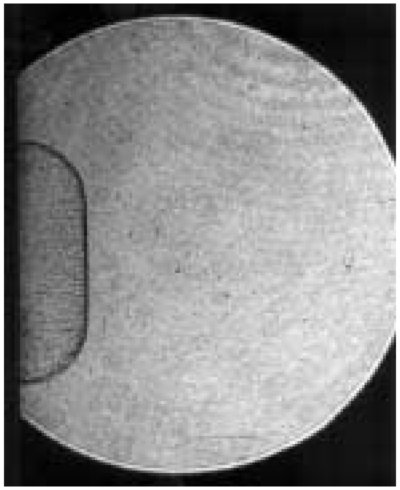
Shot 741, P_1 = 100 kPa

Stoichiometric hydrogen-oxygen mixtures with varying initial pressure

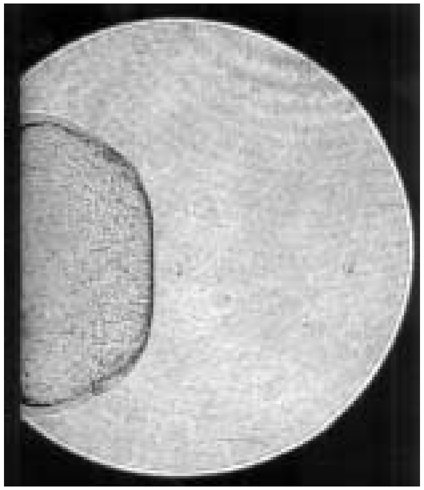

Shot 743, P_1 = 100 kPa

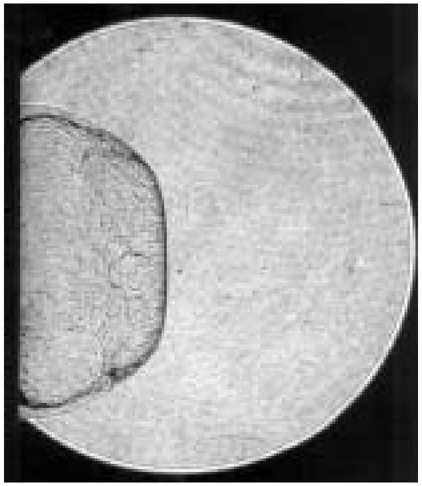

Shot 738, P_1 = 100 kPa

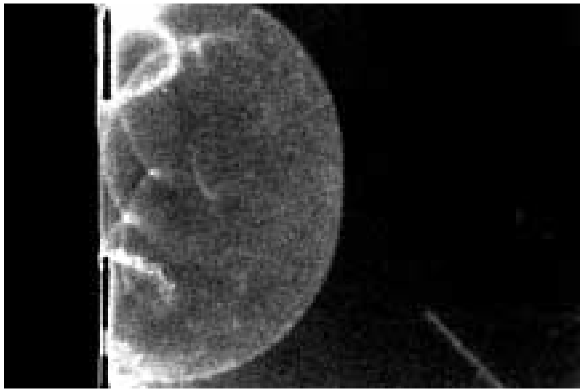

Shot 1046, P_1 = 100 kPa

Stoichiometric hydrogen-oxygen mixtures with varying initial pressure, Shot 1203, P_1 = 30 kPa

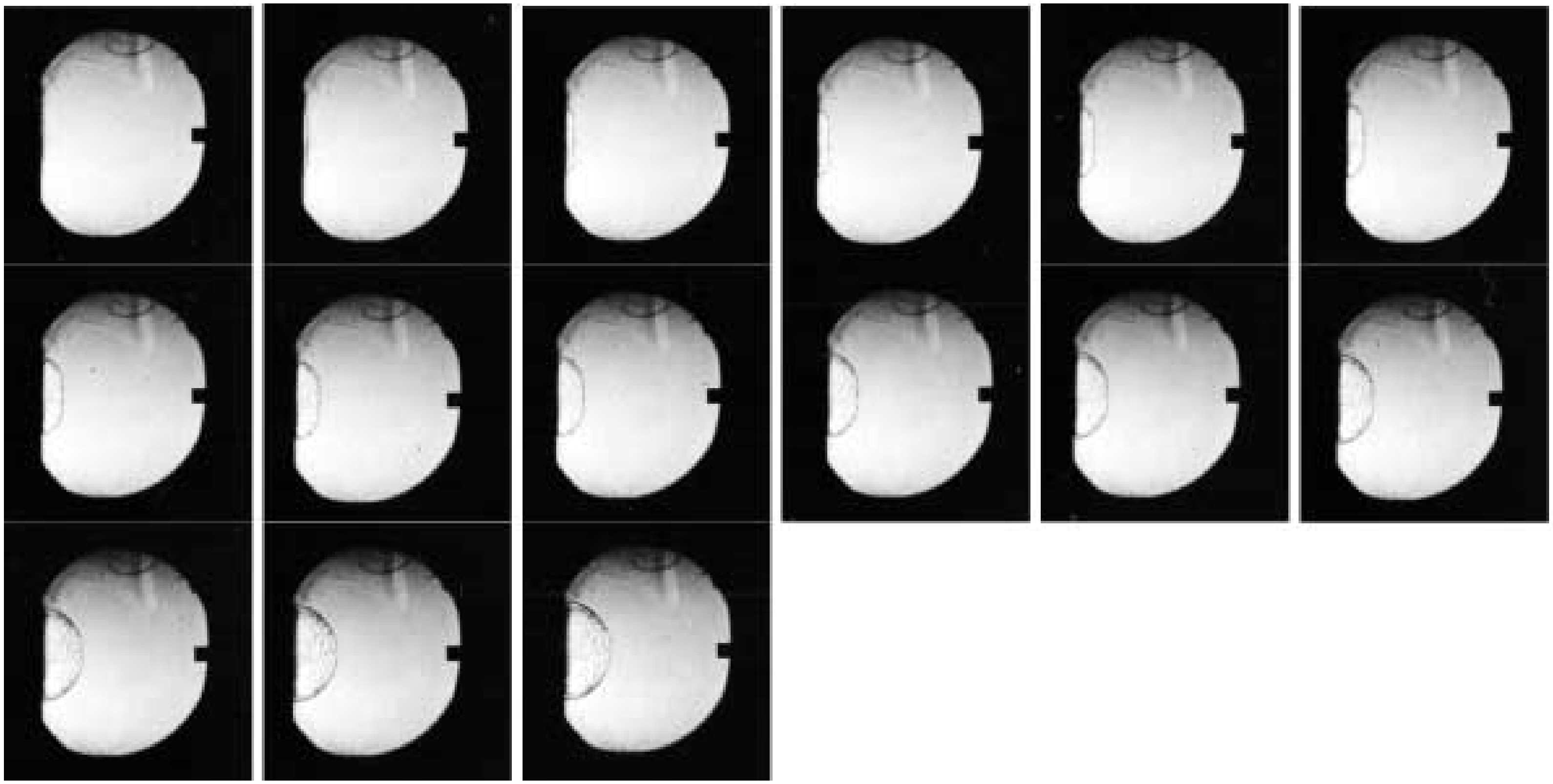

Stoichiometric hydrogen-oxygen mixtures with varying initial pressure, Shot 1076, P_1 = 50 kPa

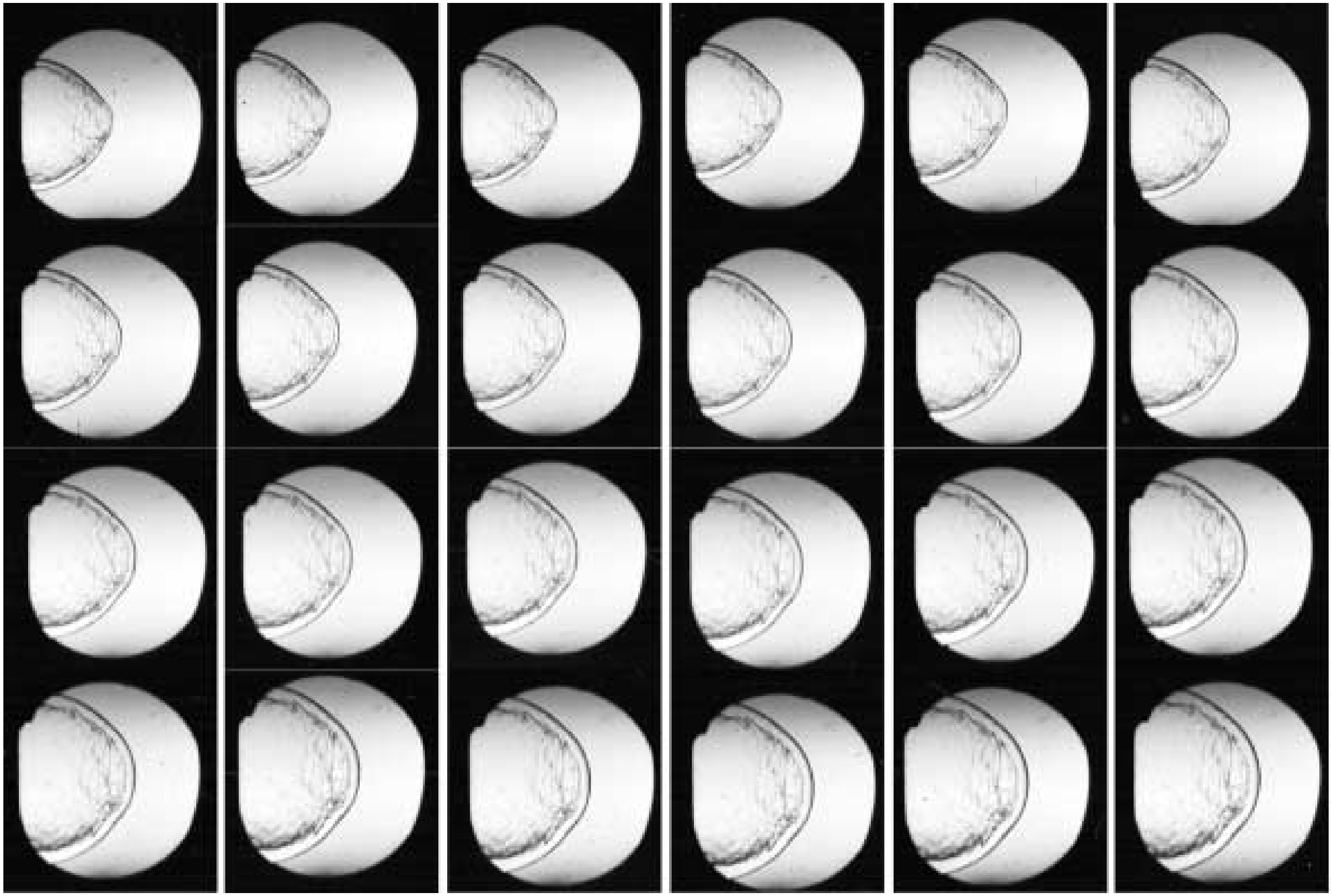

Stoichiometric hydrogen-oxygen mixtures with varying initial pressure, Shot 1077, P_1 = 50 kPa

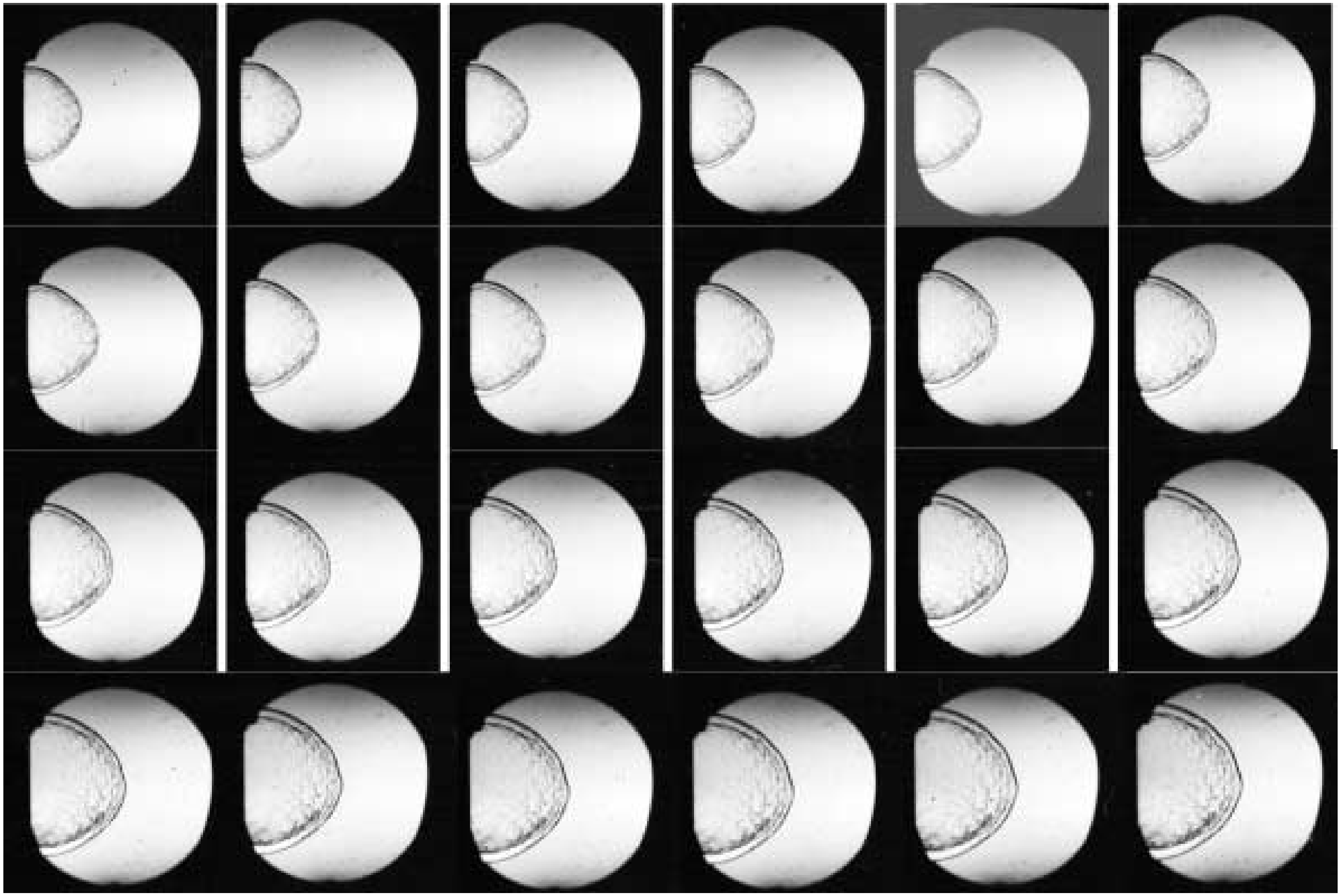

Stoichiometric hydrogen-oxygen mixtures with varying initial pressure, Shot 1193, P_1 = 50 kPa

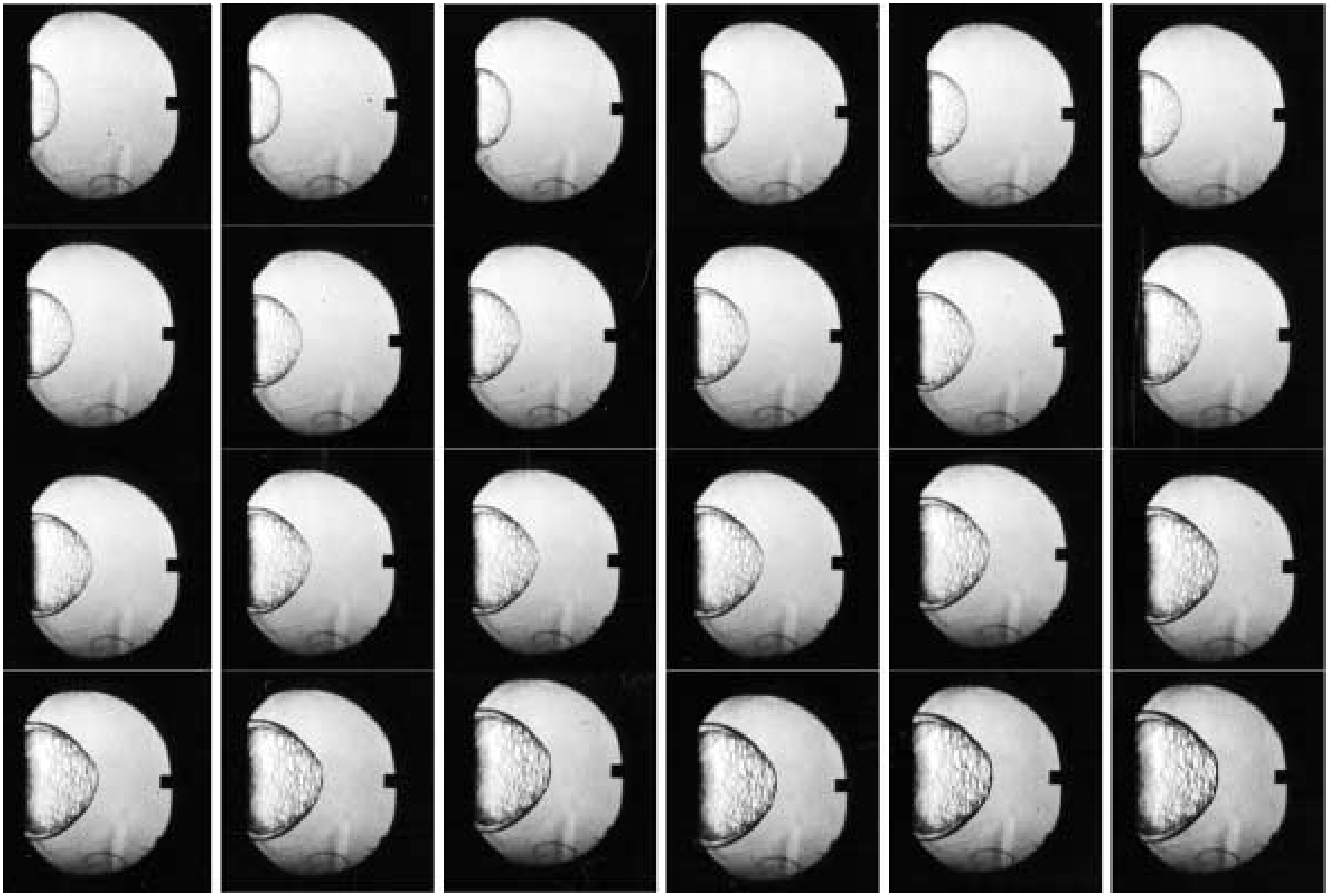

Stoichiometric hydrogen-oxygen mixtures with varying initial pressure, Shot 1195, P_1 = 50 kPa

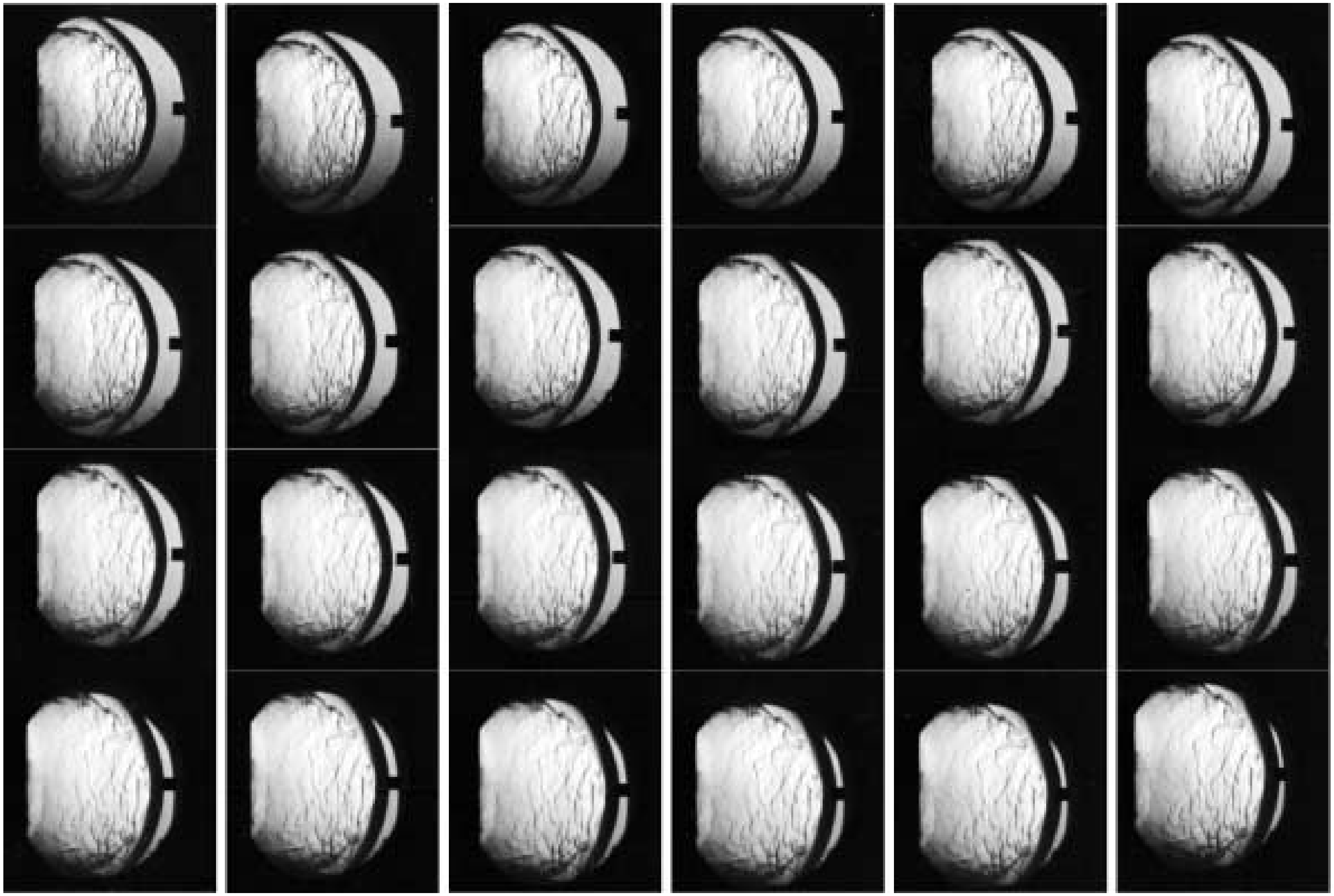

Stoichiometric hydrogen-oxygen mixtures with varying initial pressure, Shot 1196, P_1 = 50 kPa

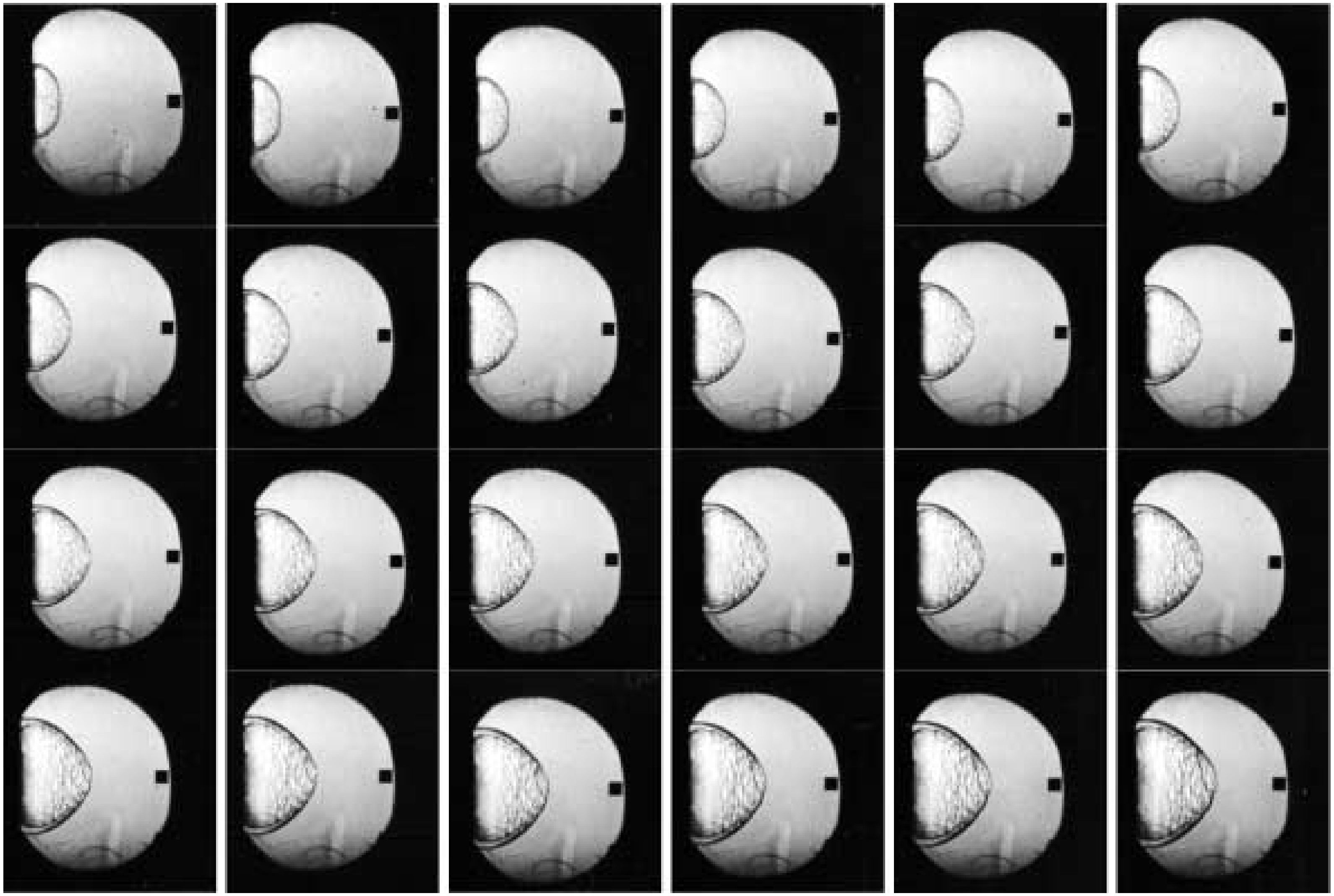

Stoichiometric hydrogen-oxygen mixtures with varying initial pressure, Shot 1078, P_1 = 62.5 kPa

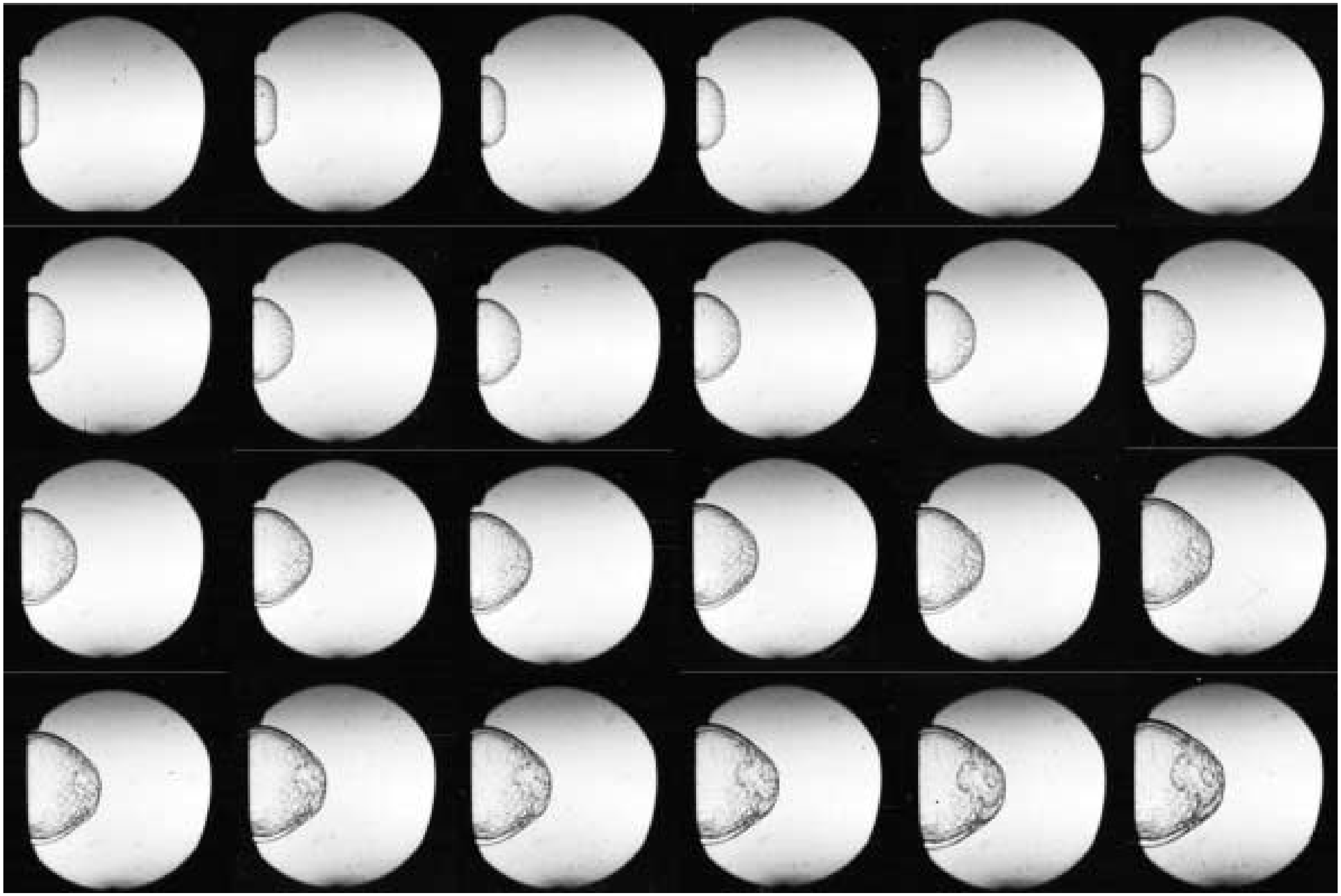

Stoichiometric hydrogen-oxygen mixtures with varying initial pressure, Shot 1079, P_1 = 100 kPa

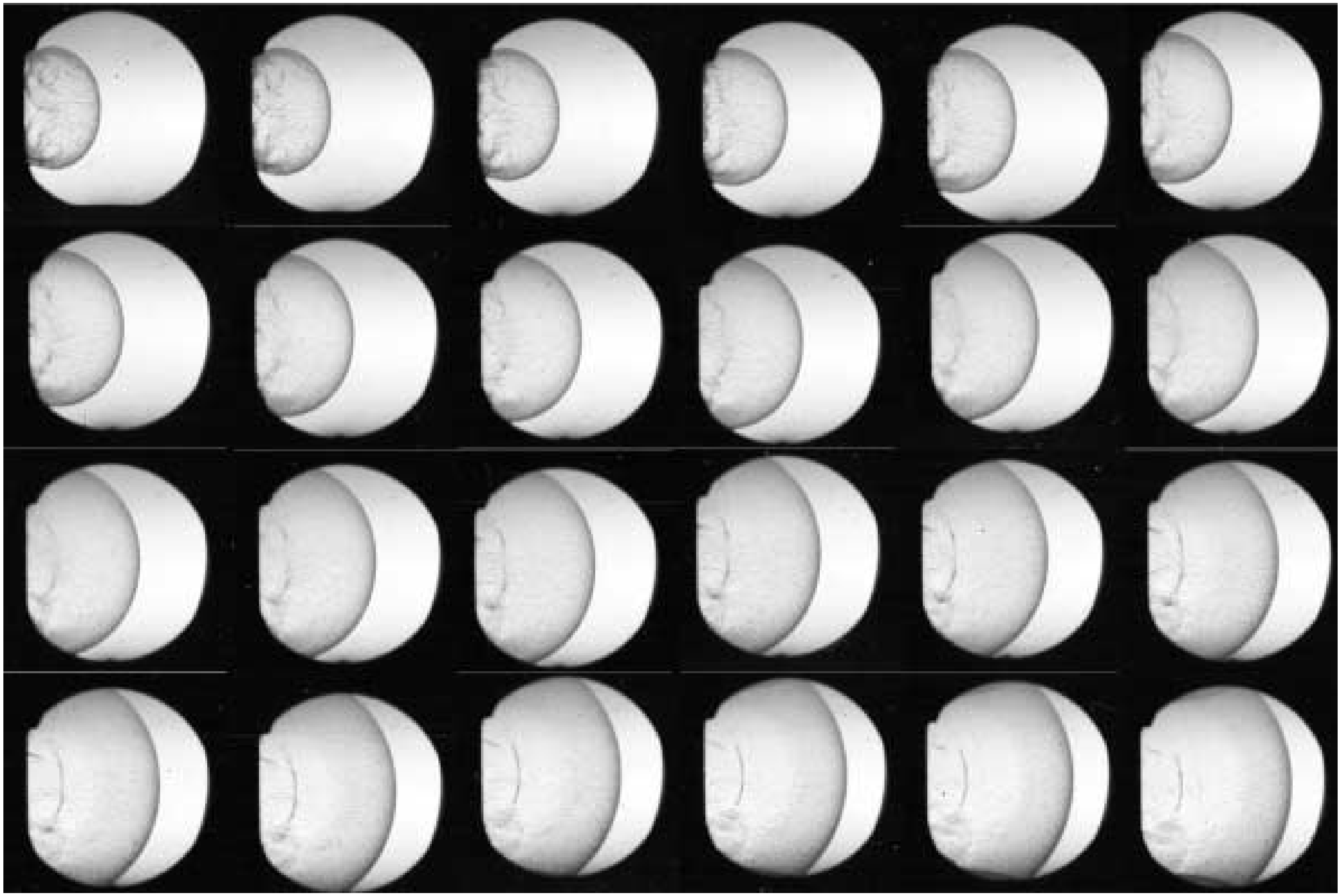

Stoichiometric hydrogen-oxygen mixtures with varying initial pressure, Shot 1194, P_1 = 100 kPa

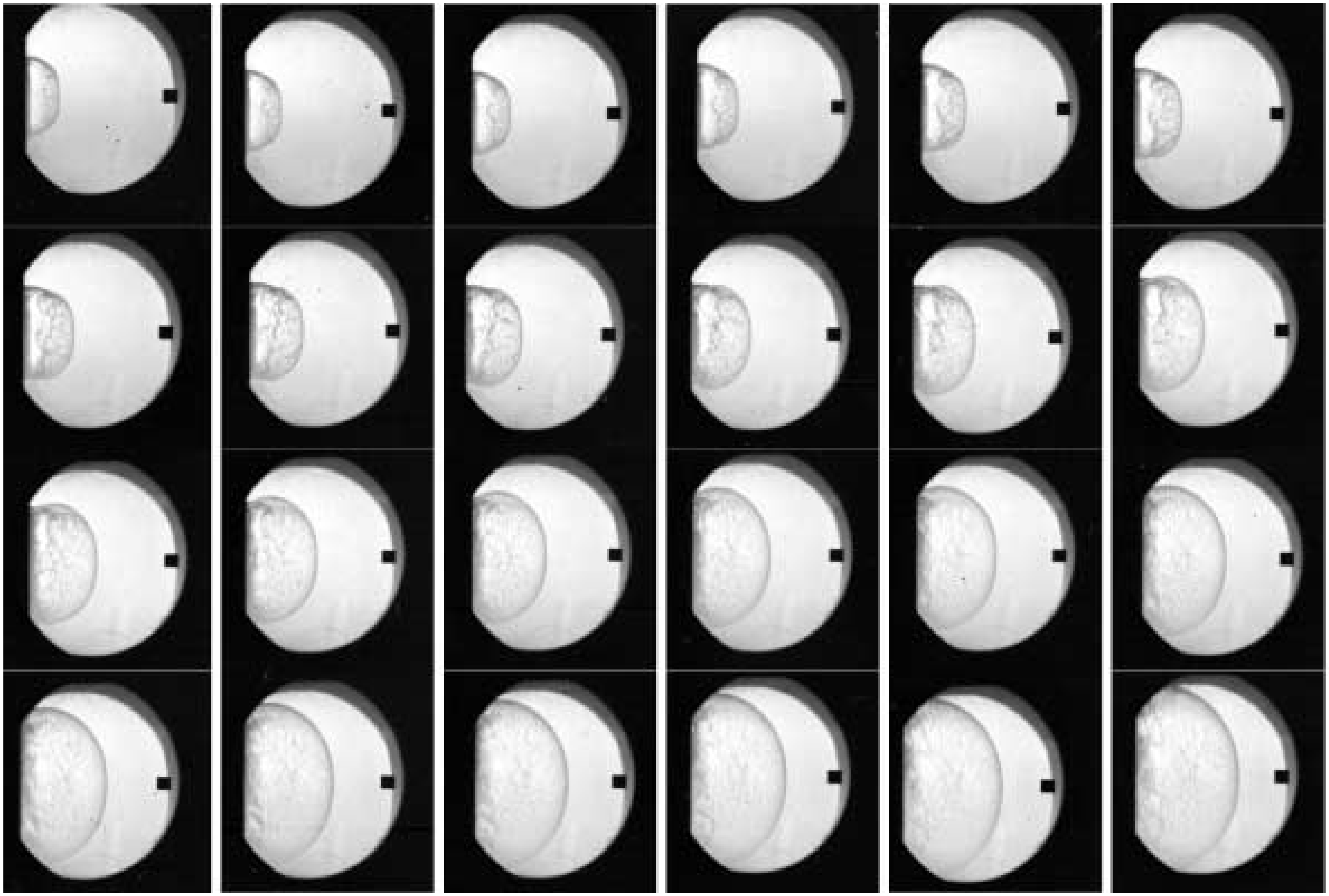

Stoichiometric hydrogen-oxygen mixtures with varying initial pressure, Shot 1199, P_1 = 100 kPa

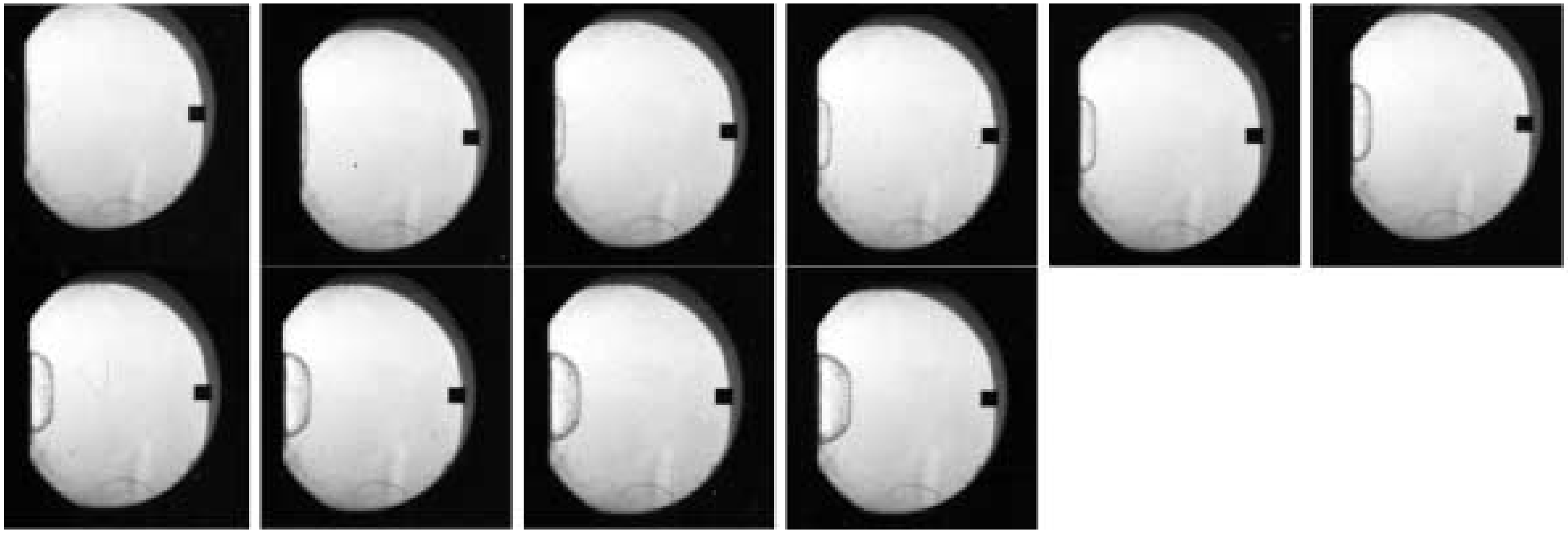

Stoichiometric hydrogen-oxygen-argon mixtures with varying argon dilution (P_1 = 100 kPa)

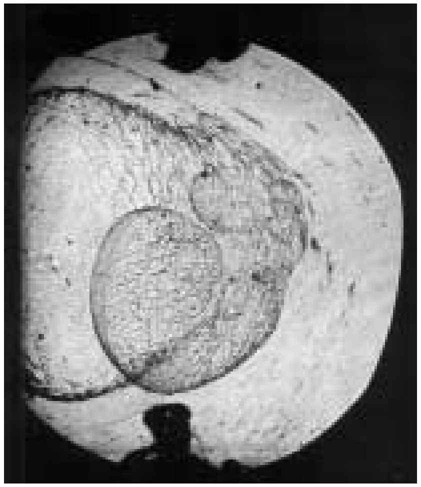

Shot 868, 65.3% Ar

Stoichiometric hydrogen-oxygen-argon mixtures with varying argon dilution (P_1 = 100 kPa), Shot 1206, 40% Ar

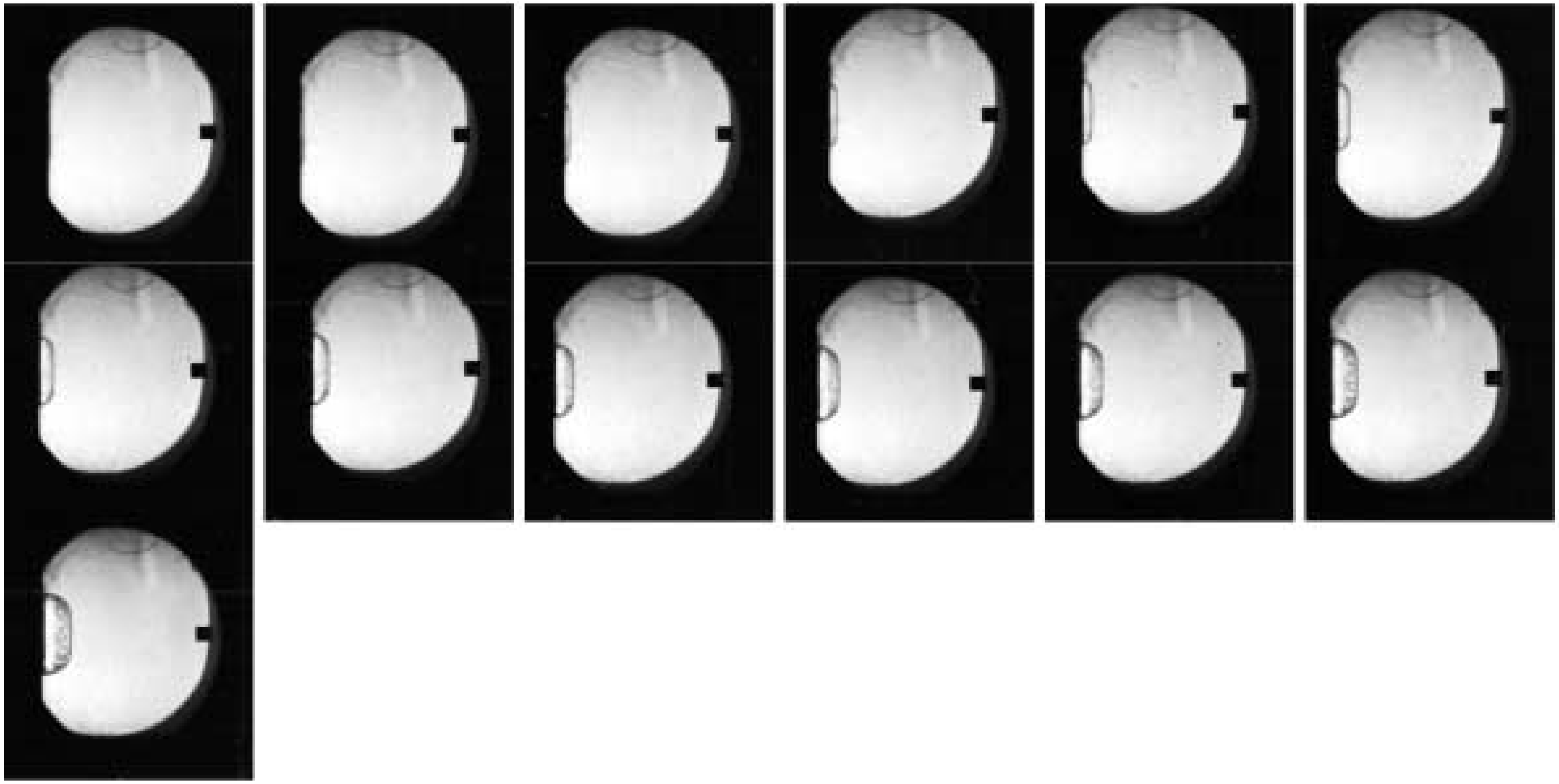

Stoichiometric hydrogen-oxygen-argon mixtures with varying argon dilution (P_1 = 100 kPa), Shot 1098, 65.3% Ar

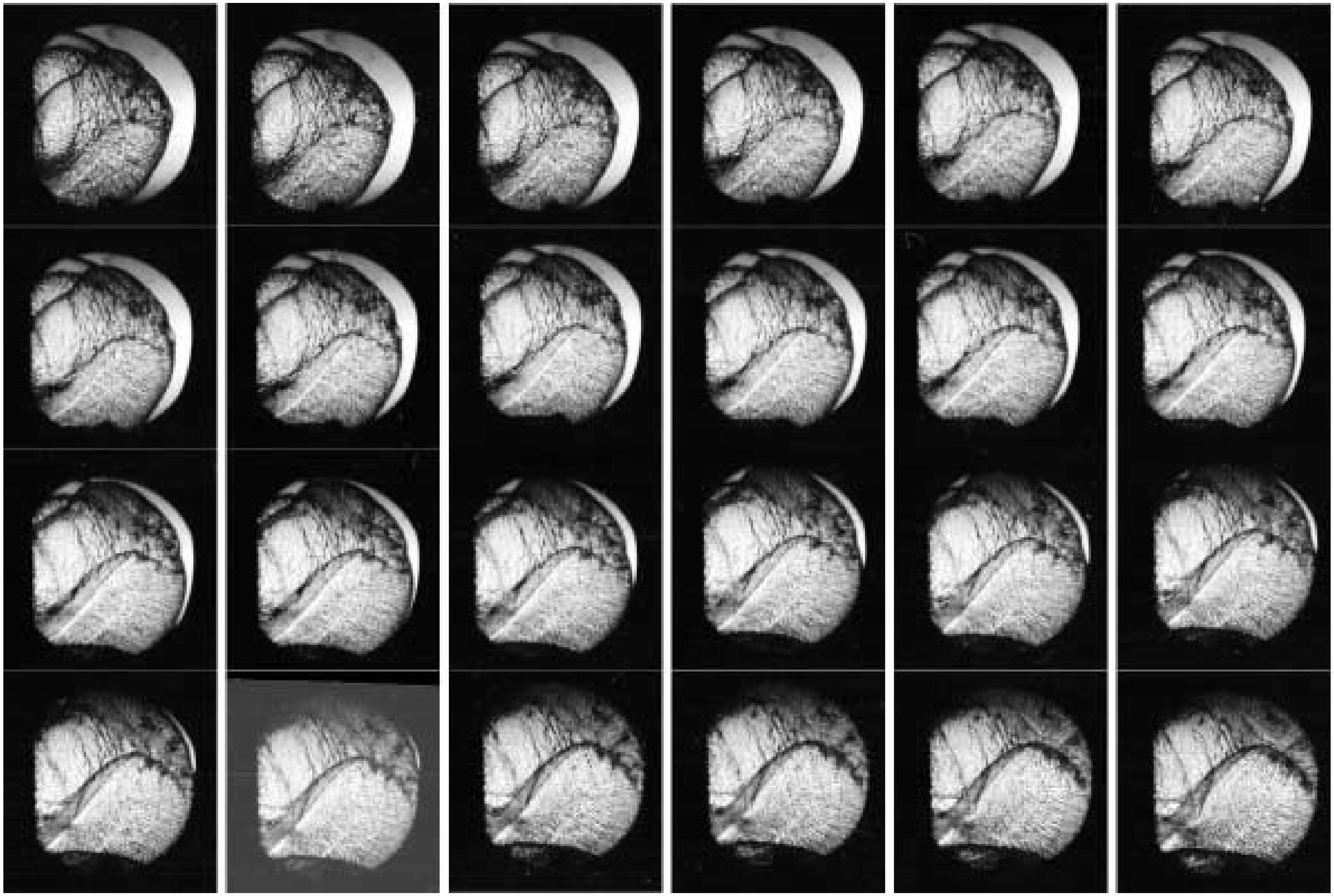

Stoichiometric hydrogen-oxygen-argon mixtures with varying argon dilution (P_1 = 100 kPa), Shot 1099, 65.3% Ar

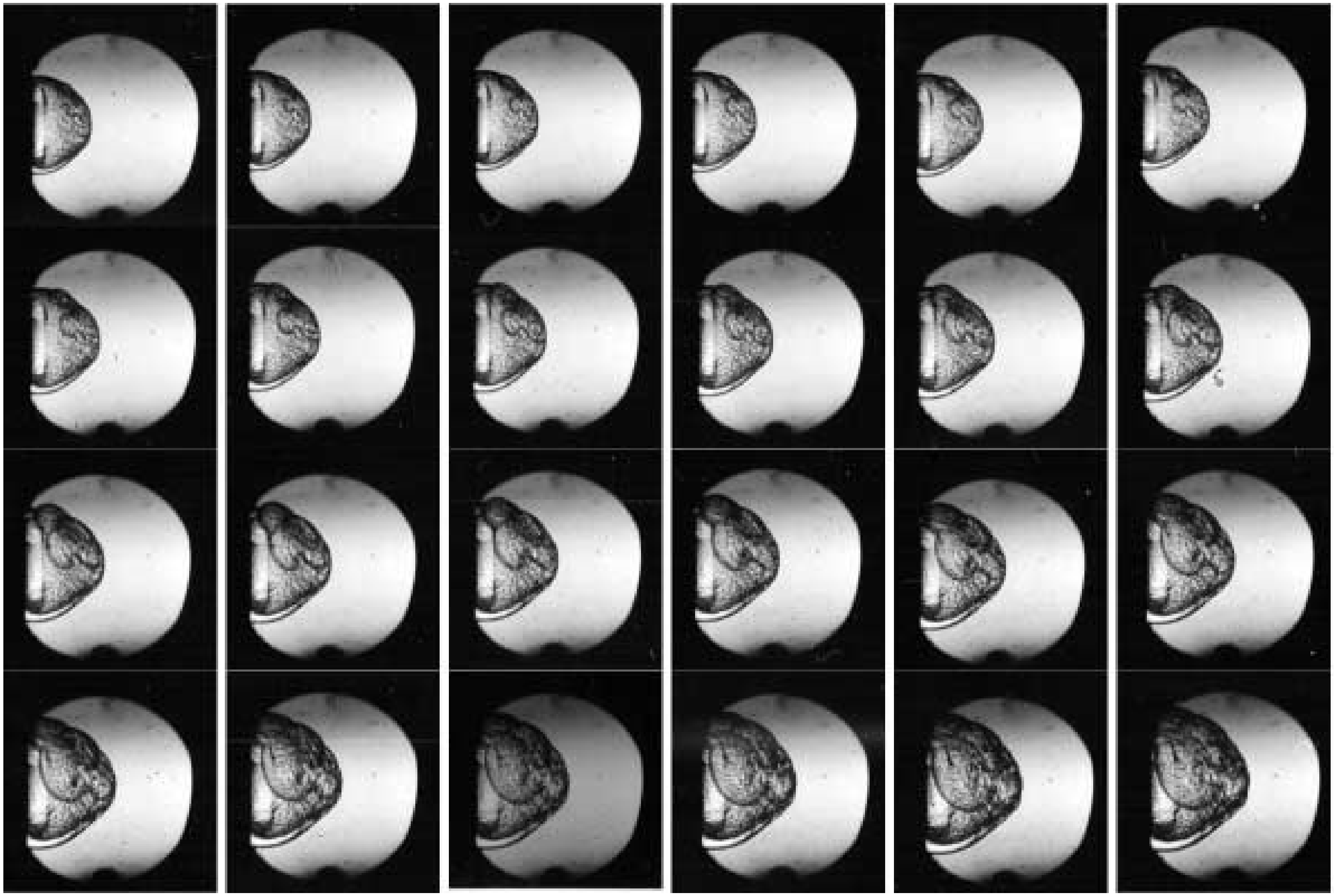

Stoichiometric hydrogen-oxygen-argon mixtures with varying argon dilution (P_1 = 100 kPa), Shot 1103, 65.3% Ar

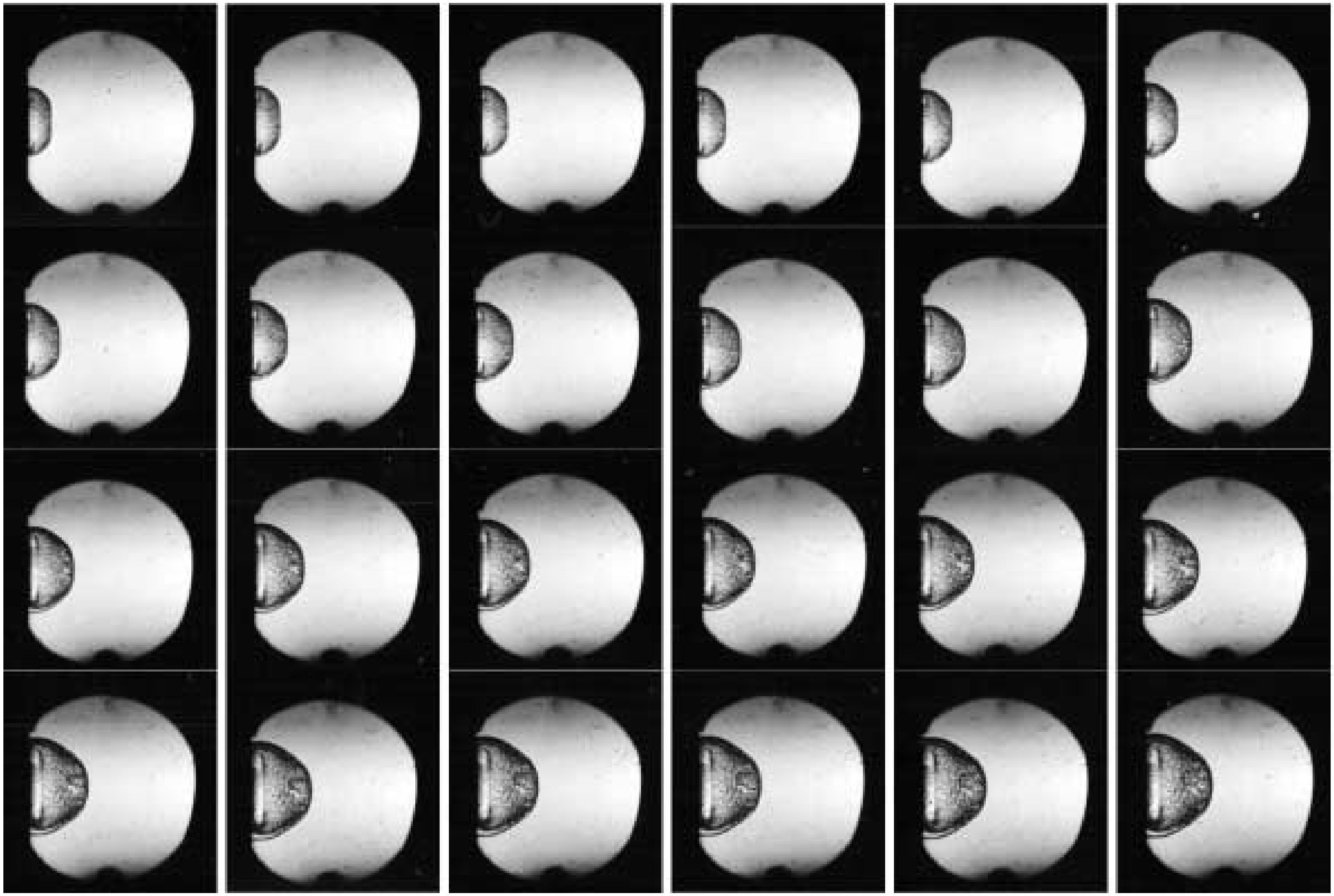

Stoichiometric hydrogen-oxygen-argon mixtures with varying argon dilution (P_1 = 100 kPa), Shot 1101, 67.5% Ar

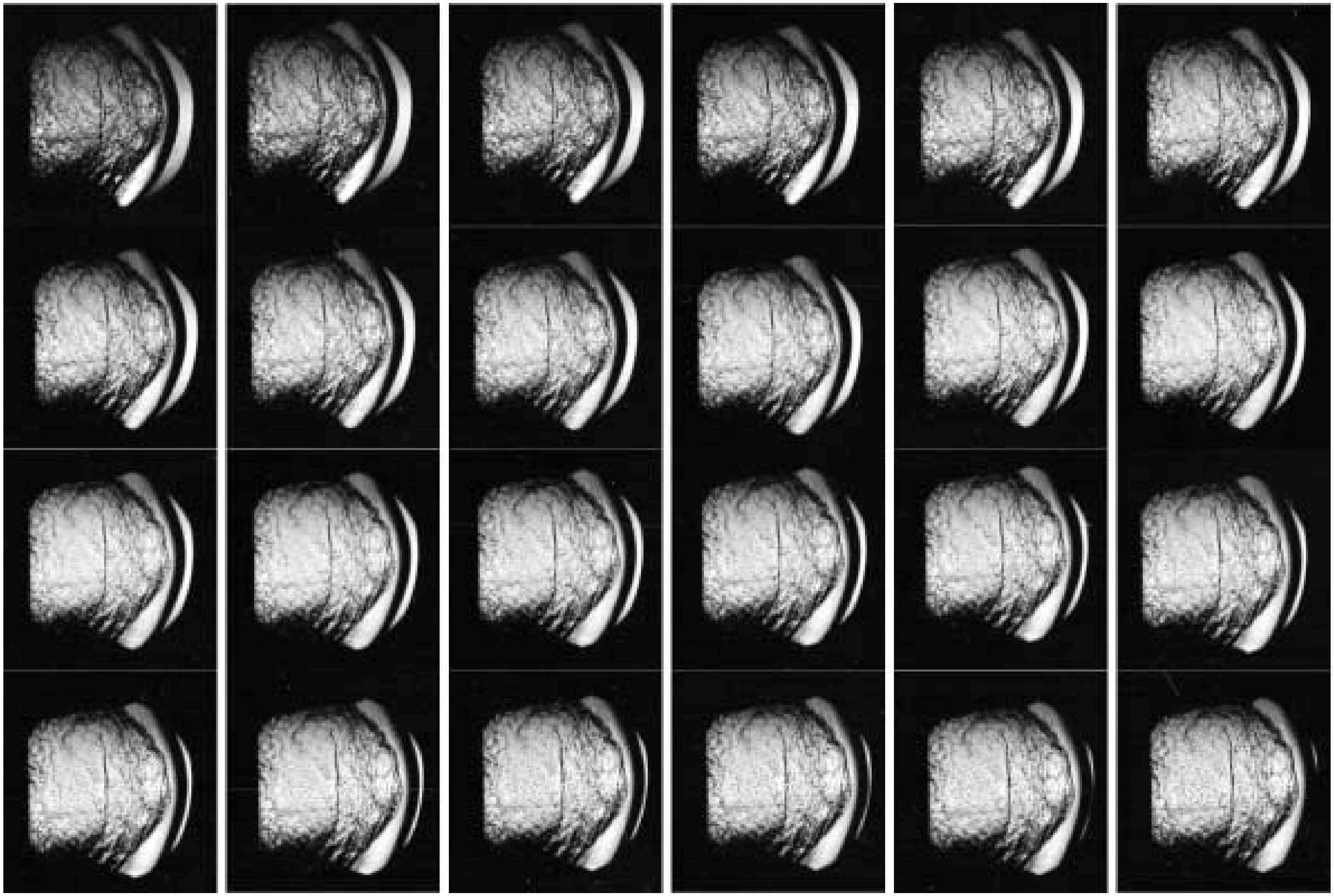

Stoichiometric hydrogen-oxygen-argon mixtures with varying argon dilution (P_1 = 100 kPa), Shot 1102, 67.5% Ar

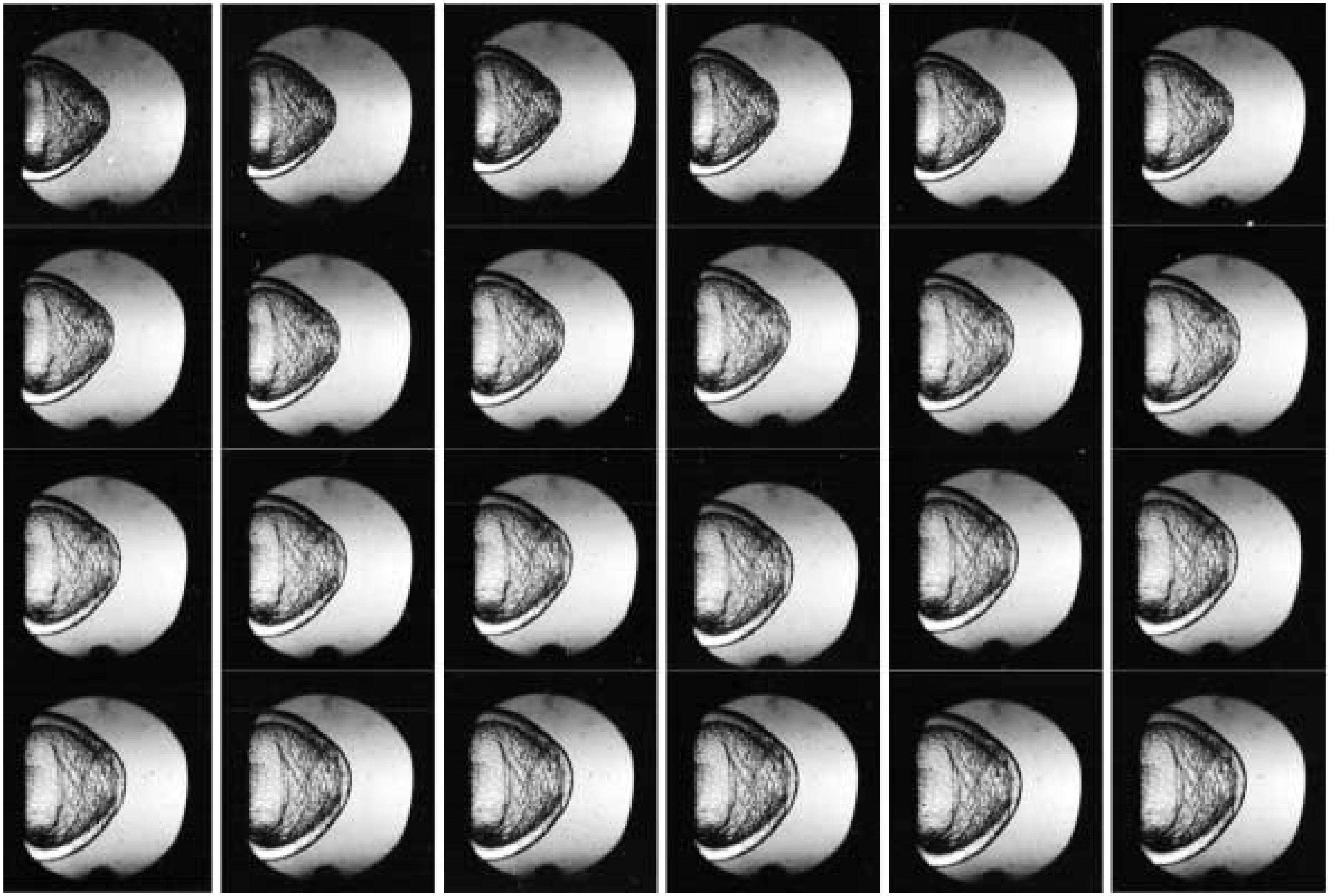

Stoichiometric hydrogen-oxygen-carbon dioxide mixtures with varying carbon dioxide dilution (P_1 = 100 kPa)

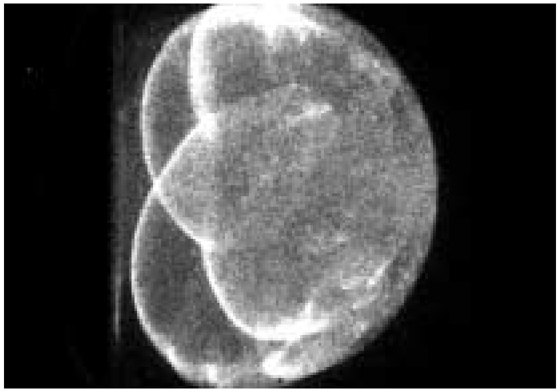

Shot 1107, 3.2% CO_2

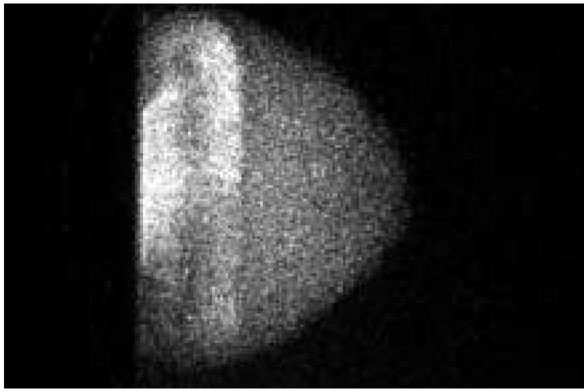

Shot 1106, 6.3% CO_2

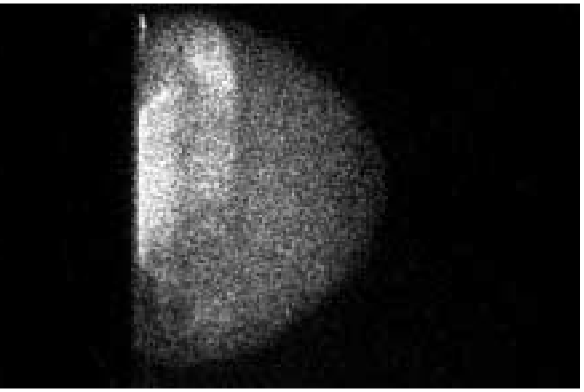

Shot 1105, 9.1% CO_2

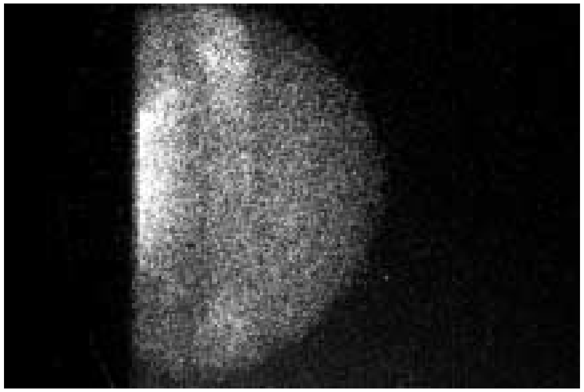

Shot 1104, 14.3% CO_2

Stoichiometric hydrogen-oxygen-carbon dioxide mixtures with varying CO_2 dilution (P_1 = 100 kPa), Shot 1113, 3.2% CO_2

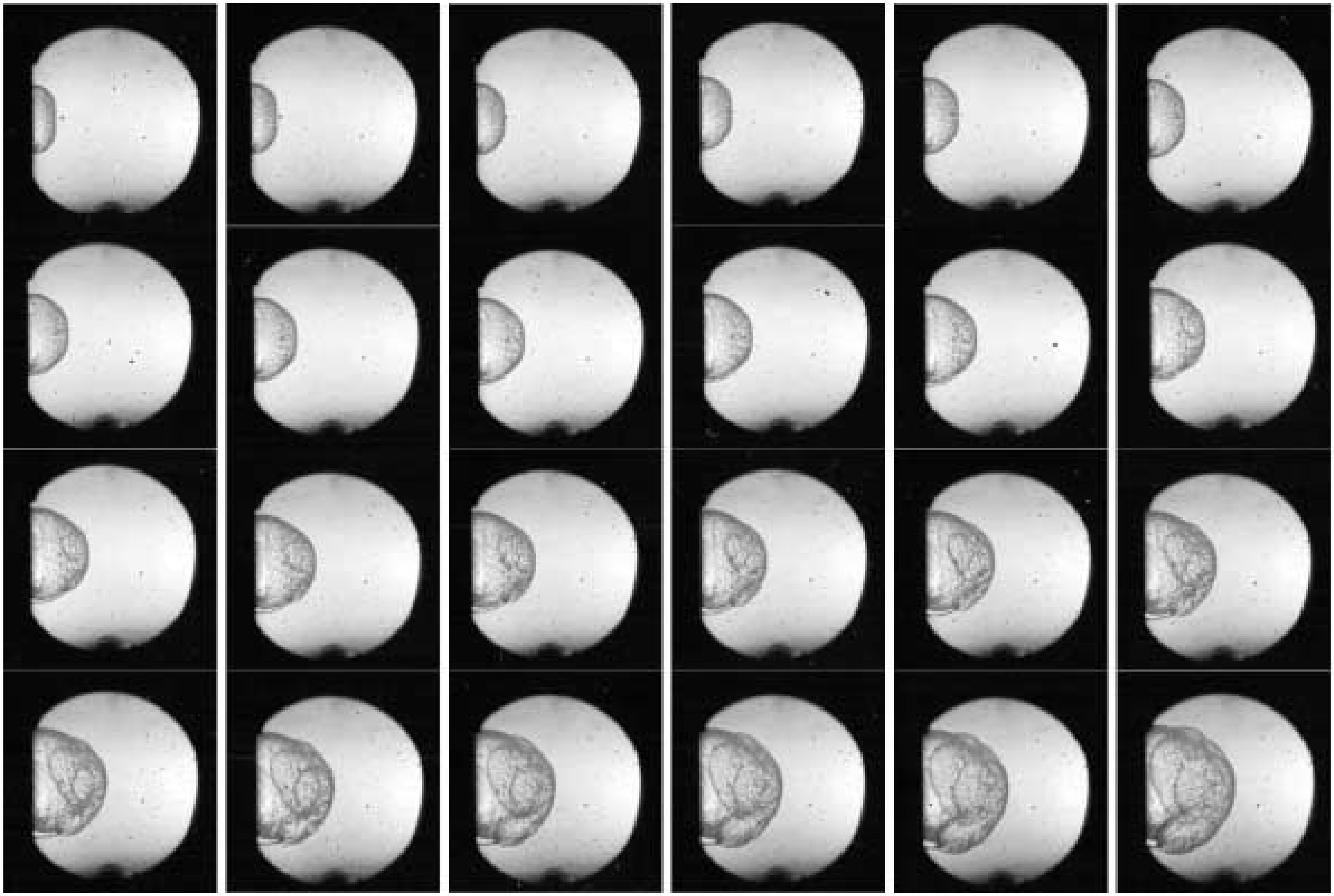

Stoichiometric hydrogen-oxygen-carbon dioxide mixtures with varying CO_2 dilution (P_1 = 100 kPa), Shot 1114, 6.3% CO_2

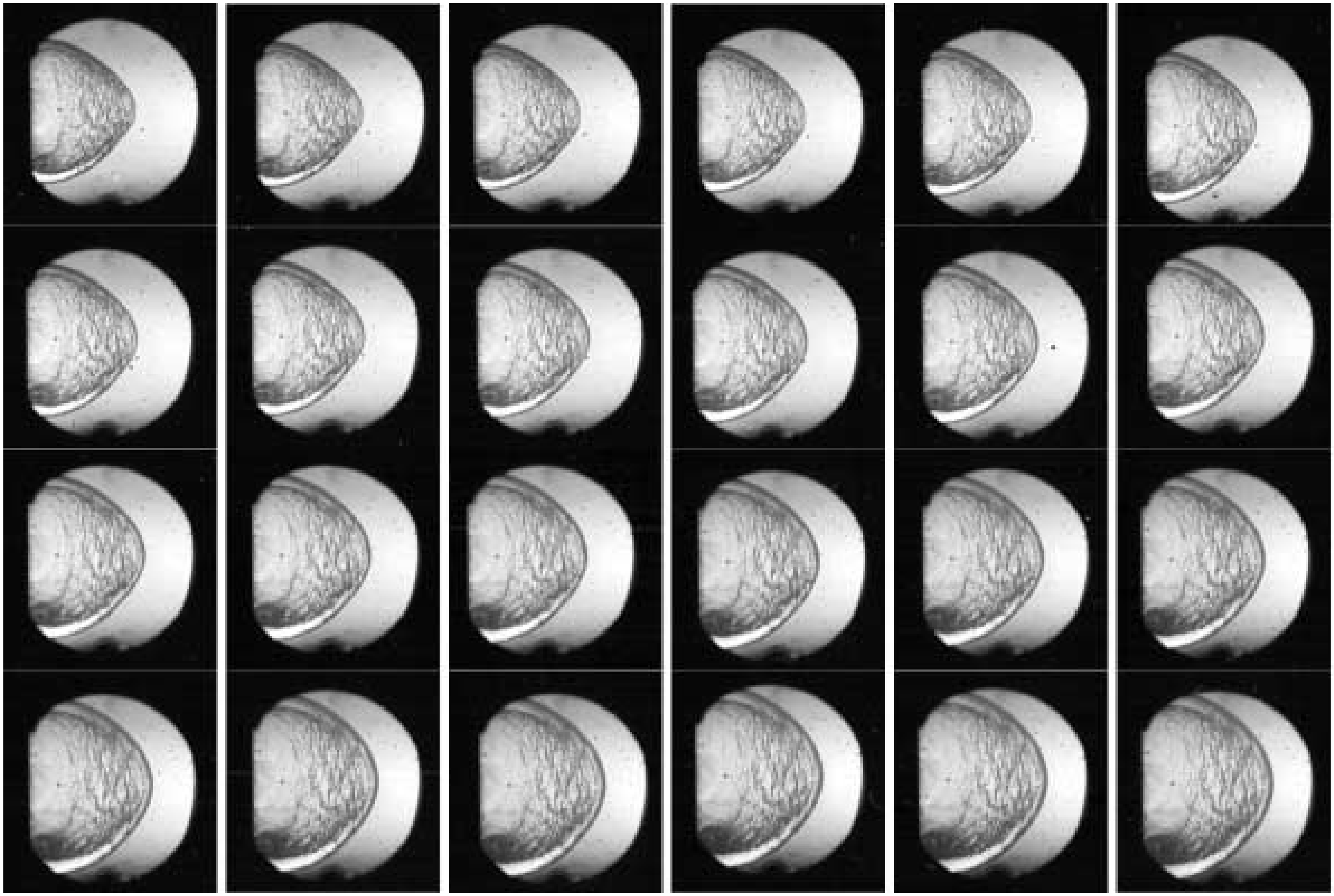

Stoichiometric hydrogen-oxygen-carbon dioxide mixtures with varying CO_2 dilution (P_1 = 100 kPa), Shot 1213, 14.3% CO_2

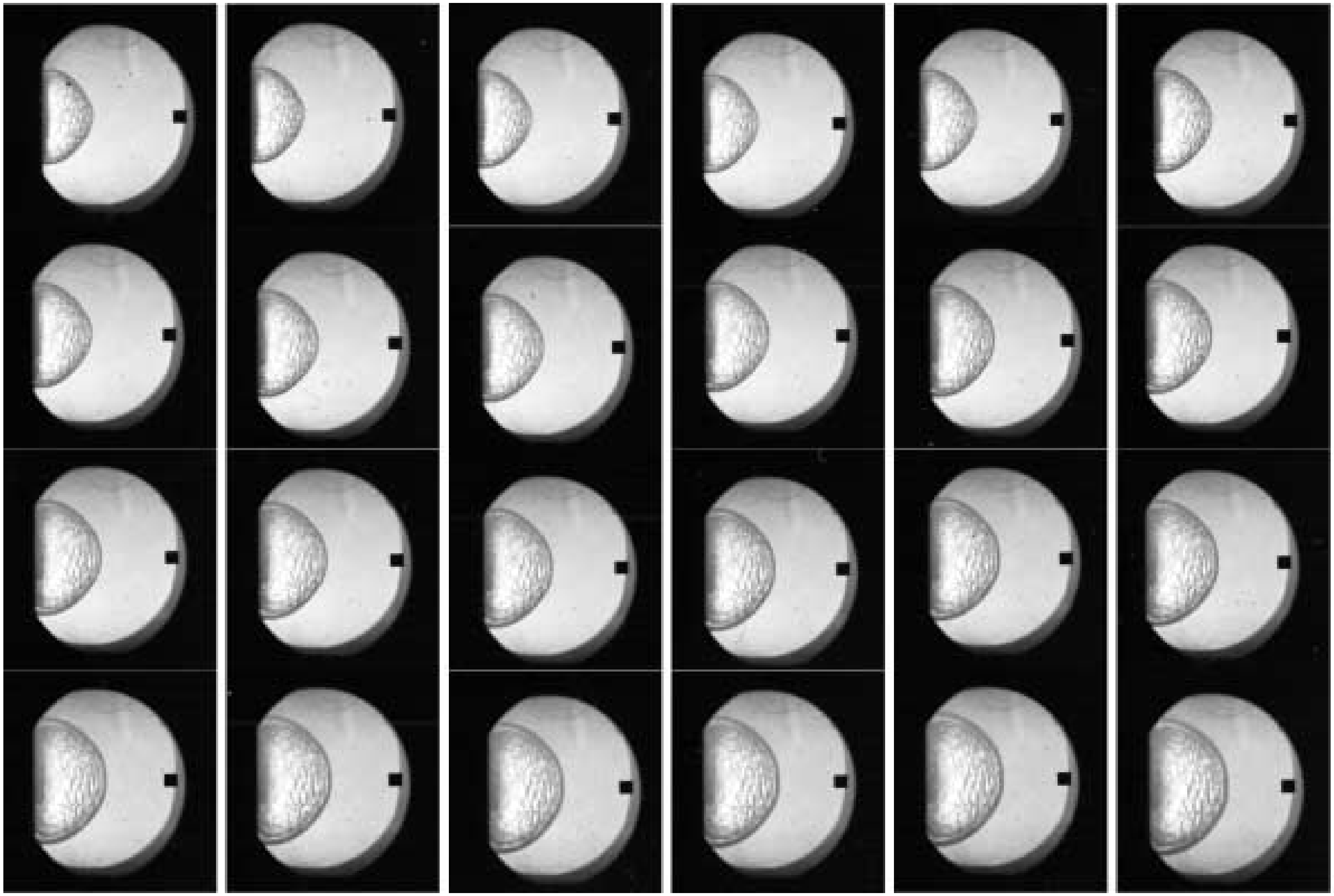

Stoichiometric hydrogen-oxygen-carbon dioxide mixtures with varying CO_2 dilution (P_1 = 100 kPa), Shot 1214, 14.3% CO_2

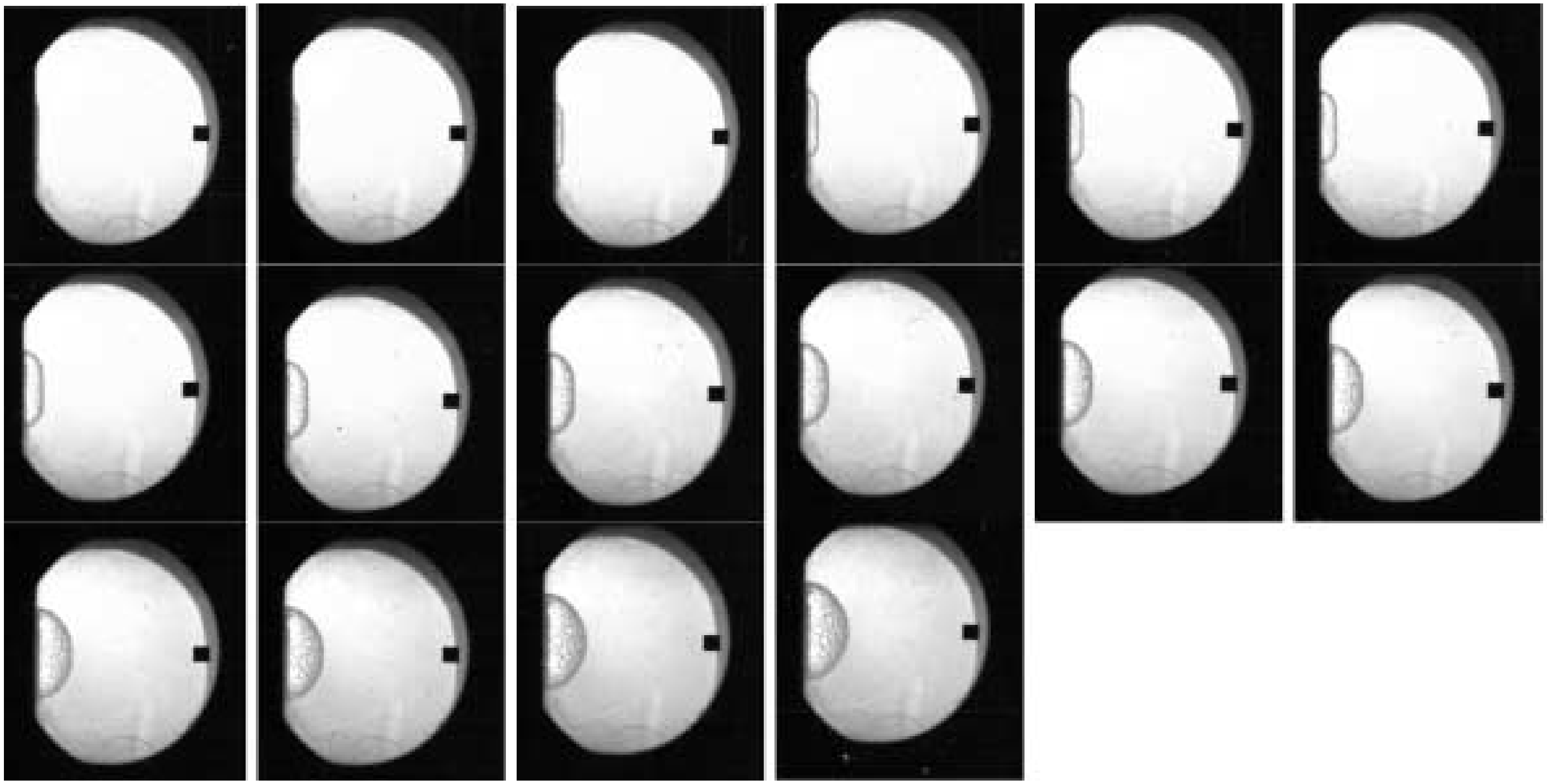

Stoichiometric hydrogen-oxygen-helium mixtures with varying helium dilution (P_1 = 100 kPa)

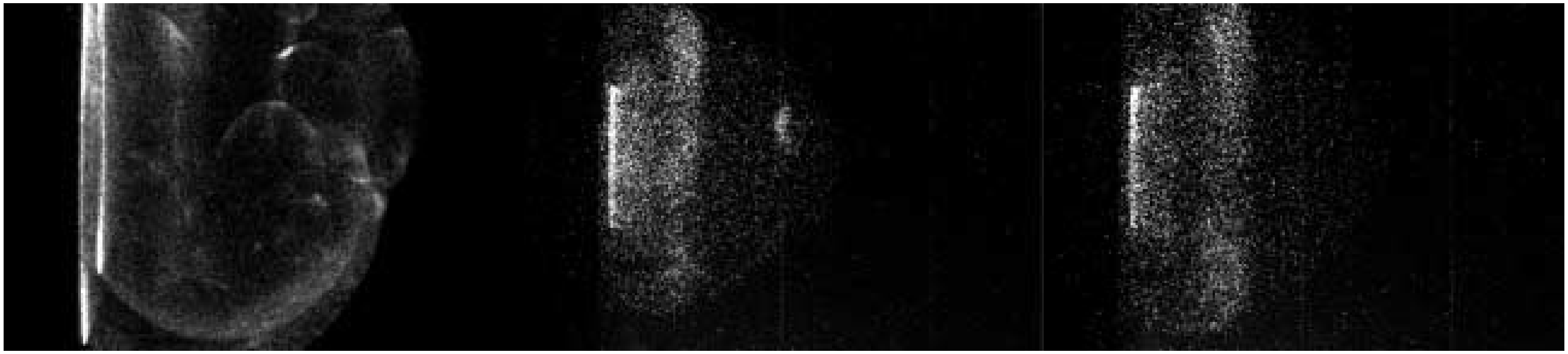

Shot 1086, 45.5% He

Shot 1084, 50% He

Shot 1087, 53.8% He

Stoichiometric hydrogen-oxygen-helium mixtures with varying helium dilution (P_1 = 100 kPa), Shot 1201, 25% He

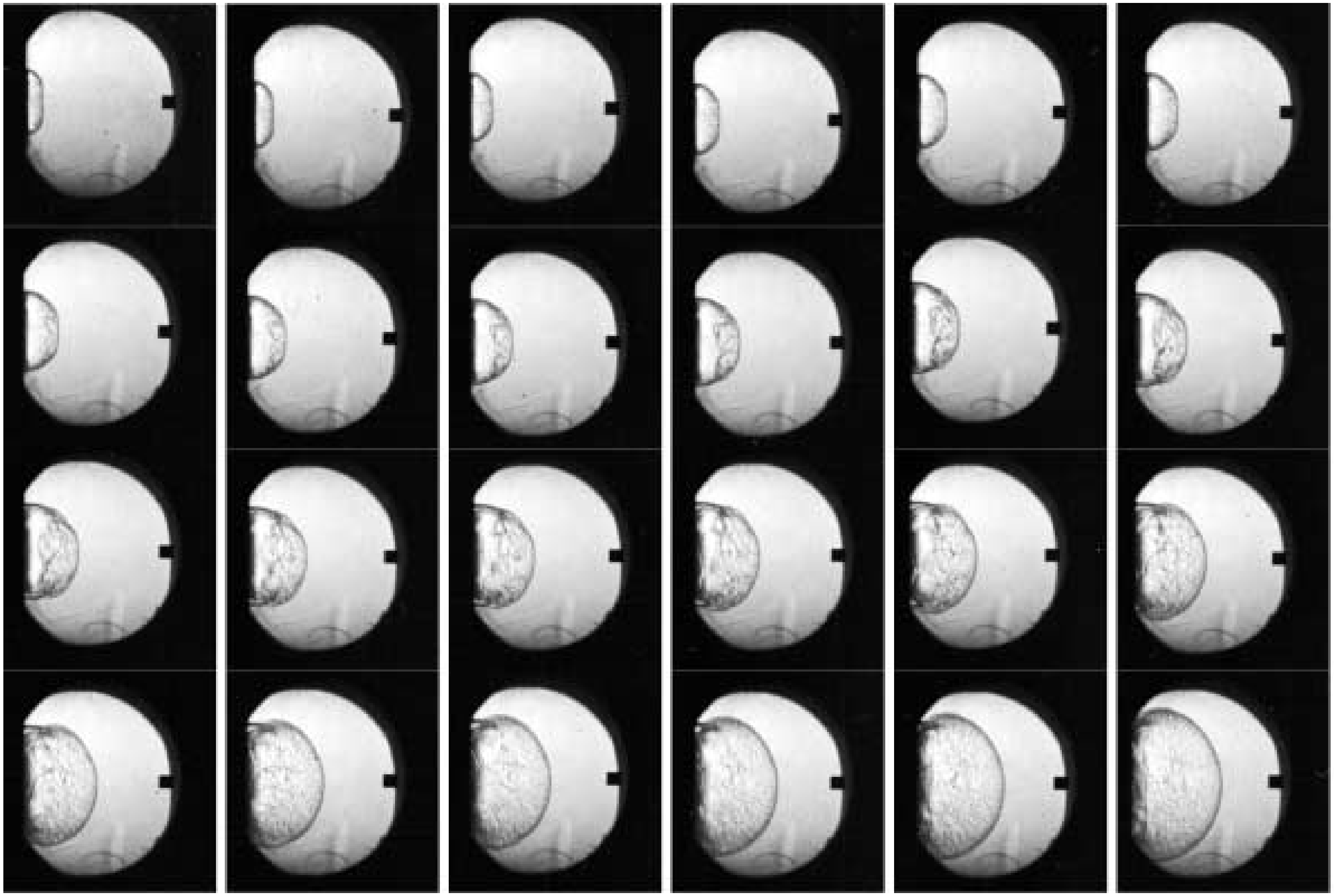

Stoichiometric hydrogen-oxygen-helium mixtures with varying helium dilution (P_1 = 100 kPa), Shot 1090, 45.5% He

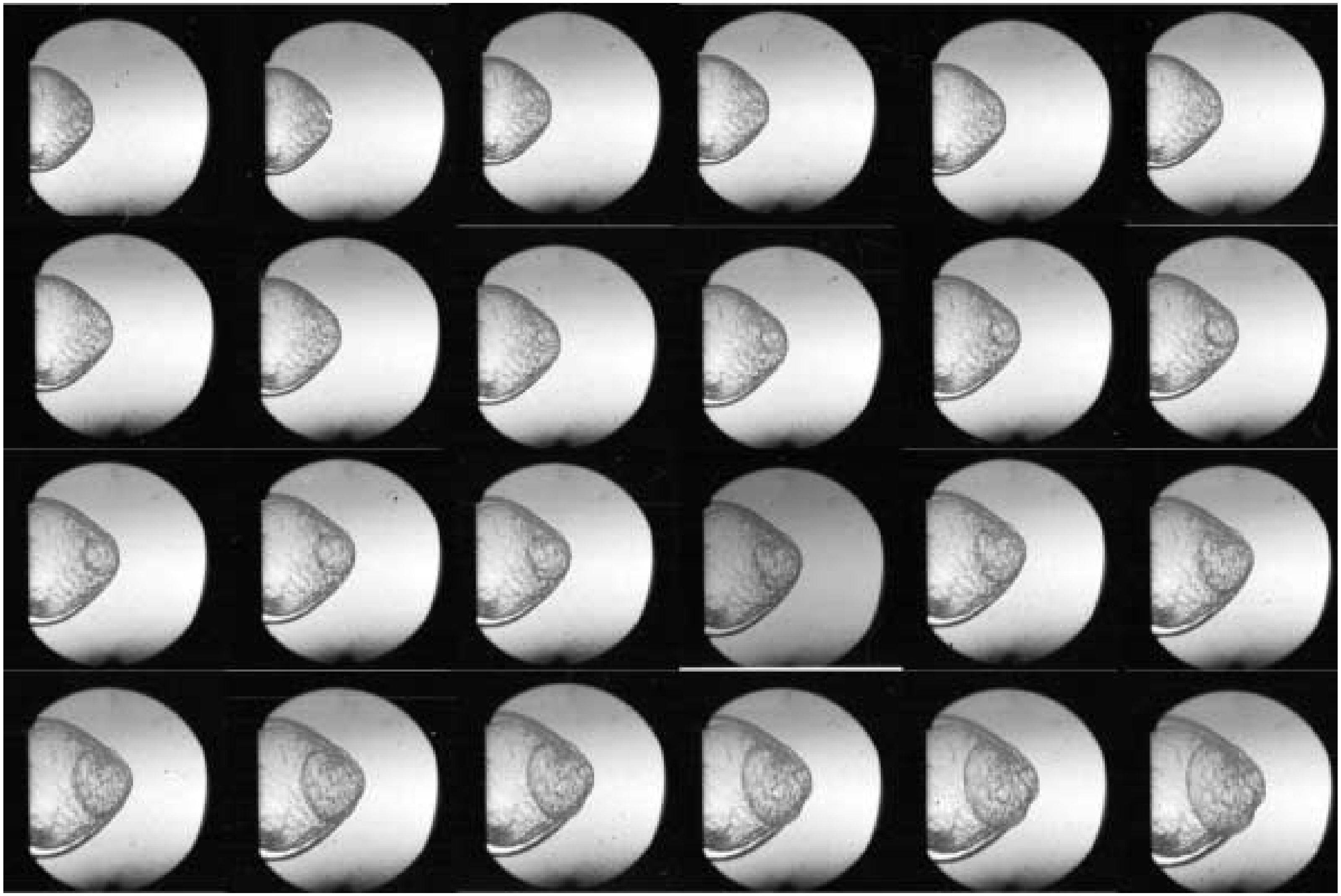

Stoichiometric hydrogen-oxygen-helium mixtures with varying helium dilution (P_1 = 100 kPa), Shot 1089, 50% He

Stoichiometric hydrogen-oxygen-helium mixtures with varying helium dilution (P_1 = 100 kPa), Shot 1197, 50% He

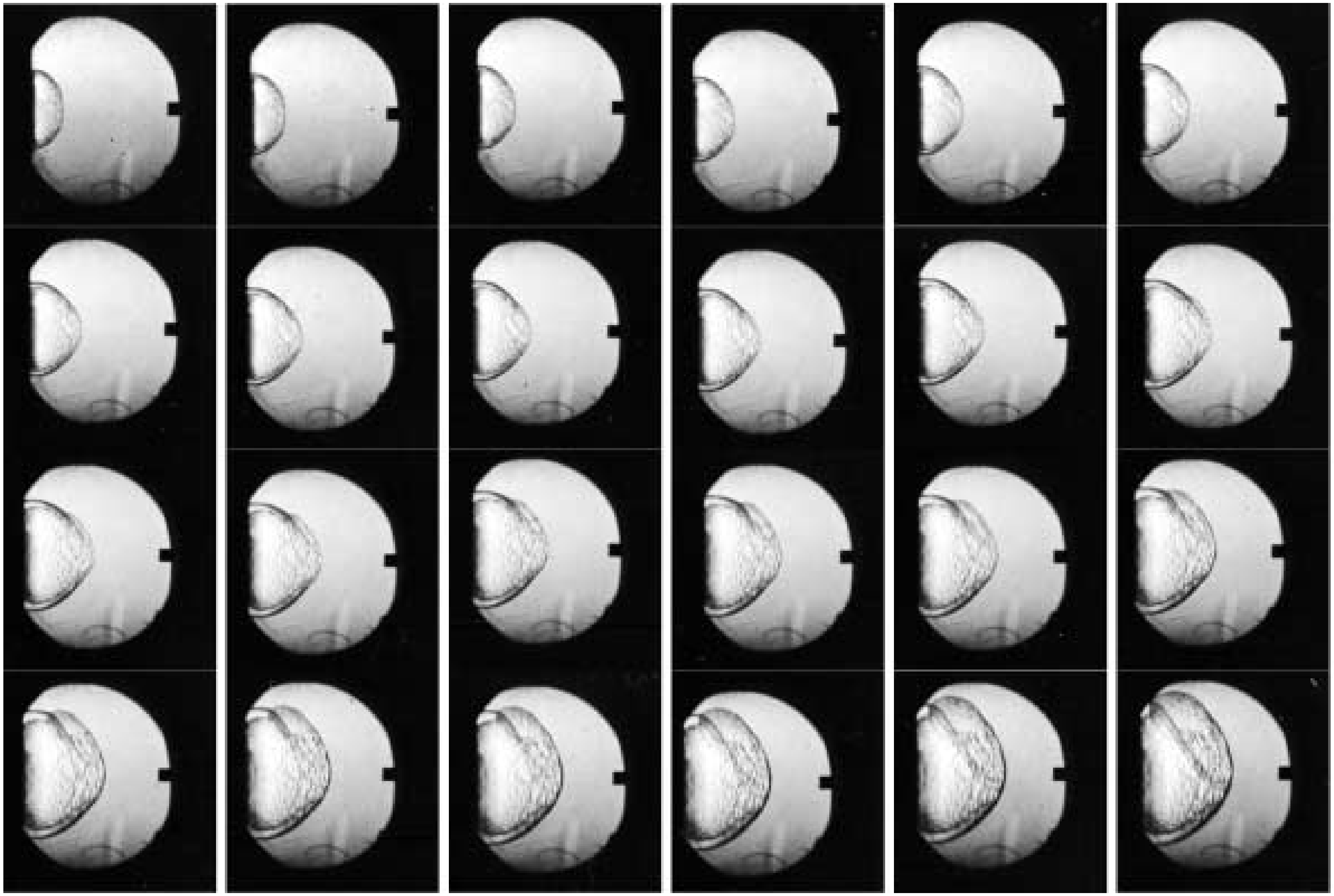

Stoichiometric hydrogen-oxygen-helium mixtures with varying helium dilution (P_1 = 100 kPa), Shot 1198, 50% He

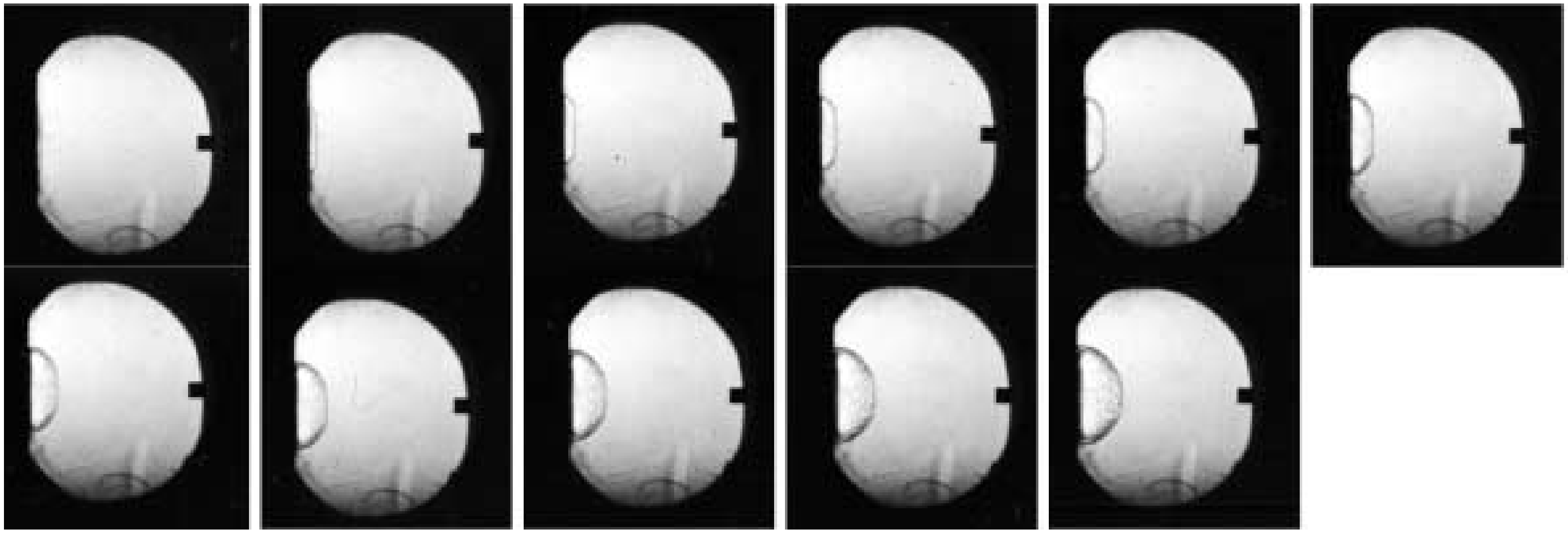

Stoichiometric hydrogen-oxygen-nitrogen mixtures with varying nitrogen dilution (P_1 = 100 kPa)

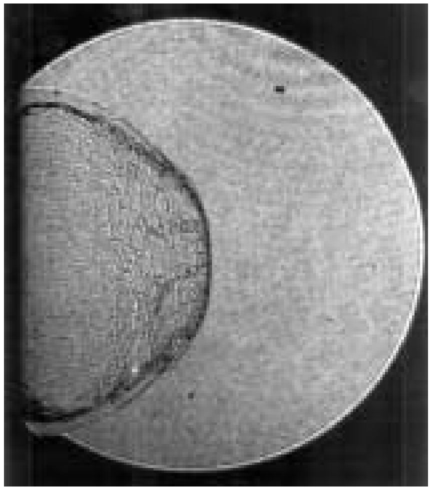

Shot 719, 14.3% N_2

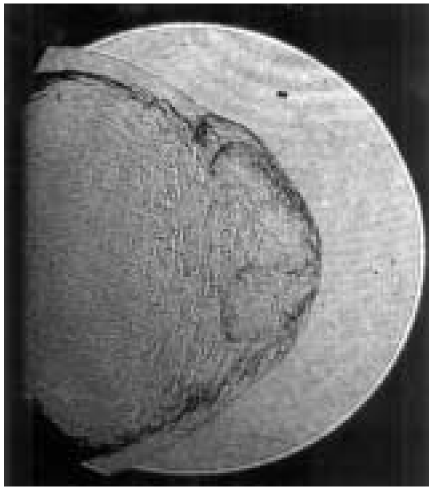

Shot 722, 17.2% N_2

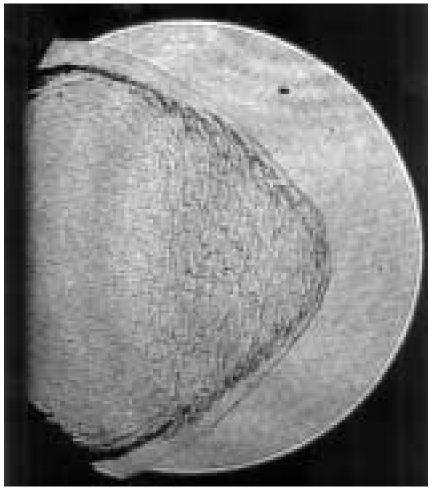

Shot 721, 20% N_2

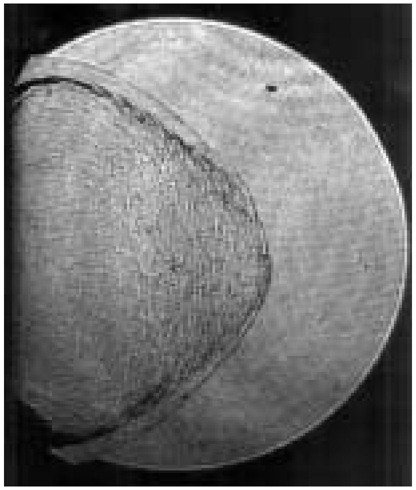

Shot 720, 25% N_2

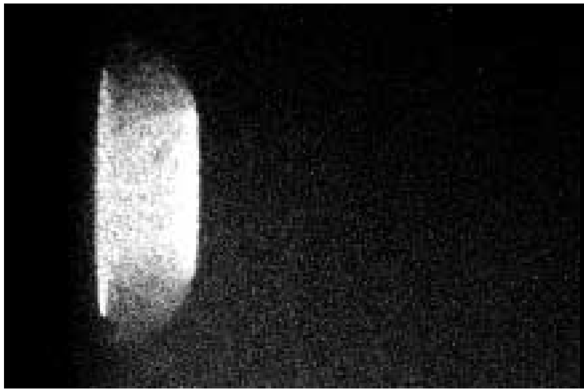

Shot 1283, 40% N_2

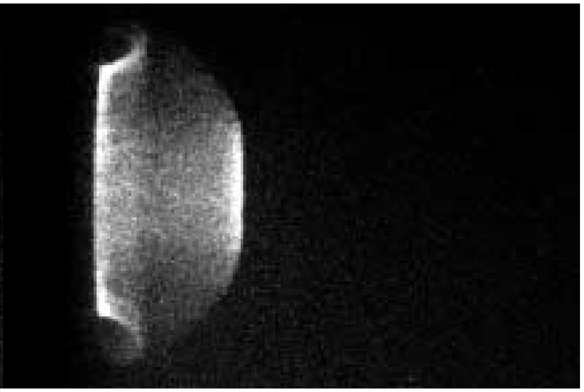

Shot 1281, 40% N_2

Stoichiometric hydrogen-oxygen-nitrogen mixtures with varying nitrogen dilution (P_1 = 100 kPa)

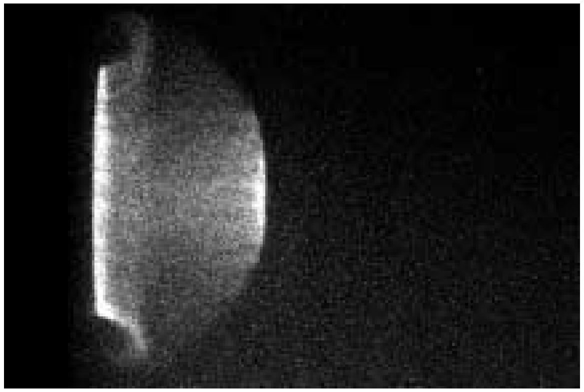

Shot 1282, 40% N_2

Stoichiometric hydrogen-oxygen-nitrogen mixtures with varying nitrogen dilution (P_1 = 100 kPa), Shot 1092, 17.2% N_2

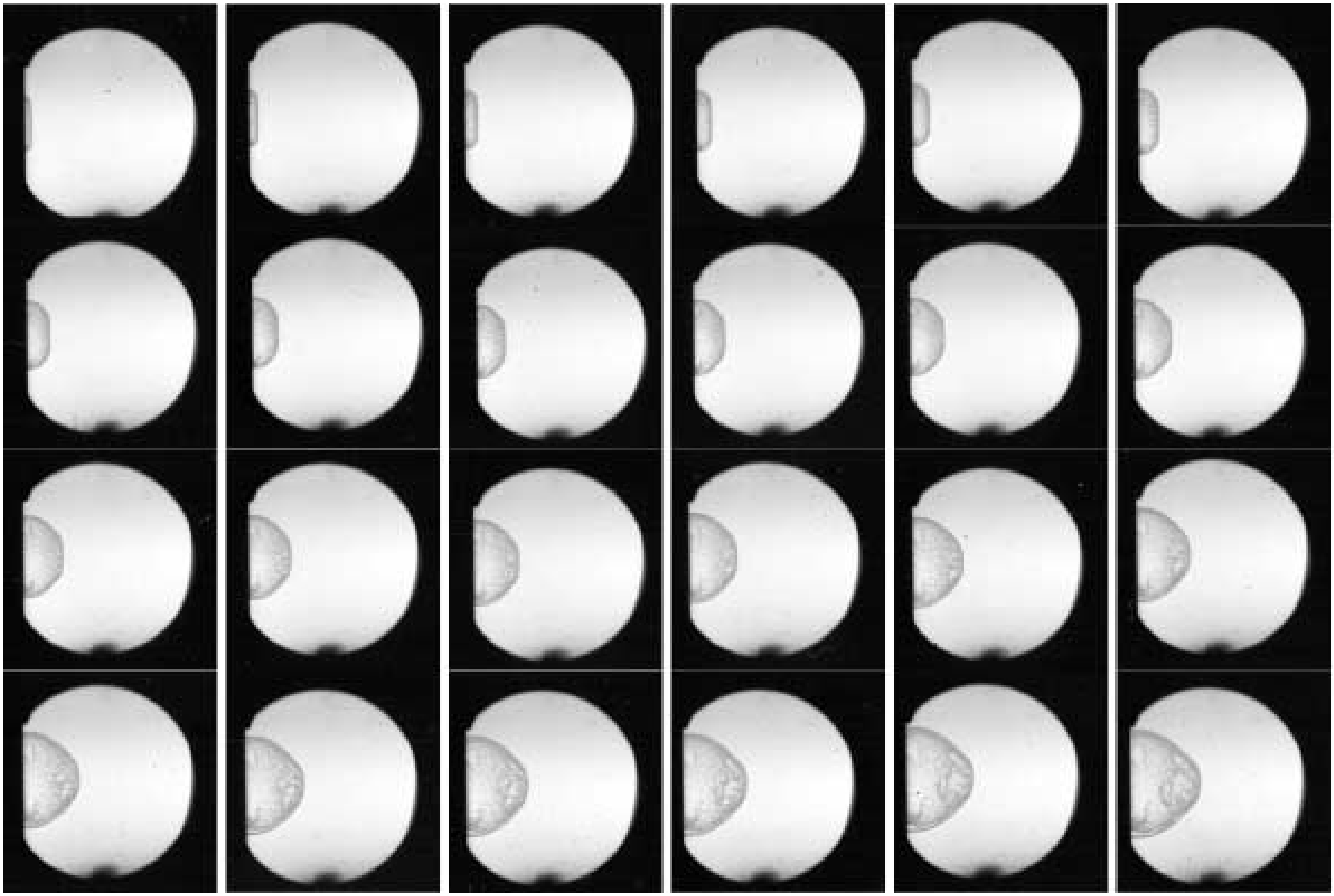

Stoichiometric hydrogen-oxygen-nitrogen mixtures with varying nitrogen dilution (P_1 = 100 kPa), Shot 1096, 17.2% N_2

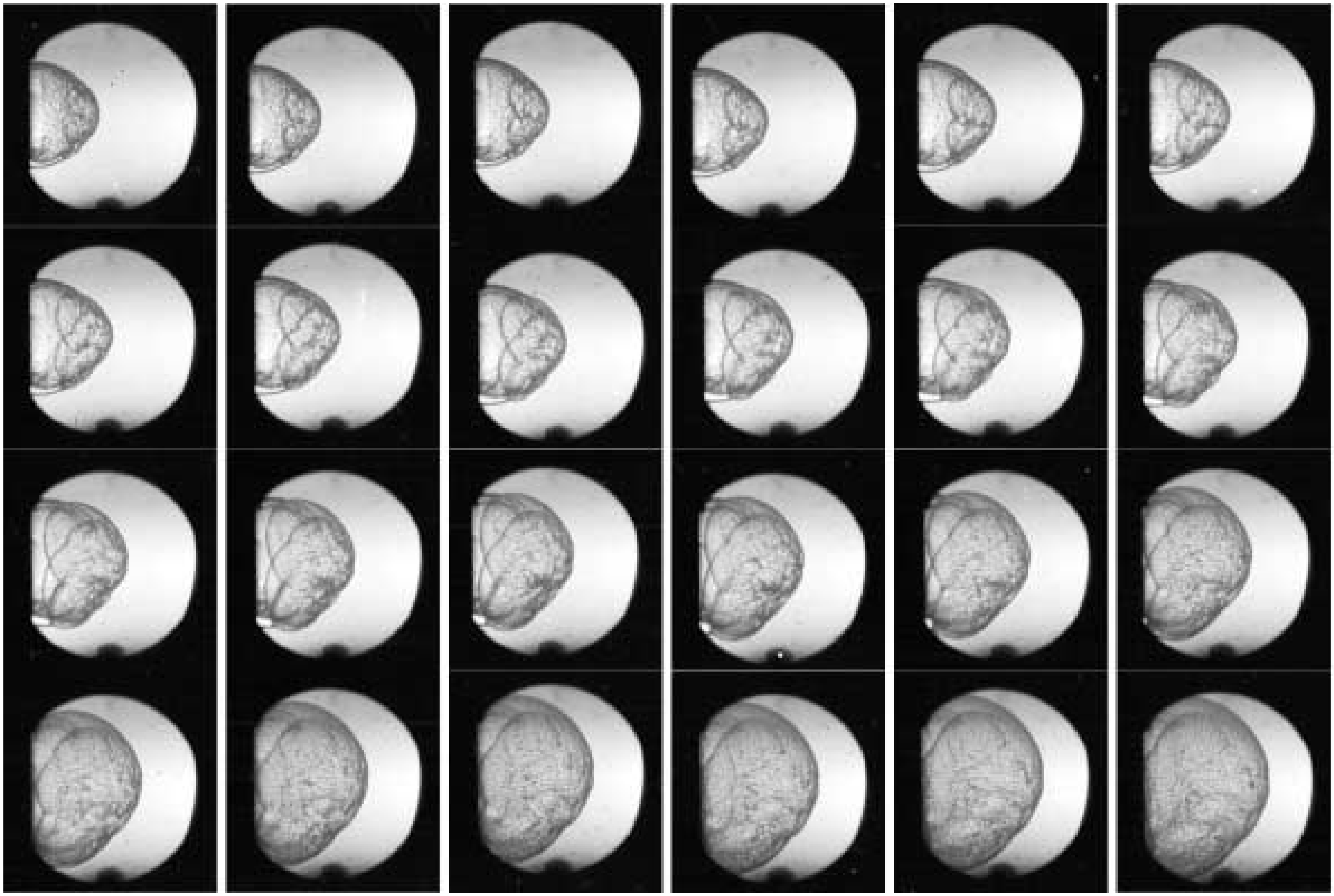

Stoichiometric hydrogen-oxygen-nitrogen mixtures with varying nitrogen dilution (P_1 = 100 kPa), Shot 1093, 25% N_2

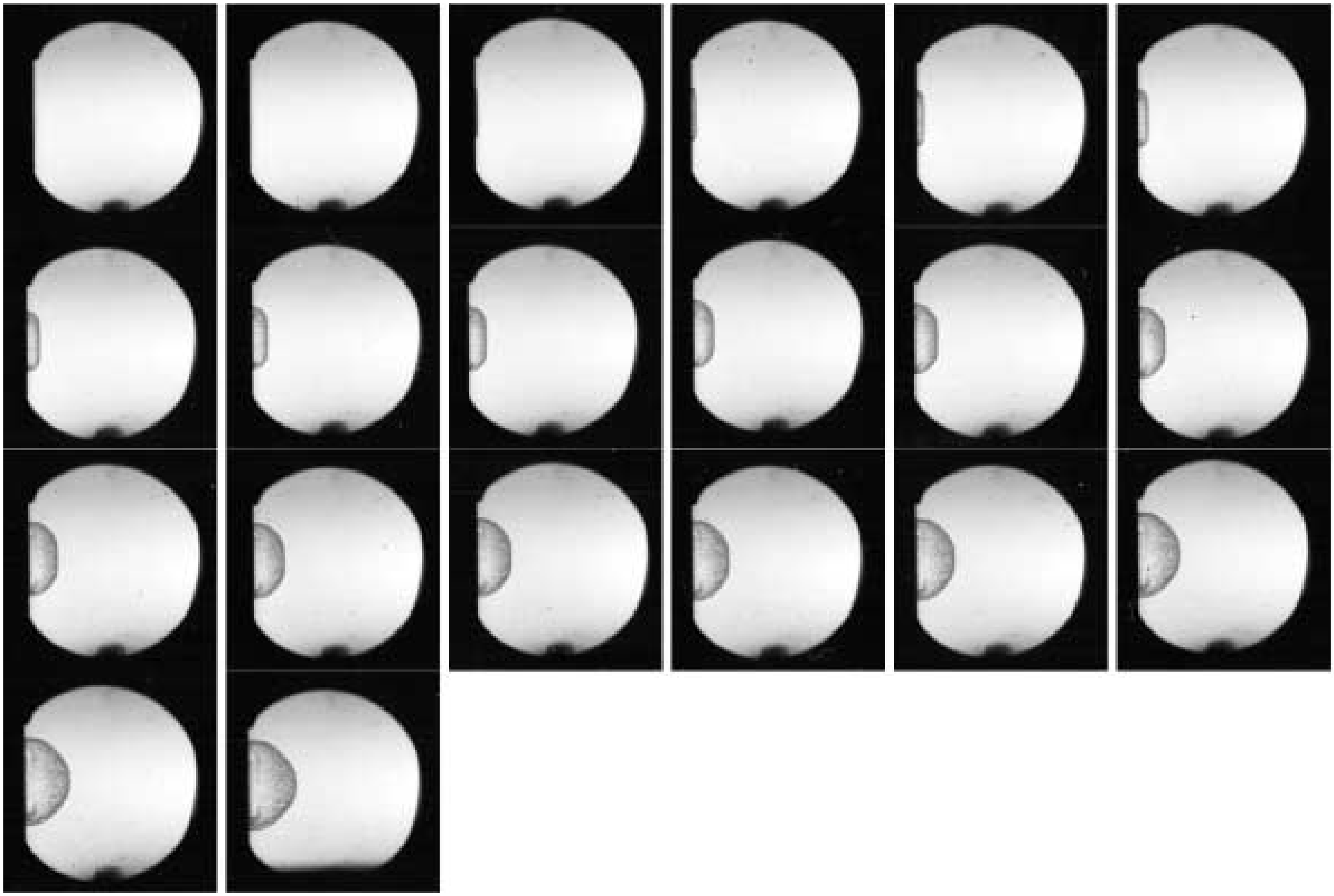

Stoichiometric hydrogen-oxygen-nitrogen mixtures with varying nitrogen dilution (P_1 = 100 kPa), Shot 1094, 25% N_2

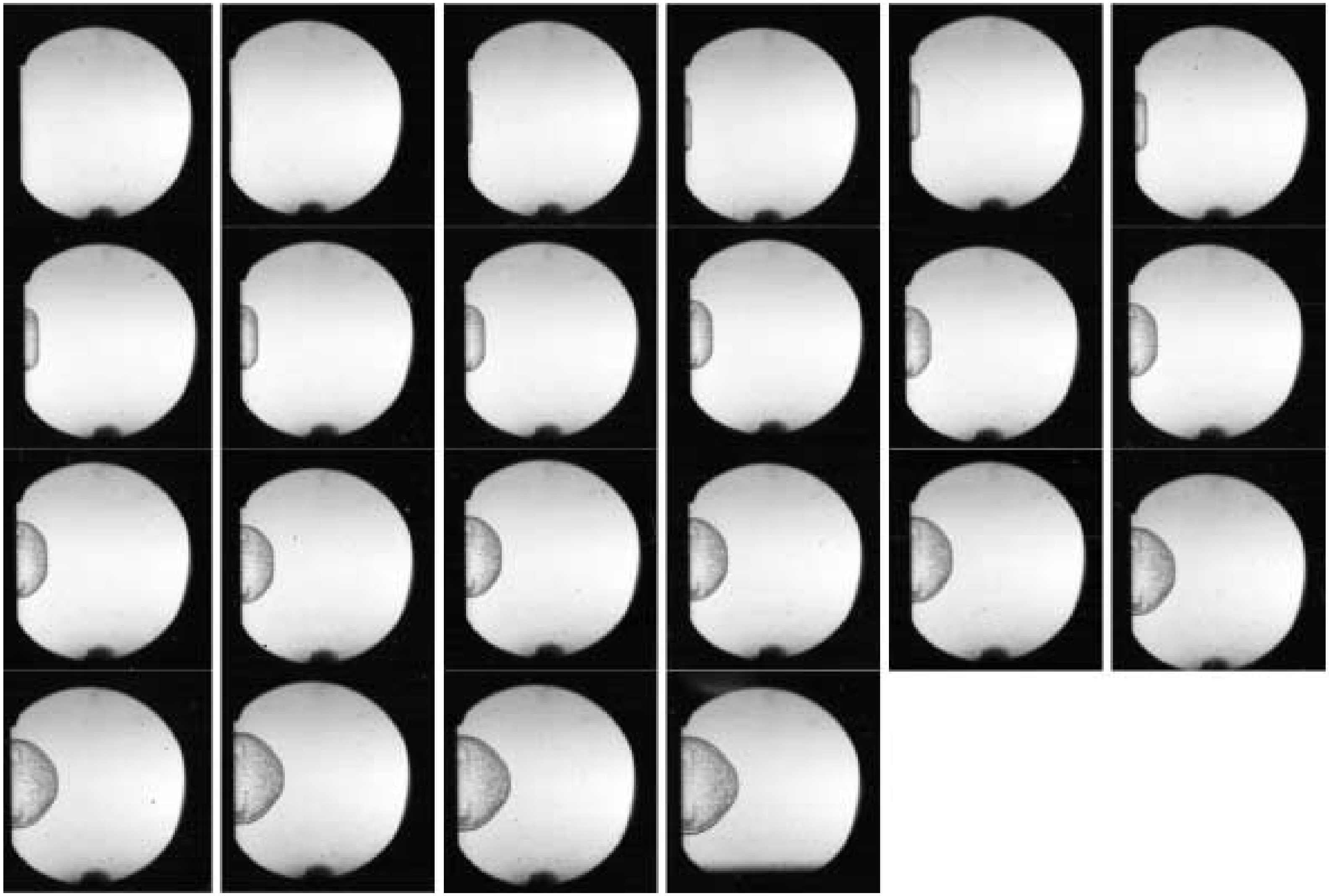

Stoichiometric hydrogen-oxygen-nitrogen mixtures with varying nitrogen dilution (P_1 = 100 kPa), Shot 1095, 25% N_2

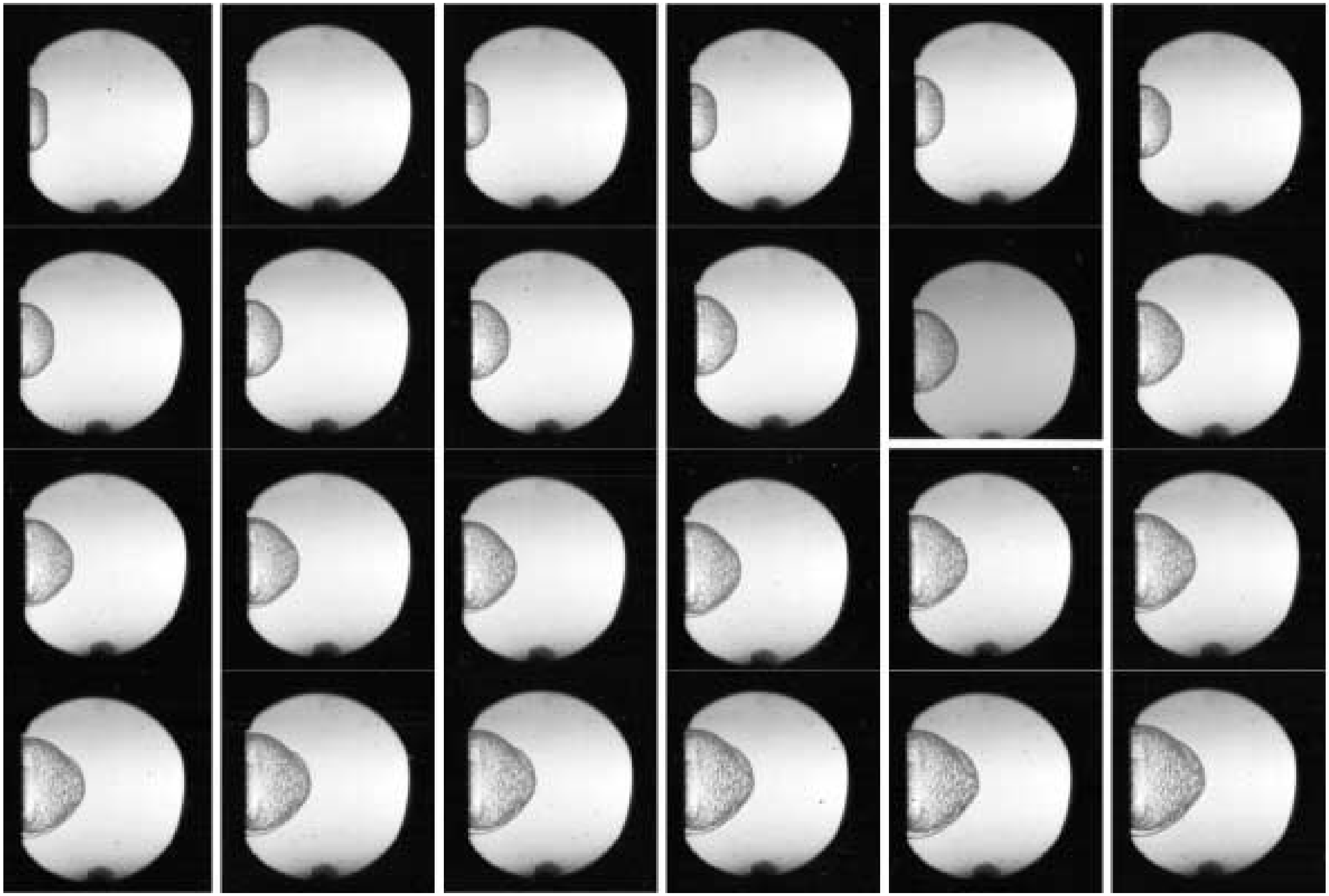

Stoichiometric hydrogen-oxygen-nitrogen mixtures with varying nitrogen dilution (P_1 = 100 kPa), Shot 1097, 25% N_2

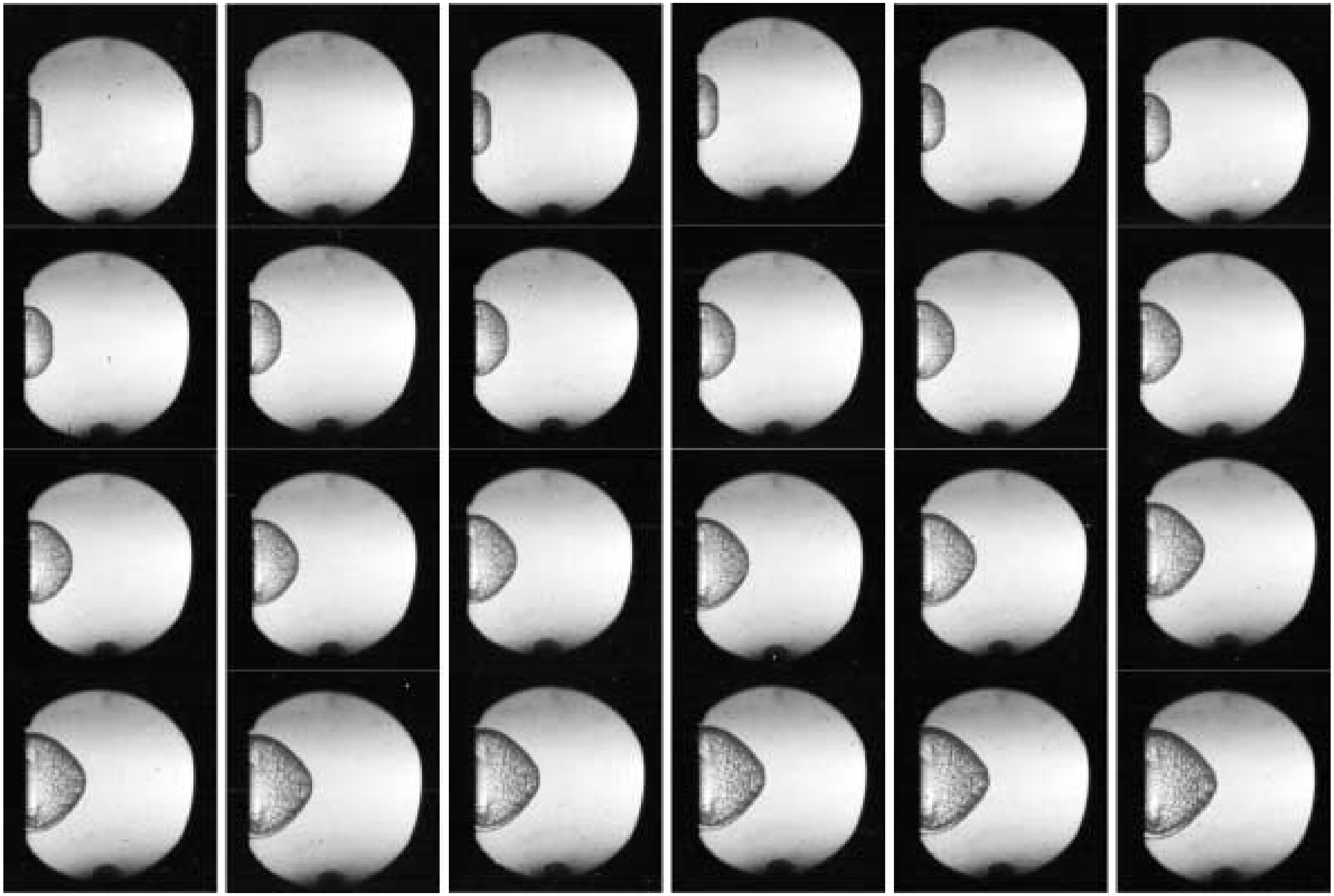

Stoichiometric hydrogen-oxygen-nitrogen mixtures with varying nitrogen dilution (P_1 = 100 kPa), Shot 1209, 40% N_2

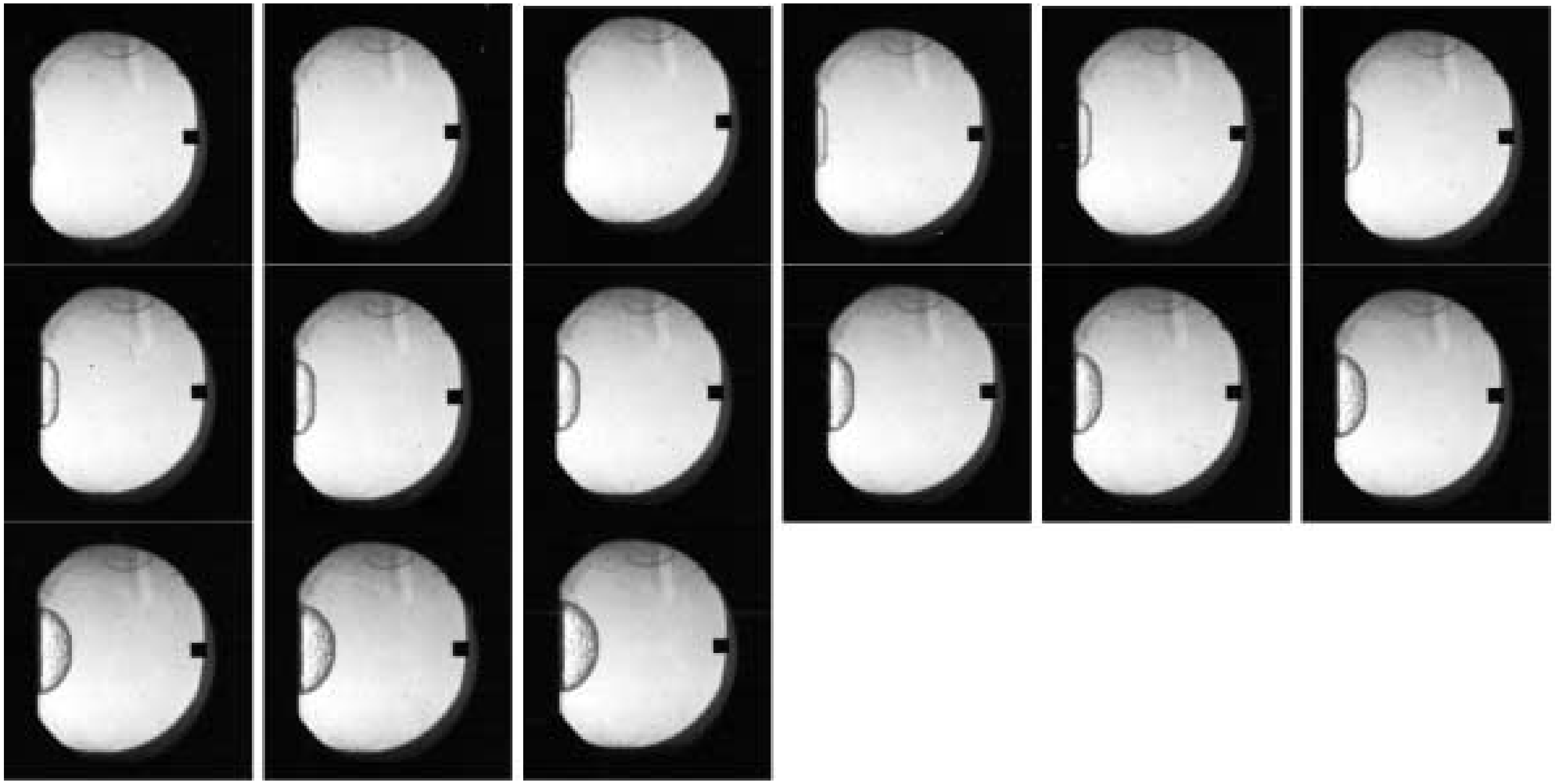

Ethylene-oxygen mixtures with varying equivalence ratio (P_1 = 100 kPa)

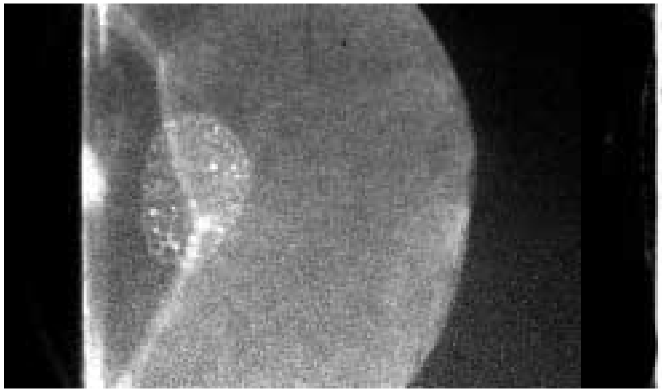
Shot 1239, ϕ = 0.4


Shot 1237, ϕ = 0.5

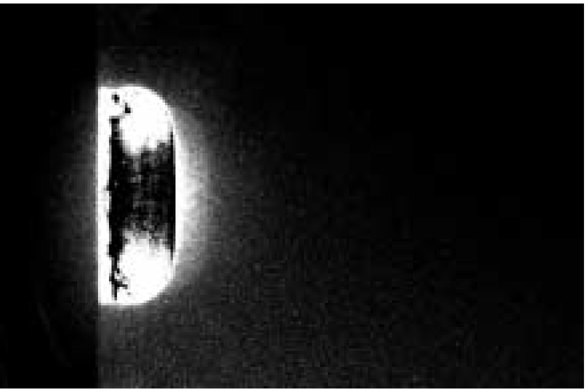
Shot 1228, ϕ = 1.8

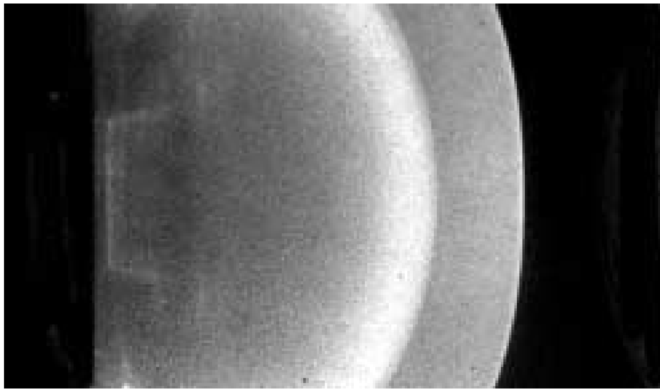
Shot 1229, ϕ = 2.0

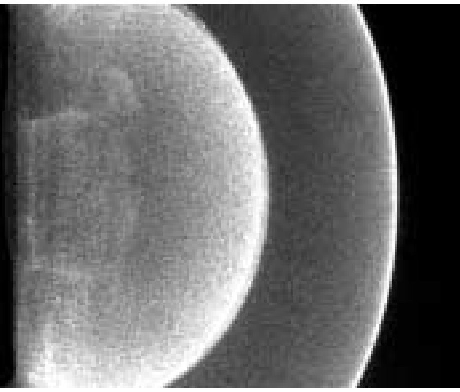
Shot 1230, ϕ = 2.4

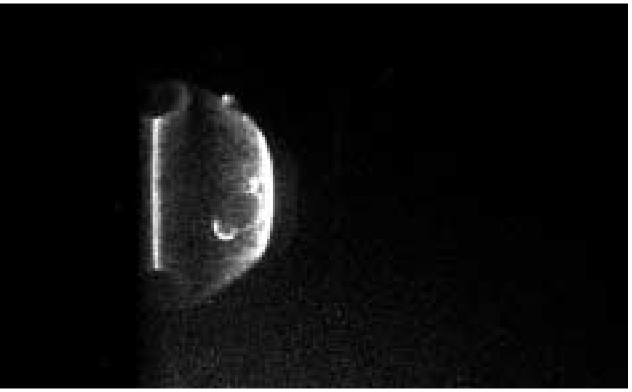
Shot 1231, ϕ = 2.8

Ethylene-oxygen mixtures with varying equivalence ratio (P_1 = 100 kPa)

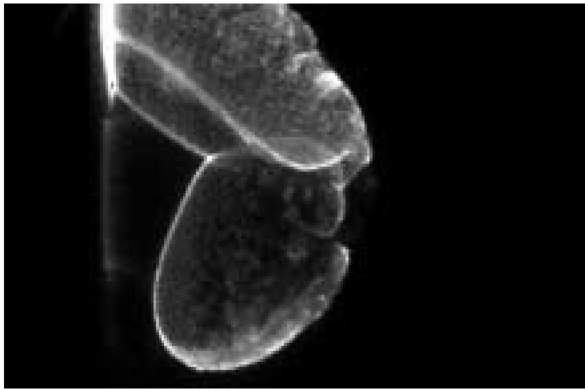
Shot 1233, ϕ = 2.9

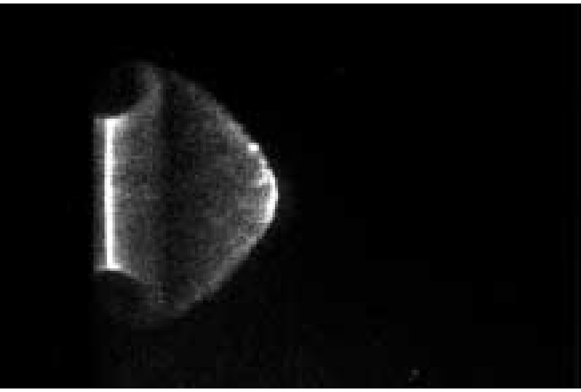
Shot 1232, ϕ = 3.0

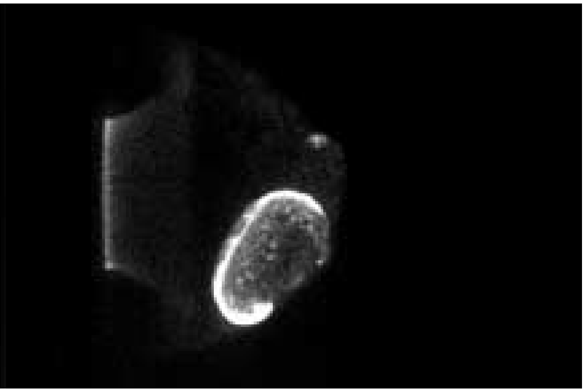
Shot 1234, ϕ = 3.0


Shot 1270, ϕ = 3.1

Ethylene-oxygen mixtures with varying equivalence ratio (P_1 = 100 kPa), Shot 1290, $\phi = 0.3$

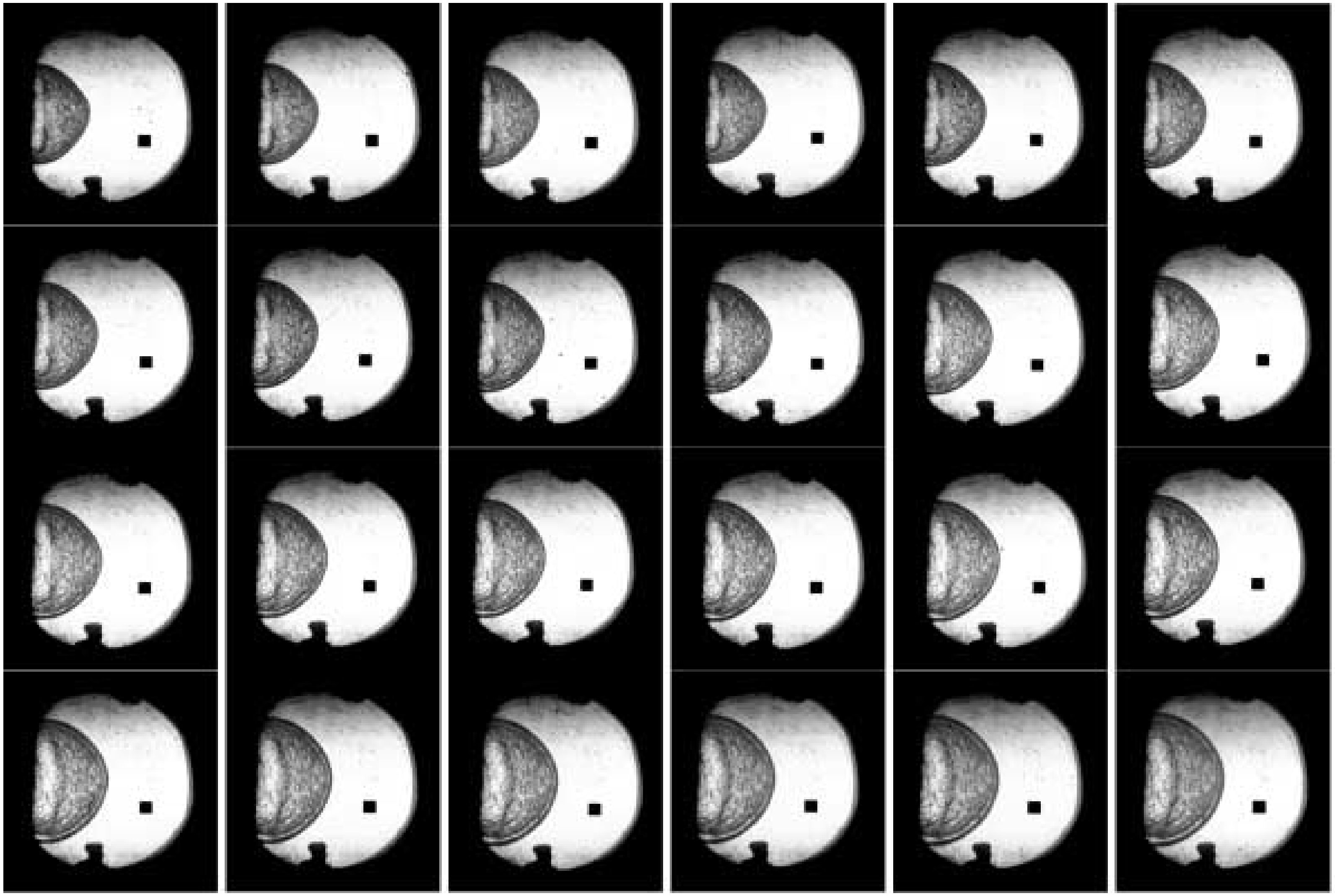

Ethylene-oxygen mixtures with varying equivalence ratio (P_1 = 100 kPa), Shot 1293, ϕ = 0.3

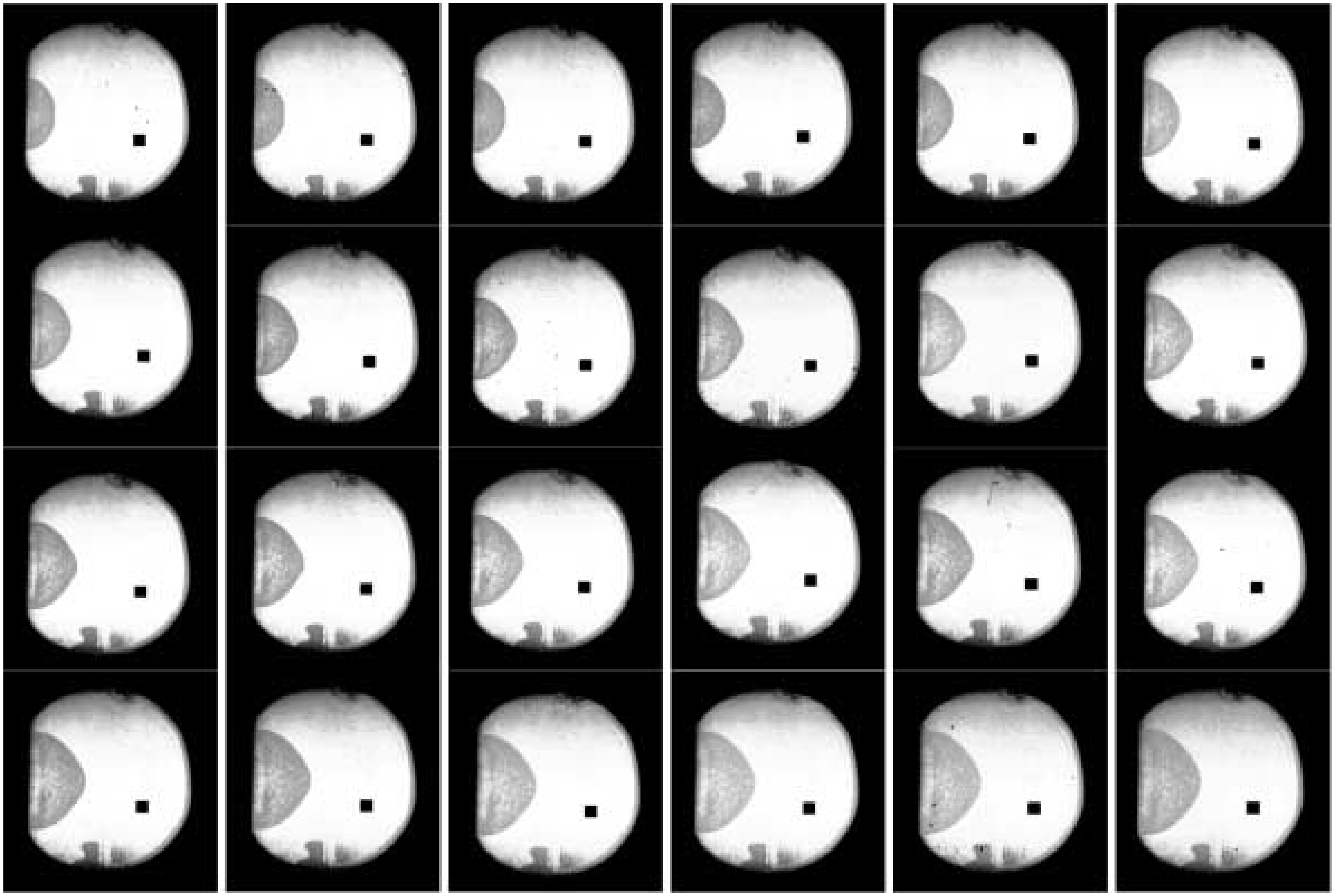

Ethylene-oxygen mixtures with varying equivalence ratio (P_1 = 100 kPa), Shot 1294, ϕ = 0.3

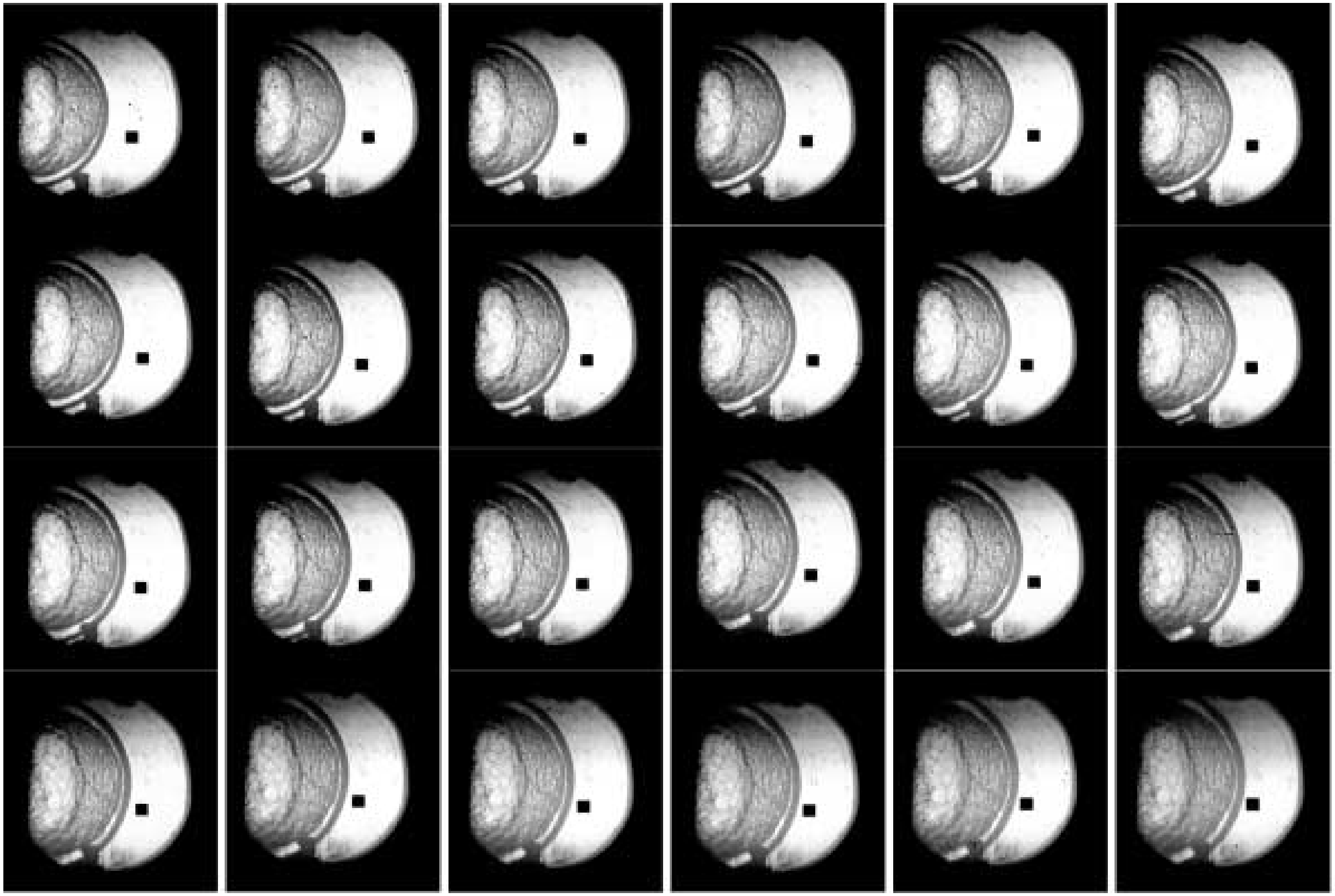

Stoichiometric ethylene-oxygen mixtures with varying initial pressure

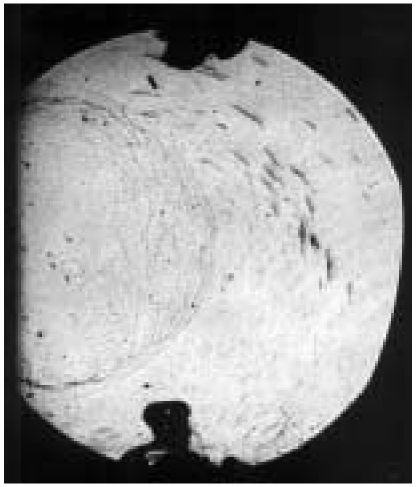

Shot 846, P_1 = 15 kPa

Shot 844, P_1 = 20 kPa

Stoichiometric ethylene-oxygen mixtures with varying initial pressure, Shot 1289, P_1 = 15 kPa

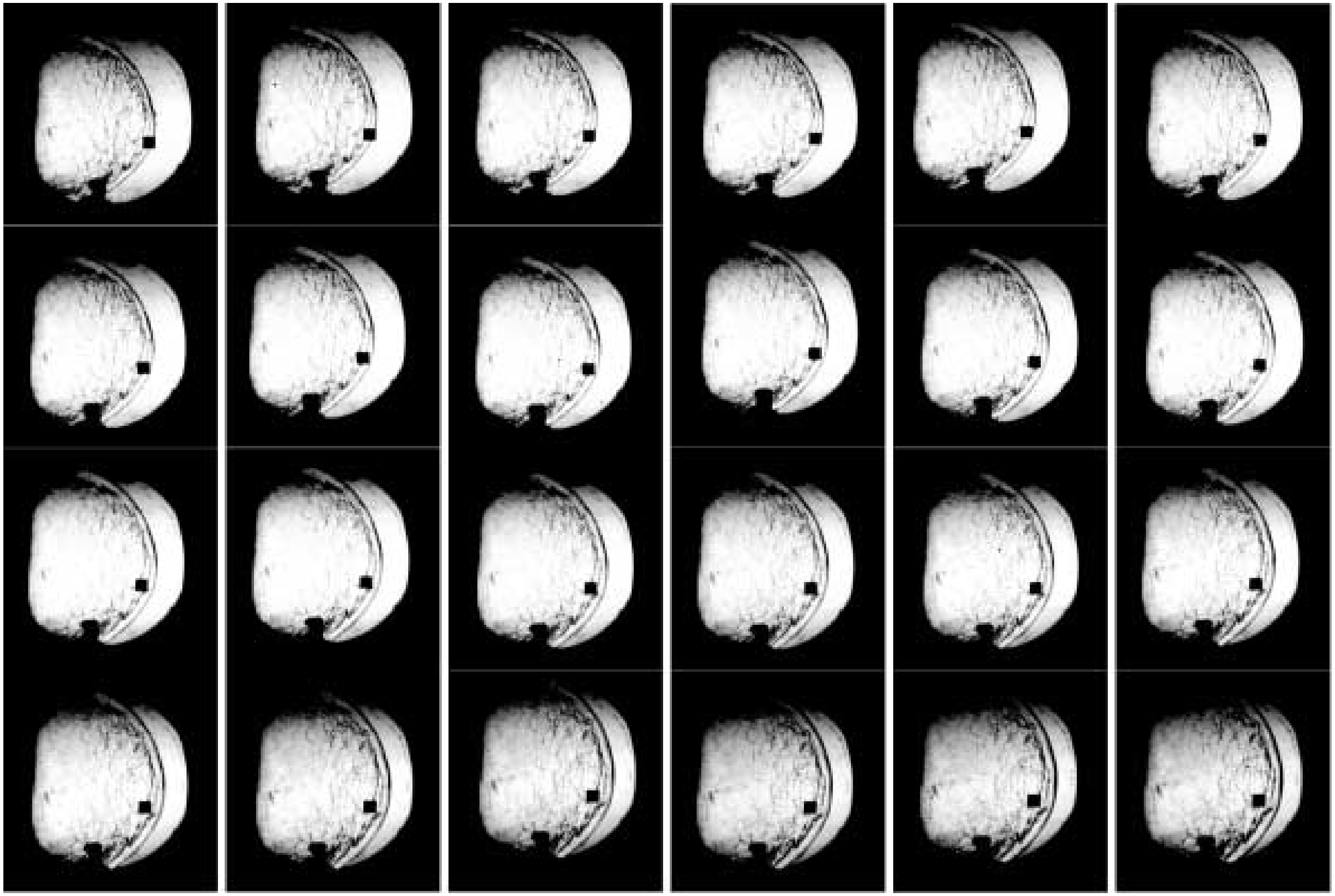

Stoichiometric ethylene-oxygen mixtures with varying initial pressure, Shot 1287, P_1 = 20 kPa

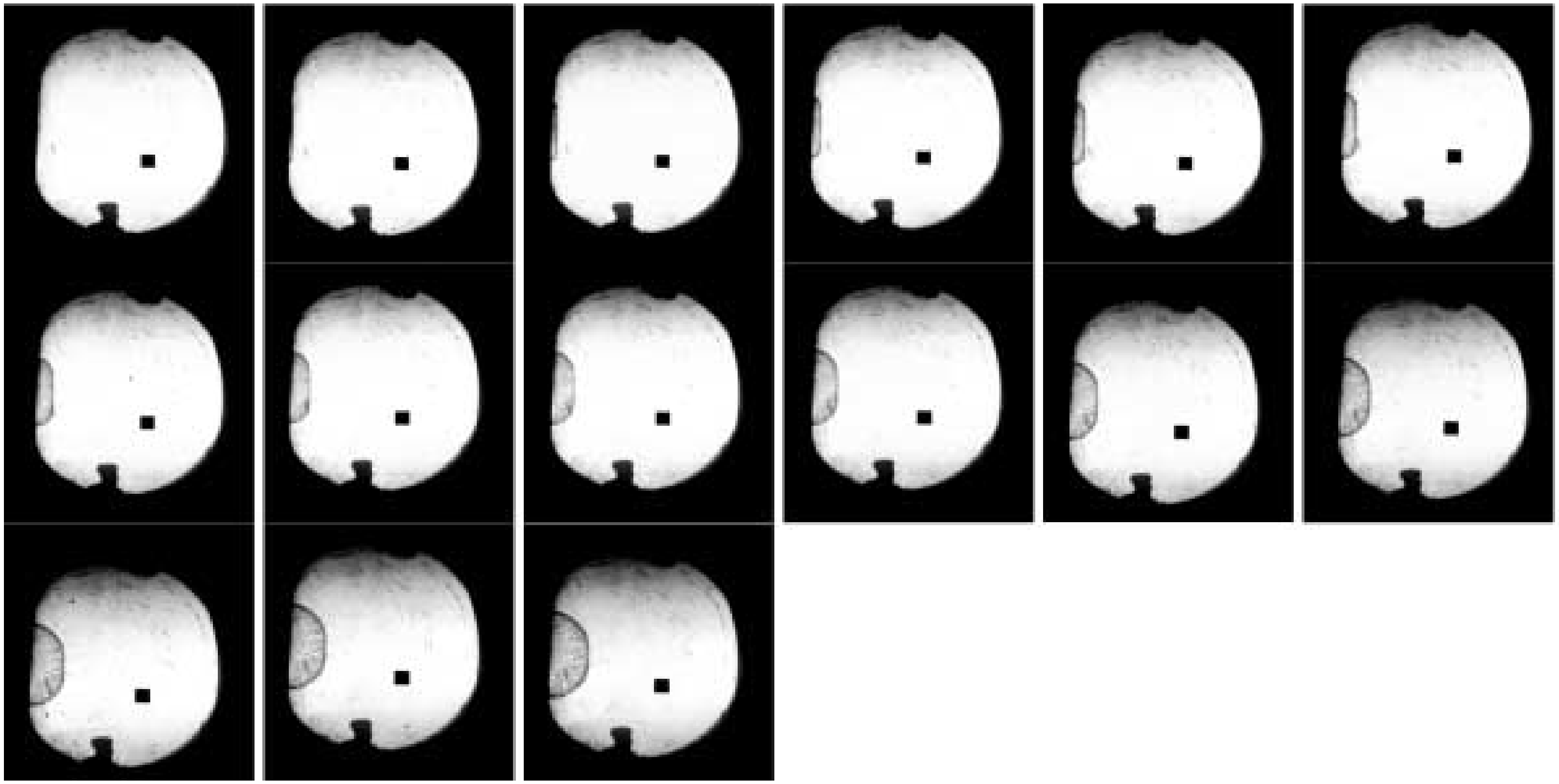

Stoichiometric ethylene-oxygen mixtures with varying initial pressure, Shot 1288, P_1 = 20 kPa

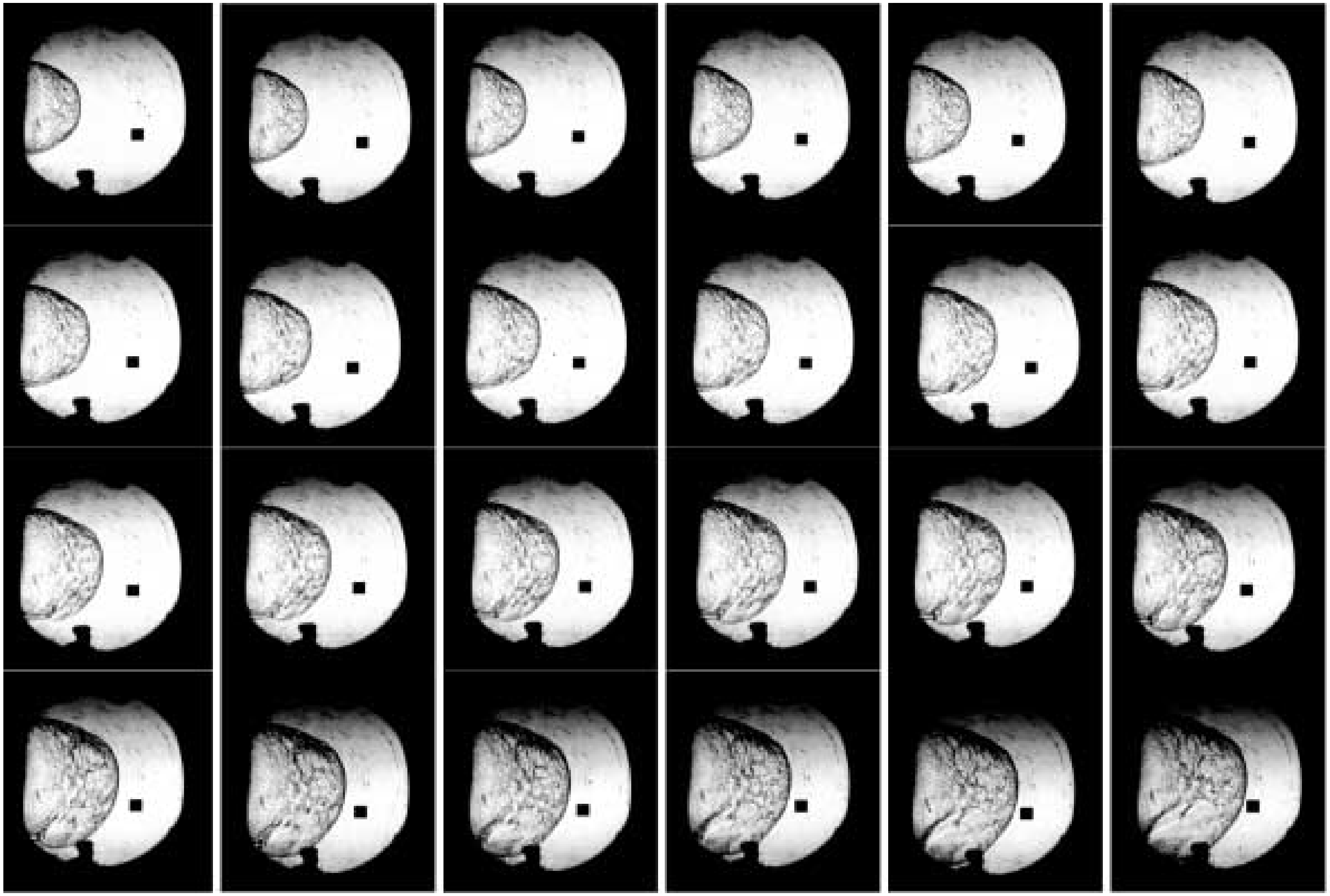

Stoichiometric ethylene-oxygen-argon mixtures with varying argon dilution (P_1 = 100 kPa)

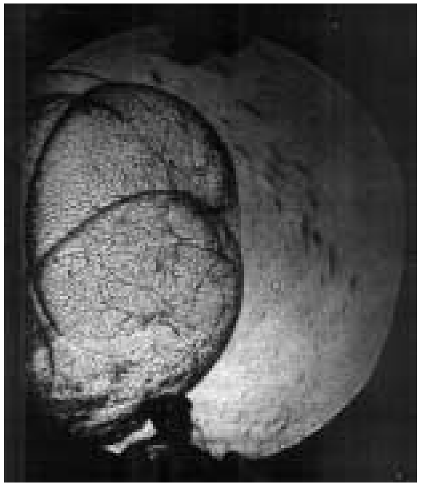

Shot 850, 75% Ar

Stoichiometric ethylene-oxygen-argon mixtures with varying argon dilution (P_1 = 100 kPa), Shot 1291, 75% Ar

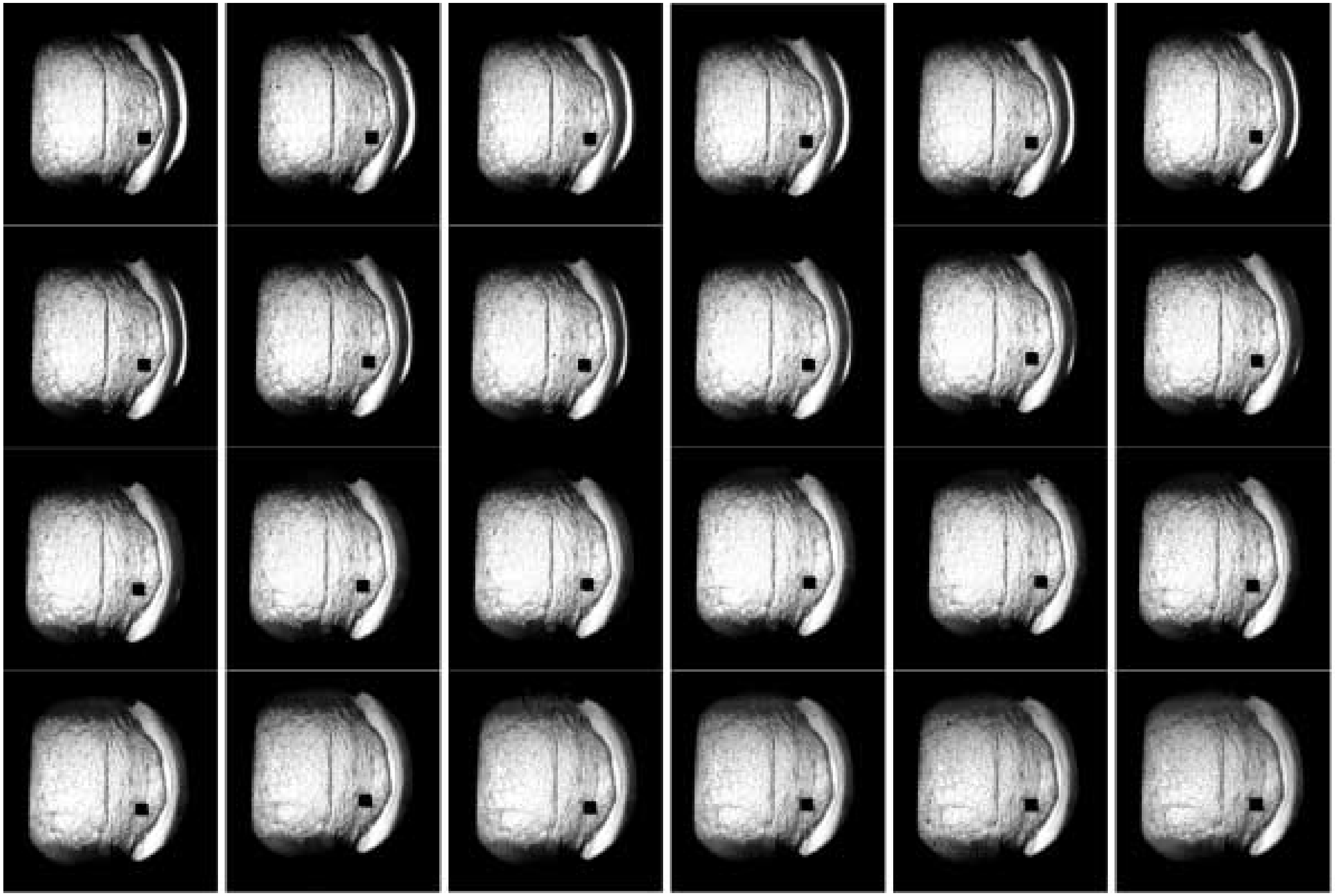

Stoichiometric ethylene-oxygen-carbon dioxide mixtures with varying carbon dioxide dilution (P_1 = 100 kPa)

Shot 1244, 5% CO_2

Shot 1245, 10% CO_2

Shot 1268, 20% CO_2

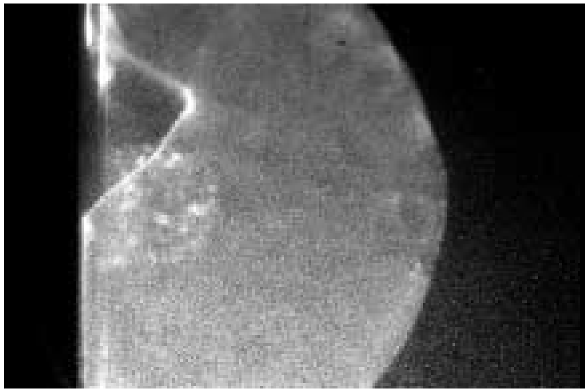

Shot 1246, 20% CO_2

Shot 1267, 25% CO_2

Stoichiometric ethylene-oxygen-helium mixtures with varying helium dilution (P_1 = 100 kPa)

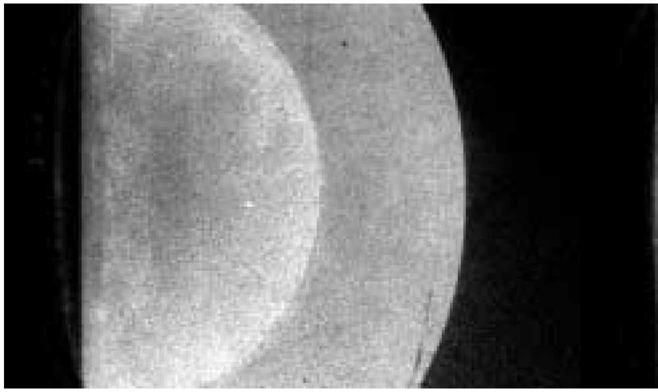

Shot 1240, 50% He

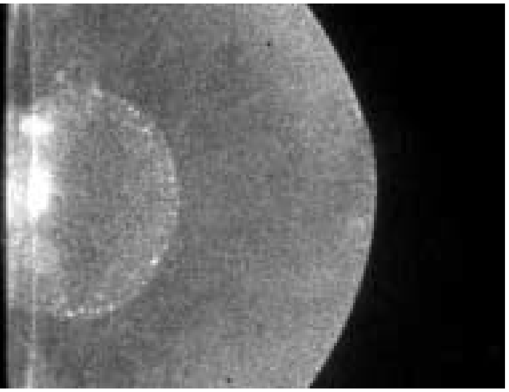

Shot 1242, 60% He

Stoichiometric ethylene-oxygen-nitrogen mixtures with varying nitrogen dilution (P_1 = 100 kPa)

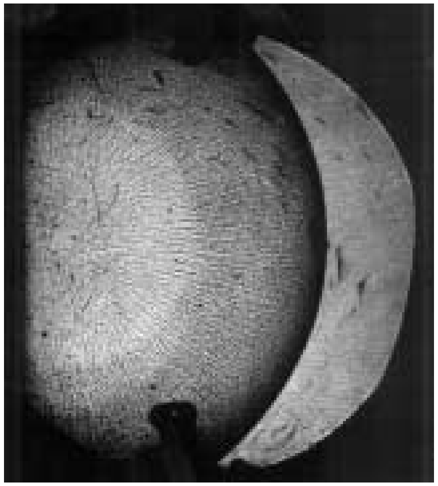

Shot 856, 33.3% N_2

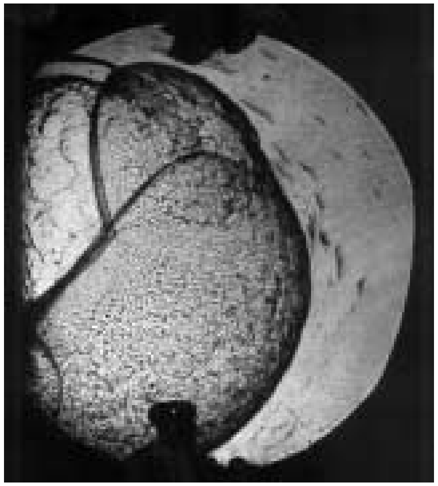

Shot 857, 42.9% N_2

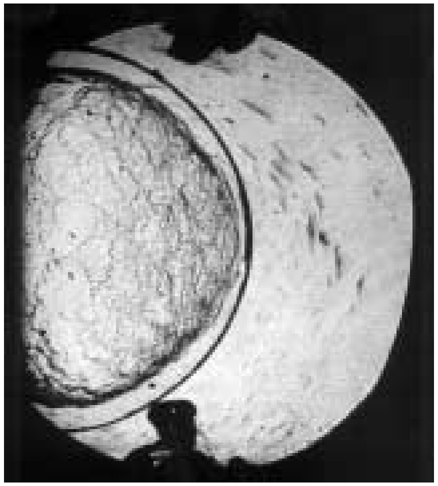

Shot 860, 44.4% N_2

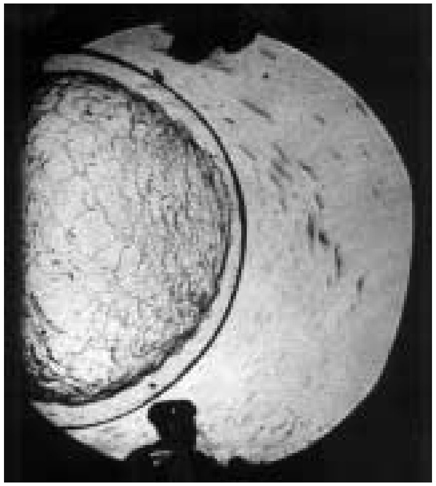

Shot 859, 46.7% N_2

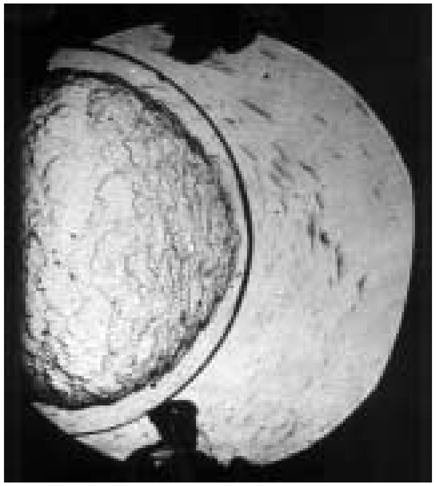

Shot 858, 50% N_2

Propane-oxygen mixtures with varying equivalence ratio (P_1 = 100 kPa)

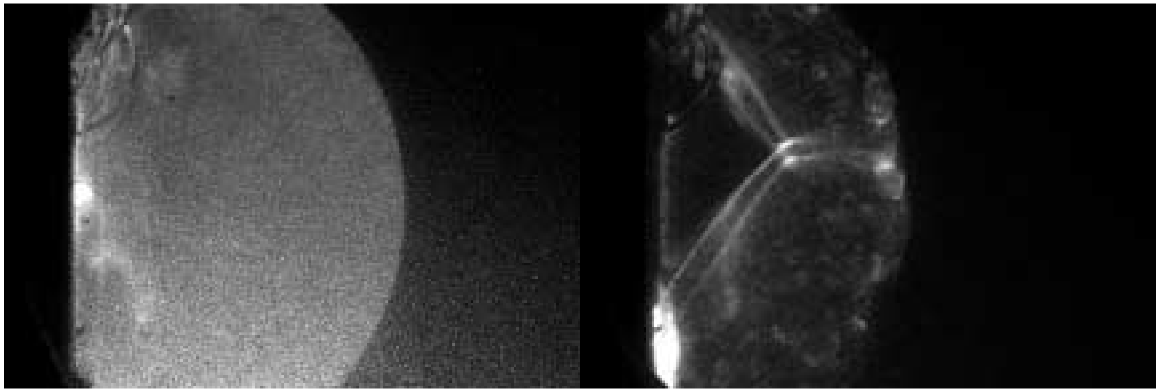

Shot 1264, ϕ = 0.6 Shot 1265, ϕ = 2.4

Stoichiometric propane-oxygen mixtures with varying initial pressure

Shot 825, P_1 = 30 kPa

Shot 826, P_1 = 35 kPa

Shot 824, P_1 = 40 kPa

Shot 823, P_1 = 50 kPa

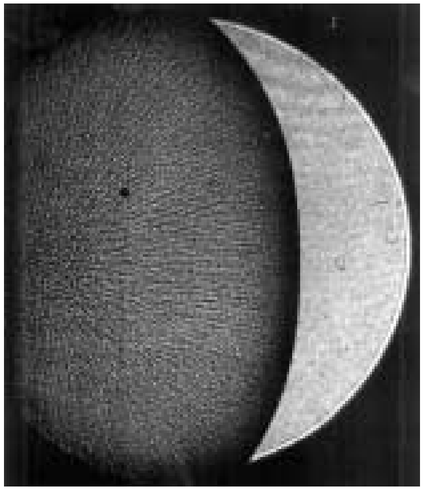

Shot 753, P_1 = 100 kPa

Stoichiometric propane-oxygen mixtures with varying initial pressure, Shot 1300, P_1 = 30 kPa

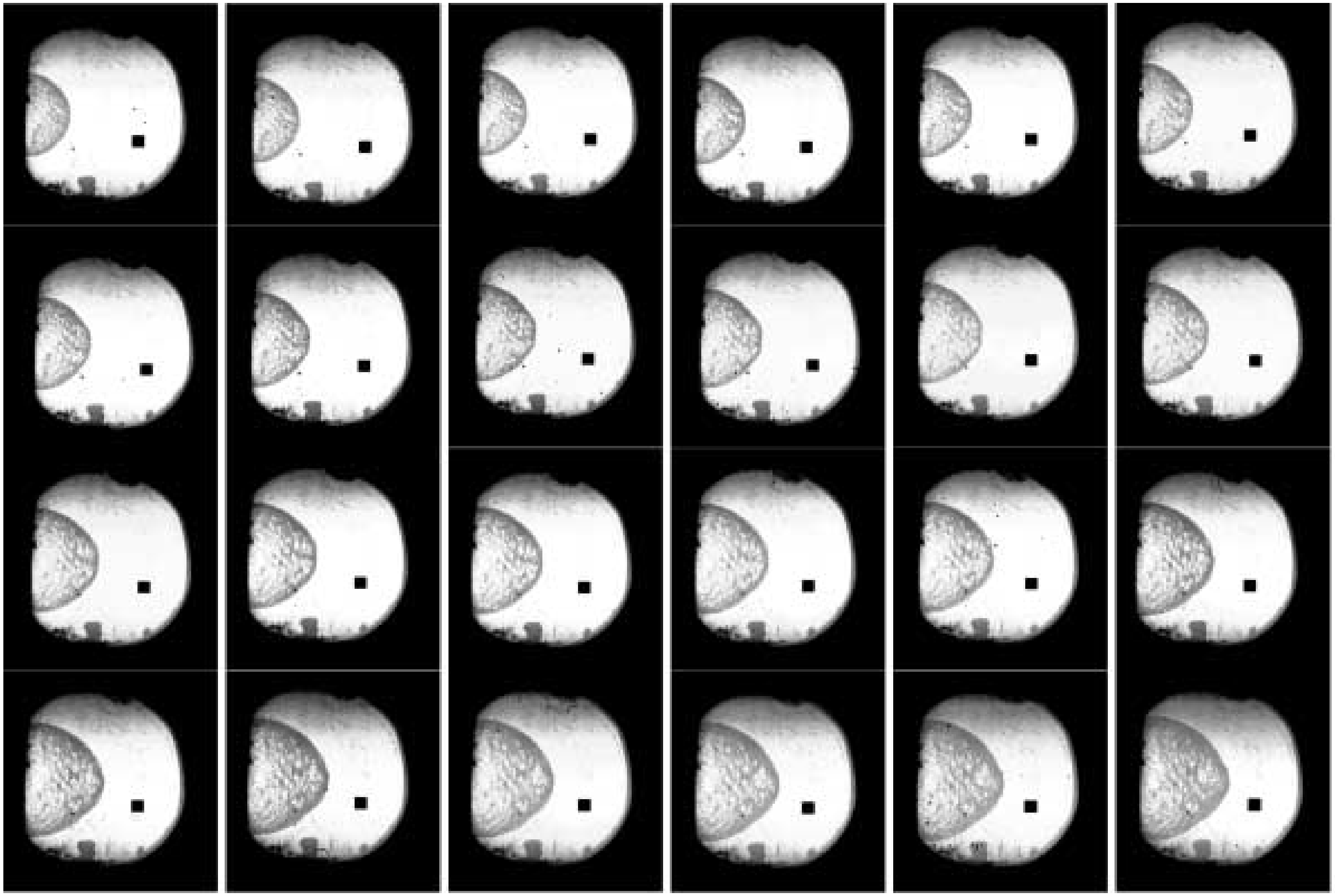

Stoichiometric propane-oxygen mixtures with varying initial pressure, Shot 1301, P_1 = 30 kPa

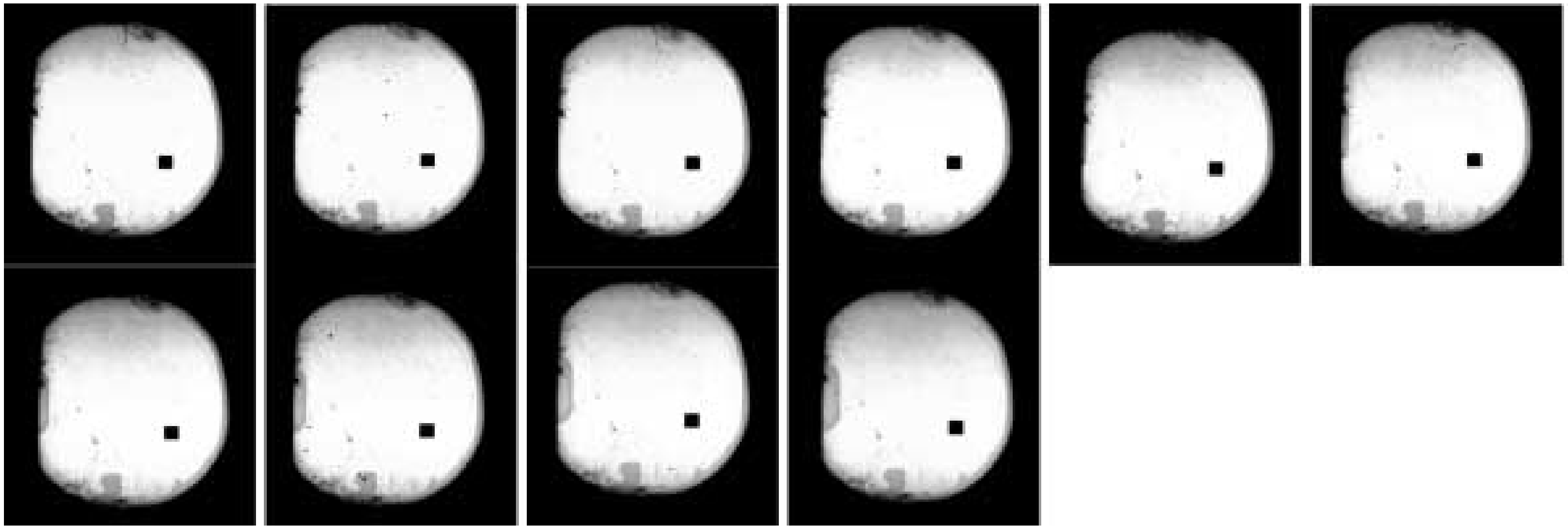

Stoichiometric propane-oxygen mixtures with varying initial pressure, Shot 1302, P_1 = 30 kPa

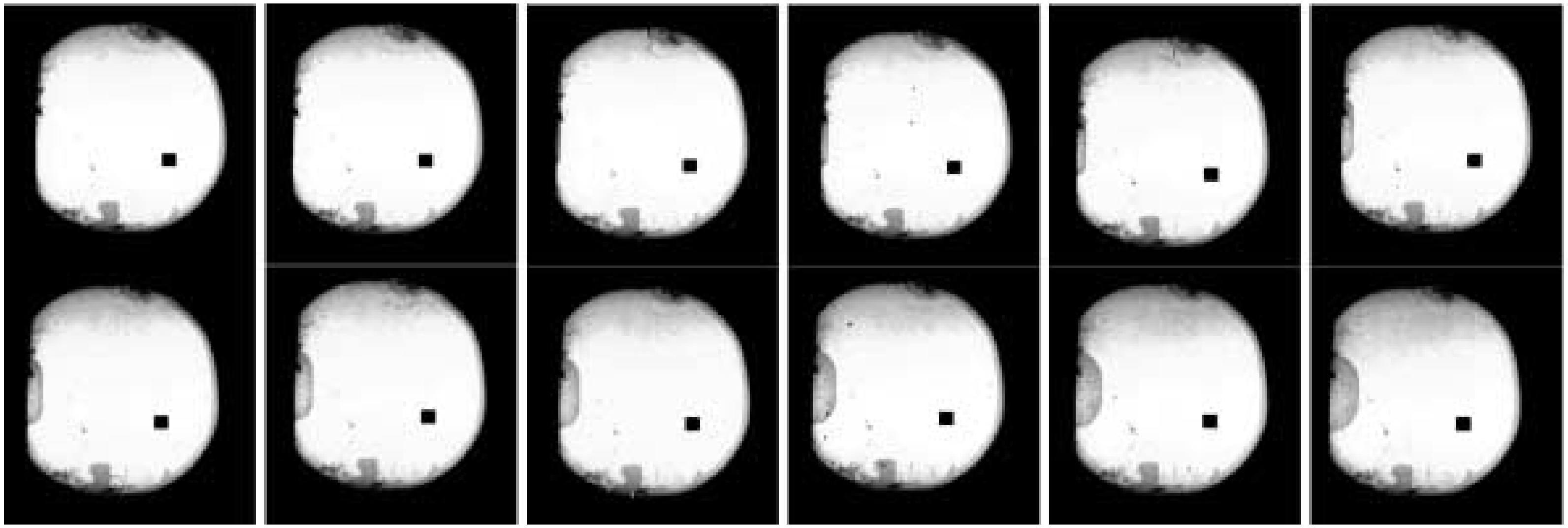

Stoichiometric propane-oxygen-argon mixtures with varying argon dilution (P_1 = 100 kPa)

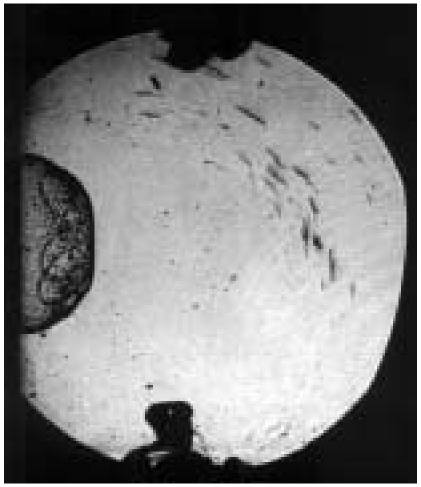

Shot 833, 40% Ar

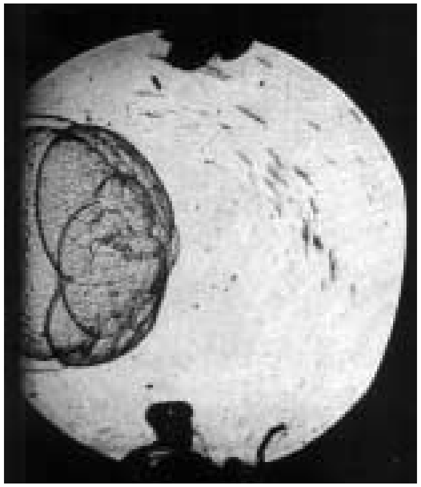

Shot 837, 64.7% Ar

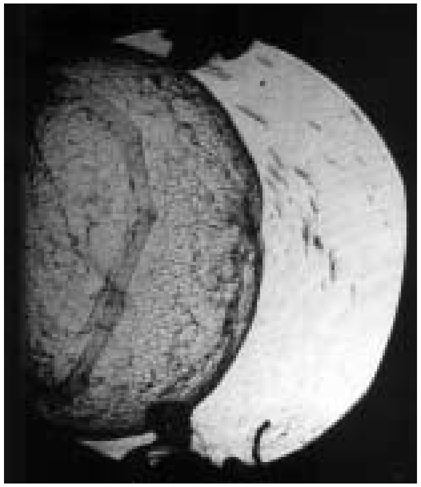

Shot 838, 67.6% Ar

Stoichiometric propane-oxygen-argon mixtures with varying argon dilution (P_1 = 100 kPa), Shot 1304, 70% Ar

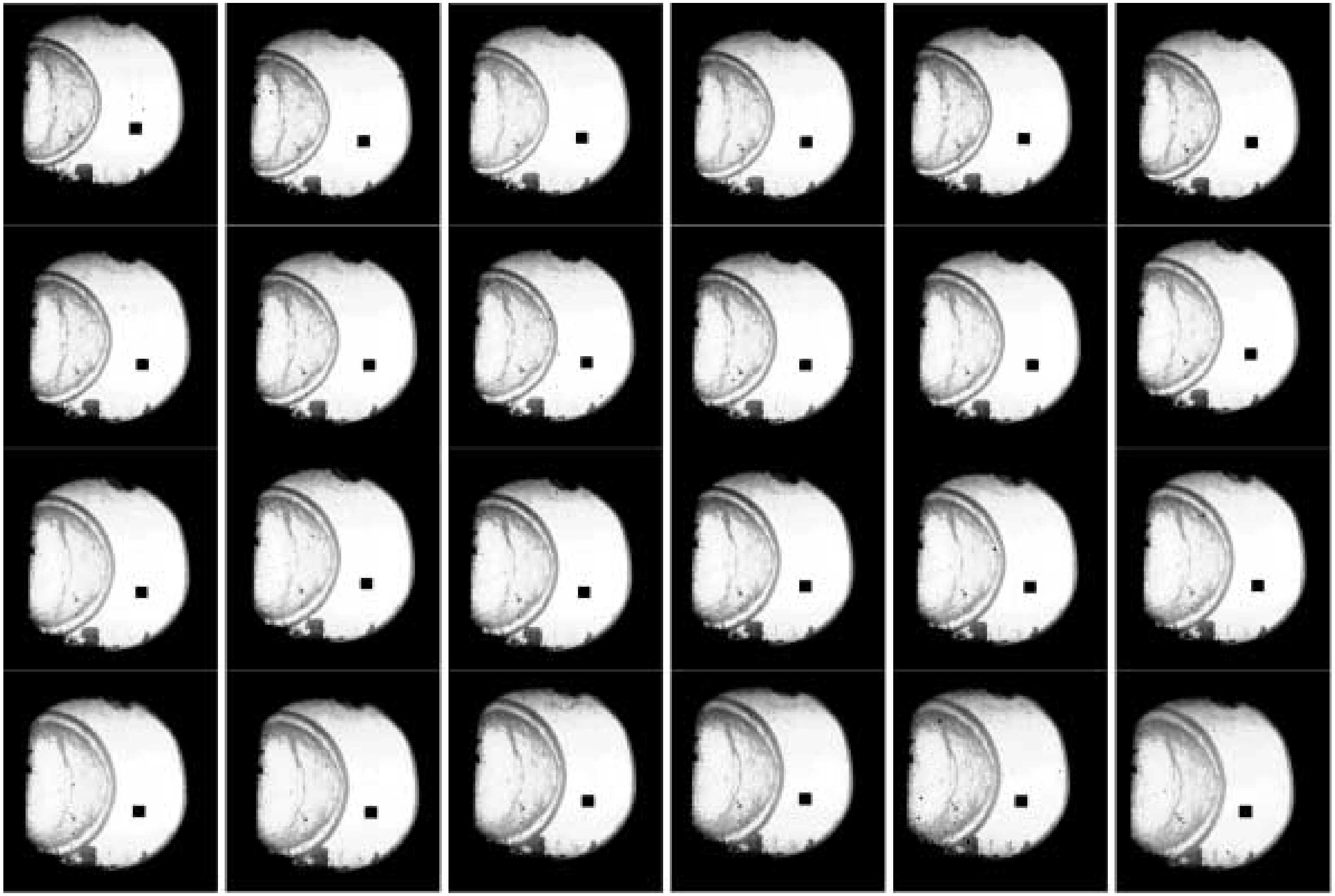

Stoichiometric propane-oxygen-argon mixtures with varying argon dilution (P_1 = 100 kPa), Shot 1307, 70% Ar

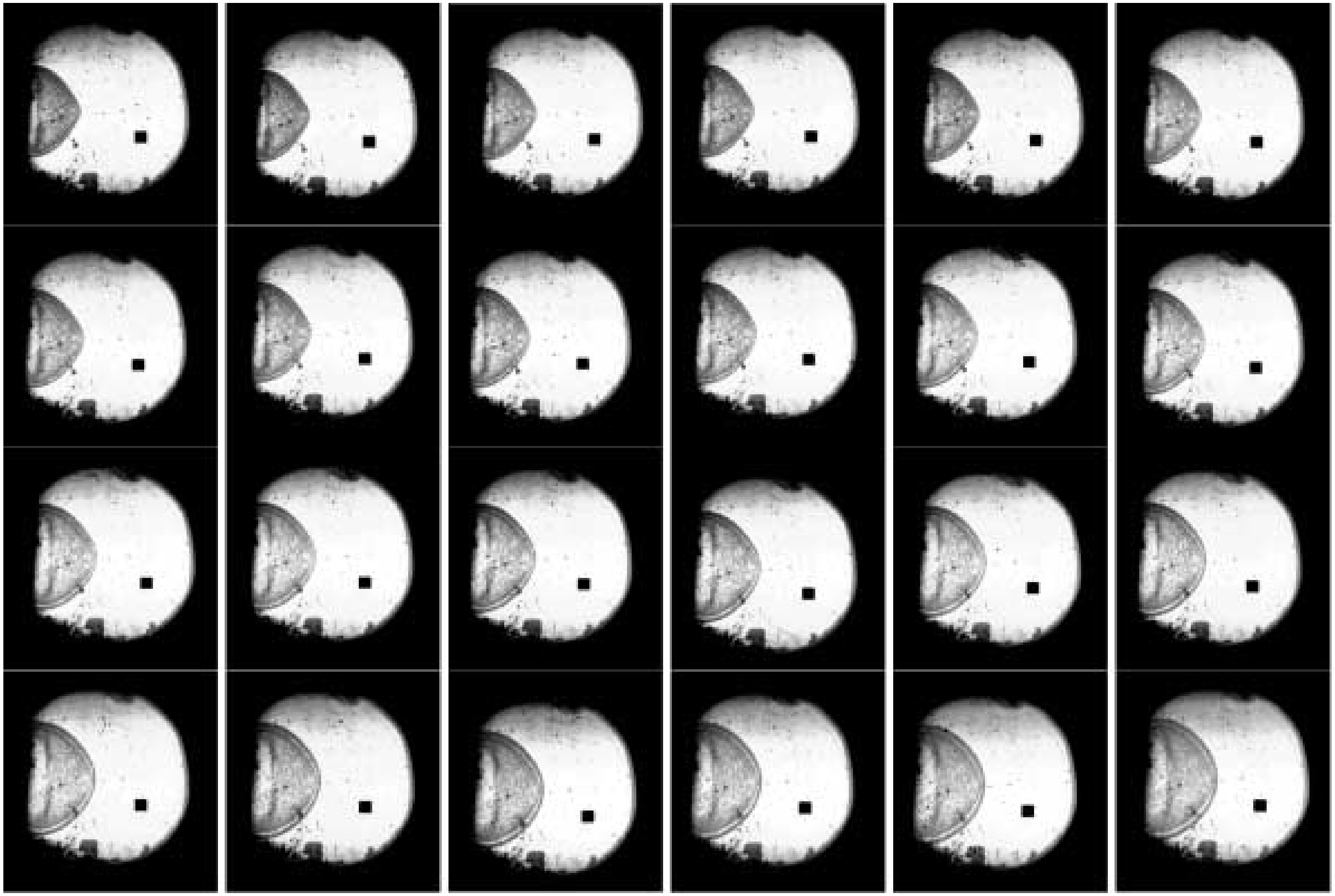

Stoichiometric propane-oxygen-carbon dioxide mixtures with varying carbon dioxide dilution (P_1 = 100 kPa)

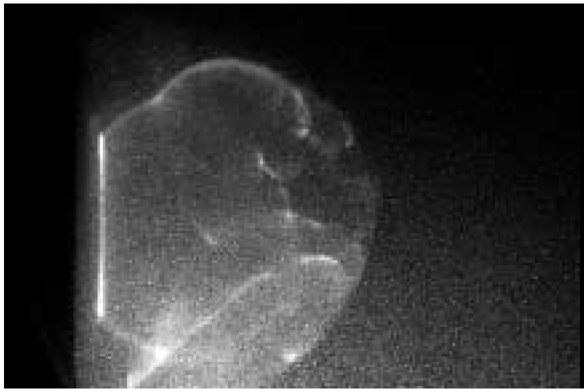

Shot 1257, 15% CO_2

Shot 1258, 20% CO_2

Shot 1259, 22.5% CO_2

Stoichiometric propane-oxygen-helium mixtures with varying helium dilution (P_1 = 100 kPa)

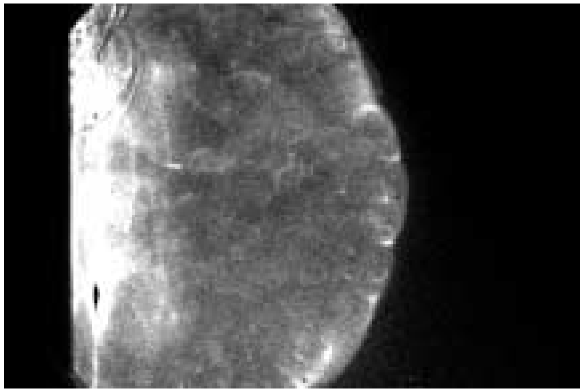

Shot 1261, 55% He

Stoichiometric propane-oxygen-nitrogen mixtures with varying nitrogen dilution (P_1 = 100 kPa)

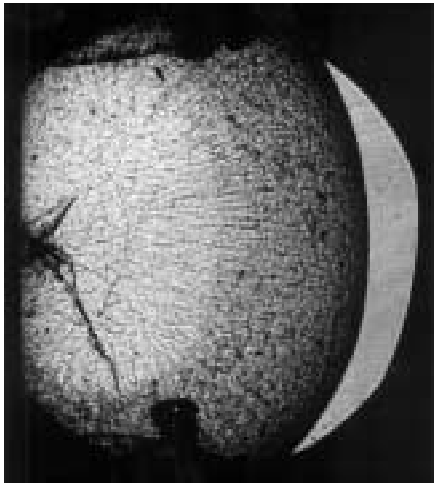

Shot 821, 29.4 $\%N_2$

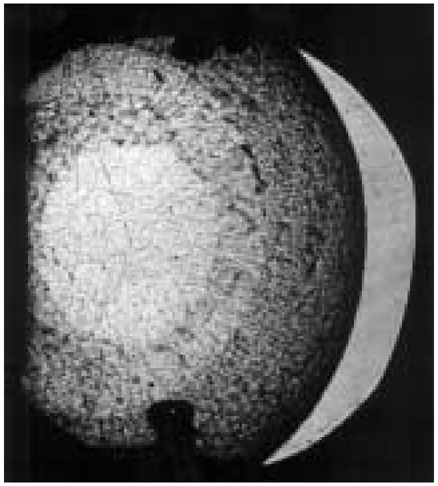

Shot 822, 31.8 $\%N_2$

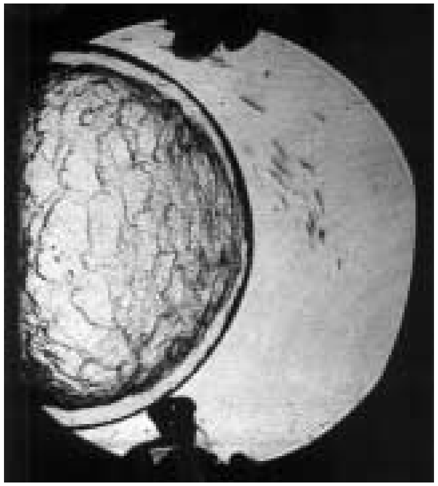

Shot 820, 33.3 $\%N_2$

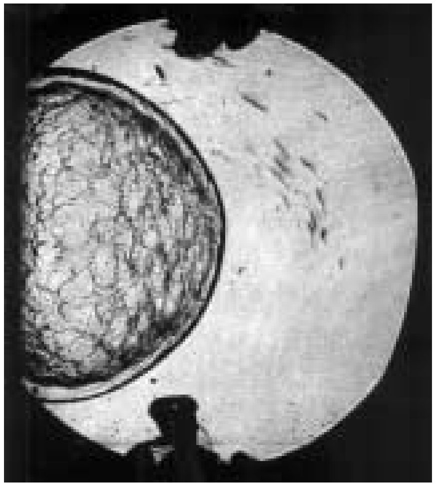

Shot 819, 36.8 $\%N_2$

Appendix F: Experimental critical diffraction conditions

The experimental critical conditions discussed in Section 5.7 and compared with the critical diffraction model results in Section 5.8 are tabulated in this appendix. The source indicates whether the data was identified through the experiments of this investigation or presented in the literature by other researchers.

Table F.1: Experimental critical diffraction conditions for hydrogen-oxygen mixtures with varying equivalence ratio.

P_1 (kPa)	ϕ	% diluent	d_c (mm)	Source
100.0	0.35	0.0	38	Schultz
101.3	0.57	0.0	25	Makris et al. (1994)
101.3	0.81	0.0	20	Makris et al. (1994)
101.3	0.95	0.0	20	Makris et al. (1994)
101.3	1.00	0.0	20	Matsui and Lee (1979)
101.3	1.22	0.0	25	Makris et al. (1994)
100.0	1.70	0.0	38	Schultz

Table F.2: Experimental critical diffraction conditions for hydrogen-air mixtures with varying equivalence ratio.

P_1 (kPa)	ϕ	% diluent	d_c (mm)	Source
101.3	0.50	65.2	1218	Guirao et al. (1982)
101.3	0.54	64.4	907	Guirao et al. (1982)
101.3	0.59	63.4	756	Guirao et al. (1982)
101.3	1.01	55.5	198	Guirao et al. (1982)
101.3	2.48	38.7	756	Guirao et al. (1982)
101.3	2.80	36.3	907	Guirao et al. (1982)
101.3	3.11	34.3	1218	Guirao et al. (1982)

Table F.3: Experimental critical diffraction conditions for hydrogen-oxygen mixtures with varying initial pressure.

P_1 (kPa)	ϕ	% diluent	d_c (mm)	Source
32.7	1.00	0.0	52	Shepherd et al. (1986a)

Table F.3: Experimental critical diffraction conditions for hydrogen-oxygen mixtures with varying initial pressure.

P_1 (kPa)	ϕ	% diluent	d_c (mm)	Source
37.0	1.00	0.0	53	Matsui and Lee (1979)
43.3	1.00	0.0	45	Moen et al. (1984b)
53.2	1.00	0.0	38	Schultz
66.1	1.00	0.0	27	Matsui and Lee (1979)
72.3	1.00	0.0	29	Moen et al. (1984b)
82.5	1.00	0.0	25	Schultz
101.3	1.00	0.0	20	Matsui and Lee (1979)
106.7	1.00	0.0	19	Zeldovich et al. (1956)
113.9	1.00	0.0	19	Matsui and Lee (1979)

Table F.4: Experimental critical diffraction conditions for hydrogen-oxygen-argon mixtures with varying dilution.

P_1 (kPa)	ϕ	% diluent	d_c (mm)	Source
101.3	1.00	0.0	20	Matsui and Lee (1979)
100.0	1.00	66.4	38	Schultz

Table F.5: Experimental critical diffraction conditions for hydrogen-oxygen-carbon dioxide mixtures with varying dilution.

P_1 (kPa)	ϕ	% diluent	d_c (mm)	Source
101.3	1.00	0.0	20	Matsui and Lee (1979)
100.0	1.00	4.8	38	Schultz

Table F.6: Experimental critical diffraction conditions for hydrogen-oxygen-helium mixtures with varying dilution.

P_1 (kPa)	ϕ	% diluent	d_c (mm)	Source
101.3	1.00	0.0	20	Matsui and Lee (1979)
100.0	1.00	50.0	38	Schultz

Table F.7: Experimental critical diffraction conditions for hydrogen-oxygen-nitrogen mixtures with varying dilution.

P_1 (kPa)	ϕ	% diluent	d_c (mm)	Source
101.3	1.00	0.0	20	Matsui and Lee (1979)

Table F.7: Experimental critical diffraction conditions for hydrogen-oxygen-nitrogen mixtures with varying dilution.

P_1 (kPa)	ϕ	% diluent	d_c (mm)	Source
101.3	1.00	7.7	24	Knystautas et al. (1982)
101.3	1.00	14.4	33	Matsui and Lee (1979)
100.0	1.00	18.6	38	Schultz
101.3	1.00	24.8	45	Matsui and Lee (1979)
101.3	1.00	28.4	52	Liu et al. (1984)
101.3	1.00	31.4	50	Knystautas et al. (1982)
101.3	1.00	36.6	91	Matsui and Lee (1979)
101.3	1.00	39.7	111	Matsui and Lee (1979)
101.3	1.00	41.0	92	Liu et al. (1984)
101.3	1.00	42.6	167	Matsui and Lee (1979)
101.3	1.00	44.2	90	Knystautas et al. (1982)
101.3	1.00	45.3	262	Matsui and Lee (1979)
101.3	1.00	46.5	127	Liu et al. (1984)
101.3	1.00	52.9	153	Knystautas et al. (1982)
101.3	1.00	54.8	200	Liu et al. (1984)
101.3	1.01	55.5	198	Guirao et al. (1982)
101.3	1.00	55.6	200	Knystautas et al. (1982)

Table F.8: Experimental critical diffraction conditions for ethylene-oxygen mixtures with varying equivalence ratio.

P_1 (kPa)	ϕ	% diluent	d_c (mm)	Source
100.0	0.35	0.0	38	Schultz
101.3	0.47	0.0	25	Makris et al. (1994)
101.3	0.51	0.0	20	Makris et al. (1994)
101.3	0.60	0.0	15	Makris et al. (1994)
101.3	0.76	0.0	10	Makris et al. (1994)
101.3	1.00	0.0	6	Matsui and Lee (1979)
101.3	1.50	0.0	5	Matsui and Lee (1979)
101.3	2.12	0.0	10	Makris et al. (1994)

Table F.8: Experimental critical diffraction conditions for ethylene-oxygen mixtures with varying equivalence ratio.

P_1 (kPa)	ϕ	% diluent	d_c (mm)	Source
101.3	2.37	0.0	15	Makris et al. (1994)
101.3	2.62	0.0	20	Makris et al. (1994)
101.3	2.81	0.0	25	Makris et al. (1994)
100.0	3.00	0.0	38	Schultz

Table F.9: Experimental critical diffraction conditions for ethylene-air mixtures with varying equivalence ratio.

P_1 (kPa)	ϕ	% diluent	d_c (mm)	Source
100.0	0.67	75.5	1284	Rinnan (1982)
100.0	0.67	75.5	1820	Moen et al. (1984a)
100.0	0.69	75.4	944	Rinnan (1982)
100.0	0.75	75.0	883	Moen et al. (1982)
100.0	0.78	74.9	433	Rinnan (1982)
100.0	0.98	73.9	444	Moen et al. (1982)
100.0	0.99	73.9	462	Moen et al. (1982)

Table F.10: Experimental critical diffraction conditions for ethylene-oxygen mixtures with varying initial pressure.

P_1 (kPa)	ϕ	% diluent	d_c (mm)	Source
13.3	1.00	0.0	50	Moen et al. (1984b)
14.6	1.00	0.0	53	Matsui and Lee (1979)
17.5	1.00	0.0	38	Schultz
27.0	1.00	0.0	27	Matsui and Lee (1979)
54.3	1.00	0.0	12	Matsui and Lee (1979)
101.3	1.00	0.0	6	Matsui and Lee (1979)
106.7	1.00	0.0	9	Zeldovich et al. (1956)

Table F.11: Experimental critical diffraction conditions for ethylene-oxygen-argon mixtures with varying dilution.

P_1 (kPa)	ϕ	% diluent	d_c (mm)	Source
101.3	1.00	0.0	6	Matsui and Lee (1979)

Table F.11: Experimental critical diffraction conditions for ethylene-oxygen-argon mixtures with varying dilution.

P_1 (kPa)	ϕ	% diluent	d_c (mm)	Source
100.0	1.00	75.0	38	Schultz

Table F.12: Experimental critical diffraction conditions for ethylene-oxygen-carbon dioxide mixtures with varying dilution.

P_1 (kPa)	ϕ	% diluent	d_c (mm)	Source
101.3	1.00	0.0	6	Matsui and Lee (1979)
100.0	1.00	22.5	38	Schultz

Table F.13: Experimental critical diffraction conditions for ethylene-oxygen-helium mixtures with varying dilution.

P_1 (kPa)	ϕ	% diluent	d_c (mm)	Source
101.3	1.00	0.0	6	Matsui and Lee (1979)
100.0	1.00	62.5	38	Schultz

Table F.14: Experimental critical diffraction conditions for ethylene-oxygen-nitrogen mixtures with varying dilution.

P_1 (kPa)	ϕ	% diluent	d_c (mm)	Source
101.3	1.00	0.0	6	Matsui and Lee (1979)
100.0	1.00	19.9	12	Moen et al. (1981)
101.3	1.00	22.0	13	Knystautas et al. (1982)
100.0	1.00	39.2	25	Moen et al. (1981)
101.3	1.00	39.6	24	Knystautas et al. (1982)
101.3	1.00	42.4	21	Matsui and Lee (1979)
100.0	1.00	43.7	38	Schultz
101.3	1.00	49.6	52	Liu et al. (1984)
101.3	1.00	50.8	50	Knystautas et al. (1982)
100.0	1.00	51.2	51	Moen et al. (1981)
101.3	1.00	52.6	46	Matsui and Lee (1979)
101.3	1.00	56.8	90	Knystautas et al. (1982)
100.0	1.00	56.9	91	Moen et al. (1981)
101.3	1.00	58.0	92	Liu et al. (1984)

Table F.14: Experimental critical diffraction conditions for ethylene-oxygen-nitrogen mixtures with varying dilution.

P_1 (kPa)	ϕ	% diluent	d_c (mm)	Source
101.3	1.00	59.7	96	Matsui and Lee (1979)
101.3	1.00	63.7	127	Liu et al. (1984)
101.3	1.00	65.1	176	Matsui and Lee (1979)
101.3	1.00	65.2	153	Knystautas et al. (1982)
100.0	1.00	65.3	153	Moen et al. (1981)
100.0	1.00	69.2	208	Moen et al. (1981)
101.3	1.00	69.2	200	Knystautas et al. (1982)
100.0	0.99	73.9	462	Moen et al. (1982)
100.0	0.98	73.9	444	Moen et al. (1982)

Table F.15: Experimental critical diffraction conditions for propane-oxygen mixtures with varying equivalence ratio.

P_1 (kPa)	ϕ	% diluent	d_c (mm)	Source
101.3	0.53	0.0	30	Makris et al. (1994)
100.0	0.55	0.0	38	Schultz
101.3	0.58	0.0	25	Makris et al. (1994)
101.3	0.67	0.0	20	Makris et al. (1994)
101.3	0.83	0.0	15	Makris et al. (1994)
101.3	1.00	0.0	10	Matsui and Lee (1979)
101.3	1.00	0.0	13	Knystautas et al. (1982)
101.3	1.25	0.0	10	Makris et al. (1994)
101.3	1.28	0.0	10	Makris et al. (1994)
101.3	1.83	0.0	15	Makris et al. (1994)
101.3	2.00	0.0	20	Makris et al. (1994)
101.3	2.12	0.0	25	Makris et al. (1994)
101.3	2.20	0.0	30	Makris et al. (1994)
100.0	>2.4	0.0	38	Schultz

Table F.16: Experimental critical diffraction conditions for propane-air mixtures with varying equivalence ratio.

P_1 (kPa)	ϕ	% diluent	d_c (mm)	Source
100.0	0.79	76.4	1830	Moen et al. (1984a)
100.0	1.14	75.4	880	Moen et al. (1984a)
100.0	1.23	75.1	863	Moen et al. (1984a)

Table F.17: Experimental critical diffraction conditions for propane-oxygen mixtures with varying initial pressure.

P_1 (kPa)	ϕ	% diluent	d_c (mm)	Source
24.6	1.00	0.0	53	Matsui and Lee (1979)
30.0	1.00	0.0	38	Schultz
45.1	1.00	0.0	27	Matsui and Lee (1979)
60.9	1.00	0.0	20	Higgins and Lee (1998)
94.5	1.00	0.0	12	Matsui and Lee (1979)
101.3	1.00	0.0	10	Matsui and Lee (1979)
101.3	1.00	0.0	13	Knystautas et al. (1982)

Table F.18: Experimental critical diffraction conditions for propane-oxygen-argon mixtures with varying dilution.

P_1 (kPa)	ϕ	% diluent	d_c (mm)	Source
101.3	1.00	0.0	10	Matsui and Lee (1979)
101.3	1.00	0.0	13	Knystautas et al. (1982)
100.0	1.00	68.8	38	Schultz

Table F.19: Experimental critical diffraction conditions for propane-oxygen-carbon dioxide mixtures with varying dilution.

P_1 (kPa)	ϕ	% diluent	d_c (mm)	Source
101.3	1.00	0.0	10	Matsui and Lee (1979)
101.3	1.00	0.0	13	Knystautas et al. (1982)
100.0	1.00	21.3	38	Schultz

Table F.20: Experimental critical diffraction conditions for propane-oxygen-helium mixtures with varying dilution.

P_1 (kPa)	ϕ	% diluent	d_c (mm)	Source
101.3	1.00	0.0	10	Matsui and Lee (1979)
101.3	1.00	0.0	13	Knystautas et al. (1982)
100.0	1.00	57.5	38	Schultz

Table F.21: Experimental critical diffraction conditions for propane-oxygen-nitrogen mixtures with varying dilution.

P_1 (kPa)	ϕ	% diluent	d_c (mm)	Source
101.3	1.00	0.0	10	Matsui and Lee (1979)
101.3	1.00	0.0	13	Knystautas et al. (1982)
101.3	1.00	20.7	24	Knystautas et al. (1982)
101.3	1.00	29.0	25	Matsui and Lee (1979)
100.0	1.00	32.6	38	Schultz
101.3	1.00	43.1	51	Ungut et al. (1984)
101.3	1.00	43.9	50	Knystautas et al. (1982)
101.3	1.00	44.7	50	Matsui and Lee (1979)
101.3	1.00	53.4	90	Knystautas et al. (1982)
101.3	1.00	55.2	103	Matsui and Lee (1979)
101.3	1.00	56.8	101	Ungut et al. (1984)
101.3	1.00	59.3	153	Knystautas et al. (1982)
101.3	1.00	59.9	140	Ungut et al. (1984)
101.3	1.00	62.3	221	Matsui and Lee (1979)
101.3	1.00	63.9	200	Knystautas et al. (1982)